PHOTOELECTROCHEMICAL AND PHOTOCATALYTIC INVESTIGATION OF SEMICONDUCTING IRON OXIDE FOR SOLAR ENERGY CONVERSION

Michael Strasik
B.S., Portland State University, 1983

A dissertation submitted to the faculty
of the Oregon Graduate Center
in partial fulfillment of the
requirements for the degree
Doctor of Philosophy
in
Materials Science
and Engineering

May, 1988

The dissertation "Photoelectrochemical and Photocatalytic Investigation of Semiconducting Iron Oxide for Solar Energy Conversion" by Michael Strasik has been examined and approved by the following Examination Committee:

Nicholas G. Eror, Thesis Advisor
Professor

Jack H. Devletian
Professor

S. Shankar
Assistant Professor

Anthony E. Bell
Associate Research Professor

TABLE OF CONTENTS

LIST OF FIGURES.....v

ABSTRACT.....x

Chapter

1. INTRODUCTION..... 1

1.1 Photoelectrochemical Cells..... 1
1.2 PEC System Requirements..... 8

1.2.1 Energetics..... 9
1.2.2 Photo-Induced Charge Transfer..... 15

1.3 Semiconductor Electrode Stability..... 17
1.4 Efficiency..... 19

2. REVIEW OF RELATED WORK..... 23

2.1 Physical Structure..... 23
2.2 Phase Transformations..... 26
2.3 Preparation Techniques..... 27
2.4 Lattice Dynamics, Raman and Infrared Spectra..... 29
2.5 Surface Properties..... 32
2.6 Optical and Dielectric Properties..... 34
2.7 Electronic Transport and Impurity Related Effects..... 35
2.8 Photoanodes..... 38

2.8.1 Single Crystals..... 38
2.8.2 Thin Films..... 40
2.8.3 Polycrystalline Electrodes..... 44
2.8.4 Heterojunctions..... 57

2.9 Metallized Electrodes..... 62
2.10 Photocathodes..... 64
2.11 Photocatalysts..... 65

3. EXPERIMENTAL PROCEDURES..... 68

3.1 Sample Preparation..... 68

3.1.1 Solid State Mixing Technique..... 68
3.1.2 Freeze-Drying Technique..... 69

3.2 Structural Characterization..... 72
3.3 Electron Microscopy Studies..... 72
3.4 Electrical Conductivity and Dielectric Measurements..... 73
3.5 Photoelectrochemical and Capacitance Measurements..... 74
3.6 Cyclic Voltammetry Measurements..... 77
3.7 Photoconductivity Measurements..... 79
3.8 Photocatalytic Measurements..... 81

4. EXPERIMENTAL RESULTS AND DISCUSSION..... 83

4.1 Structural and Microscopic Characterization of Fe_2O_3..... 83
4.2 Electrical Conductivity and Dielectric Constant of Doped Fe_2O_3.....112
4.3 Photoactivity of Pure and Platinized Si Doped Fe_2O_3.....119
4.4 Photoactivity of Pure and Platinized Mg Doped Fe_2O_3.....152
4.5 Spectral Response of Doped and Platinized Fe_2O_3.....166
4.6 Capacitance Studies and Flat-Band Potentials for Fe_2O_3.....178
4.7 Cyclic Voltammetry Experiments of Doped and Platinized Fe_2O_3.....197
4.8 Photocatalytic Studies.....207

5. CONCLUSIONS.....223

REFERENCES.....227

VITA.....246

LIST OF FIGURES

Figure		Page
1.1	Solar spectrum	3
1.2	Energy band structure of PEC	5
1.3	Energy level diagram for semiconductor/electrolyte interface	10
1.4	Energy correlations between band edges and decomposition Fermi levels	20
2.1	Phase diagram of the Fe-O system	24
2.2	Structure of magnetite	25
2.3	I and quantum efficiency vs. V for Fe_2	
2.4	I and quantum efficiency vs. V for Fe_2O_3 (400 nm)	45
2.5	I and quantum efficiency vs. V for Fe_2O_3 (400 nm)	46
2.6	I and quantum efficiency vs. V for Fe_2O_3 (400 nm)	46
2.7	Mott-Schottky plots for Fe_2O_3	52
2.8	Energy level diagram for polycrystalline Fe_2O_3	54
2.9	Energetics of the n-Fe_2O_3/p-GaP diode	59
2.10	A p/n Fe_2O_3 assembly	60
2.11	Photocurrents for Si-doped and Mg-doped Fe_2O_3	61
3.1	A schematic diagram of the freeze-drying apparatus	71
3.2	Experimental arrangements for the photoelectrochemical measurements	76
3.3	Experimental arrangements for the cyclic voltammetry experiments	78
3.4	Experimental arrangements for the quantum efficiency measurements	80
4.1	SEM micrograph, commercial Fe_2O_3 (1000X)	86

4.2	X-ray spectrum of commercial Fe_2O_3	87
4.3	X-ray spectrum of Fe_2O_3 (1420° C for 24 hours)	88
4.4	FT-IR of commercial Fe_2O_3	89
4.5	SEM micrograph of freeze-dried Fe_2O_3 (2000X), pH=3.7	90
4.6	SEM micrograph of freeze-dried Fe_2O_3 (2000X), pH=5.5	91
4.7	FT-IR of freeze-dried Fe_2O_3 (from $FeCl_3$ sol)	93
4.8	FT-IR of freeze-dried Fe_2O_3 (from $FeCl_3$ sol)	94
4.9	FT-IR of freeze-dried Fe_2O_3 (from $Fe(NO_3)_3$ sol)	95
4.10	FT-IR of freeze-dried Fe_2O_3 (from $Fe(NO_3)_3$ sol)	96
4.11	Surface area vs. T for the freeze-dried Fe_2O_3	98
4.12	SEM micrograph of freeze-dried Fe_2O_3 (1300° C) (1000X)	99
4.13	FT-IR of platinized freeze-dried Fe_2O_3	100
4.14	SEM micrograph of a pure Fe_2O_3 sintered 1385° C (1000X)	102
4.15	Grain size vs. Pt for pure and 0.1%Si Fe_2O_3	103
4.16	Grain size vs. Pt for 1% and 5%Si Fe_2O_3	104
4.17	SEM micrograph of solid state 1%Pt Fe_2O_3 1385°C (1000X)	105
4.18	SEM micrograph of solid state 1%Si Fe_2O_3 1385°C (1000X)	106
4.19	SEM micrograph of freeze-dried 1%Mg Fe_2O_3 1385°C(1000X)	108
4.20	SEM micrograph of solid state 1%Mg Fe_2O_3 1385°C (1000X)	109
4.21	SEM micrograph of freeze-dried 1%Pt Fe_2O_3 1385°C(1000X)	110
4.22	Grain size vs. Pt for 1% and 5% Mg	111
4.23	Log resistivity vs. Pt for pure FD Fe_2O_3	113
4.24	Log resistivity vs. Pt for Si doped FD Fe_2O_3	115
4.25	Log resistivity vs. Pt for Si doped solid state Fe_2O_3	116
4.26	Log resistivity vs. Pt for Mg doped FD Fe_2O_3	117
4.27	Log resistivity vs. Pt for Mg doped solid state Fe_2O_3	118

4.54	I-V for solid state Pt and 1%Mg doped Fe_2O_3	155
4.55	I-V for solid state Pt and 5%Mg doped Fe_2O_3	156
4.56	I-V for freeze-dried Mg doped Fe_2O_3	157
4.57	I-V for freeze-dried Pt and 1%Mg doped Fe_2O_3	158
4.58	I-V for freeze-dried Pt and 5%Mg doped Fe_2O_3	159
4.59	Charge transfer resistance vs. Pt for Mg doped Fe_2O_3	161
4.60	Charge transfer resistance vs. Pt for Mg doped Fe_2O_3	162
4.61	Exchange current density at 0V vs. Pt in FD Mg-Fe_2O_3	164
4.62	Exchange current density at 0V vs. Pt in SS Mg-Fe_2O_3	165
4.63	Spectral response of pure Fe_2O_3	167
4.64	Bandgap determination from photocurrent efficiencies	168
4.65	Spectral response of pure and platinized Fe_2O_3	169
4.66	Spectral response of pure and Si doped Fe_2O_3	170
4.67	Spectral response of Pt and Si doped Fe_2O_3	171
4.68	Spectral response of Pt and Si doped Fe_2O_3	172
4.69	Spectral response of 1%Si + 5%Pt(surface) doped Fe_2O_3	174
4.70	Spectral response of Mg doped Fe_2O_3	175
4.71	Spectral response of Pt and Mg doped Fe_2O_3	176
4.72	Spectral response of Pt and Mg doped Fe_2O_3	177
4.73	I^2 vs. V for pure FD Fe_2O_3	181
4.74	Mott-Schottky plot for a pure FD Fe_2O_3	183
4.75	I^2 vs. V for Pt doped FD Fe_2O_3	184
4.76	I^2 vs. V for Pt and 0.1%Si doped FD Fe_2O_3	185
4.77	I^2 vs. V for Pt and 1%Si doped FD Fe_2O_3	186
4.78	I^2 vs. V for Pt and 5%Si doped FD Fe_2O_3	187
4.79	I^2 vs. V for Pt and 1%Mg doped FD Fe_2O_3	188

4.80	I^2 vs. V for Pt and 5%Mg doped FD Fe_2O_3	189
4.81	Mott-Schottky plot for Pt doped FD Fe_2O_3	190
4.82	Mott-Schottky plot for Si doped FD Fe_2O_3	191
4.83	Mott-Schottky plot for Pt and 0.1%Si doped FD Fe_2O_3	192
4.84	Mott-Schottky plot for Pt and 1%Mg doped FD Fe_2O_3	193
4.85	Energy level diagram for Fe_2O_3	195
4.86	Cyclic voltammogram of 0.1%Pt doped FD Fe_2O_3	198
4.87	Cyclic voltammogram of 0.1%Pt doped FD Fe_2O_3	199
4.88	Cyclic voltammogram of 1%Si+0.1%Pt doped FD Fe_2O_3	201
4.89	Cyclic voltammogram of 1%Si+1%Pt doped FD Fe_2O_3	202
4.90	Cyclic voltammogram of 1%Si+5%Pt doped FD Fe_2O_3	203
4.91	Cyclic voltammogram of 1%Si+0.1%Pt doped FD Fe_2O_3	204
4.92	Cyclic voltammogram of 5%Mg+0.1%Pt doped FD Fe_2O_3	205
4.93	Cyclic voltammogram of 5%Mg+0.1%Pt doped FD Fe_2O_3	206
4.94	Absorption spectrum of Fe_2O_3 sol	208
4.95	O_2 content vs. time for oxygen absorption	209
4.96	O_2 content vs. time for deionized H_2O	211
4.97	O_2 content vs. time for 20mg Fe_2O_3/l + $AgNO_3$	212
4.98	O_2 content vs. time for 100mg Fe_2O_3/l + $AgNO_3$	213
4.99	O_2 content vs. time for 20mg Si-Fe_2O_3/l + $AgNO_3$	215
4.100	O_2 content vs. time for 20mg Pt-Fe_2O_3/l + $AgNO_3$	216
4.101	O_2 content vs. time for 20mg Si+Pt-Fe_2O_3/l + $AgNO_3$	217
4.102	O_2 content vs. time for 20mg Si+Pt-Fe_2O_3/l + $AgNO_3$	218
4.103	O_2 content vs. Pt for 20mg Si-Fe_2O_3/l + $AgOO_3$	220
4.104	Quantum efficiencies vs. Pt for 20 mg Fe_2O_3/l	221
4.105	Quantum efficiencies vs. Fe_2O_3 content	222

ABSTRACT

PHOTOLECTROCHEMICAL AND PHOTOCATALYTIC INVESTIGATION OF SEMICONDUCTING IRON OXIDE FOR SOLAR ENERGY CONVERSION

Michael Strasik, Ph.D.
Oregon Graduate Center, 1988

Supervising Professor: Nicholas G. Eror

Well characterized and reproducible semiconducting Fe_2O_3 was prepared by freeze-drying. This technique produced very homogeneously Si, Mg, or Pt doped semiconducting Fe_2O_3 that was used successfully in the photoelectrochemical and photocatalytic solar cell for the production of gaseous hydrogen and oxygen by dissociating water. Photocurrents obtained with the photoelectrodes prepared from the freeze-dried samples were more stable and up to ten times higher than with the samples prepared by the conventional solid state mixing technique. The maximum photocurrent density obtained with the freeze-dried samples was 10 mA/cm^2 at 0.8 V vs SCE for the 0.1 at.% Si + 5 at.% Pt doped Fe_2O_3. The photocurrent also increased with increasing amounts of platinum. The added platinum was shown to have several beneficial effects on the n-type and p-type photoelectrodes. In the Si doped n-type semiconduc-

tor the platinum increased the carrier concentration via a shallow donor level within the bandgap. It was also shown that the platinum enhanced the probabilities of electron exchange and increased the reaction kinetics between the electrode and electrolyte species. The efficiency of the photoelectrochemical reactions was increased with added platinum by eliminating the transient currents. In the cyclic voltammetry experiments it was shown that the platinum in the n-type semiconductor at negative potentials acts as a local cathode and enhances the production of hydrogen. In the p-type Fe_2O_3, the platinum acts as an electrocatalyst and lowers the overpotential for hydrogen reduction.

A p/n heterojunction was used in the photoelectrochemical solar cell to photodissociate water into oxygen and hydrogen with visible light. This important result was further improved by using Fe_2O_3 electrodes prepared by freeze-drying and by the addition of platinum. The photogeneration of oxygen was also achieved in the photocatalytic solar cell by irradiating doped and platinized Fe_2O_3 in the presence of an electron scavenger.

The Fe_2O_3 was found to be stable against photocorrosion for extended periods of illumination and photocurrent generation in a basic electrolyte. It was shown that doped and platinized freeze-dried Fe_2O3 can be used more efficiently than the Fe_2O_3 prepared by the solid state technique in the photoelectrochemical and photocatalytic cell for the gaseous fuel generation using solar energy.

CHAPTER ONE

INTRODUCTION

1.1 Photoelectrochemical cells

Mankind has regarded the sun as the source of life and energy since time immemorial. In fact, our traditional energy resources (such as oil and coal) are all products of photosynthesis. With the increasing energy crisis, man is again looking towards the prime energy giver, the sun. Harnessing solar energy has therefore attracted the attention of the scientists, technologists, economists, sociologists and politicians. All the solar energy converters utilize the radiation received from the sun. Hence, an understanding of the nature of the radiation is imperative.

Forming fuels photochemically would convert sunlight to a useful form of energy that can be stored and transported. Thus, using the sun's energy to generate fuels can be envisioned as part of the ultimate solution to the world's energy problems. Raw materials such as water, nitrogen, oxygen, and carbon dioxide exist in sufficient abundance and at low enough cost to be viewed as the feedstocks of solar reactors to produce fuels of the future.

A lot of progress has been made in the art of photovoltaics [1-4], where sunlight is captured by a semiconducting material (usually silicon) and converted into electrical energy. This energy can then either be used immediately or collected in a storage device such as a

battery. An alternative method of collecting solar energy is to convert it into chemical energy that can be easily stored. This is done naturally in photosynthesis. To do this artificially would require the selection of a two level chemical reaction reasonably well matched to the solar spectrum.

The solar spectrum peaks at a wavelength of about 460 nm, corresponding to an energy of 2.70 eV, and drops to zero at a wavelength of about 300 nm (4.13eV). Figure 1.1 shows the spectral distribution of sunlight at air mass one. The bulk of the solar energy is found in the range 1.13-4.13 eV (1100 to 300 nm), and any chemical reaction chosen to capture that energy efficiently must have an oxidation/reduction potential overlapping that range. In addition, the chemical reaction products must be suitable for use as a storable, portable fuel with a minimum energy cost of retrieval. The photodissociation of water is ideally suited for this purpose.

The oxidation/reduction potential of the reaction:

$$H_2O + \text{light} \rightarrow H_2 + \tfrac{1}{2}O_2 \qquad (1.1)$$

is 1.23 eV, but oxygen electrode overpotential considerations [5] actually place the minimum at about 1.60 eV. This overpotential is caused by barriers to charge transfer at the semiconductor/electrolyte interface. The energy of 1.60 eV approximately corresponds to a wavelength of 770 nm, a wavelength available in solar radiation. Unfortunately, water does not have a strong absorption coefficient in this region. So, either the chemical entities

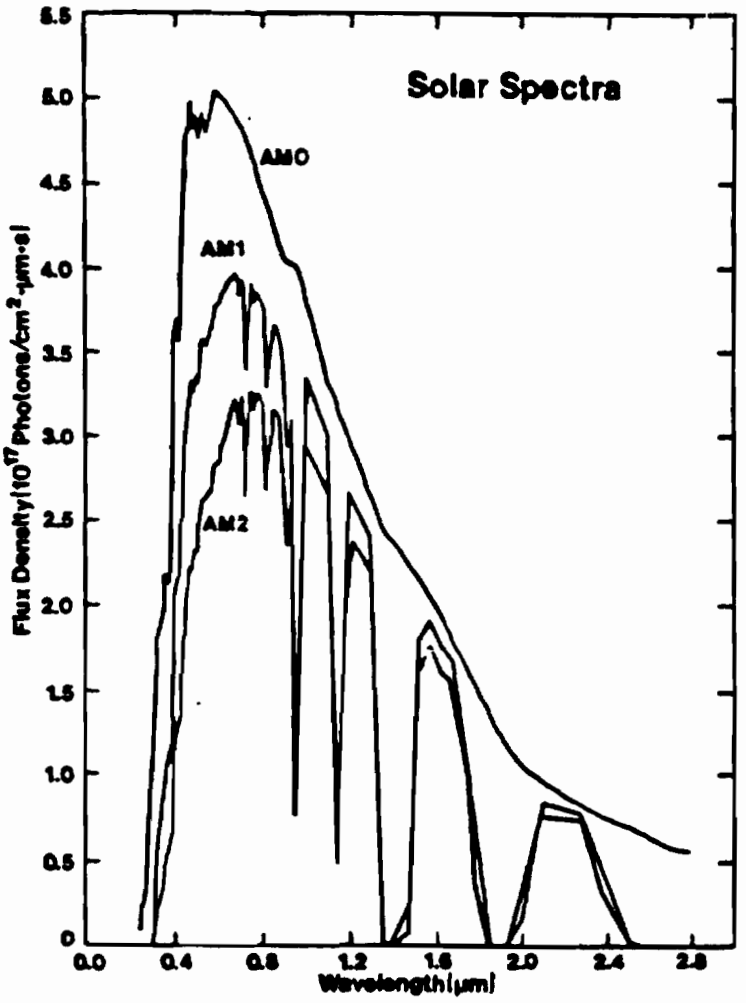

Figure 1.1. Spectral distribution curve of solar irradiation at AM0, AM1, and AM2.

H_2 and O_2 are not formed or whatever small amounts are formed tend to recombine to yield water. There exists a threshold energy of about 6.5 eV (190 nm) only beyond which direct photodecomposition is possible. Such high-energy radiation does not reach the earth's surface from the sun. So, the strategy adopted for splitting of water by photons has been to carry out the photodecomposition sequentially. The agents employed for the purpose are known as photocatalysts.
The common photocatalysts are: common salt, photosynthetic dyes, semiconductors, etc.

The reaction in Eqn. 1.1 can be utilized in a photoelectrochemical cell (PEC). Most commonly this is a liquid-semiconductor junction device where sunlight is absorbed by a photoactive semiconducting electrode. Figure 1.2 is a schematic energy diagram of such a device using an n-type semiconducting photoanode and a metallic cathode. In this device absorption of sunlight of energy greater than the semiconductor bandgap energy, E_g, would produce electron-hole pairs available for conduction. Equilibration of the Fermi level, E_f, throughout the cell results in the formation of a space charge region within the semiconductor [6-7]. The pairs created in this region can then be separated to produce current through the cell.

The potential distribution within the semiconductor is such that the holes are driven towards the surface and electrons towards the bulk of the material. The holes are transferred at the semiconductor surface to water molecules, resulting in release of oxygen. If the photovoltage is large enough to raise the Fermi level of the metal above the normal potential of the H_2O/H_2 couple, electrons can than be

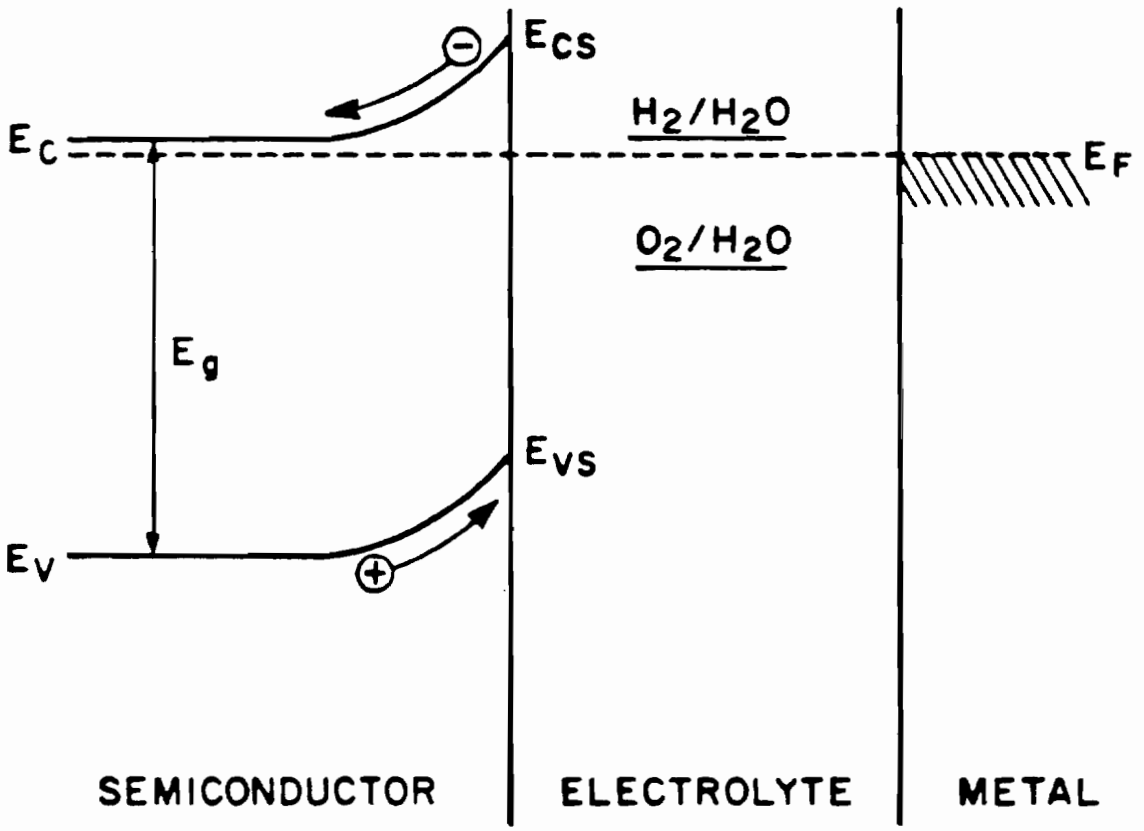

Figure 1.2. Energy band structure of photoelectrochemical cell.

transferred from the metal to the water.

The electrode reactions are:

At the semiconductor electrode

$$H_2O + 2h^+ \rightarrow 2H^+ + \tfrac{1}{2}O_2 \qquad (1.2)$$

At the metal electrode

$$2H_2O + 2e^- \rightarrow 2OH^- + H_2 \qquad (1.3)$$

Two simple conditions must be met for the above overall reaction to materialize:

(a) The flat band potential of the semiconductor must be more negative than the potential of the H_2O/H_2 couple. In other words, conduction band energy must lie above the $E_{H2O/H2}$ level.

(b) The valence band should lie below the $E_{H2O/O2}$ couple, otherwise no transfer of holes from the valence band is possible.

Both conditions can be fulfilled simultaneously if:

$$E_g = E_c - E_v > E_{H2O/H2} - E_{H2O/O2} = 1.23 \text{ eV} \qquad (1.4)$$

The energy consumed by photogenerated electrons to move from the conduction band via the external circuit to the counter electrode is:

$$(E_c - E_f) + e.V_b \qquad (1.5)$$

where V_b is the band bending. The net energy available for photoelectrolysis reaction would be:

$$E_g - [(E_c - E_f) + e.V_b] \qquad (1.6)$$

The energy available must be equal to or greater than the combined energy necessary for:

(a) Photoelectrolysis.

(b) Ohmic loss (IR).

(c) Photoelectrode overpotential (η_a) associated with the evolution of O_2 which is the difference between the valence band edge and the H_2O/O_2 level.

(d) Counter electrode overpotential (η_c) associated with the evolution of H_2 which is the difference between the conduction band edge and H_2/H_2O level.

(e) Potential across the Helmholtz layer (V_H), since during photoexcitation the Helmholtz layer relaxes.

Hence, an energy balance equation for an n-type semiconductor and metal counter electrode can be written as:

$$E_g - [(E_c - E_f) + e.V_b] = \frac{G}{n.F} + [\eta_a + \eta_c + IR + V_H]e \qquad (1.7)$$

where n is the number of electrons transferred in a single step of the

reaction.Obviously, the energy available for photoelectrolysis is smaller than E_g. So a natural choice would be to use a wide band gap semiconductor. However, a very wide band gap is not acceptable because it would meanthat fewer carriers would bephotogenerated and only a small portion og solar spectrum could be utilized. As a compromise, materials with $E_g \sim 2.2$ eV are taken as suitable (1.23 eV for photoelectrolysis and 1 eV for losses including oxygen overpotential).

1.2 PEC System Requirements

A number of excellent theoretical and experimental reviews [8-32] has been written on the development and requirements of photoelectrochemical solar cells. The choice of semiconductor materials is a very complex problem for photoelectrochemical cells. The following basic requirements should be fulfilled:

(a) The band gap of the material should be such that the maximum part of solar spectrum is used. Most of the visible part of solar energy reaching the earth's surface is centered in the range 1.0-3.0 eV (See Figure 1.1). Therefore, very wide band gap semiconductors are not suitable.

(b) The efficiency ofthe cell should be high which depends upon absorption coefficient, band gap, diffusion length, conductivity, recombination, surface states, etc.

(c) The electrode must be stable against corrosion when placed in the specific redox electrolyte. Low band gap semiconductors are generally easily corroded, as will be discussed later.

Thus, before choosing a particular semiconductor it is important to

understand the various controlling factors.

1.2.1 Energetics

All phenomena associated with photoelectrochemical systems are based on the formation of a semiconductor-electrolyte junction [33-36] when an appropriate semiconductor is immersed in a suitable electrolyte. The junction is characterized by the presence of a space charge layer in the semiconductor adjacent to the interface with the electrolyte. A space charge layer generally develops in a semiconductor upon contact and equilibration with a second phase whenever the initial chemical potential of electrons is different for the two phases. For semiconductors, the chemical potential of electrons is given by the Fermi level in the semiconductor. For liquid electrolytes, it is determined by the redox potential of the redox couples present inthe electrolyte [37]. If the initial Fermi level in an n-type semiconductor is above the initial Fermi level in the electrolyte (or any second phase), then equilibration of the two Fermi levels occurs by transfer of electrons from the semiconductor to the electrolyte. This produces a positive space charge layer in the semiconductor (also called a depletion layer since the region is depleted of majority charge carriers). As a result, the conduction and valence band edges are bent such that a potential barrier is established against further electron transfer into the electrolyte (see Figure 1.3) [11].

The inverse but analogous situation occurs with p-type semiconductors having an initial Fermi level below that of the electrolyte. A negative space charge or depletion layer is formed in the semi-

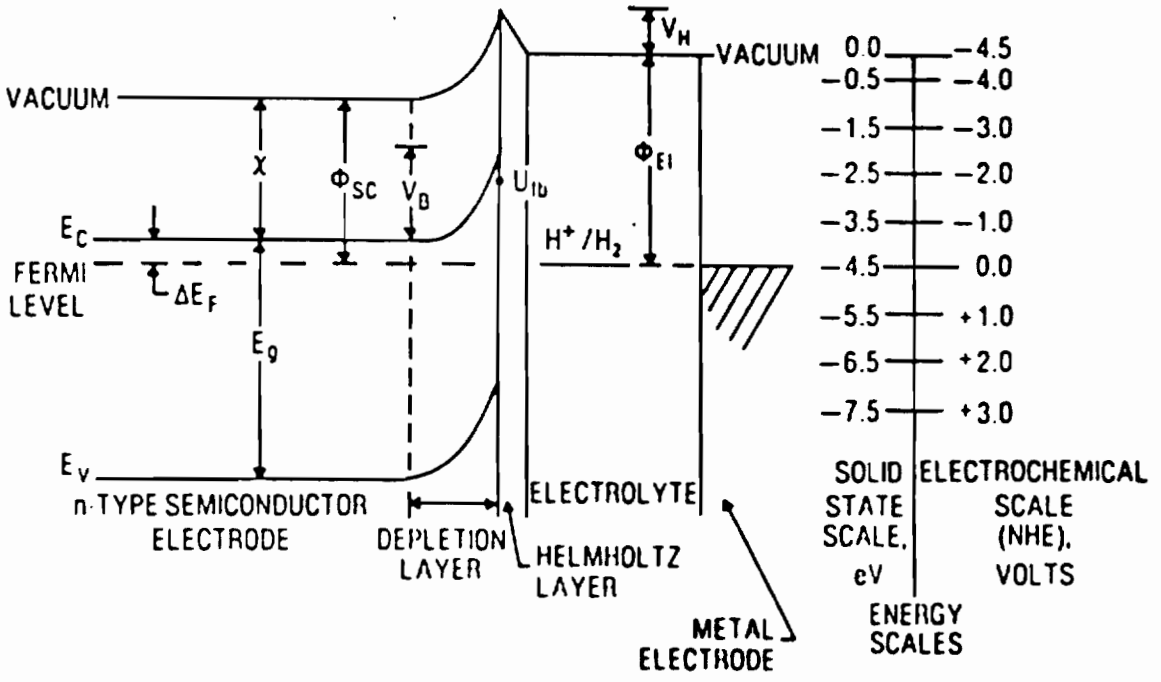

Figure 1.3. Energy level diagram for semiconductor-electrolyte junction.

conductor, with the valence and conduction bands bending to produce a potential barrier against further positive hole transfer into the electrolyte.

The width of the depletion layer w is given by:

$$w = (2\epsilon\epsilon_0 V_b/qN)^{\frac{1}{2}} \tag{1.8}$$

where V_b is the amount of band bending in the depletion layer, N is the charge carrier density in the semiconductor, q is the electronic charge, ϵ is the dielectric constant of the semiconductor, and ϵ_0 is the permitivity of free space. In semiconductors, w can be quite large depending upon the conductivity and the band bending; in typical cases it ranges from 100 Å to several microns. This is in contrast to metal electrodes, where the space charge layer is infinitesimally small, and charges induced in the electrode essentially reside at the surface.

A charged layer also exists in the electrolyte adjacent to the interface with the solid electrode, the Helmholtz layer [38]. This layer consists of charged ions from the electrolyte adsorbed on the solid electrode surface; these ions are of opposite sign to the charge induced in the solid electrode. The width of the Helmholtz layer is generally of the order of a few angstroms. The potential drop across the Helmholtz layer depends upon the specific ionic equilibrium at the surface.

To make the connection between the energy levels of the electrolyte and the semiconductor it is necessary to introduce the flat-band potential V_{fb}, as a critical parameter characterizing the semiconductor

electrode. The flat-band potential is the electrode potential at which the semiconductor bands are flat (zero space charge in the semiconductor); it is measured with respect to a reference electrode, usually either the normal hydrogen electrode (NHE) or the standard calomel electrode (SCE). The band bending is given by:

$$V_b = V - V_{fb} \tag{1.9}$$

where V is the electrode potential (Fermi level) of the semiconductor. At equilibrium in the dark, V is identical with the potential of the redox couple in the electrolyte.

The effect of the Helmholtz layer on the semiconductor band bending is contained within the flat-band potential. This important parameter is a property both of the bulk semiconductor and the electrolyte, as seen from the following relationship [11]:

$$V_{fb}(NHE) = (\tau + \Delta E_f + V_H) - 4.5 = (\varnothing_{sc} + V_H) - 4.5 \tag{1.10}$$

where τ is the electron affinity of the semiconductor, $\varnothing_{sc}$ is the work function of the semiconductor, ΔE_f is the difference between the Fermi level and majority carrier band edge of the semiconductor, V_H is the potential drop across the Helmholtz layer, and 4.5 is the scale factor relating the H^+/H_2 redox level to vacuum.

Equation 1.10 suggests that V_{fb} can be predicted from a knowledge of electron affinities. Butler and Ginley [39-40] have proposed a theoretical model where τ is calculated from the electronegativities of

the constituent elements of the material in question. They found that flat-band potentials for metal oxides can be predicted to within ~ 0.2 V in this manner if specific adsorption of OH^- and H^+ ions can be properly accounted for. The variation of V_{fb} with electrolyte pH is expected to be -0.059 V per pH unit, due to the change in V_H with specific adsorption. V_H is accounted for by first establishing the point of zero potential (PZZP) [51]; this is the condition where the number of adsorbed positive and negative ions is equal, so that $V_H = 0$. For many semiconductors in aqueous electrolyte, H^+ and OH^- are the relevant adsorbed ions, and the PZZP is thus the pH at which $V_H = 0$. In these cases, the change of V_H with pH follows a simple relationship:

$$V_H = 0.059(pH_{PZZP} - pH) \tag{1.11}$$

Under short circuit conditions, V_{fb} represents the maximum Fermi level possible for the system [17]. Hence if V_{fb} for a material lies below the H^+/H_2 potential, H_2 can not be evolved at the cathode. Current flow will then be accomplished by the decomposition of O_2 at the cathode and the cell will be operating in the photovoltaic mode. The application of an external bias will then be required to raise the Fermi level above the H^+/H_2 redox potential. Knowledge of V_{fb} is consequently of fundamental importance, and a variety of techniques have been developed for its measurement.

The most basic of such methods utilizes cell capacitance measurements as a function of applied potential. The Mott-Schottky relationship for a PEC is given by [20,37,41-46]:

$$1/C^2 = (2/q\epsilon\epsilon_o n_o)(V - V_{fb} - kT/q) \quad (1.12)$$

where ϵ is the semiconductor dielectric constant, n_o is the carrier concentration, and V is the applied potential. The cell capacitance consists of three capacitors in series: the semiconductor space charge region (C_{sc}), the Helmholtz layer including the interface region, and the solution diffuse double layer (Guoy layer). Normally, C_{sc} is much smaller than the other components of the total capacitance. When this is true, a plot of $1/C^2$ versus V will yield a straight line from which no and V_{fb} can be obtained. The effects of non-ideal contacts at the semiconductor surface on capacitance measurements have been thoroughly analyzed by Goodman [47].

Another method for determining V_{fb} for both polycrystalline and single crystal materials relying on differential stress measurements has been developed by Handley and Bard [48]. This is based on the relationship between the differential surface stress, the surface charge density and the deformation of an electrode as given below:

$$\delta\sigma/\delta E = -q - \delta q/\delta\theta \quad (1.13)$$

where $(\delta\sigma/\delta E)$ is the differential surface stress, q the surface charge density, and θ the ratio of the surface area before and after deformation. The surface charge density will dominate the terms on the right of Eqn. 1.13, and both terms will go to zero at the flat-band potential. At potentials negative of V_{fb}, Eqn. 1.13 will be positive (since

the space charge region will have an excess of electrons) and at potentials positive of V_{fb}, it will be negative. Hence a plot of the differential stress versus potential will give V_{fb} at the intercept.

A third technique for determining V_{fb} utilizes the photoresponse of the material [49]. This is based on the measurement of the photocurrent as a function of applied potential, where the intercept of the I^2_{ph} versus V plot yields V_{fb}.

An alternative technique is by rectified alternating photocurrent voltammetry (RAPV). This is an AC phase-sensitive detection technique based on the same principle as that mentioned in the paragraph above. McCann and Pezy [50] have demonstrated the simplicity of this AC technique over the DC photocurrent method, and found good agreement with capacitance measurement for a wide variety of materials.

1.2.2 Photo-Induced Charge Transfer Reactions

When the semiconductor-electrolyte junction is illuminated with light, photons having energies greater than the semiconductor band gap (E_g) are absorbed and create electron-hole pairs in the semiconductor. Photons absorbed in the depletion layer produce electron-hole pairs that separate under the influence of the electric fieldpresent in the space charge region. Electron-hole pairs produced beyond the depletion layer will separate if the minority carriers can diffuse to the depletion layer before recombination with the majority carriers occurs. Photons will be absorbed in the depletion layer if their absorption coefficient, α (cm^{-1}), is sufficiently large such that $1/\alpha < w$.

The photo production and subsequent separation of electron-hole

pairs in the depletion layer cause the Fermi level in the semiconductor to return toward its original position before the semiconductor-electrolyte junction was established. That is, under illumination, the semiconductor potential is driven toward its flat-band potential (see Figure 1.3). Under open circuit conditions between an illuminated semiconductor electrode and a metal counter electrode, the photovoltage produced between the electrodes is equal to the difference between the Fermi level in the semiconductor and the redox potential of the electrolyte (as sensed by the metal counter electrode). Under closed circuit conditions, the Fermi level in the system is equalized and no photovoltage exists between the two electrodes. However, a net charge flow does exist. Photo-generated minority carriers in the semiconductor are swept to the surface where they are subsequently injected into the electrolyte to drive a redox reaction. For n-type semiconductors, minority holes are injected to produce an anodic oxidation reaction, while for p-type semiconductors, minority electrons are injected to produce a cathodic reduction reaction. The photo-generated majority carriers in both cases are swept toward the semiconductor bulk, where they subsequently leave the semiconductor via an ohmic contact, traverse an external circuit to the counter electrode, and are injected at the counter electrode to drive a redox reaction inverse to that occurring at the semiconductor electrode.

Two very different types of photoelectrochemical cells can be created depending upon the nature of the electrolyte. If the electrolyte contains only one effective redox couple, then the oxidation reaction at the anode is simply reversed at the cathode and no net

chemical change occurs in the electrolyte. The electrode reactions merely serve to shuttle charge across the electrolyte and maintain current continuity. In this case, the cell behaves as an electrochemical photovoltaic cell [1-4], and the incident optical energy is converted into electrical energy of the external photocurrent and photovoltage.

If the electrolyte contains two effective redox couples, then the respective oxidation and reduction reactions at the anode and cathode are different. This leads to a net chemical change in the electrolyte, and the cell behaves as photoelectrolysis cell [17,52-53]. Here, the incident optical energy is converted into the chemical free energy characteristic of the net oxidation-reduction reaction generated in the electrolyte.

The general energetics and kinetics of charge transfer reactions at semiconductor-electrolyte interfaces have been extensively studied [54-63].

1.3 Semiconductor Electrode Stability

For a practical long-life photoelectrochemical cell, the semiconductor electrode must be stable against: (i) dissolution; (ii) photocorrosion; and (iii) electrochemical corrosion. The instability of semiconductor electrodes under photo-electrochemical operation is probably the greatest and least understood problem in further development of useful photoelectrochemical cells. A minority carrier trapped in a surface state represents a weakened bond at the semiconductor surface [64-65]. If such bonds at the surface can be restored by an

electron exchange with the electrolyte, without the chemical involvement of the electrode, then the electrode will be stable. Most reactions of interest, however, require the transfer of more than one electron and thus involve several partial reactions with at most one electron transfer in each step. These partial reactions produce intermediate states, often in the form of highly reactive radicals, that are chemically bound to the semiconductor surface [66]. The intermediates must have sufficient lifetime on the surface to permit the next reaction step to occur. This next step might be to another intermediate in the chain of desired reactions, e.g. the electrolysis of water, or it might further weaken the bonds by which a surface atom of the semiconductor is held to its neighbors. In this way, the surface atom may be released as a solvated ion. In a longer chain of intermediate events, surface atoms may be removed over the surface, or removed and redeposited, thereby changing the nature of the surface [17].

This general discussion shows that the property necessary for effective electrolysis of water is also the one that can lead to corrosion. It is the ability to chemisorb the intermediates that makes an electrode a good catalyst for water splitting. Thus the desired electrolyte reaction (water decomposition) and the undesired corrosion reactions are competitive. Both may be characterized by standard redox potentials that may be helpful in determining which reactions will predominate [67-69].

If E_D, the redox potential for the electrode decomposition reaction, lies below the valence band edge (more positive in potential) of an n-

type electrode and E_R, the redox potential for the desired reaction, lies above the valence band, then the electrode is stable and the desired reaction can occur. If both lie above the valence band edge, both reaction can occur; which will predominate depends on kinetic factors [70], but the relative positions of E_R and E_D are also important. If E_R lies below E_D, the oxidation product of the desired reaction will be thermodynamically capable of oxidizing the electrode, even in the dark (see Figure 1.4). It is therefore preferable to have E_R above E_D, but it is also necessary that the desired reaction be so favored kinetically that it prevents the decomposition from occurring [71-76].

1.4 Efficiency

The output voltage/power is mostly limited by the band bending at the semiconductor-electrolyte interface. The maximum photopotential is obtained at the flat-band situation with high light intensity. The maximum photopotential is:

$$(V_{ph})_{max} = E_g/e \qquad (1.14)$$

The solar cell efficiency, η, is defined as:

$$\eta = (\text{output power/input power}) \times 100\% \qquad (1.15)$$

The quantum efficiency or quantum yield is defined as:

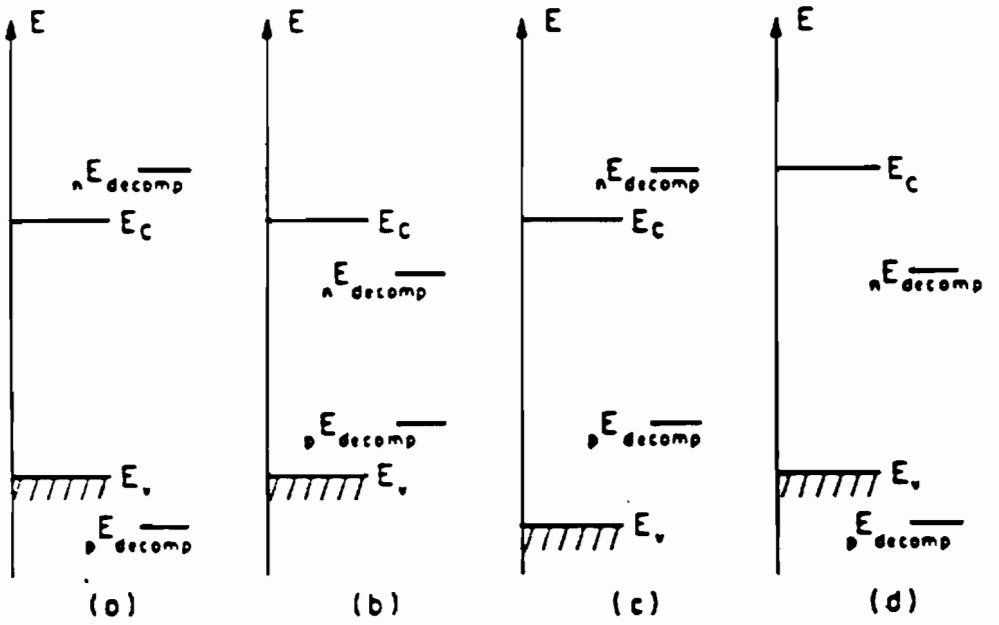

Figure 1.4. Energy correlations between band edges and decomposition Fermi levels, characterizing susceptibility to photodecomposition.
(a) Stable, (b) unstable, (c) susceptible to anodic photodecomposition, (d) susceptible to cathodic photodecomposition.

$$\eta_q = \frac{\text{number of photoelectrons flowing per unit area}}{\text{\# of incident photons with energy } h\upsilon \text{ per area}} \qquad (1.16)$$

$$= N(e)/N(h\upsilon)$$

The various expressions for efficiency used by different authors [77-81] are just variations of Equations (1.15) and (1.16).

The quantum efficiency is also given by [82]:

$$\eta_q = J/e\theta_0 = [1 - \exp(-\alpha W)/1+\alpha L_P] \qquad (1.17)$$

where J is the total photocurrent, θ_0 is the photon flux, W is the depletion layer width, L_P is minority carrier diffusion length, and α is the absorption coefficient.

From the above equation, it is obvious that for high quantum efficiency, the following conditions are necessary [82]:

(a) The absorption coefficient, α, must be large.

(b) The diffusion length for minority carriers, L_P, must be large.

(c) As a consequence of condition (b), the grain boundaries and surface states have also pronounced effect on the efficiency.

(d) Depletion layer width, W, should be large.

(e) As a consequence of condition (d), the Debye length must be large. Hence, the value of donor atom concentration, N_D, should be small. However, N_D cannot be made very small since it would lead to increased ohmic losses within the semiconductor.

The optimal donor concentration, N_D, is about $3x10^{15}$ cm^{-3}.

(f) Another consequence of condition (d) is that the value of flat-band potential, V_{fb}, should be small. However, if V_{fb} is too small then a reduced band bending results.

The following points should also be considered while designing an efficient photoelectrochemical solar cell:

(a) The electrolyte should be transparent to light or else many photons would not be able to reach the semiconductor electrode, resulting in reduction of efficiency.

(b) Ionic species participating in the redox reaction are diffusion limited. Hence, stirring the electrolyte may lead to improved efficiencies [83].

(c) A proper choice of counterelectrode is important. The counterelectrode should be a low overpotential for redox reaction to take place and of a large area for reducing concentration polarization. Platinum seems quite suitable [84].

(d) The cell efficiency also changes with operating temperature [85].

CHAPTER TWO

REVIEW OF RELATED WORK

IRON OXIDE

2.1 Physical Structure

Iron is the most abundant transition metal that is present on our planet. The metal and its oxides have desirable structural, magnetic, electrical and chemical properties that are employed in a multitude of applications. It has a body-centered cubic crystal structure at room temperature, but undergoes a phase transformation of face-centered cubic structure at higher temperatures that involve some volume change.

Iron oxides have a very complex phase diagram that is shown in Figure 2.1, consisting of at least three distinct iron-oxygen compounds [86].

The lowest of the oxides, wustite (FeO), has a NaCl type cubic lattice formed by close-packing of the relatively large oxide ions with the smaller iron ions arranged in the interstices [87].

The mineral magnetite, Fe_3O_4, has been known since ancient times, and its ferromagnetic properties were at the origin of the study of magnetism. The Hl_1 cubic structure is that of spinel $MgAl_2O_4$ (Figure 2.2) where the compact arrangement of oxygen atoms provides one tetrahedral site (A) and two octahedral sites (B) per O_4 group.

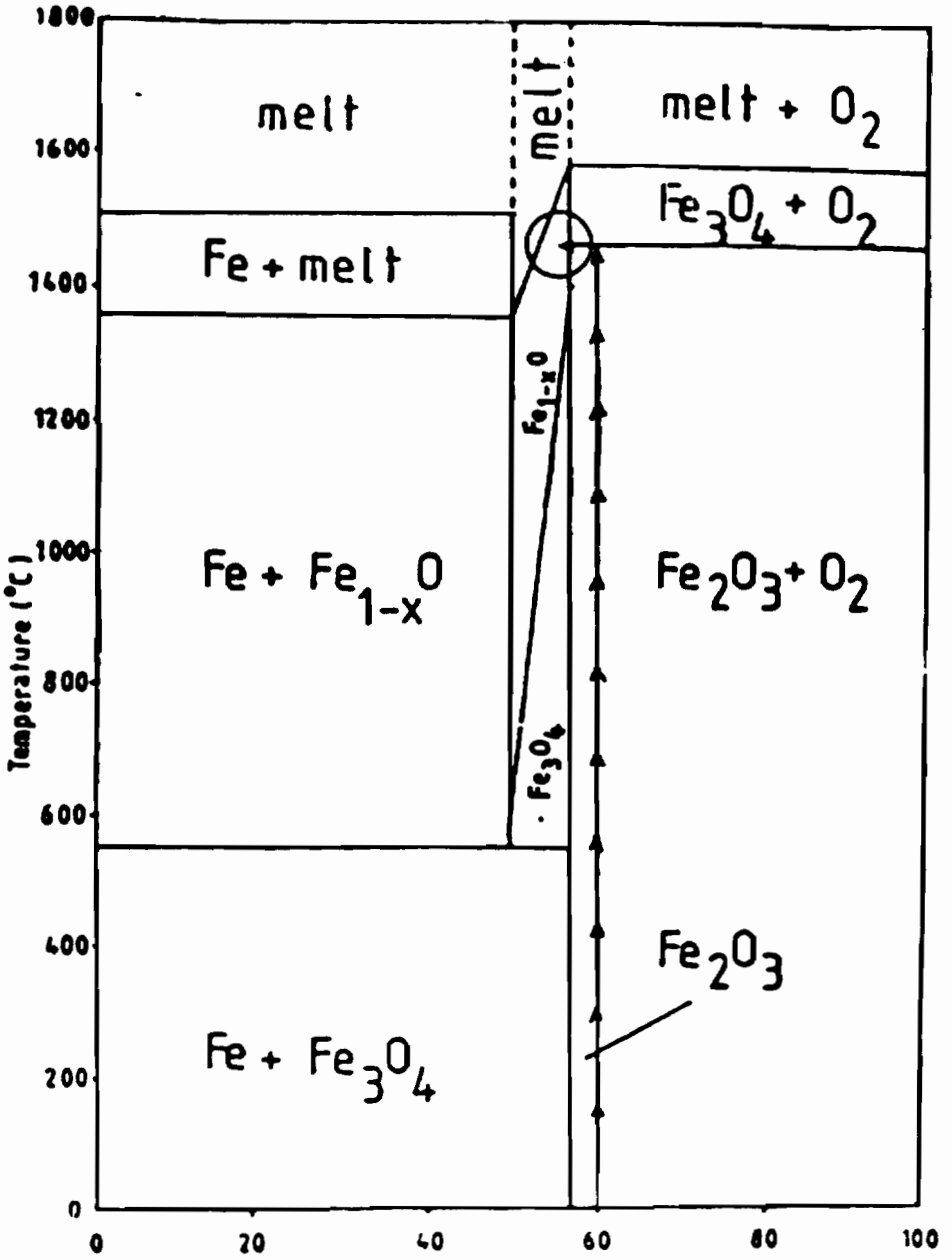

Figure 2.1. Phase diagram of the Fe-O system.

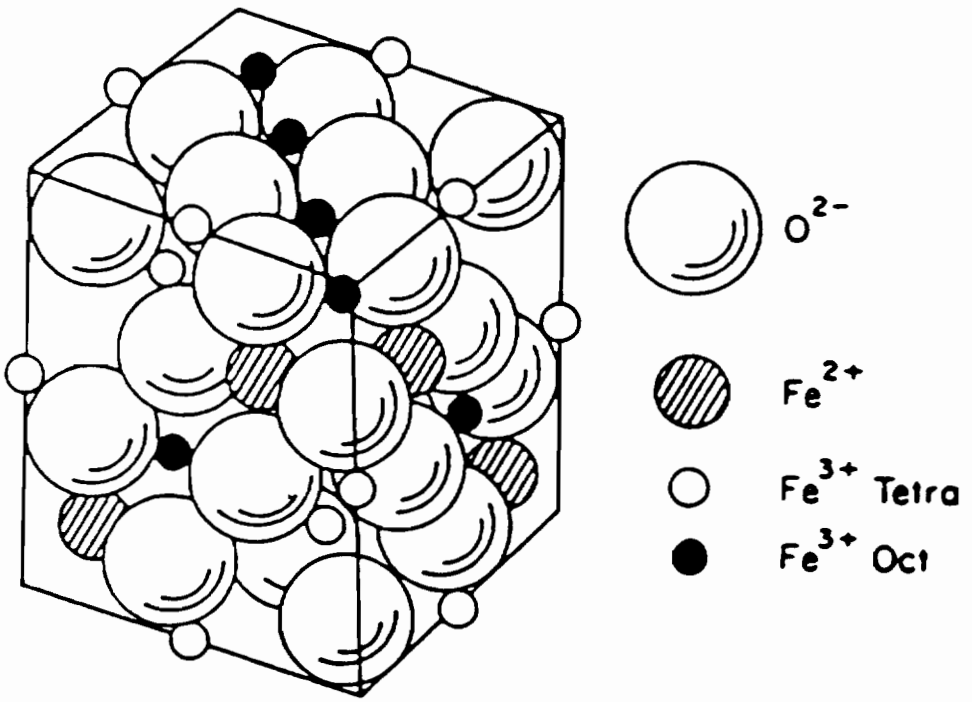

Figure 2.2. Structure of magnetite Fe_3O_4.

While the divalent atoms occupy the A sites in the "normal" structure, they can occupy half the B sites in an "inverted" structure [88]. Verwey and de Boer [89] have shown that magnetite is inverted and could be written as $[Fe(III)]_A[Fe(II)Fe(III)]_BO_4$.

Hematite, α-Fe_2O_3, has the $D5_1$ rhombohedral structure of corundum α-Al_2O_3 [90] with cell dimensions a = 5.4271 Å, α = 55°17' or conveniently described as a hexagonal structure with a = 5.0345 Å, c = 13.749 Å.

2.2 Phase Transformations

There exist several other important phases of Fe_2O_3. There is ß-Fe_2O_3, body centered cubic phase, that can be prepared by vacuum dehydration of ß-FeOOH [91]. The σ-Fe_2O_3 has an inverse spinel structure [92] with cell dimension a = 8.322 Å and 2 2/3 vacancies per unit cell in the cation lattice and is very widely used in magnetic recording devices. The σ-Fe_2O_3 can be prepared from lepidocrocite, σ-FeOOH, by heating at 250° C for a few hours [92]. The σ-Fe_2O_3 can also be prepared by oxidation of Fe_3O_4 up to 400°C [87]. The detailed study of the α-FeOOH and σ-FeOOH into σ-Fe_2O_3 phase transformation has been conducted [93].

The transformation of σ-Fe_2O_3 to α-form occurs irreversibly above 400°C [92,109]. Bernal et al. [94] studied this transformation using X-ray and electron diffraction techniques. The σ-FeOOH or σ-Fe_2O_3 is transformed into α-Fe_2O_3 upon heating above 400°C [93].

The mechanical dehydration of σ-FeOOH leads to α-Fe_2O_3 as confirmed by X-ray analysis and Mossbauer spectroscopy [95-96].

The α-Fe_2O_3 can be transformed into σ-Fe_2O_3 by first transforming α-

Fe_2O_3 into Fe_3O_4 by heating in a reducing atmosphere and then oxidizing it to σ-Fe_2O_3 as was investigated by Weisweiler [97].

The α-Fe_2O_3 can be prepared by phase transformation of α-FeOOH at 300°C [98-100]. Watari et al. [101] studied the dehydration transformation of α-FeOOH to α-Fe_2O_3 by high resolution electron microscopy. α-Fe_2O_3 can also be prepared by thermal decomposition of ß-FeOOH [102]. A solid state conversion of pure α-FeOOH into α-Fe_2O_3 may be also achieved by mechanical grinding as studied by Mendelovici et al. [103-104].

The production of α-Fe_2O_3 in vacuum at 200°C from α-FeOOH decomposition gives very microporous product. Such microporosity tends to disappear as the decomposition temperature and the water vapor pressure increase [105].

The reduction reaction of α-Fe_2O_3 to Fe_3O_4 has been studied in great detail [106-108]. El-Geassy [107] studied gaseous reduction of Fe_2O_3 compacts at 600 to 1050°C using H_2, CO, and H_2-CO mixtures.

2.3 Preparation Techniques

There are many possible preparation techniques for α-Fe_2O_3, such as solid state transformations, liquid mix techniques, precipitation techniques, sol-gel techniques and cryogenic techniques. Some of the techniques will be briefly discussed in this part.

Leskela et al. [110] studied the preparation of yellow α-FeOOH from $FeSO_4$ solution by alkali precipitation and gas oxidation methods. Needle-like α-FeOOH transforms into red α-Fe_2O_3 at 300°C. Subrt et al. [111-112] and Kuo et al. [113] also

prepared iron oxide by oxidation precipitation of aqueous solutions of $FeSO_4$ by oxygen gas. The product contained about 3-5% structurally bonded water. The effect of heating up to 700°C prepared by this method were studied [114]. It was found that the water was lost, accompanied by the formation and removal of pores, the lattice constant changed and the optical properties were slightly modified. Christensen et al. [115] used iron(III)nitrate solutions which were hydrolyzed at constant temperature for several hours. Crystal growth of iron oxide and iron hydroxide were studied by X-ray diffraction. Christensen et al. also studied transformation of iron(III)hydroxide into α-Fe_2O_3 as a function of time [116], temperature and pH [117]. Kriger et al. [118] studied structures of iron-(III)hydroxides and their ageing products.

The relationship between the activity of ferric oxyhydroxides (α-, ß-, and τ-FeOOH) and structural changes has been investigated by determining the heat of immersion in H_2O and H_2O vapor adsorption [119]. Thermal analysis studies of several different iron(III)-hydroxides from different sources has been studied by several authors [120-122].

Gallagher et al. [121-122] prepared iron oxide by high temperature decomposition of 12 different Fe(III) salts. They studied the surface area, reactivity, aggregate size distribution, and structure of the resulting iron oxides.

For many applications (photocatalysis, freeze drying) it is very desirous to prepare sols or colloidal suspensions of iron oxide of precise particle size, shape, and distribution. There are several

excellent review articles on this subject [123-125].

Matijevic et al. [124-126] used Fe(III)-chloride, -nitrate, and -perchlorate solutions for careful temperature controlled hydrolysis of these sols to produce uniform particle size α-Fe_2O_3 sols. Other preparation techniques involve hydrolysis of metal chelates [127], ethanolic solutions [128], and chlorides [129].

Thermal transformation of hydrated ferric oxide gel and ultrafine oxide has been studied by Rajendran et al. [130]. There are many other papers on preparation and characterization of precipitated iron oxides [131-133].

Colloidal iron oxides or sols of iron oxides can be also used to prepare reactive powdered iron oxide of very high surface area by employing a freeze-drying technique. This technique is discussed by Tseung et al. [134-135]. Several different cryogenic techniques were also used to prepare iron oxide [122,136].

2.4 Lattice Dynamics, Raman and Infrared Spectra

The Raman and Infrared spectroscopy can be used very effectively to determine which phases of iron oxide are present in the sample of interest. Raman spectroscopy can be used for example in situ to analyze corrosion product films on metal surfaces in gaseous and aqueous environments. Thibeau et al. have analyzed corrosion products on iron by Raman spectroscopy [137]. The group theoretical symmetry calculations were performed for iron oxide by several investigators [138-140].

α-Fe_2O_3 crystallizes into a D^6_{3d} structure with ten atoms per unit

cell. Below the Morin [141] transition (260° K) the four iron atoms, spin 5/2, align the c-axis in a antiferromagnetic arrangement [142]. Between 260° K and the Curie temperature (950° K) the spins lie in the basal plane with a slight canting which results in a small ferromagnetic moment [143]. The group theoretical calculations for this space group give [139]:

$$\chi = 2A_{1g} + 2A_{1u} + 3A_{2g} + 2A_{2u} + 5E_g + 4E_u \qquad (2.1)$$

where A_g and E_g are the Raman active modes. The seven phonon lines predicted by this calculation have been identified [138].

The A_{1g} modes at 225 and 498 cm^{-1} were identified by their appearance in the (zz) polarization and E_g modes at 247, 293, 299, 412, and 612 cm^{-1} by their appearance in the (xy) polarization. Since iron oxide is opaque color it is difficult to obtain a good spectrum under regular conditions, therefore, it is necessary to scatter from a polished surface of the crystal at shallow angles [144].

Hamilton et al. [145] have used Raman spectroscopy combined with ion bombardment to obtain chemical compound identification as a function of depth in films containing Fe_2O_3. Low sensitivity to sputter induced chemical changes is a major advantage of the technique.

Farrow et al. [146] have used backscattering Raman spectroscopy to study in situ oxide films at high temperature for different iron-based alloys.

Infrared spectroscopy is easier and very good technique for qualitative and to some extent quantitative analysis of iron oxide. Serna et

al. [147] have analyzed group theoretical calculations for iron oxide and predicted 6 IR active modes. The two A_{2u} modes with polarization parallel to the crystalline c-axis and the four E_u modes with polarization perpendicular to the c-axis are IR active. There are many experimental application of IR in studying iron oxide [147-157]. A number of investigators studied phase transformations of iron oxide [148,150,152-153] using infrared spectroscopy. Yariv et al. [149] studied the effect of degree of crystallinity on the infrared spectrum of Fe_2O_3. By the position and sharpness of the absorption peaks they were able to distinguish poorly crystalline and very crystalline samples. They also found that grinding during the preparation of the disks may also affect the infrared spectra and the location of the characteristic absorption maxima of the various iron oxide phases [158].

Rendon et al. [154] studied the effect of particle shape on the IR absorption of powdered oxides by means of classical electromagnetic scattering theory. The extreme variation of the IR spectrum with shape factor emphasizes the danger of reporting IR spectra of powder oxides without taking into account the actual particle shape. This factor is usually minimized in practice because usually the sample is ground to sizes much smaller than the radiation wavelength in order to obtain good resolution IR spectra.

Lorenzelli et al. [151] have studied adsorption of water, pyridine, ammonia, carbon monoxide, and methanol on the surface of iron oxide using infrared spectroscopy. They also studied absorption of O_2, N_2, NO, and H_2 adsorbed on Fe_2O_3 [155,157].

Busca et al. [156] have also studied adsorbed forms of water on α-Fe_2O_3 obtained by thermal decomposition of α-FeOOH.

2.5 Surface Properties

Many of the crystal faces of metallic iron have been subjected to low energy electron diffraction studies. The surface structure of the (110), (111) and (100) faces show no reconstruction. However, there is strong relaxation of the more open (111) and (100) surfaces. That is, the interlayer spacing between the first and second layer is appreciably smaller than the interlayer spacing in subsequent layers below [159-160]. The several ordered surface structures of chemisorbed oxygen have been investigated. The formation of FeO in the surface layer has been detected and the structure of this complicated but important layer has been solved [161]. Oxygen chemisorption, the initial stages of oxidation and bulk oxide formations have all been studied by electron spectroscopy techniques [162]. X-ray photoelectron spectroscopy revealed the various oxidation states of the transition metal ions as a function of oxygen partial pressure and surface concentrations [163]. Ultraviolet photoelectron spectroscopy showed drastic changes in the density of states at the Fermi level and changes in work function as oxygen chemisorption and oxidation proceeds. Auger electron spectroscopy clearly detected different Auger peak intensity ratios for the iron and oxygen Auger peaks when FeO, Fe_2O_3, and Fe_3O_4 are present. These Auger peak ratios can then be used to determine the surface stoichiometry of the iron oxides samples [164]. The chemisorption of small molecules, including water have been studied on iron oxide

surfaces [165]. The stoichiometric basal plane of the corundum phase Fe_2O_3 is extremely inert. Water physisorbs only as ice at low temperatures and it desorbs around 175 K. Argon ion sputtering produces oxygen vacancies that expose Fe^{2+} species on the outermost atomic layer that lower the work function of the sample. These reduced iron species are unstable and disappear rapidly from the surface layer upon heating above 375 K. However, the Fe^{2+} species that can be detected under the surface are stable at temperatures up to 775 K for extended periods of time. The surface Fe^{2+} species, when present in the outermost layer, can adsorb water strongly and evolve hydrogen upon heating [164].

Morimoto et al. [166] measured the first and second water adsorption isotherms and the water content on the Fe_2O_3 surface. X-ray photoelectron spectroscopy [167] and X-ray diffraction [168] have been used to characterize surfaces of hydrous iron oxide and thin films of Fe_2O_3. Youssef et al. [169] studied surface properties of Mn-doped Fe_2O_3 by DTA and X-ray.

The residual porosity of sintered iron oxide was shown to have a major influence on the electrical properties of Fe_2O_3 [170]. Coble et al. [171] described that the initial sintering behavior between 1150 and 1350°C of submicron α-Fe_2O_3 powder was governed by bulk diffusion of Fe, the slower diffusion species in Fe_2O_3. De Witt et al. [172] studied the sintering behavior of pure and impure Fe_2O_3. The ultimate density of impure oxide was 85% while the impure material reaches a density of 95% at 1300°C. Since compacts also based on Fe_3O_4 reach this higher density, while the resulting microstructure is similar, a reduction-oxidation process at the surface of the grains is a possible

mechanism. Also the formation of a low melting eutectic phases in the impure material may result in liquid phase sintering. The acicular powder gave a dense material more than 99% theoretical density [173]. Arora et al. [174] studied relationship between surface area and temperature of sintering for several oxide systems.

2.6 Optical and Dielectric Properties

Like most higher oxides of transition metals with partly filled cation d-shells, α-Fe_2O_3 belongs to the class of semiconductors with controllable valence. Koshcheev et al. [175] have used photoemission, optical spectra, and electrical conductivity to investigate the energy spectrum of Fe_2O_3. The energy of the top of the 3d states relative to the vacuum level is equal to 5.9 eV. The maximum of the density of 2p states of O^{2-} lies 10.5 eV below the vacuum level. In photoemission from iron oxide the fine structure of the energy spectra of photo-electrons is due to multiparticle interactions in the process of photodetachment of an electron from the 3d states of Fe^{3+}. Optical absorption bands in the near IR to UV region of the optical spectra of α-Fe_2O_3 [176] and Fe^{3+} in Fe_2O_3 have been attributed to either crystal field or charge transfer electronic processes [177]. The bands at 18690, 16670, and 12000 cm^{-1} in optical absorption spectrum [178] are considered to arise from spin-forbidden ligand field transition. The transitions at 11560, 12900, 16670, and 18690 cm^{-1} have been assigned to various ligand field transitions. The bands occurring at 20408 and 23800 are considered to arise from spin-flip transitions among the $2t_{2g}$ and $3e_g$ states. The peaks at 26670 and 31750 cm^{-1} arise from $O^{2-}$to

Fe^{3+} charge transfer between the O_{2p} nonbonding orbitals and the lowest empty orbital. The peaks at 38900 and 44840 cm^{-1} are charge transfer transitions from O_{2p} nonbonding levels to the 3_{eg} orbital. In Fe_2O_3 the lowest band gap is indirect at 1.88 eV. The first direct transition is at 2.75 eV [177].

The dielectric constant measurements of high density, insulating α-Fe_2O_3 were made at various frequencies using a parallel plate capacitance method [179]. The dielectric constant, e, was calculated from capacitance data according to the following equation:

$$\epsilon = 9.0x10^{11}(4\pi t/A)\Delta C \qquad (2.2)$$

where t and A are the disk thickness and area and ΔC is the difference in the capacitance with and without the sample. A dielectric constant value of 80 was obtained. Quinn et al. [180] reported a value of 120 for a single face Fe_2O_3. There are reports in literature of dielectric constant ranging from 70-140 [181].

2.7 Electronic Transport and Impurity Related Effects

Stoichiometric α-Fe_2O_3 is an intrinsic n-type semiconductor with a band gap of 2.2 eV. The early semiconducting properties for pure and Ti-doped iron oxide have been examined by Morin [182-183]. The resistivity of a pure stoichiometric sample at room temperature is estimated at 10^{14} Ω-cm. An extraordinary Hall effect has been observed. The carrier density, worked out from the Seebeck effect, leads to the mobility being calculated at less than 10^{-2} cm^2 V^{-1} sec^{-1},

increasing exponentially with temperature [183]. It is possible to produce a less resistive iron oxide by reducing some of the Fe^{3+} to Fe^{2+} state. The Fe_2O_3 is then a mixed valence compound with enhanced conductivity at room temperature which is due to a hopping process for electrons between Fe^{2+} and Fe^{3+} ions [184]. The Fe^{2+} ions can be introduced by producing oxygen deficiencies or by adding a dopant, which induces a charge compensation process. However, the corundum α-Fe_2O_3 phase has a low solubility for divalent ions [185-186], since the Fe^{3+}_{2-x}-Fe^{2+}_{x}-O_3 stoichiometry induces the formation of the Fe_3O_4 spinel phase. Thus, it is difficult to prepare homogeneous doped semiconducting samples of Fe_2O_3 without Fe_3O_4 phase inclusions [187].

Warnes et al. [184] studied electrical conductivity and Seebeck voltage for 99.9997% Fe_2O_3 as a function of temperature and oxygen pressure, and donor and acceptor doped Fe_2O_3 as a function of temperature. The results indicate that Fe_2O_3 is an intrinsic semiconductor above 650°C, where the conductivity is described by:

$$\sigma = 9191.2 \exp(-1.11eV/kT)(1/\Omega cm) \qquad (2.3)$$

and it is oxygen-pressure independent. The Seebeck voltage shows that Fe_2O_3 is n-type below 800°C and p-type above this temperature. Conductivity measurements on doped samples were used to calculate the carrier mobilities and these are given by the expressions:

$$\mu(\text{electrons}) = (1998/T)\exp(-0.17eV/kT)(cm^2/Vs) \qquad (2.4)$$

$$\mu(\text{holes}) = (9298/T)\exp(-0.29\text{eV}/kT)(\text{cm}^2/\text{Vs}) \quad (2.5)$$

The electrons are the most mobile carrier below ~ 800°C, but the hole is more mobile above 800°C, and this probably explains the conversion from n- to p-type behavior. The concentration of electrons is greater than that of the holes above 650°C, and the carrier concentration product is given by:

$$(np) = 1.34\text{x}10^{42}\exp(-0.78\text{eV}/kT) \quad (2.6)$$

The formation expressions for atomic imperfection defects are:

$$Fe_2O_3 = 2(Fe_{int}) + 2Nn + 3/2O_2 \quad (2.7)$$

where N = 2 or 3 and

$$Fe_2O_3 = 2Fe_{Fe} + 3V_O^{\cdot\cdot} + 6n + 3/2O_2 \quad (2.8)$$

There are other numerous studies of electrical conductivities of doped Fe_2O_3 for example hydrous Fe_2O_3 [188], Cd-doped Fe_2O_3 [189], τ-Fe_2O_3 [190].

R. Dieckmann [191] studied the nonstoichiometry and point defect structure of Fe_3O_4 by thermogravimetry covering the stability range of magnetite between 900 and 1400°C. He observed a cation deficit at high oxygen activities and a cation excess at low oxygen activities corresponding to cation vacancies and iron interstitials as the predomin-

ant point defects, respectively.

2.8 Photoanodes

In 1972 Fujishima and Honda [192] first reported on the successful photodissociation of water using n-TiO_2 as the semiconducting photoanode [193]. Since that time a wide variety of materials and combinations of materials have been tested in the hope of finding the right combination to yield a satisfactory energy conversion efficiency. The list of articles published on this subject is far too lengthy to acknowledge here. This work concentrated on studying Fe_2O_3 photoelectrodes, therefore, a detailed literature survey dealing with iron oxide will be presented in this section.

2.8.1 Single Crystals

Quinn et al. [180] first studied as grown (012) face of single crystal α-Fe_2O_3 in photoassisted electrolysis of water. Photocurrents were observed at wavelengths shorter than 565 nm (2.2 eV). Although about 29% of the AM1 solar energy is absorbed, efficient solar conversion cannot be obtained without a small positive bias due to insufficient band bending with no applied bias. However, at a bias of 0.5 V, approximately 20% collection efficiency of the 3.4 eV light (475 nm) is observed. The electrodes were stable for pH > 6.3 and potentials anodic of -0.4 V (pH = 6.3).

Pollert et al. [194] studied high purity single crystals grown by CVD technique. Two indirect electronic transitions were observed at 2.04 and 2.32 eV and were ascribed to iron-iron charge transfers. They

also showed that the difference between the flat-band potential and the photocurrent onset potential increases strongly with increasing donor concentration.

Kung et al. [195] showed that Fe_2O_3 was the first material whose optical and photoelectrochemical spectra were different.
In the optical spectrum there are two features. The peak at 850 nm and sharp edge beginning at 705 nm are due to the two crystal field (or color-center) transitions. The charge-transfer bands at higher energies were not resolved in the optical spectrum. In the photo-electrochemical spectrum the edge is due to the lowest energy charge-transfer band at 390 nm. The onset at 600 nm is from the tail of the intensely absorbing peak which is broadened by the relatively large slit width used when obtaining the spectrum.

Single crystals of Nb-doped Fe_2O_3 were grown by a CVD technique [196] with room temperature resistivity of 85 Ω-cm. Magnetic susceptibility studies suggested that the conductivity of the samples resulted from charge compensation resulting from reduction of Fe^{3+} to Fe^{2+} upon niobium substitution in the structure. Electrical measurements gave an activation energy for the electron hopping of 0.22 eV.
The voltammograms in the dark showed very low dark current (1 $\mu A/cm^2$) in the range between -1.0 and +0.7 V (SCE). Under illumination they showed photocurrents in the range of 500 to 700 $\mu A/cm^2$ at +0.4 V (SCE).

Redon et al. [197] studied differences in the optical and photo-electrochemical behaviors of single crystal and amorphous Fe_2O_3 layer formed by sputtering. The most important differences were the p-type behavior of the sputtered amorphous Fe_2O_3 versus n-type behavior for

the single crystal. This result may be due to impurities or to the gold contact on the electrode which may also be illuminated because the layer of Fe_2O_3 was very thin.

Capacitance-voltage measurements have been carried out on Zr-doped α-Fe_2O_3 single crystal electrodes [198]. Two types of behavior have been observed on the Mott-Schottky plots of the capacitance data. The first one occurs near the flat-band potential and has been attributed to a localized interface state. The second one is observed far from the flat-band potential and can be explained by a deep donor level. Evidence for the deep level has also been obtained from a sub-band gap photocurrent peak, and from the shift of the band-gap photocurrent onset with regard to the flat-band potential.

2.8.2 Thin Films

Thin films of iron oxide were prepared on a variety of substrates (Ti, Pt, glass, quartz, Al_2O_3, Nb, and Ta) by chemical vapor deposition (CVD) from ferrocene and by spray pyrolysis of ferric citrate solution, in the presence of oxygen [199]. The films obtained by spray pyrolysis [200] were not very good for photoelectrochemical cells, because of the nonuniformity of the surface. At low deposition temperatures it is possible to get amorphous films of Fe_2O_3. At intermediate temperatures α-Fe_2O_3 coexists with ß-Fe_2O_3, whereas at higher deposition temperatures (>450°C) only α-Fe_2O_3 is formed.

Hardee et al. [201-202] prepared polycrystalline n-type Fe_2O_3 thin films by a CVD technique on Ti and Pt substrates. They studied current-voltage relationships for these thin films. The cathodic

currents observed in the dark were attributed to the reduction of dissolved oxygen and of the Fe_2O_3. When nitrogen was bubbled through the solution, the current at potentials more positive than -0.4 V markedly decreased; however the currents at more negative potentials were not affected appreciably. Under illumination there was a large rise in anodic current commencing at about +0.2 V vs. SCE, with both Pt and Ti substrates. Gas evolution appeared promptly with the anodic current and was quite noticeable on the electrode surface, implying that the reaction was the photoassisted oxidation of water to produce oxygen. In the dark at +1.2 V, the Fe_2O_3 coated substrates exhibited a large current rise with simultaneous gas evolution. This probably represents the direct oxidation of water at these potentials as a result of tunneling through the film. The transient currents observed in these samples can be explained in terms of surface recombination or backreaction of the photogenerated species. Thus the oxygen (or hydroxyl radicals) which is produced by the photogenerated holes is thermodynamically reducible at potentials on the rising portion of the I-V curve. A backreaction between these and any electrons at the surface produces a backreaction (which is equivalent to a surface electron-hole recombination) and a cathodic current component. This component decreases as the potential is made more positive.

Fredlein et al. [203] studied CVD films of Fe_2O_3 in acetonitrile solutions by cyclic voltammetry. There is evidence that surface electronic states capable of mediating electron transfer exist at ~ 0.9 eV and ~ 1.8 eV negative of conduction band edge. The results are interpreted in terms of a narrow conduction band of width dependent on

the dopant level.

The general discussion on theory and use of cyclic voltammetry is described in several references [204-206]. Also the subject is covered in detail in any advanced electrochemistry text.

Tjong [207] prepared thin films by r-f sputtering technique. X-ray diffraction and Auger electron spectroscopic techniques showed that the films were α-Fe_2O_3. A-C impedance techniques were used to determine the electrochemical properties of the films which exhibited semiconducting properties in the borate buffer solution at the anodic potentials below +0.7 V vs. RHE.

A potentiostatic transient study has been made of the deposition of iron oxides on a rotating platinum ring electrode from pH 4-5 $FeSO_4$ solutions [208]. The rate of film deposition is found to increase with ferrous concentration, pH, and rotational speed. The results indicate that the oxide deposition is a diffusion-controlled process, possibly due to the transport of $FeOH^+$ ions to the ring surface and of H^+ ions to the bulk of the electrolyte.

Yun et al. [209] studied dielectric properties of thermally grown oxide films on iron by measuring the frequency and the temperature dependence of the capacitance in aqueous electrolyte solutions. The ionization energy of donor states in the n-type iron oxide was obtained from calculation of the conductivity profile (0.64 eV) and from Mott-Schottky plots (0.69 eV).

Photoelectrochemical properties of iron oxide thin film photoelectrodes grown by thermal oxidation of iron have been investigated by numerous investigators [210-213]. The findings of these investigators

are comparable to results obtained by other investigators discussed above.

Pajkossy studied theoretical mechanism of hole injection of thermally grown thin film iron oxide photoelectrodes [214].
The aim of this investigation was to determine whether hole injection at the interface proceeds directly from the valence band or via surface states. The photocurrent was measured on ferric oxide electrodes at constant electrode potential and slightly modulated illumination as a function of reducing agent concentration. It was determined from this investigation that holes are injected into the solution directly from the valence band, not via surface states.

Itoh et al. [215] studied laser-induced fast transient photopotentials on thin film Fe_2O_3 electrodes. A photopotential rise within 300 ns was interpreted in terms of charge separation processes in the film, considering the contributions from both the electron and hole. The time course of the photopotential up to 10 λs was attributed to the electron-hole recombination process and the interfacial charge transfer.

Itoh et al. [216-217] also investigated stacked thin film iron oxide photoelectrode. For photoanodes of materials with low mobilities it is advantageous to use several layers of thickness less than the space-charge region, thereby decreasing recombination. If the substrate on which the iron oxide is deposited were transparent, light transmitted through the electrode could be utilized by a second electrode.
Repetition of this principle should allow most of the incident light to be absorbed within the space-charge regions. To compensate losses due

to lack of absorption, ten thin (600 Å) semiconductor layer electrodes were placed one behind the other. The resulting current increased four times compared to a thick electrode.

2.8.3 Polycrystalline Electrodes

Kennedy et al. [218-220] extensively studied photoactivities of polycrystalline Fe_2O_3 doped with Zr, Ce, Si, Al, Hf, Nb, Sn, Ca, Pb, Ti, W, Ta, Ge, and V. Some of their results are presented in Figures 2.3 through 2.6. As can be seen from these results many dopants of oxidation state +4 to +6 are effective donors for α-Fe_2O_3. It was found that Ti is less effective compared to other +4 ions. The difference may result from additional energy levels introduced by the dopant ion. Such sites may also act as electron-hole recombination centers. Lower members of group IVB elements, Zr and Hf, show higher photocurrent efficiencies at low applied potentials compared to those measured at Ti-doped samples. This may reflect the fact that the +3 oxidation state is much less stable than the +4 oxidation state for the heavier elements. Iron oxide samples were also thermally reduced in a He atmosphere. This produced a surface layer of Fe_3O_4 which acts as a recombination center, hence the photoactivity was much smaller.

McAlpine et al. [221] studied oxygen reduction on Ti-doped - Fe_2O_3 electrodes in aqueous alkali. Cyclic voltammograms for Ti-doped iron oxide electrodes in 0.1 M NaOH exhibited small reduction and re-oxidation peaks negative of -0.4 V (SHE) and for electrodes initially held negative of this potential, the onset of the photocurrent occurred

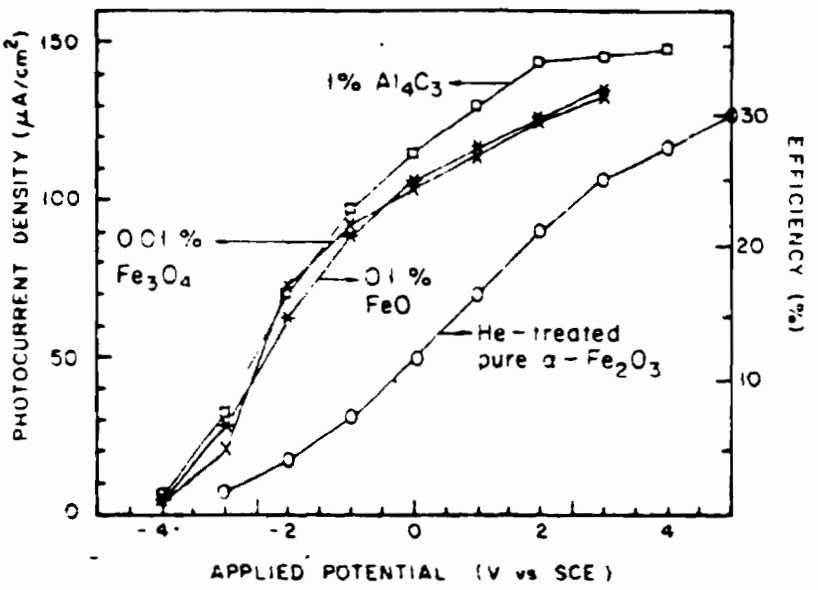

Figure 2.3. Photocurrent density and quantum efficiency as a function of applied potential at 400 nm for doped Fe_2O_3 electrodes in 1F NaOH.

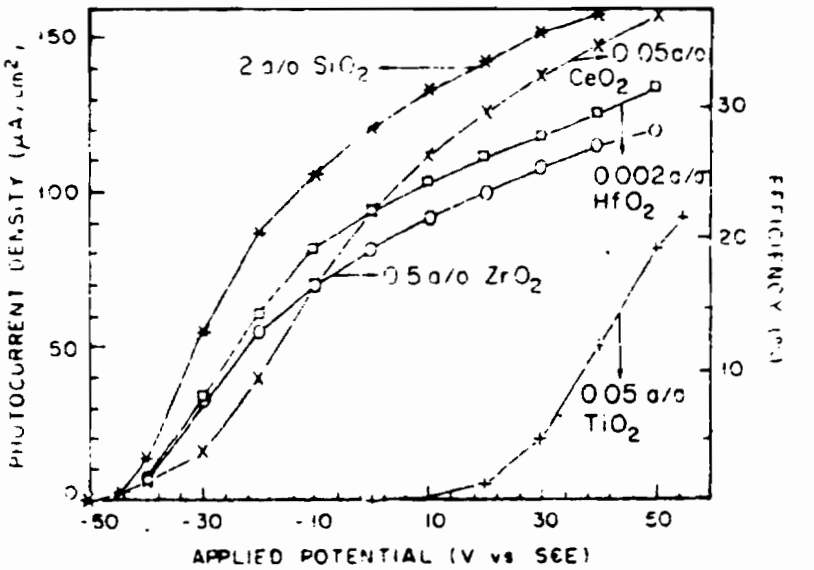

Figure 2.4. Photocurrent density and quantum efficiency as a function of applied potential at 400 nm for doped Fe_2O_3 electrodes in 1F NaOH.

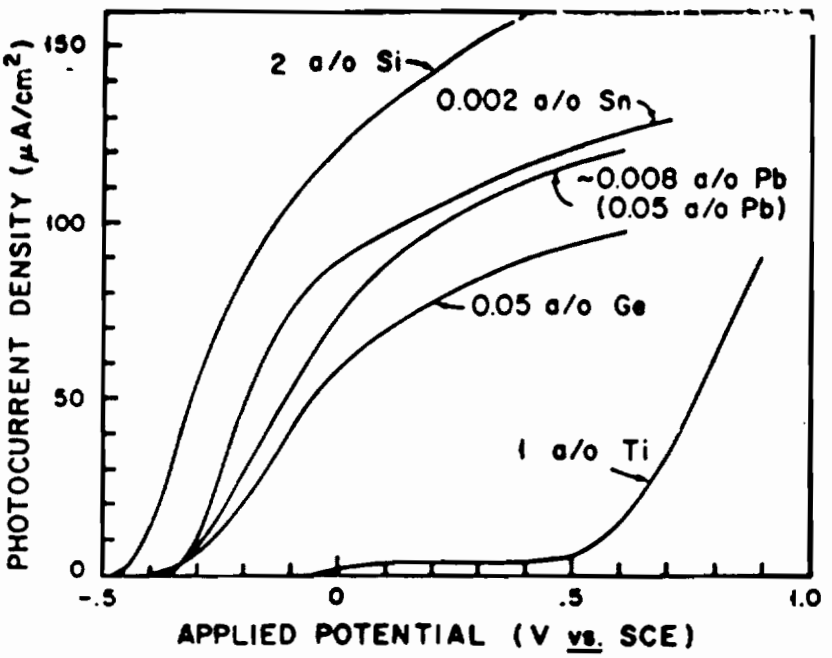

Figure 2.5. Photocurrent density as a function of applied potential for doped Fe_2O_3 electrodes.

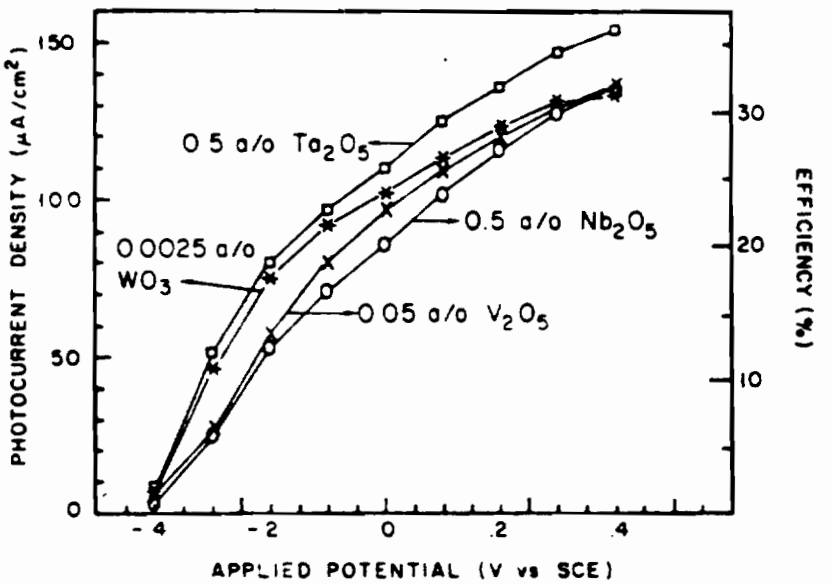

Figure 2.6. Photocurrent density and quantum efficiency as a function of applied potential at 400 nm for doped Fe_2O_3 electrodes in 1F NaOH.

at potentials well positive of V_{fb}. These results are interpreted as due to the penetration of hydrogen into the lattice. The activity of oxygen reduction increases with dopant concentration. No oxygen reduction current was observed for oxygen partial pressures less than 0.45 atm. This effect was independent of electrode potential, dopant concentration and almost independent of pH. The results are interpreted in terms of the step:

$$O_2 + H_2O + e^- = HO_2(ad) + OH^- \qquad (2.9)$$

being rate-determining with titanium donors mediating charge transfer.

Shinar et al. [222] studied open-circuit photopotentials at doped α-Fe_2O_3 electrodes in aqueous solution. The behavior of Fe_2O_3 in acid-base solution is in accordance with the ideal model that assumes fixed band edges. The observed difference in the dark potential between single crystal and sintered electrodes were due to grain boundaries [223]. The $V_{oc(max)}$ vs. V_{redox} relationship may result from a change in V_{fb} with V_{redox} due to surface states [224-227]. The density of surface states on an α-Fe_2O_3 surface is apparently not high enough to cause complete Fermi level pinning [228-229] which would result in an output voltage that is constant over a wide range of V_{redox} values. Decomposition and/or oxidation (Fe^{2+} to Fe^{3+}) probably take place in acidic solutions at high positive redox potential values under open-circuit conditions. Equilibration with some redox couples in the dark occurred only when relatively high concentrations of the oxidized forms were used.

Sahami et al. [230] investigated photoelectrochemical behavior of Si-doped sintered polycrystalline Fe_2O_3 in acetonitrile solutions containing the redox couples ferrocene, Cl^-, Br^-, I^-, $Ru(bpy)_3^{2+}$, $Fe(bpy)_3^{2+}$, and $Fe(phen)_3^{2+}$. There was no oxidation in the dark at the iron oxide electrode for these couples, but they all showed photo-oxidation at potentials negative of their oxidation potential at Pt. Cathodic back reactions of all couples, except halides, were observed. This indicates that surface states capable of mediating electron transfer from the conduction band to the oxidized form of the couples exist in the band gap region of the iron oxide. In addition, open-circuit photovoltages were found to increase with increasing redox potentials of these couples. An open circuit photopotential as high as 0.8 V was obtained for $Ru(bpy)_3^{3+/2+}$.

Photoanodic oxidation of iodide and bromide ions at polycrystalline doped α-Fe_2O_3 electrodes in competition with oxygen production was investigated in the pH range 0-13 in aqueous media [231-232]. It appears that at high pH values only iodide oxidation could compete effectively with water oxidation. However, in addition to the photo-electrochemical oxidation of iodide, evidence for secondary reactions involving electrogenerated species was observed mainly in highly basic solutions. Adsorption of I^- plays a significant role in the reaction as well as in the photoelectrochemical properties of α-Fe_2O_3. Photo-oxidation of organic compounds at Si-doped Fe_2O_3 was investigated by Kennedy et al. [233-234]. Oxalic acid and, with less efficiency, formic acid were able to compete with water for the photogenerated holes at the semiconductor surface. In a nonaqueous solvent the

reactivity of alcohols could be compared, and methanol was found to be much more reactive than isopropanol. The increase of current and organic oxidation product upon addition of water can be explained by, first, the high rate of water reaction with holes at the surface decreases recombination and results in higher photocurrents. Second, an intermediate in the water oxidation, such as the hydroxyl radical, reacts more rapidly with the organic solute than its own reaction leading to O_2. This increases the rate of organic oxidation allowing water to play a catalytic role.

Kennedy et al. [235] measured the absorption coefficient for α-Fe_2O_3 spectrophotometrically and from I-V curves. The calculated absorption coefficient, , was $1x10^4$ cm^{-1}. The diffusion length found for α-Fe_2O_3 was $2\text{-}4x10^{-7}$ cm. The absorption coefficient from optical measurement did not correspond to the absorption coefficient for the excitation process giving rise to the photocurrent. It is reasonable to presume that the absorption coefficient derived from I-V characteristics corresponds to the ligand to metal charge transfer ($O^{2-}$to Fe^{3+}), yielding reactive holes on the oxygen sites (valence band). The spectrophotometric measurements show that another process with comparable absorption is occurring, i.e., there is an overlap of at least two absorption bands. The large absorption coefficient indicated for this overlapping process may mean that another type of charge transfer is occurring, possibly metal to metal, which would give rise to a second type of hole, now on an iron site with a different energy level than the hole in the oxygen valence band.

Anderman et al. [236] studied diffusion controlled and transient

photocurrents of photo-oxidation reactions at polycrystalline α-Fe_2O_3. Steady-state photooxidation currents at α-Fe_2O_3 electrodes with low band bending were found to be significantly dependent on the reducing agents present in the electrolyte. Photooxidation of water at low band bending exhibited only transient character. Diffusion-controlled photocurrents for the photooxidation of I^- and $Fe(CN)_6^{4-}$ in acidic solutions, and OH^- in unbuffered neutral solution were observed at an α-Fe_2O_3 ring disk electrode and could be fitted to the Levich equation [237].

Photocurrent-potential curves at polycrystalline α-Fe_2O_3 electrodes in acidic solutions are similar to those found in basic solutions [238]. Stable photocurrents have been demonstrated in various acidic media, and trace amounts of Fe(III) detected in the working solutions gave an indication of the dissolution of the electrodes. The open circuit dissolution of iron oxide in acidic solutions can be described by the following reaction:

$$Fe_2O_3 + 6H^+ = 2Fe^{3+}(aq) + 3H_2O \qquad (2.10)$$

The typical rate of dissolution under open circuit conditions was found to be 3-7 μm in 24 hours. Dissolution and passivation of iron and mechanism of passive film formation in aqueous solutions has been studied in great detail [239-241]. Yonayama et al. [242] studied electrochemical properties of α-Fe_2O_3 in sulfuric acid solutions. The anodic current, indicating the dissolution reaction, was almost constant and was not affected by the activity of H^+ in the potential

range 0.4-1.0 V vs. SCE, but it was dependent on the conductivity of the electrode. The flat-band potential shifted in the positive direction with increasing activity of H^+. In a study of the affects of various redox reagents in the PEC behavior of iron oxide, Iwanski et al. [243] and Yoneyama et al. [244] found that a significant effects exist due to the action of surface states in mediating a backreaction between photogenerated holes with conduction band electrons. This is assumed to partially account for the low collection efficiency.

Capacitance and conductivity measurements were made on high purity α-Fe_2O_3 and Ti-doped α-Fe_2O_3 in liquid junction cells [179]. Flat-band potentials and donor densities were determined from Mott-Schottky plots (see Figure 2.7). The break in the slopes can be explained assuming the existence of two kinds of donors, one very close to the conduction band and the other at about 0.6 V below the conduction band. The two slopes for each of the plots suggest that the Mott-Schottky slope may be written as:

$$s_1 = 2/\epsilon\epsilon_0 q N_1 \text{ for } V < V_c \tag{2.11}$$

and

$$s_2 = 2/\epsilon\epsilon_0 (N_1 + N_2) \text{ for } V > V_c \tag{2.12}$$

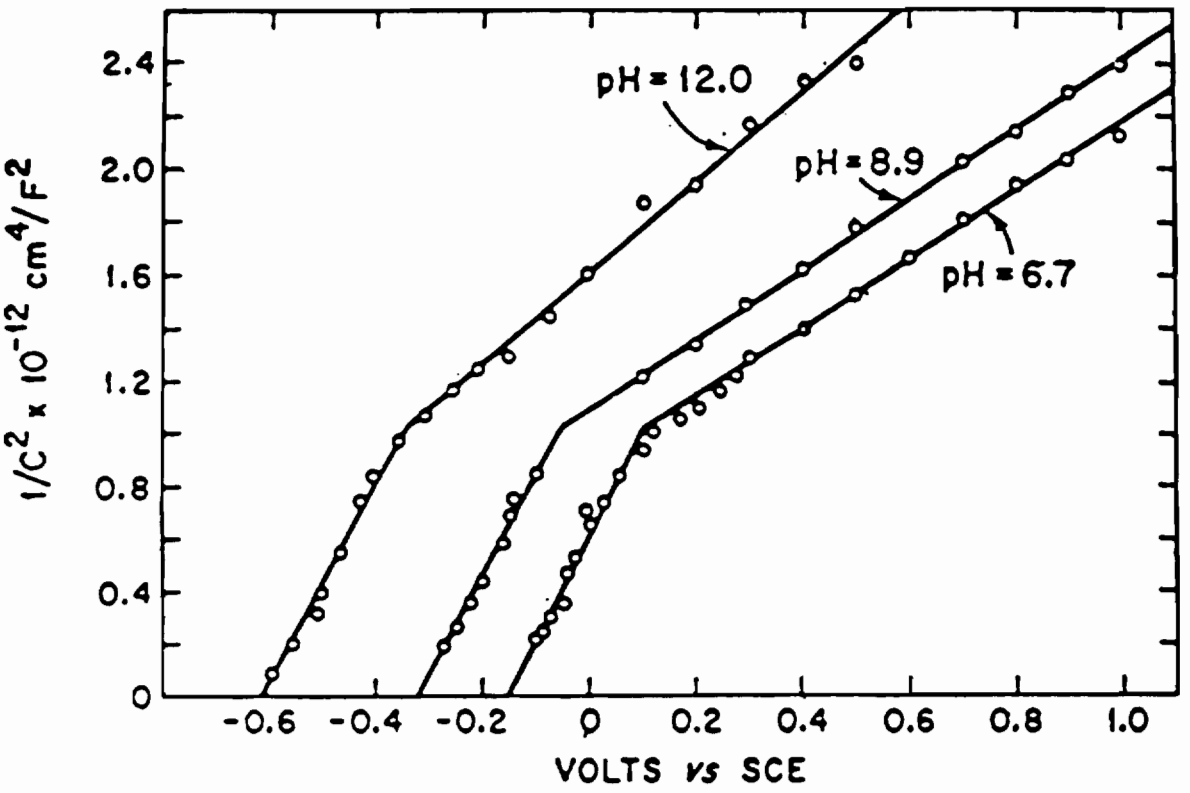

Figure 2.7. Mott-Schottky plots for polycrystalline Fe_2O_3.

where N_1 and N_2 are the densities of the shallow and deep donors, respectively, and V_c is a critical voltage for ionization of the deep donors in the space-charge layer. The data show that the deep donor is located about 0.3 V below E_F. Flat-band data can give the position of the Fermi level relative to the bottom of the conduction band (E_c) provided the density of states in the conduction band, N_c, is known:

$$E_c - E_F = kT\ln N_c/N_1 \qquad (2.13)$$

assuming each shallow donor donates one electron to the conduction band. For iron oxide N_c has been assumed to be $4x10^{22}$ cm^{-3} [182], the number of cations in the lattice. The Fermi level is then calculated to be 0.3 V below the conduction band. Energy level diagram based on these results can be seen in Figure 2.8. The following results were obtained, V_{fb} = -0.64 V vs. SCE in 0.1 M NaOH for pure α-Fe_2O_3 and V_{fb} = -1.0 V vs. SCE in 1M NaOH for Ti-Fe_2O_3. Potentials for zero photocurrent [245-249] were determined using chopped light and were in excellent agreement in basic solution with flat-band potentials calculated from capacitance measurements. The observations and conclusions described above were also reported by many other investigators [250-273] but since their work and results were very similar they will not be discussed in detail.

Pajkossy [61-62] studied phenomenological kinetics of photoelectrochemical processes on iron oxide electrodes. The dependence of photocurrent on reducing agent concentration was described in terms of a model of competition kinetics. A simple mechanism was proposed:

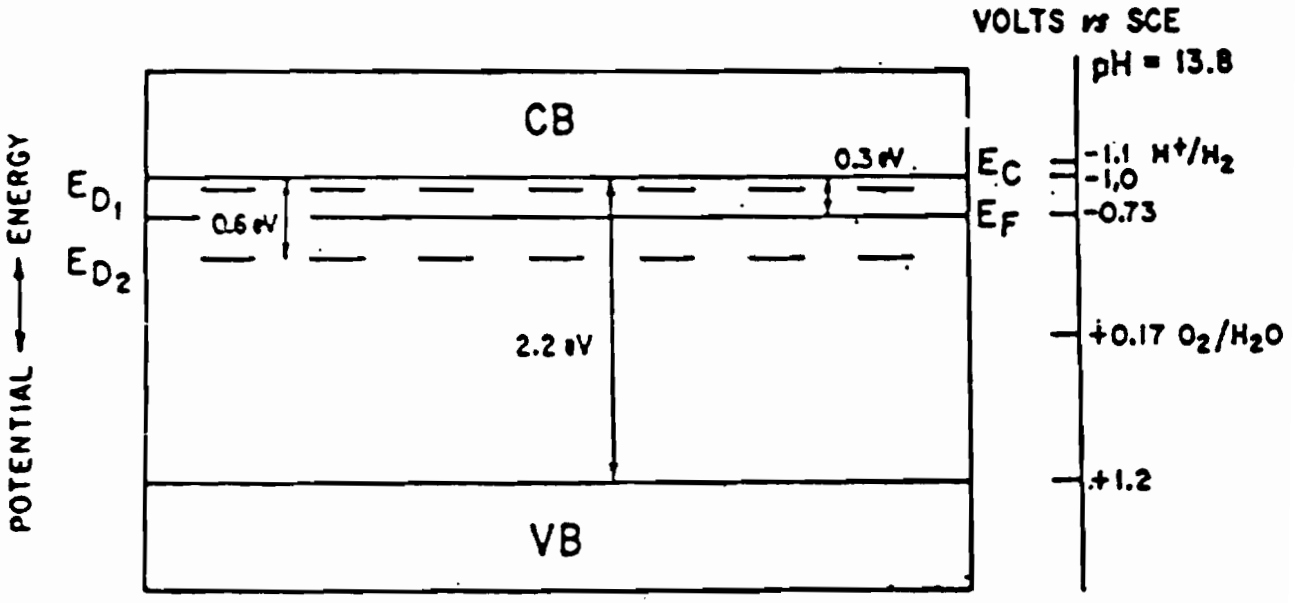

Figure 2.8. Energy level diagram for polycrystalline Fe_2O_3.

photogenerated minority carriers, arriving at the surface are either injected into the solution or recombine. The flux of minority carriers, i. e. hole flux can be determined as a parameter of the kinetic equation. Indirect evidence has been found that the experimentally determined hole flux as a function of light intensity and electrode potential cannot be described in terms of Gartner's depletion layer theory. Pajkossy et al. [274] studied impedance spectra of thermally grown α-Fe_2O_3 in aqueous solution system. An equivalent circuit was constructed and its elements determined by parameter fitting. The equivalent circuit consisting of three resistance and two non-identical constant phase angle impedances (CPAI) was found to be adequate for fitting the experimental data. The effect of experimental conditions on circuit parameters enabled the identification of one of the resistances as the element which characterizes charge transfer between the two phases, one of the CPAI corresponds to the space charge layer and some indication can be given regarding the role of further elements.

Dare-Edwards et al. [275] studied Fe_2O_3 as a possible semiconductor for use in solar photoelectrolysis cells. The results of this study indicate that the problems encountered in the study of iron oxide as a photoanode can be traced to unfavorable surface rather than bulk properties. These unfavorable surface properties might have two origins. The first is that the surface may be induced to reconstruct, at least partially, to a form that has electrochemical properties very similar to those of Fe_3O_4. The second is that the intrinsic faradaic rate constant for the oxidation of water on Fe_2O_3 is substantially smaller than on other semiconductors studied. This fact lends strong

support to a placement of any hole energies in the Fe^{3+} e_g^2 level above the top of the O $2p^6$ band. Rapid hole capture by these levels at or near the surface leads to the fact that oxidation of water must take place from holes on Fe^{3+} ions rather than holes in the O $2p^6$ band [276].

Benko et al. [277] made a comparison of the photoelectrochemical properties of Sn-doped Fe_2O_3 in amorphous and polycrystalline forms. There were no real differences in optical band gaps, Mott-Schottky intercepts, band-edge positions, and optical absorption spectra. For the photo-oxidation of water, the difference between instantaneous and steady-state photocurrents is much larger for the amorphous than for the crystalline form, which indicates a difference in the density and/or effectiveness of surface states. The dark current of the amorphous form is larger, and its quantum efficiency in the ultraviolet is smaller.

Schiller et al. [278-279] studied the effect of gamma radiation on the photoelectrochemical response of thermally grown iron oxide. A dose dependent decrease in the photocurrent was found. The data, discussed in terms of Gartner theory, enable one to evaluate the width of the space-charge layer and the diffusion length of the minority charge carriers as a function of dose. There are number of papers discussing photoelectrochemical properties of n-type semiconducting ferrite electrodes [280-285].

Benko et al. [281] and Haart et al. [281] investigated $MgFe_2O_4$ with spinel structure. Matsumoto et al. [285] investigated electronic and photoelectrochemical properties of Zn-Ti-Fe spinel oxides. Wakabayashi

et al. [282] studied electrochemical properties of Mn, Zn, Co, and Ni ferrites.

2.8.4 Heterojunctions

One of the possible techniques to find a breakthrough in the photoelectrolysis of water may be the employment of a heterostructure semiconductor electrode, instead of using a single homogeneous material electrode in a photocell.

Liou et al. [286-287] prepared Fe_2O_3/TiO_2 heterojunction electrodes by CVD application of TiO_2 onto Fe_2O_3 substrates. They calculated the band edge mismatches to be 0.38 eV at the conduction band and 0.42 eV at the valence band. They theorized that if the TiO_2 films were made thin enough (~ 1000 Å), the depletion layer of the sample might extend through the TiO_2 film into the substrate. This will then allow photogenerated pairs to be separated, bringing the holes from the substrate to the film barrier. The application of a small anodic bias will then allow the holes to overcome the valence band energy barrier. They found that this occurs, but the necessity of an external bias remains a problem.

Ono et al. [288-289], Osaka et al. [290], and Tsubomura et al. [291] have studied photoelectrochemical properties of Fe_2O_3/n-Si heterojunctions for photoelectrochemical solar energy conversion. A heterostructure electrode which was composed of n-type Si coated with a thin layer of Fe_2O_3 showed O_2 evolution current as high as 50 $\mu A/cm^2$ under an illumination of 0.1 W/cm^2. The highly efficient conversion of light into photocurrent was due to the efficient hole injection from Si

across the interface of the heterostructure. The spectral response of the photocurrent covered the range between 250 and 1140 nm, and the quantum yield was nearly 80% in the range between 480 and 850 nm at 2 V vs. SCE for an electrode with a 200 Å thick iron oxide film.

Mettee et al. [292] assembled a p/n monolithic photochemical diode consisting of n-Fe_2O_3 anode and Zn-doped p-GaAs cathode (see Figure 2.9). When this cell was exposed to visible and near UV radiation in aqueous solution, hydrogen was produced in relatively low quantum yields. This unit also splits sea water using incident solar radiation. Both photoelectrode materials showed enhancements of their photocurrents when catalysts (RuO_2 on n-Fe_2O_3 and Pt on p-GaAs) were deposited on their surfaces.

Somorjai et al. [293-296] reported successful photodissociation of water to produce hydrogen and oxygen without any bias using a polycrystalline p/n assembly made out of Mg-, and Si-doped Fe_2O_3. By connecting n-type and p-type iron oxide polycrystalline pressed disks with a conducting wire, immersing the assembly in a 0.1 M Na_2SO_4 aqueous solution and irradiating the electrodes hydrogen evolution and a photocurrent across the samples were detectable (see Figure 2.10 and 2.11). The hydrogen production rate was in the range of 1-2 hydrogen molecules per site per minute and the photocurrent was of the order of 10 $\mu A/cm^{-2}$. The reaction is thus catalytic and can be carried out for 6-8 hours without any sign of poisoning. When the photoinduced hydrogen production and the corresponding photocurrent eventually decline they can be regenerated by passing oxygen gas over the catalyst iron oxide surfaces. The poisoning effect is not observed as

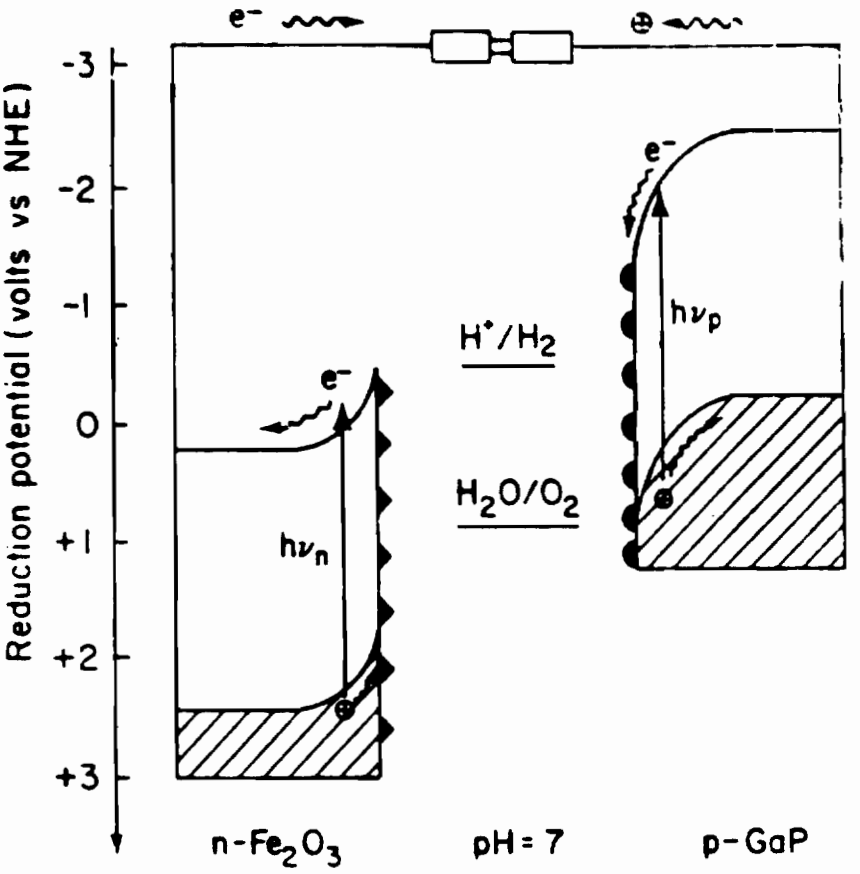

Figure 2.9. The dark equilibrium energetics of the n-Fe_2O_3/p-GaP photochemical diode at pH=7 shows the disposition of the valence band of n-Fe_2O_3 and the conduction band of p-GaP sufficient to oxidize and reduce water, respectively.

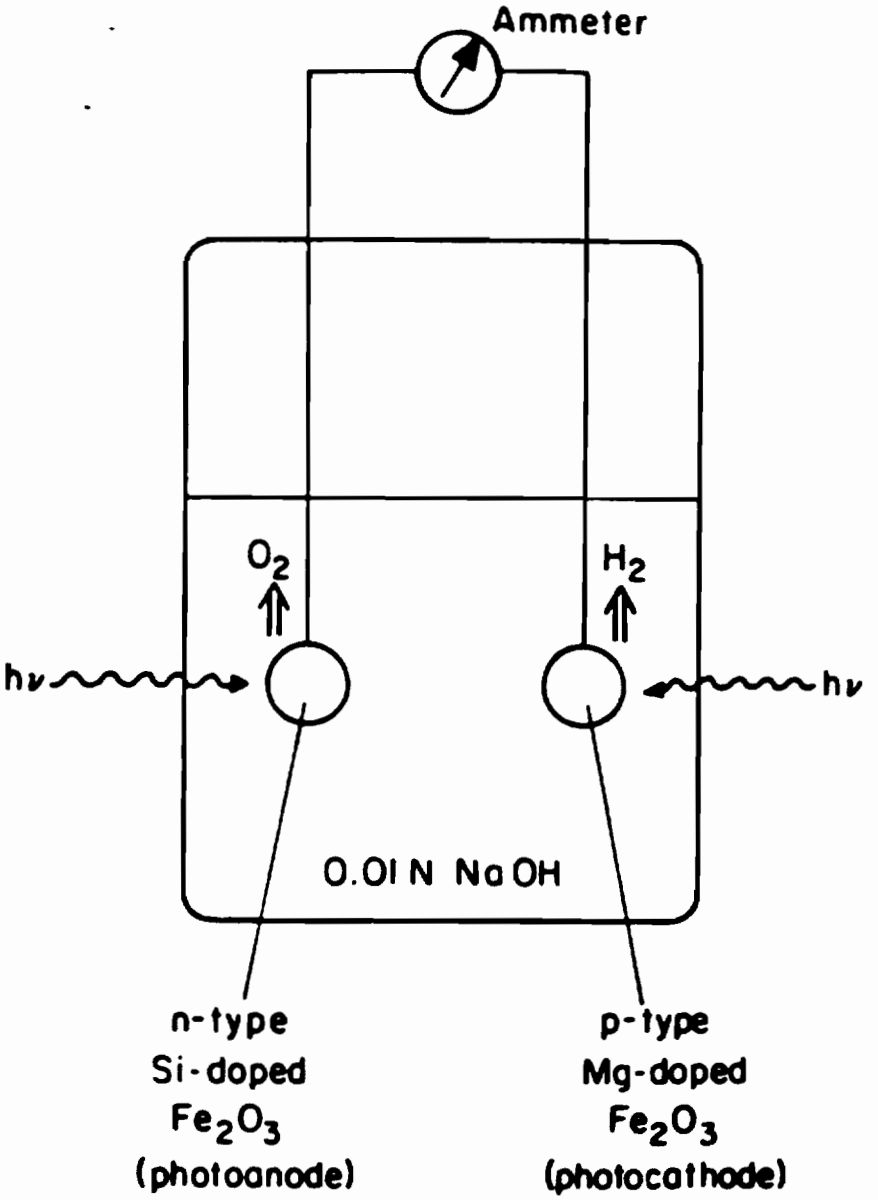

Figure 2.10. Schematic illustration of p/n assembly for the photodissociation of water using doped Fe_2O_3 electrodes.

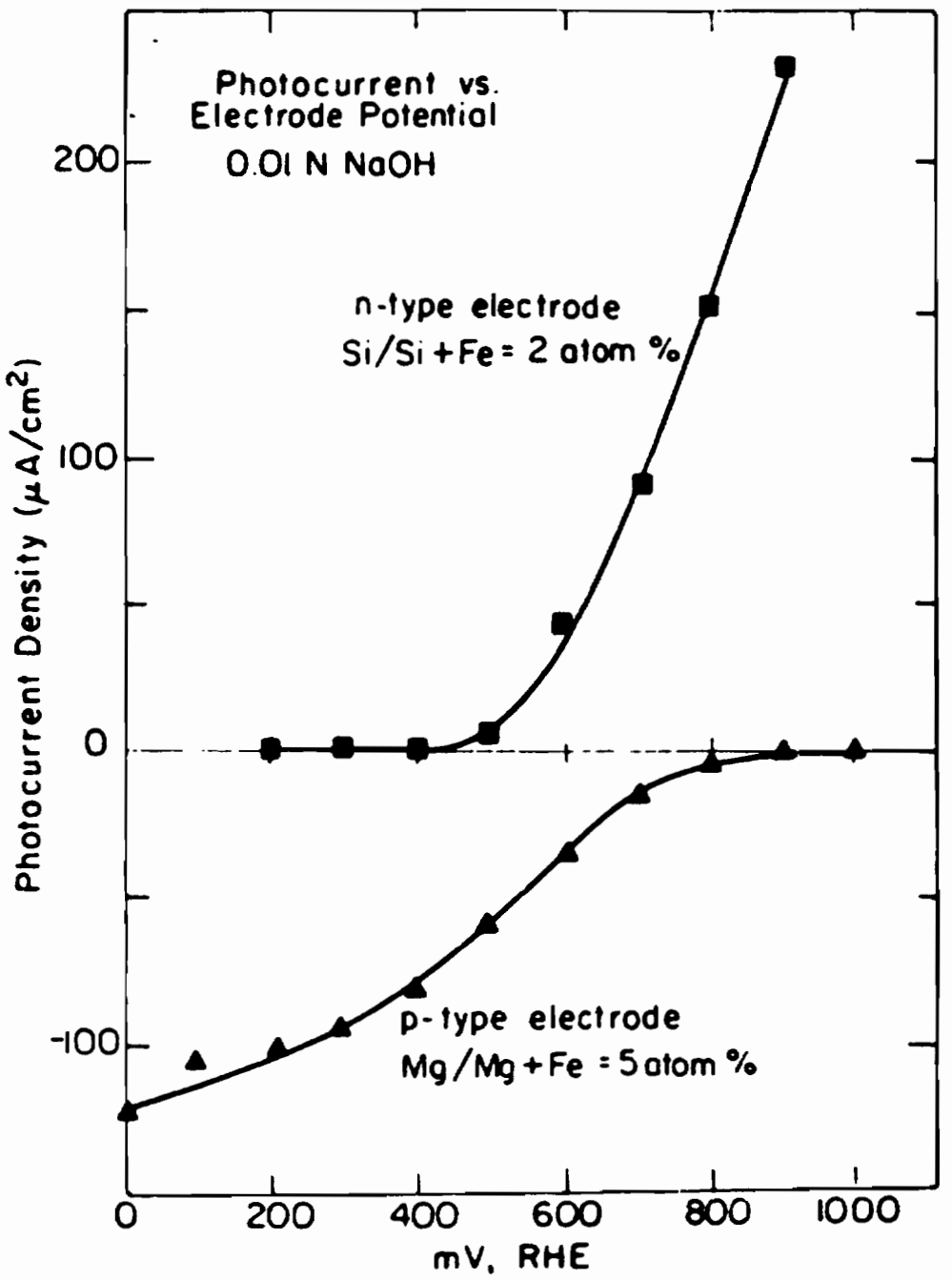

Figure 2.11. Photocurrents for n-type (Si-doped) and p-type (Mg-doped) Fe_2O_3 electrodes under biased conditions.

long as oxygen is continuously passing over the surface.

2.9 Metallized Electrodes

Wrighton et al. [297] showed that platinized n-type $SrTiO_3$ and $KTaO_3$ evolve oxygen and hydrogen from alkaline aqueous solutions when irradiated with ultraviolet light. The irradiated portions of the metal oxide behave as the photoanode and the dark platinized portions behave as the cathode. The nonplatinized oxides are energetically capable of evolving H_2 and O_2 upon irradiation but the overvoltage for H_2 is too great [298-300]. The general requirement for the short-circuit redox chemistry at the irradiated n-type semiconductor surface is that the dark cathodic reaction occur at a potential more positive than the anodic reaction upon irradiation [301]. The role of the platinum coating is to reduce the H_2 overvoltage to meet this requirement.

Also Koudelka et al. [302] and Heller [303] discussed cathodic behavior of platinized TiO_2 electrodes, important strong metal-support interactions with respect to various gas phase reactions.

Heller et al. [304] and Nakato et al. [305] reported preparing very thin transparent films of platinum and also discontinuous platinum films on semiconductors. The use of the thin metal coating has, however, a problem in that electrodes coated with continuous metal layers generally lose photovoltages arising from semiconductor/liquid junctions, showing only small photovoltages arising from semiconductor/metal junctions. For a discontinuous metal coated semiconductor

covered parts is different from that at the naked parts. Therefore a microscopically discontinuous layer on a semiconductor electrode does not destroy the photovoltage arising from a semiconductor/solution junction and yet it retains the catalytic and the stabilizing functions.

Kobayashi et al. [306] studied the role of Pt overlayers on TiO_2 electrodes in enhancement of the rate of cathodic processes. Improvements in the cathodic properties by platinization occur in two different modes. One is related to high electrocatalytic activity of Pt, the other results from enhancement of probabilities of electron exchange between the electrode and electrolyte species caused by platinization.

Sammells et al. [307] noticed enhanced photocurrent in platinized Fe_2O_3 electrodes. The platinum was sputtered on the Fe_2O_3 surface. The increase in photocurrent was ascribed to the electrocatalytic nature of platinum in oxygen evolution as previously discussed.

Richardson et al. [308] studied the effect of Rhodium on Fe_2O_3 and TiO_2 electrodes. They also observed similar effects in enhancing the photocurrent by Rh addition. They suggested that the noble metal enhances the kinetics of photoanodic oxygen evolution reaction.

St. John et al. [309] have investigated photochemistry of thermally grown platinum containing iron oxide photoanodes. They also reported enhancement in photoactivity of platinized samples. They found that the platinum gave a more negative flat-band potential.

Because these results were very interesting and promising and no detailed investigation has been performed on determining the platinum

detailed investigation has been performed on determining the platinum effect on iron oxide photoelectrodes this work will be concerned with that question.

2.10 Photocathodes

Somorjai et al. [164,310-312] and Holihan et al. [313-314] have prepared Mg doped Fe_2O_3 which showed photocathodic behavior in a photoelectrochemical cell. The resistivity of the samples with low doping density (< 2% Mg) was on the order of 10^3 Ω-cm which is very high for efficient PEC, so the samples were doped with up to 20 atomic percent magnesium which decreased the resistivity to 10 Ω-cm. Seebeck voltages showed that material was n-type but photoelectrochemistry showed cathodic photocurrents or p-type behavior. These discrepancies were assigned to poor preparation technique producing multiphase inhomogeneous samples. Samples showed a very small photocurrent and the dark current was almost the same magnitude as the photocurrent which was due to the high resistance of the samples.

Tinnemans et al. [315-316] also studied the photoelectrochemical and interfacial phenomena in polycrystalline Mg-doped Fe_2O_3. The materials prepared by solid state reaction are essentially single-phase for Mg concentrations not exceeding 0.5%. The positive sign of the photovoltage and of the thermoelectric power η, confirmed that the material was a p-type semiconductor. Carrier concentrations calculated from η, revealed that for up to about 0.1% Mg, each Mg^{2+} introduces one electron-hole. The a.c. conductivities, yielded conductivity activation enthalpies of about 0.5 eV in the temperature region 300-800 K,

and were affected by grain growth and porosity. The flat-band potential was determined to be +2.2 V vs. SCE at pH = 10. PEC photocurrents in the visible region correspond to very low (~ 0.1%) monochromatic quantum efficiency which was due to the low electron-hole mobility. The electronic transition in the visible region is indirect, and evidence has been found for this transition to be Fe-Fe charge transfer.

2.11 Photocatalysts

In the field of artificial photosynthesis [317-319] attempts are presently made to design functional molecular assemblies that achieve the task of fuel formation by visible light. Colloidal semiconductors [320-324] exhibit several advantegous features that make them attractive candidates to be employed as light harvesting units in such devices. These particles combine a number of desirable properties, such as high extinction coefficients, fast carrier diffusion to the interface and suitable positioning of their valence and conduction bands, to achieve high efficiencies in the light energy conversion process. Furthermore, the possibility of modifying the surface of the semiconductor particle by chemisorption, chemical derivatization [325] and/or catalyst deposition [326-332] to assist light-induced charge separation and subsequent fuel-generating dark reaction is particularly attractive.

Photochemistry of iron oxide colloids [333] and colloidal iron oxide polymorphs [334] has been studied in detail. Gratzel et al. [335]

of chloride ions. The rate of corrosion was enhanced by a factor of ten upon band gap excitation using visible light. Surface adsorption and ease of complex formation with solution species are shown to be a major factor in the dissolution process.

Moser et al. [336] studied laser photolysis of halide oxidation with colloidal Fe_2O_3 (600 Å particle radius). For I_2 formation, the quantum yield exceeds 0.9 which indicates almost quantitative hole scavenging by iodide.

Dimitrijevic et al. [337] investigated the kinetics and equilibria of electron transfer between methylviologen cation radicals and Fe_2O_3 colloidal particles with the pulse-radiolysis technique. The rate of electron transfer is lower than predicted for a diffusion-controlled reaction. The flat-band potential appears to be more negative (-0.1 to -0.2 V) than the corresponding single crystal electrode.

Haupt et al. [338] produced oxygen from water upon illumination of a solution of ferric oxide colloid with visible light. Silver nitrate was used as an electron scavenger and quantum efficiencies of the order of 1% were obtained.

Nakanishi et al. [339] photochemically produced hydrogen from small particles of Mg-doped iron oxides in a methanol-water (1:1) mixture. The efficiency of the reaction increased substantially when the powders were loaded with platinum. Hydrogen production from these Mg-Fe_2O_3 particles is photocatalytic and occurs mainly as a result of band gap irradiation, but also occurs in small amounts with sub-band gap irradiation. There was a linearly increasing dependence of the H_2 production with increasing light intensity.

Khader et al. [340] produced H_2 and NH_3 from suspensions of reduced Fe_2O_3 (10% Fe_3O_4) catalyst particles or sintered pellets in water. Catalytic action was demonstrated by detecting H_2 yields many times the stoichiometric equivalent of the measured Fe(II) content of the catalyst, up to a factor 80 for H_2 and 20 for NH_3. The initial rate of formation of H_2 was 40 μmol/h.g of catalyst and for NH_3 was 10 μmol/h.g of catalyst. The formation of O_2 was shown by mass spectrometric observation using ^{18}O labeled water.

CHAPTER THREE

EXPERIMENTAL PROCEDURES

3.1 Sample Preparation

The samples used in this investigation were prepared primarily by two preparation techniques. The first technique is a solid state reaction of mixed oxides and second technique is by freeze-drying [134-135]. The samples prepared by the freeze-drying technique will be compared to the samples prepared by the solid state mixing technique. Parameters that will be compared in the samples prepared by the two technique are: structure, surface area, homogeneity of doping, electrical conductivity, photoactivity, photoelectrochemical behavior, photocatalytic behavior, and capacitance.

3.1.1 Solid State Mixing Technique

The samples were prepared from high purity, 99.999% α-Fe_2O_3 (Johnson Matthey Inc.), 99.999% SiO_2 (Johnson Matthey Inc.), 99.999% MgO (Johnson Matthey Inc.), and 99.999% Platinum black (Johnson Matthey Inc.). The silicon or magnesium doped samples were prepared by grinding and mixing of stoichiometric amounts of oxides in a methanol slurry using an agate mortar. The platinum doped samples were prepared by mixing other oxides with powdered platinum. The oxides were first ground dry in the mortar for about 20 minutes, then the methanol was added and the slurry was then mixed for an additional 20 minutes.

After about 45 minutes of grinding and mixing, the slurry was dried in an oven at 70°C under flowing nitrogen to eliminate adsorbed methanol. The dried powder was ground again in the mortar for a few minutes, then mixed with polyvinyl alcohol (used as a binder) and pressed under a load of 40,000 psi into discs of about 1 cm diameter and about 0.1 cm thickness. The pellets were placed on a bed of a material of the same composition (to prevent contamination) in an alumina boat and sintered in air at 1385°C for 48 hours. The sintered pellets were then quenched in air to room temperature.

3.1.2 Freeze-Drying Technique

Colloidal sols of Fe_2O_3, SiO_2, Pt, and MgO were prepared first. The colloidal Fe_2O_3 was prepared by hydrolyzing $Fe(NO_3)_3.6H_2O$ (99.99% Baker) or $FeCl_3.6H_2O$ (99.99% Baker) salt solutions [124-126]. The solutions were hydrolyzed at 90-100°C by adding the solutions dropwise into hot deionized water while constantly stirring the reaction mixture. The colloidal sols were then cooled to room temperature and transferred into a dialyzing cellulose tubing. The sols were then dialyzed against deionized water for several days until no Cl^- or NO_3^- ions could be detected and the pH of the sols reached the pH of the deionized water (pH ~ 5.5). The resulting sol concentrations ranged from 1 gram Fe_2O_3 per 1 liter of the sol to as high as 15 grams Fe_2O_3 per 1 liter of the sol. The concentration of the Fe_2O_3 sol was determined spectrophotometrically [341] by complexing Fe^{3+} with SCN^- and measuring the absorbance of the red complex at 480 nm on a Lambda-9 UV/VIS Perkin-Elmer spectrophotometer.

The magnesium sol was prepared by hydrolysis of $Mg(OH)_2$. The concentration of the MgO sol was determined spectrophotometrically [342] by complexing the Mg^{2+} with the Titan Yellow (Thiazol yellow) and measuring the absorbance of the pink complex at 545 nm.

The colloidal SiO_2 sol was prepared by hydrolyzing $SiCl_4$ in deionized water at 0°C [343-344]. The acidic sol was then dialyzed against deionized water until all chloride ions were removed. The concentration of the SiO_2 sol was determined spectrophotometrically by a complexing reaction with ammonium molybdate and reduction to the heteropoly blue with 1-amino-2-naphthol-4-sulfonic acid. The absorbance of the blue complex was measured at 811 nm [345].

The platinum sol was prepared by reduction of $H_2PtCl_6.nH_2O$ (99.999% Aldrich) with sodium citrate at 100°C [346]. The black platinum sol was then dialyzed for a week to remove any excess of the reducing agent. The typical concentration of the platinum sol was 200 mg/L.

The prepared colloidal sols were then used to prepare silicon, magnesium, and platinum doped Fe_2O_3 with dopant concentrations ranging from 0.1 to 5 atomic percent. Stoichiometric amounts of the colloidal oxides were thoroughly mixed in a reaction vessel. The mixed sols were then quickly frozen by submerging the vessel in a liquid nitrogen bath. An alternative freezing method was used in which the sols were atomized directly into the liquid nitrogen. The reaction vessel with a frozen sample was attached to a freeze-drying apparatus consisting of the reaction vessel connected to a liquid nitrogen trap supported by a vacuum pump. Figure 3.1 shows a schematic of the freeze-drying apparatus. An infrared lamp was used to speed up the drying process.

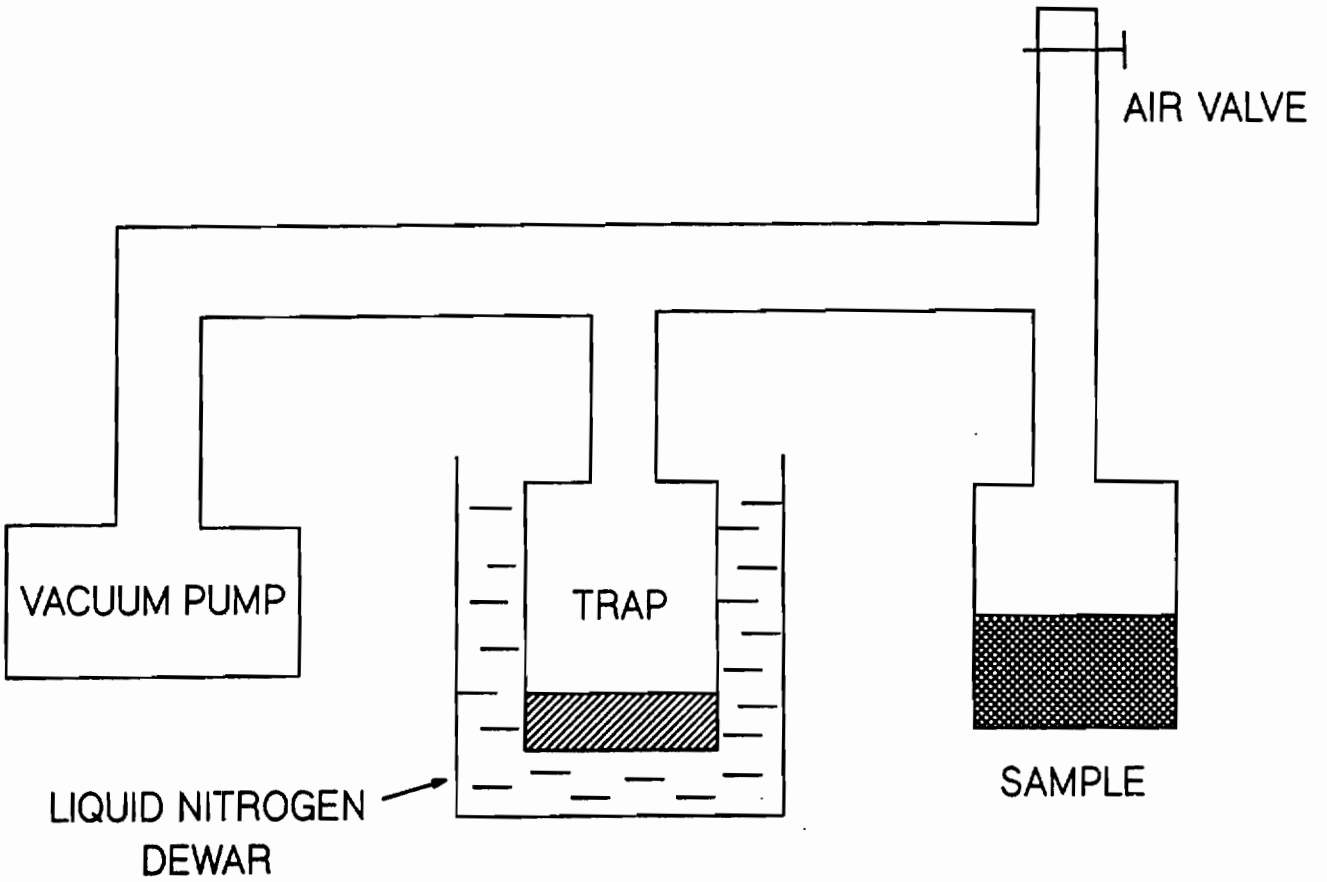

Figure 3.1. A schematic diagram of the freeze-drying apparatus.

The resulting fine powder was processed as described in section 3.1.1.

3.2 Structural Characterization

The powdered and sintered samples were characterized by Perkin-Elmer 1800 FT-IR in the form of KBr pellets. The samples were purged with dry nitrogen prior to scanning to eliminate adsorbed moisture. The infrared investigation was usually performed in the 4000-400 cm^{-1} region by scanning each sample at least 10x to minimize the noise.

The samples (both powders and pellets) were also characterized by a Siemens X-ray diffractometer (Tektronix Inc.). The samples were scanned four times at 0.02°/second from 4° to 104° using Cu-Kα radiation. The pellets were scanned directly and powders were arranged on a special aluminum holder capable of holding six powdered samples.

Surface area of the samples was determined by nitrogen desorption technique on a Quantasorb instrument (Portland State University).

3.3 Electron Microscopy Studies

The powdered samples were examined with a Hitachi HU-800 scanning transmission electron microscope (STEM) and with a JEOL 35C scanning electron microscope (SEM) equipped with a Tracor Northern 5500 energy dispersive X-ray analyzer (EDX). To prevent surface charging of the semiconducting Fe_2O_3 in the SEM, samples were coated with Au-Pd film (~ 200 Å) using a Technics Hummer II sputtering system. SEM analysis consisted of studying powder morphology and grain size; grain size, porosity and chemical composition on the surface of sintered pellets; grain size and chemical composition on the fracture surface of the

pellets. SEM analysis was also performed on the samples after photo-electrochemical and photocorrosion experiments.

The powdered samples for STEM analysis were prepared by suspending the powder in an alcohol and depositing the suspension on a copper grid coated with a Formvar film. The grid with the sample was then coated with carbon in an Elion DV-502 carbon evaporator.

3.4 Electrical Conductivity and Dielectric Measurements

The electrical conductivity was measured on the sintered pellets by a four point Van der Pauw technique [346-348] and with a Hewlett-Packard 4260A ac impedance conductivity bridge operating at 1kHz frequency. The problems of producing ohmic contacts of low resistance to semiconductors was studied and discussed in detail by Odekirk [349]. The contacts were made by rubbing the surface of the sample with an $In_{0.995}Ga_{0.005}$ alloy, then coating the contact with a DuPont conductive silver paste, and finally soldering a fine copper wire to the sample with the $In_{0.995}Ga_{0.005}$ alloy. A current to the sample was supplied by a Keithley 225 current source and voltage was measured using a Keithley 191 or 175 digital multimeter.

The dielectric constant was measured using a parallel plate technique [179]. The dielectric cell was a parallel plate type made of copper with the area of one plate much larger (~ 100x) than the other. The sample was coated from both sides with a DuPont conductive silver paste. The cell was connected to a Hewlett-Packard 4260A capacitance bridge and the capacitance measured with and without the Fe_2O_3 sample at 1 kHz frequency.

The dielectric constant, ϵ, was calculated from capacitance data according to the following equation:

$$\epsilon = 9.0x10^{11}(4\pi t/A)(C_S - C_O) \qquad (4.1)$$

where t and A are the disk thickness and area, C_S is the capacitance with the sample, and C_O is the capacitance without the sample.

3.5 Photoelectrochemical and Capacitance Measurements

A single compartment, gas tight photoelectrochemical reaction cell was designed and constructed from an optically transparent quartz with two optical windows. A top cover for the reaction cell was made from a pyrex glass with openings for a working electrode, reference electrode, counter electrode, gas sampling valve, and inert gas inlet and outlet ports. A platinum mesh electrode was used as a counter electrode. A standard calomel electrode (SCE) or a silver/silver chloride electrode (SSE) were used as a reference electrodes. Argon gas was used as an inert atmosphere for most of the experiments.

The photoanodes or photocathodes were prepared from sintered ceramic disks or pieces of the disks of thickness about 0.1 cm and of a known surface area. Ohmic contact was provided by rubbing the back surface of each photoelectrode with $In_{0.995}Ga_{0.005}$ alloy and DuPont conducting silver paste. Indium solder was then used to attach a tinned copper wire to this back surface, which was then coated with DuPont conducting silver paste. The photoelectrodes were then sealed with epoxy resin (Armstrong Industrial Epoxy, kit A-2/W) to the lower open end of an L-

shaped pyrex glass tube, so that only the untreated front face was exposed to the electrolyte and the rear contact being protected inside the glass tube. The electrolyte used in these experiments was 1M NaOH + 0.01M KNO_3 prepared from analytical grade NaOH and KNO_3 and deionized water. The electrolyte pH of 13.6 was measured with a Cole-Palmer digital pH meter.

Figure 3.2 demonstrates the photoelectrochemical experimental arrangement. The open circuit dark potential was measured first by connecting a working electrode to a positive side of a Keithley 175 autoranging digital multimeter and connecting the reference electrode to a negative side of the multimeter. The open circuit photopotential was measured after a photoelectrode was irradiated with an Oriel 150 watt compact xenon illuminator.

The current-potential measurements were performed under a flowing argon atmosphere while stirring the electrolyte with a magnetic stirring bar on a stirring plate. The electrode potential was set by an M 4100 Petrolyte Instruments potentiostat. Continuous dark current versus time was monitored on an M 4100 potentiodyne X-Y-t analyzer until the dark current became stable and then the photoelectrode was illuminated with an Oriel 150 W compact xenon illuminator. The radiation was filtered through a 10 cm long quartz water filter to remove infrared radiation and prevent heating of the sample, and 420 nm cut off filter to remove ultraviolet radiation. The resulting photo-current was monitored continuously versus time on the same instrument. The applied voltages and resulting currents were monitored with a Keithley 175 autoranging digital multimeter. The gaseous products of

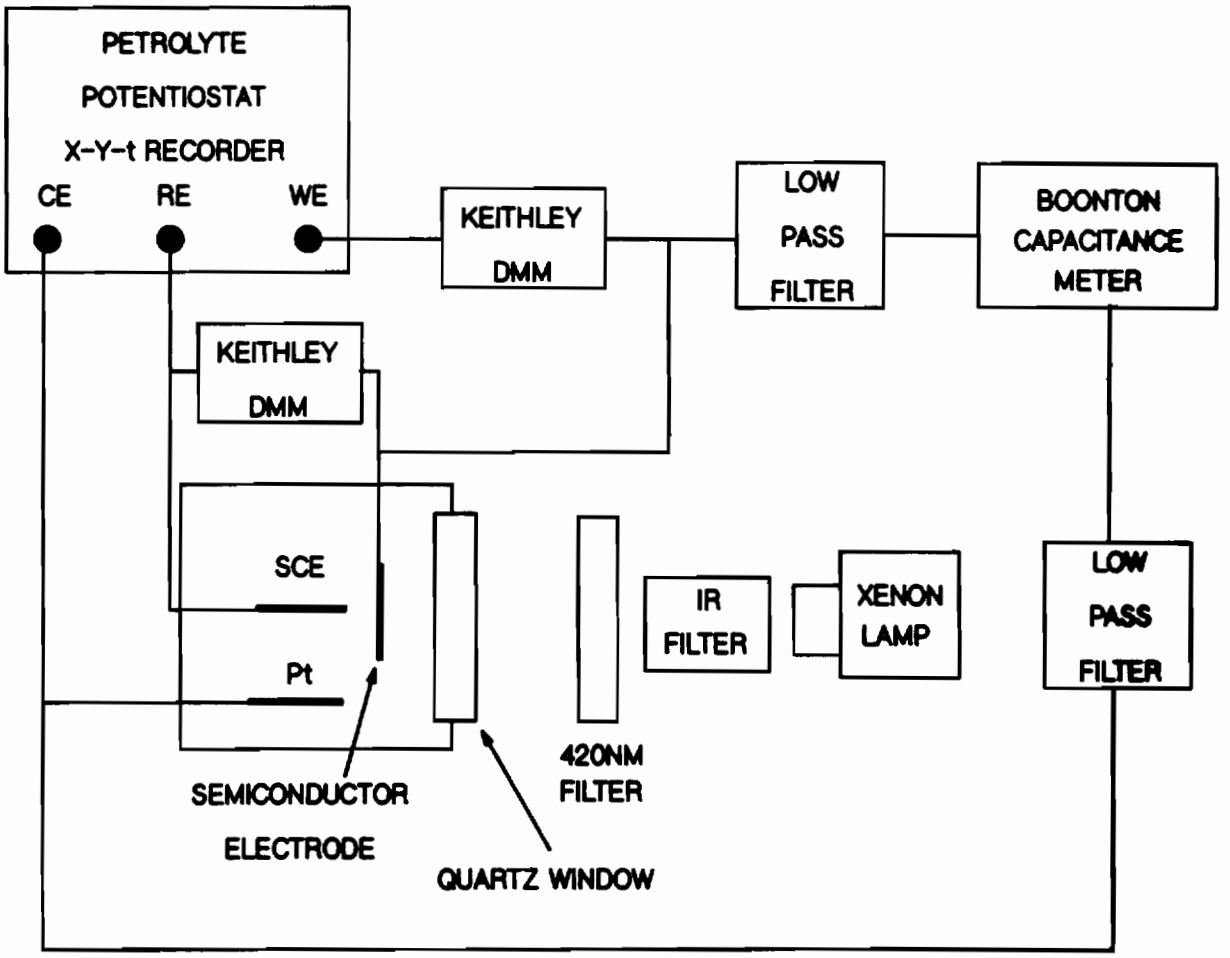

Figure 3.2. Experimental arrangement for the photoelectrochemical measurements.

the electrochemical reactions were analyzed by an Aerograph A 90-P3 gas chromatograph equipped with a glass column packed with a molecular sieve 5A and an argon carrier gas. Qualitative and quantitative analysis of the peaks was performed on a Spectra Physics SP 4270 integrator.

The corrosion measurements were performed in the dark and under illumination using the same experimental arrangement as depicted in Figure 3.2. An M 4100 potentiodyne analyzer was used in the potentiodynamic mode where the applied potential was continuously changing at 10 mV/second from positive potential to negative potential. The current versus voltage was continuously monitored on an M 4100 Petrolyte Instruments X-Y recorder.

The capacitance was measured in the potentiostatic mode at each applied potential with a Boonton 72BD digital capacitance meter at 1kHz frequency. A low pass filters were used to filter out an ac component in the circuit between the electrodes and the potentiostat.

3.6 Cyclic Voltammetry Measurements

Cyclic voltammetry studies, as discussed in Section 2.8.2, were planned as a means of determining the nature of reactions occurring on the photoelectrodes during photoelectrolysis of water. These cyclic voltammetry curves can be also used to determine kinetic information about a given electrochemical system.

Sample preparation and mounting procedures were the same as those described in Section 3.5. Figure 3.3 depicts the experimental arrangement involved in cyclic voltammetry studies.

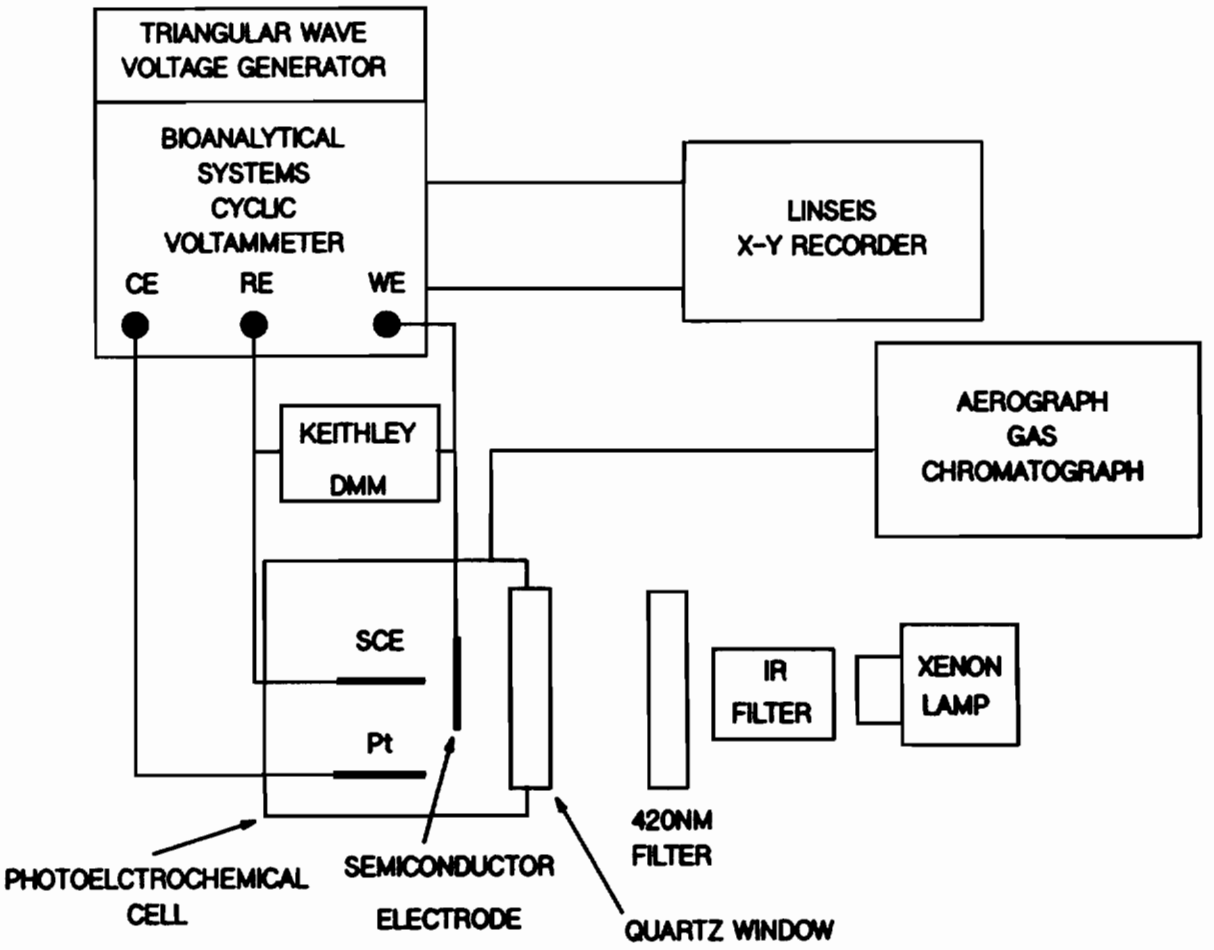

Figure 3.3. Experimental arrangement for cyclic voltammetry experiments.

A triangular voltage wave was generated in Bioanalytical Systems CV-1B cyclic voltammeter which was connected to the three electrode reaction cell. The potential was continuously scanned and cycled between +1.5 and -1.5 V vs. SCE at 10 mV/second. Slow scanning speed was chosen to minimize charging current and approach a steady-state current conditions. The potential versus current was being continuously recorded on a Linseis LY 18100 X-Y recorder. Voltage was also monitored with a Keithley 175 autoranging multimeter during scanning cycle. These experiments were performed in the dark and under illumination. Illumination was provided with an Oriel 150 W compact xenon illuminator with light filtered through a 420 nm cut off and an infrared filter. The gaseous products of the electrochemical reactions were analyzed by an Aerograph A 90-P3 gas chromatograph equipped with a glass column packed with a molecular sieve 5A and an argon carrier gas. Qualitative and quantitative analysis of the peaks was performed on a Spectra Physics SP 4270 integrator.

3.7 Photoconductivity Measurements

Sample preparation and mounting procedures were identical to those described in Section 3.5. Figure 3.4 shows the experimental arrangement. An Oriel 150 W compact xenon illuminator with 420 nm and infrared filter was used for illumination. The light was chopped with a 270 Hz Rofin chopper wheel, whose frequency was fed into a reference input of a Princenton Applied Research (PAR) 5101 Lock-In amplifier. The chopped light was focused onto the entry slit of a Jarrell-Ash Mark X variable slit monochromator, equipped with a direct drive motor with

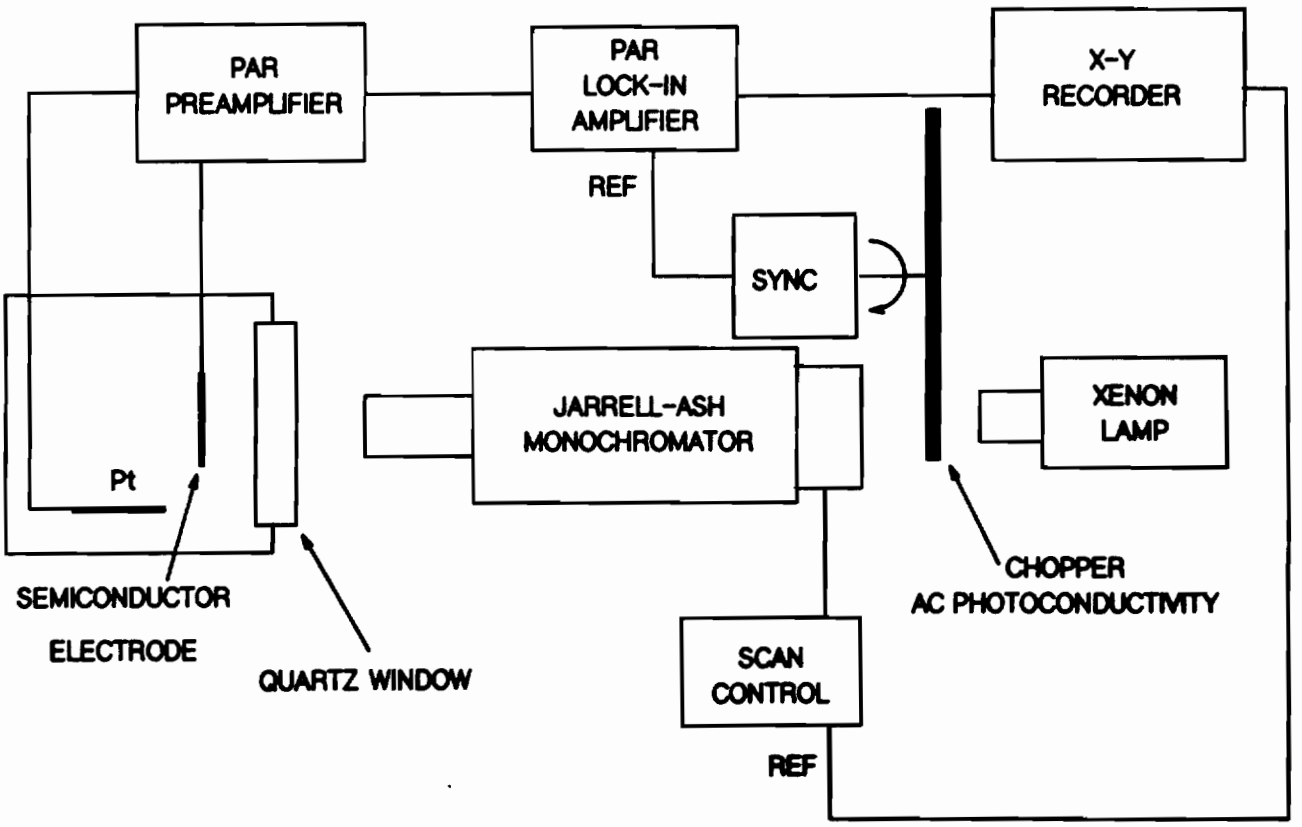

Figure 3.4. Experimental arrangement for the quantum efficiency measurements.

spectral speed control. The output of the monochromator was directed on the working electrode tested. Sometimes, the sample voltage was amplified in a PAR 113 pre-amplifier before being sent into the Lock-In amplifier, and the phase relationship between the reference and signal inputs was adjusted to maximize the signal. The output of the Lock-In was then plotted on the y-axis of a Hewlett-Packard 7045B X-Y recorder, and signal from the monochromator spectral drive was plotted on the x-axis of HP 7045B X-Y recorder. The spectral curves were obtained under no applied bias conditions. The spectral scanning speed was 50 nm/minute.

3.8 Photocatalytic Measurements

A gas tight reaction cell was constructed from pyrex glass with one optically flat window mounted on the side for horizontal irradiation, and one optical window on the bottom for vertical irradiation. A reaction mixture was deaerated with argon before each experiment. The powdered suspensions or colloidal samples were irradiated with an Oriel 150 W compact xenon illuminator filtered through a 420 nm and an infrared filter. The reaction cell was also cooled by blowing air on it during irradiation to maintain a constant temperature of 30°C. The gaseous products of the photocatalytic reactions were analyzed by an Aerograph A 90-P3 gas chromatograph equipped with a glass column packed with a molecular sieve 5A and an argon carrier gas. Qualitative and quantitative analysis of the peaks was performed on a Spectra Physics SP 4270 integrator. Following the experiment, the reaction mixture was analyzed for Fe^{3+} ions present in the mixture using a Perkin-Elmer

Lambda-9 spectrophotometer as previously described in Section 3.1.1.

CHAPTER FOUR

EXPERIMENTAL RESULTS AND DISCUSSION

4.1 Structural and microscopic characterization of Fe_2O_3

There is not much evidence in the literature on the comparisons of different preparation techniques of Fe_2O_3 and resulting photoactivities of these oxides. In fact, many investigators just use commercially available iron oxide and usually do not report its characteristics as to what the crystallinity is, if they are using Fe_2O_3, Fe_2O_3.FeO, Fe_3O_4 or any of several FeOOH oxy-hydroxides, or even the mixture of several or all of these oxides. As will be apparent from the results presented in this investigation, the presence of different iron oxides is very much dependent on starting materials, experimental procedures used and on subsequent treatments of the products. Thus, a large portion of this investigation was concerned with preparation and characterization of Fe_2O_3 by several experimental techniques and then comparing their differences in photoelectrochemical and photocatalytic cells for production of fuel gasses. Several experimental techniques were used in this investigation to prepare doped and platinized Fe_2O_3 samples. The first technique involved solid state reaction of respective dopant oxides with commercial Fe_2O_3. The powders prepared by this technique are inhomogeneous, particle size and shape is non-uniform, impurity levels are high since the powder goes through several processing steps

where contamination is possible, and powder structure and composition is not easily reproducible. Other powder synthesis methods which have been used in preparation of Fe_2O_3 are coprecipitation of iron oxide or iron oxy-hydroxide from iron chloride or iron nitrate solutions, and a freeze-drying process. The coprecipitation offers some advantages over the solid state mixing method. The process is more controllable and reproducible with improvement in purity and homogeneity. There are also some disadvantages to this method. It involves the use of precipitating agents which may remain in small quantities in the powder. Additionally, coprecipitation may not be uniform or complete and material may be lost in the washing process. The freeze-drying process was previously used with other semiconductor systems, where coprecipitation and phase transformation or changes in stoichiometry were a problem, but no detailed studies were ever performed on Fe_2O_3 using this technique. Freeze-drying is an ideal preparation technique for the doped Fe_2O_3 where homogeneous mixing of the dopants is of crucial importance. A major advantage of the freeze-drying process is the lack of need for organic impurities (like ethylene glycol or citrates in a widely used liquid mix technique) to effect homogeneous dispersion and diffusion into the structure. Homogeneous mixing is assured in the freeze-drying process by spraying the atomized solution (sol) into liquid nitrogen in which the solution is almost instantaneously frozen. This effectively achieves mixing on nearly a molecular scale that is unique to this process.

SEM and STEM analysis was undertaken on powdered samples as well as on sintered ceramic samples of solid state doped and freeze-dried

Fe_2O_3. The typical morphology of the commercial Fe_2O_3 is observed in the SEM micrograph (1000X) in Figure 4.1. It shows large clusters of particles partially fused together, probably due to high processing temperatures during manufacturing. The surface area of the commercial powder is 2.5 m^2/gram. Figure 4.2 shows the X-ray powder diffraction spectrum for the as received commercial Fe_2O_3. The major peaks characteristic of α-Fe_2O_3 are at 33.3° from (104) diffraction, 35.7° from (110) diffraction, and 54.2° from (116) diffraction. Figure 4.3 shows the X-ray spectrum of the commercial sample heat treated at 1420° C in air for 24 hours. The spectrum shows the major α-Fe_2O_3 peaks as well as major peaks resulting from the presence of Fe_3O_4 in the sample as is expected from the phase diagrams and thermodynamic results discussed in detail in section 2.7. Figure 4.4 shows a typical Fourier Transform infrared spectra (FT-IR) of the commercial Fe_2O_3 with two sharp and well resolved peaks at 560 and 475 cm^- characteristic of α-Fe_2O_3.

The freeze-drying method produced very different Fe_2O_3 material as can be seen for example in Figure 4.5 which shows a SEM micrograph (2000X) of an unheated flake-like Fe_2O_3 prepared from the Fe_2O_3 sol (from hydrolyzed $FeCl_3$, pH = 3.7). The flakes are several microns to several tens of microns long and few nanometers thick. The final morphology of a freeze-dried Fe_2O_3 was found to be very dependent on a starting iron salt used in preparing the Fe_2O_3 sol as well as on the pH of the sol before freeze-drying [123-125]. This observation can be illustrated in Figure 4.6 which shows a SEM micrograph (1000X) of a freeze-dried Fe_2O_3 produced from Fe_2O_3 sol (pH of the sol was 5.5).

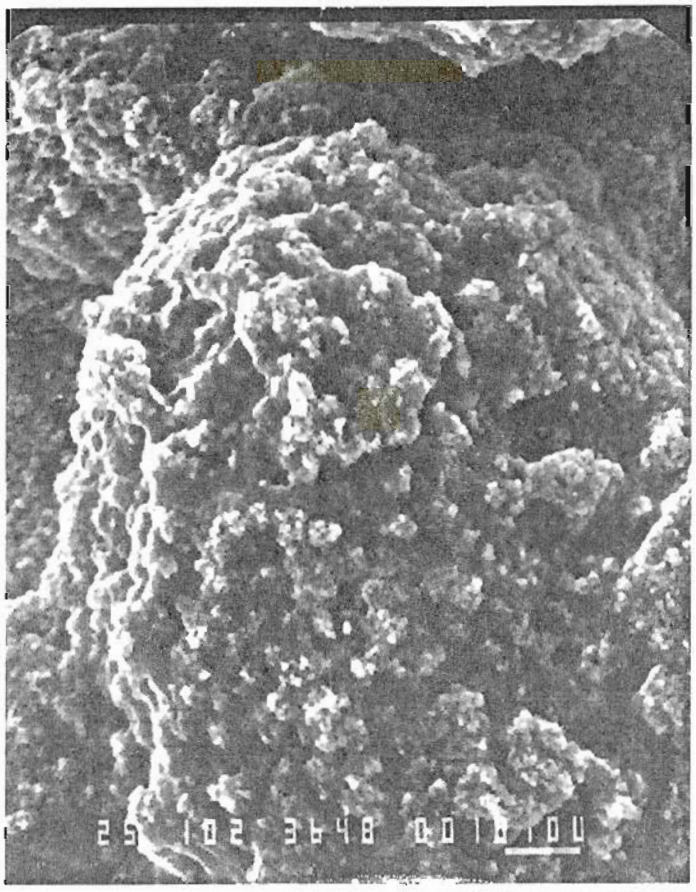

Figure 4.1. SEM micrograph of as received commercial Fe_2O_3 (Johnson Matthey Inc.), (1000X).

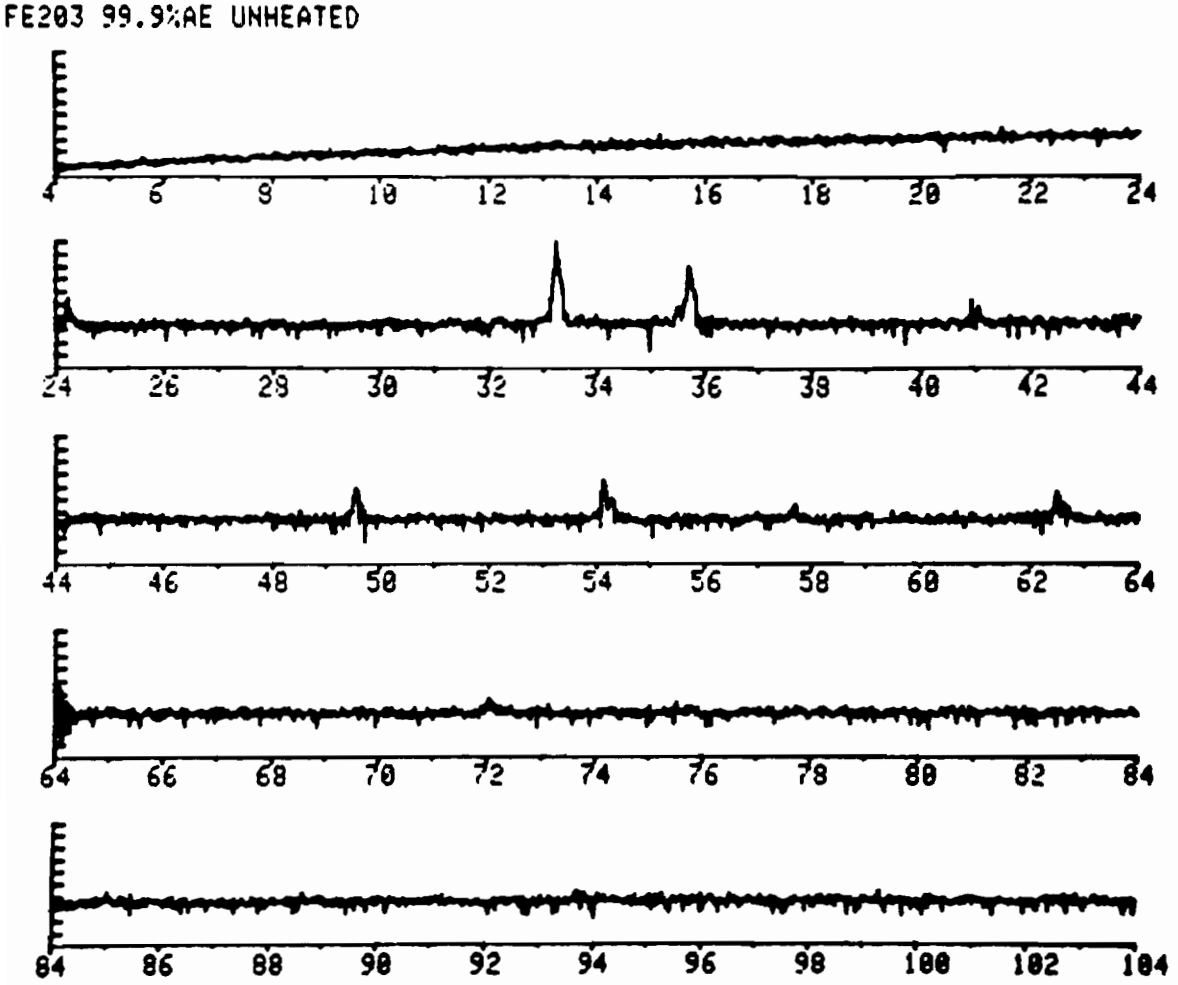

Figure 4.2. X-ray powder diffraction spectrum of as received commercial Fe_2O_3.

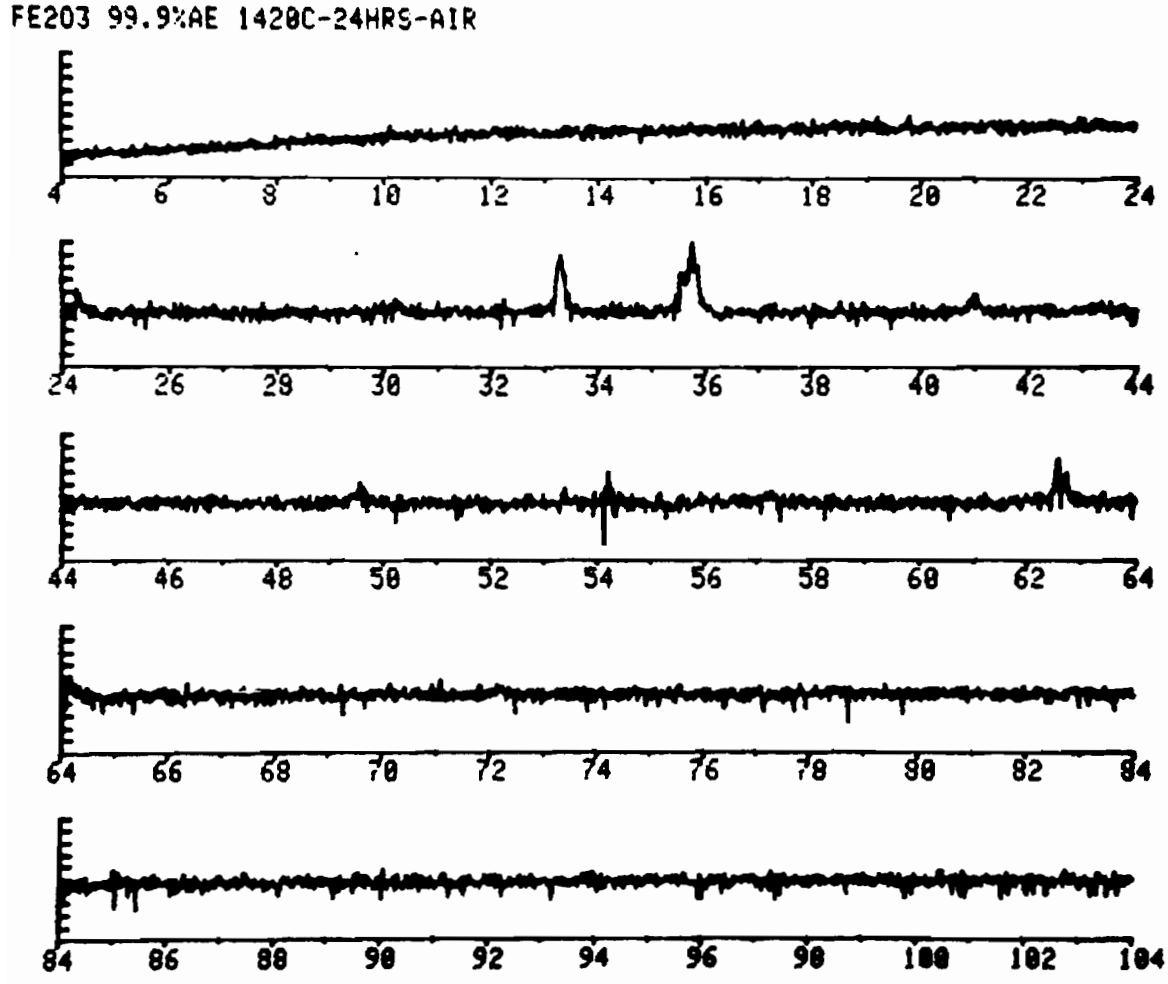

Figure 4.3. X-ray powder diffraction spectrum of the commercial Fe_2O_3 heated to 1420° C for 24 hours in air.

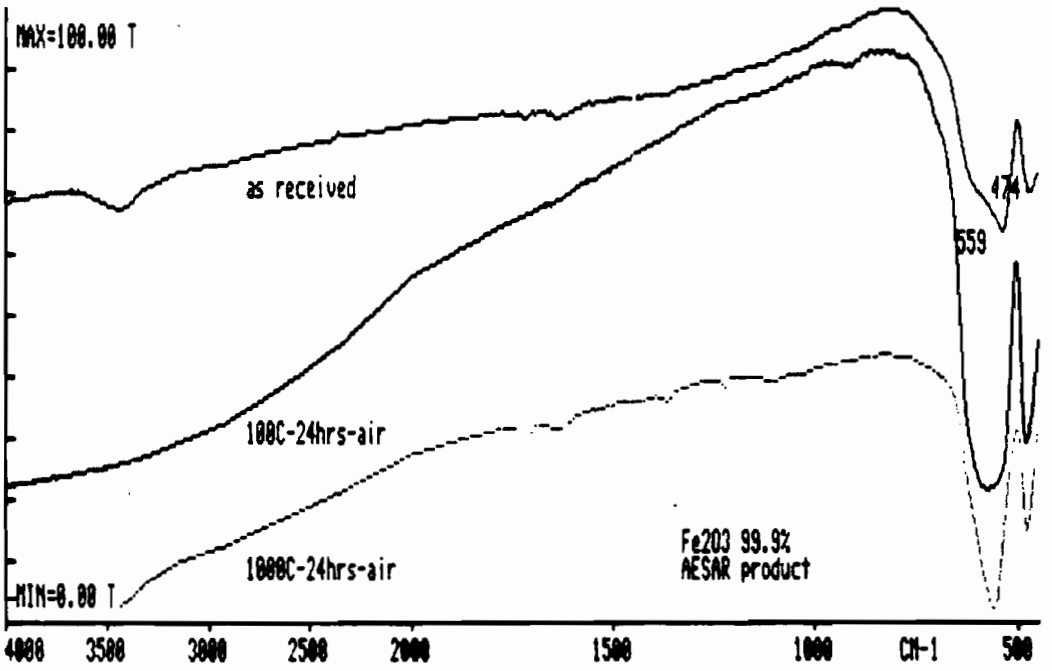

Figure 4.4. FT-IR spectra of the commercial Fe_2O_3.

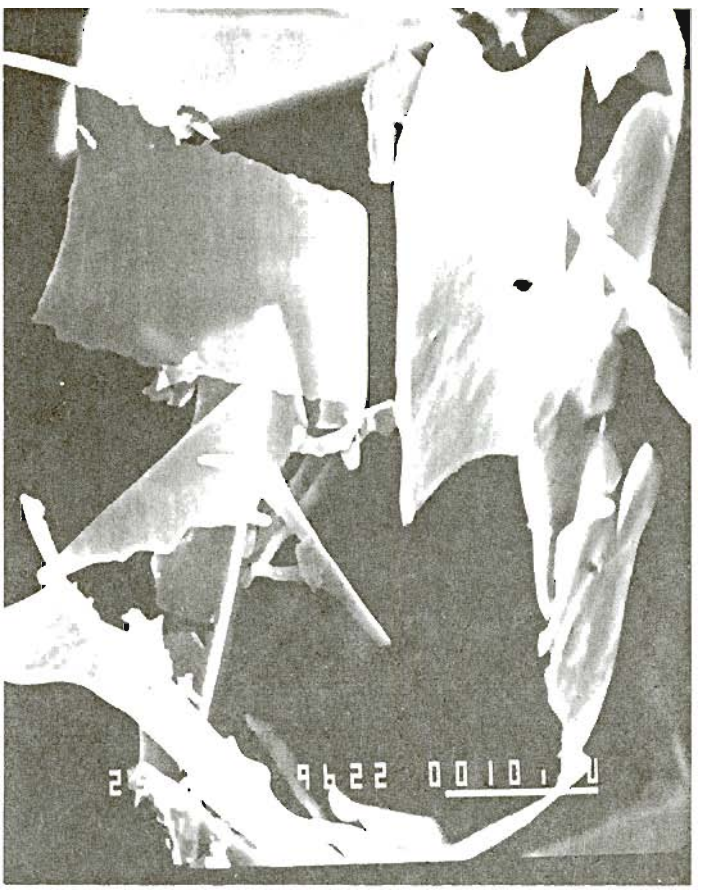

Figure 4.5. SEM micrograph of the freeze-dried Fe_2O_3 (2000X), pH of a starting sol was 3.7.

Figure 4.6. SEM micrograph of the freeze-dried Fe_2O_3 (1000X), pH of a starting sol was 5.5.

This sol produced almost spherical red particles of fairly uniform size. Size of the colloidal particles in the Fe_2O_3 sol was determined by TEM to be on the order of 150-300Å. STEM analysis of the freeze-dried samples showed that the samples were very uniform in size with very poor crystallinity as determined by electron diffraction. In fact some samples were amorphous. These results were confirmed by x-ray and infrared spectroscopy. Figures 4.7-4.8 show FT-IR spectra of heat treated freeze-dried samples prepared from $FeCl_3$ based sol and Figures 4.9-4.10 show FT-IR spectra of heat treated freeze-dried samples prepared from $Fe(NO_3)_3$ based sol. The FT-IR spectra and x-ray powder diffraction results show an almost amorphous structure of the unheated $FeCl_3$ based Fe_2O_3 sample. Between 300 and 400° C the characteristic peaks of crystalline α-Fe_2O_3 are developed. In the case of the freeze-dried sample prepared from $Fe(NO_3)_3$ based sol we can see in Figure 4.9 that even the unheated sample shows the characteristic α-Fe_2O_3 peaks. From the x-ray diffraction it was also determined that the peaks in this sample were sharper than the peaks in the previous sample. With increasing heating temperature, the x-ray diffraction results of the undoped freeze-dried samples showed only α-Fe_2O_3 peaks. Heating the samples at 1385° C produced a small amount of oxygen deficient Fe_3O_4 phase (about 5% by x-ray). The addition of dopants effected the resulting structures of the doped samples. With the addition of Si and Mg up to 0.5 atomic % x-ray showed only α-Fe_2O_3 peaks. The energy dispersive x-ray spectroscopy (EDXS) performed on TEM and SEM samples proved the fact that the freeze-drying technique can produce very homogeneously mixed oxide samples. The Si, Mg, and Pt dopants were

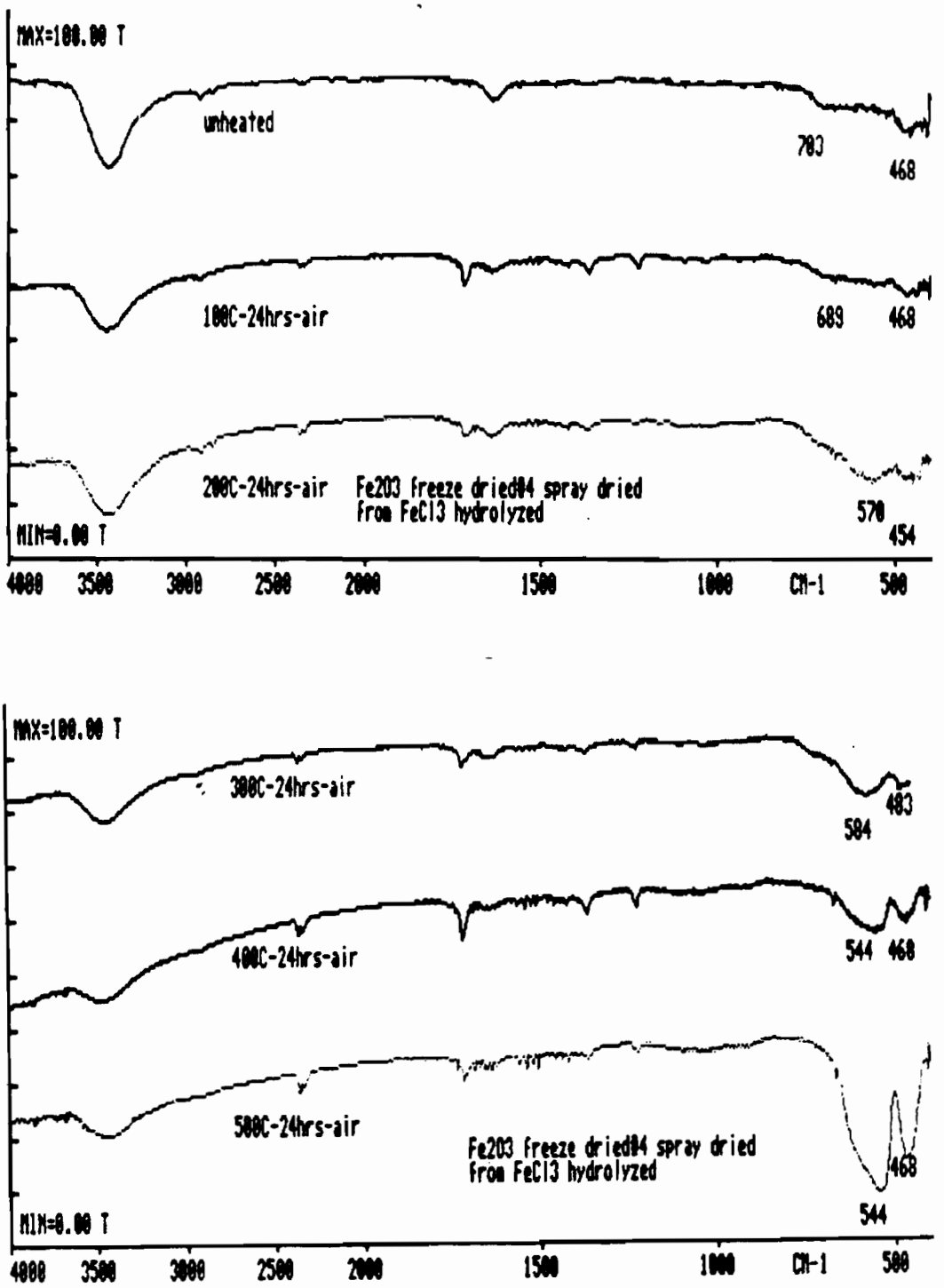

Figure 4.7. FT-IR spectra of the freeze-dried Fe_2O_3 (prepared from $FeCl_3$ based sol).

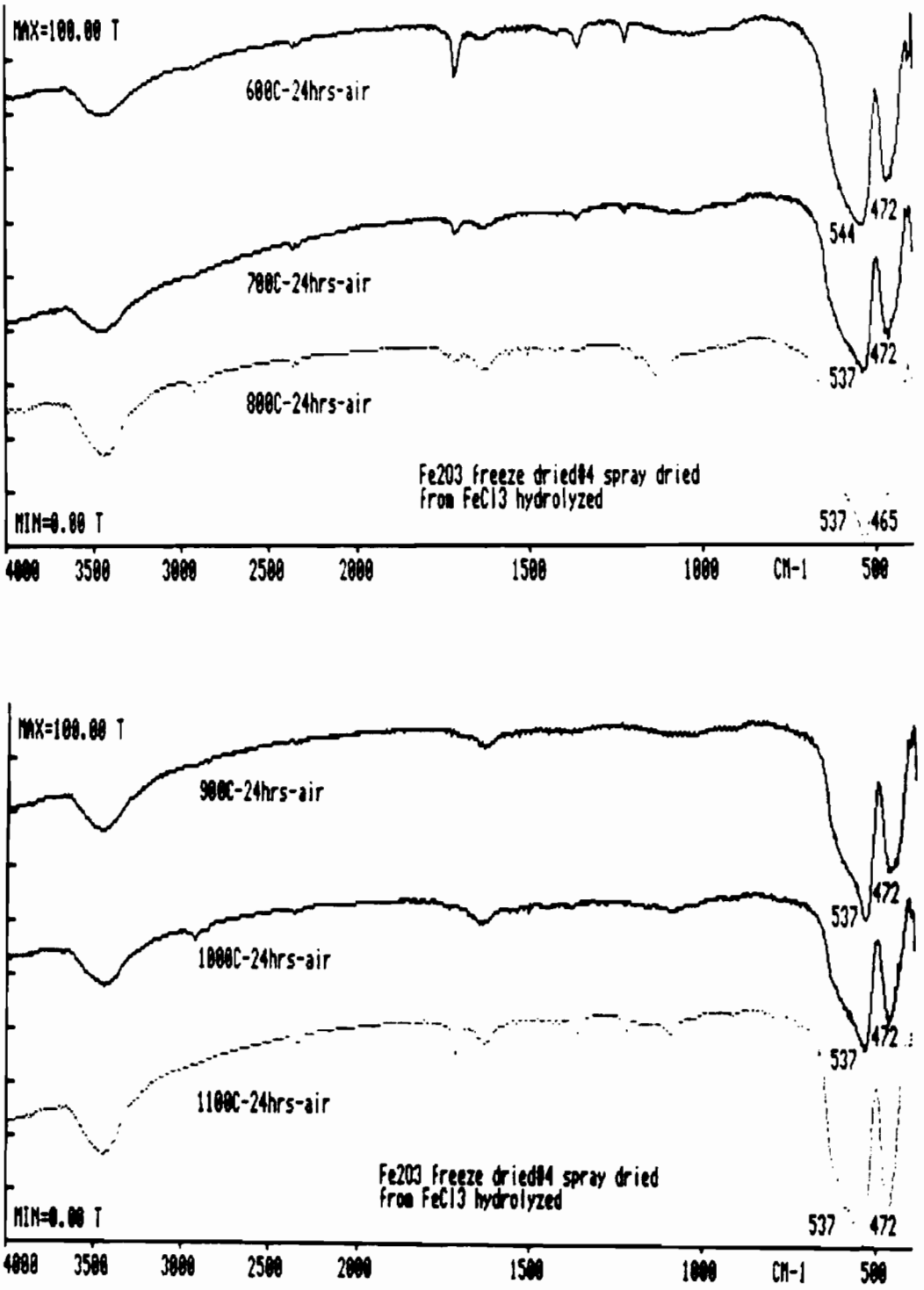

Figure 4.8. FT-IR spectra of the freeze-dried Fe_2O_3 (prepared from $FeCl_3$ based sol).

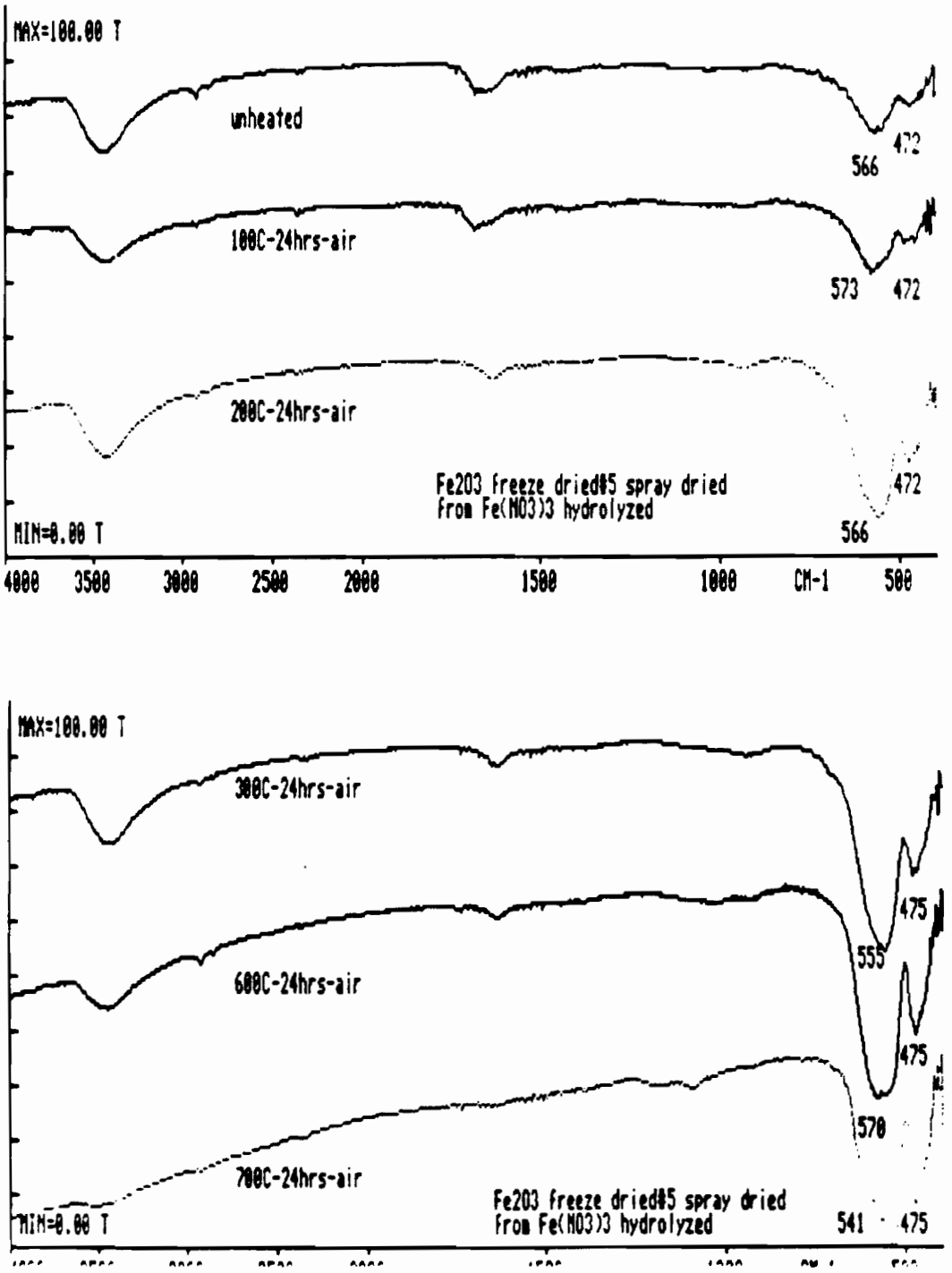

Figure 4.9. FT-IR spectra of the freeze-dried Fe_2O_3 (prepared from $Fe(NO_3)_3$ based sol).

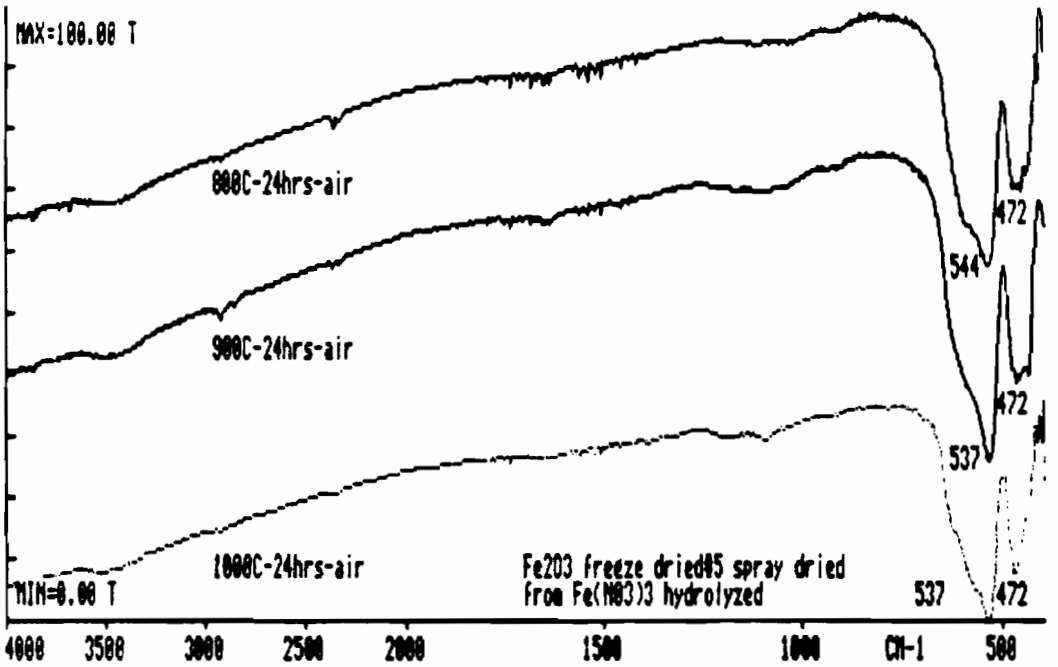

Figure 4.10. FT-IR spectra of the freeze-dried Fe_2O_3 (prepared from $Fe(NO_3)_3$ based sol).

very uniformly distributed throughout the freeze-dried samples. The solid state mixed samples (powders and sintered pellets) did not show nearly as good homogeneity as the freeze-dried samples as determined by EDXS on SEM.

Phase transformation studies of Fe_2O_3 samples prepared by freeze-drying and by coprecipitation show that the α-FeOOH and ß-FeOOH phases present in some freeze-dried samples transform into α-Fe_2O_3 at lower temperatures than the same phases present in the coprecipitated samples. This behavior is expected from very reactive powders, such as the freeze-dried samples, and is due to a very high surface energy associated with a very high surface area of these powders. The surface area versus heating temperature relationship is shown in Figure 4.11 where it is apparent that these powders have a typical surface area of 200 m^2 per gram of powder. Figure 4.12 shows a SEM micrograph of the freeze-dried powder heated to 1300° C. It may be apparent that the surface area of this sample is still rather large compared to the commercial Fe_2O_3, in fact the surface area of the freeze-dried sample at this temperature (5.5 m^2/g) is 50% higher than the commercial Fe_2O_3.

The platinized freeze-dried samples were also analyzed in TEM and SEM. The particle size of the colloidal platinum was determined in TEM to be about 200Å, very similar in size to the Fe_2O_3 particles. The homogeneity of dispersion of Pt in the freeze-dried samples was also found to be very uniform. The color of the resulting freeze-dried powder was progressively more gray with increasing Pt content in the samples. Figure 4.13 shows FT-IR spectra of unheated platinized freeze-dried samples prepared from $FeCl_3$ based sol. From the results

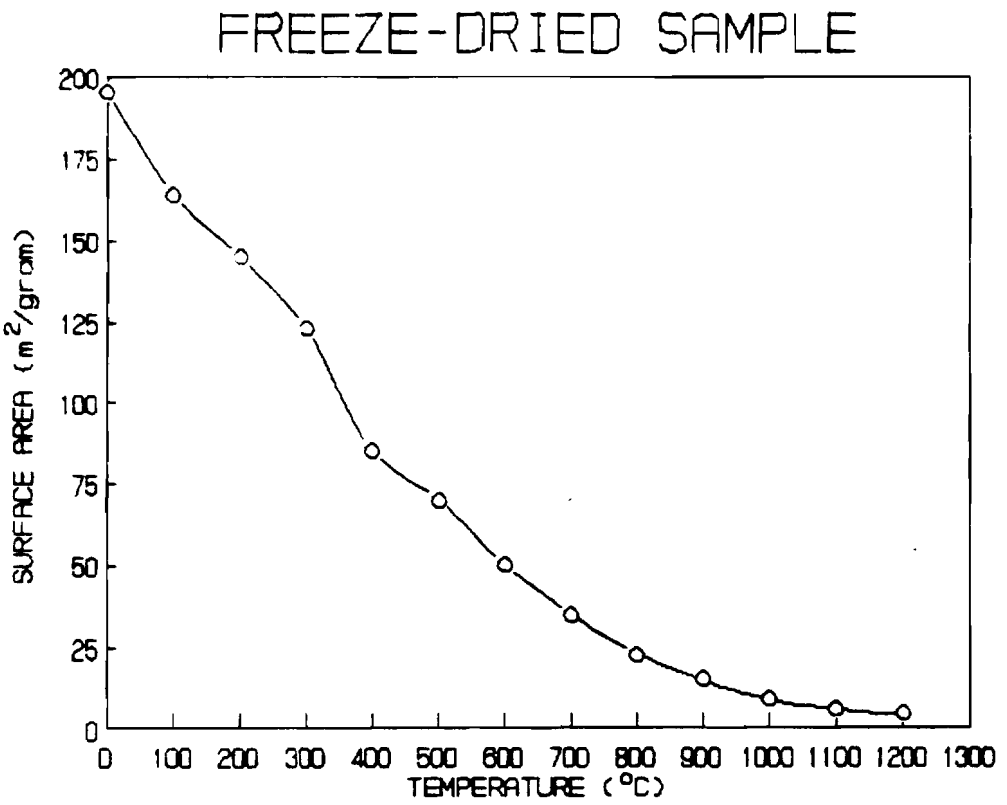

Figure 4.11. Surface area versus heating temperature for freeze-dried Fe_2O_3

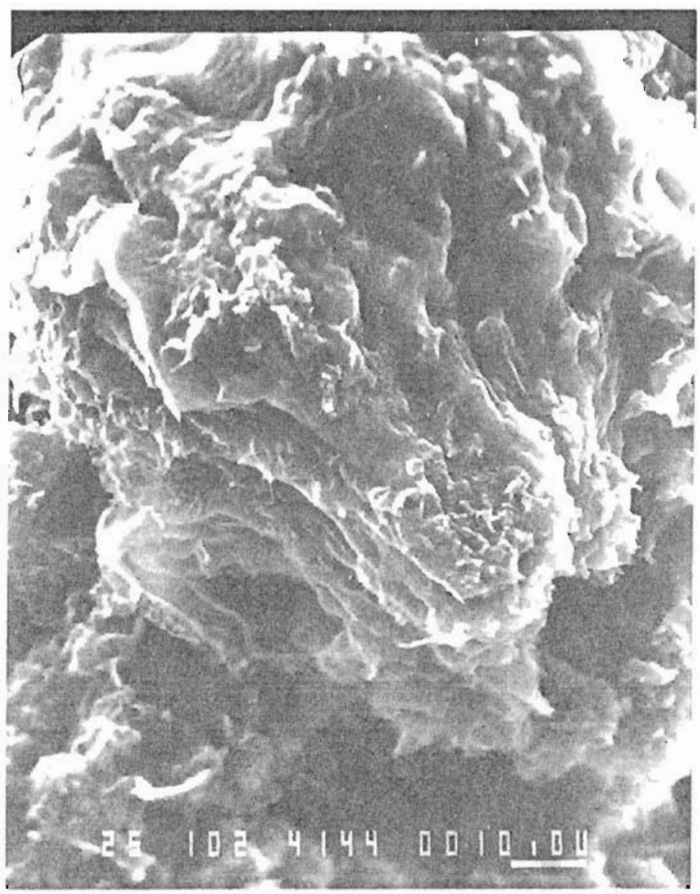

Figure 4.12. SEM micrograph of a freeze-dried powdered sample heated to 1300° C for 24 hours in air (1000X).

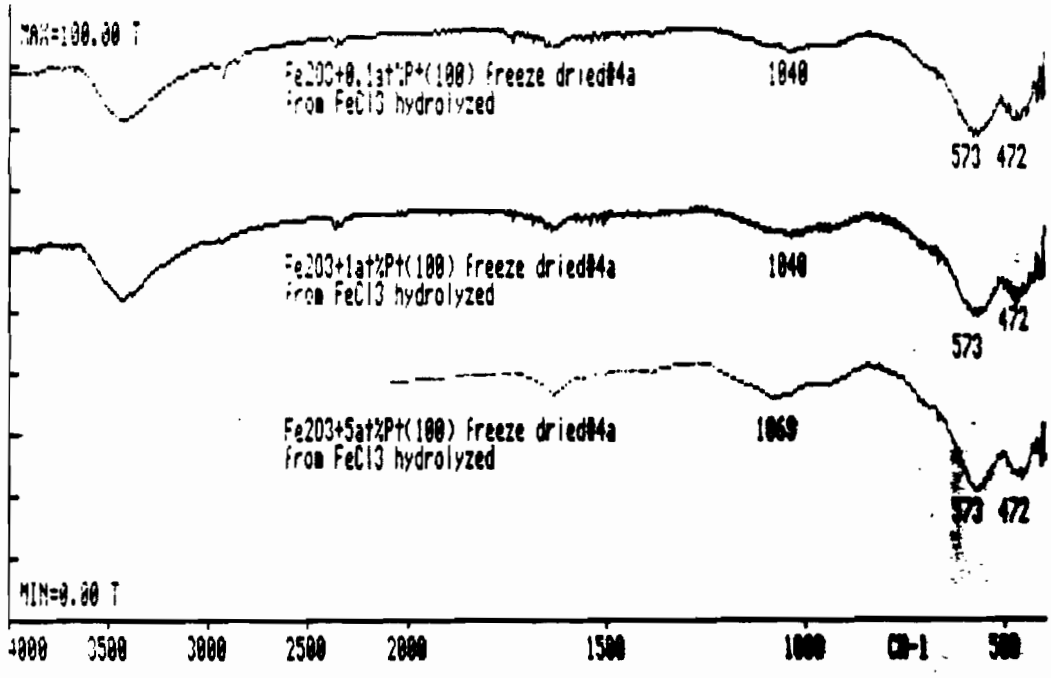

Figure 4.13. FT-IR spectra of platinized freeze-dried Fe_2O_3 (prepared from $FeCl_3$ based sol).

we can see that crystallinity of the platinized Fe_2O_3 samples increases with increasing platinum content. These spectra can be compared with the results presented in Figure 4.7 which show amorphous structure for the same sample without the platinum. The platinum particles may act as nucleation sites for crystallization in Fe_2O_3.

A typical SEM micrograph (1000X) of sintered commercial undoped Fe_2O_3 pellet is shown in Figure 4.14. The sample was sintered in air at 1385° C for 48 hours. The grain size of the pure sample ranges from 40-80 microns. The grain size and morphology of a pure freeze-dried sample is very similar to the commercial sample. The silicon and platinum doped solid state mixed samples (up to 0.5 atomic % Si or Pt) exhibited similar sintering behavior as pure samples with smooth grain structure. The grain size decreased with increased doping level. The relationship between the grain size and doping level of pure and platinized solid state mixed and freeze-dried samples is demonstrated in Figures 4.15-4.16. Higher doping levels of platinum (>1 atomic % Pt) in the solid state mixed samples also produced clean homogeneous grains as seen in Figure 4.17 of 1 at.% Pt doped Fe_2O_3 (1000X). The particle size of the platinum powder used in the solid state mixing technique was smaller than the particle size of the commercial Fe_2O_3, thus yielding more homogeneously doped samples. On the other hand, when we compare the grain structure of the Si doped (>0.5 at. % Si) solid state mixed sample in Figure 4.18 (1 at. % Si doped Fe_2O_3 at 1000X), we can see the differences in the homogeneity of the dopants. The Si doped samples show some second phase segregation along the grain boundaries as seen in Figure 4.18. This observation was also confirmed

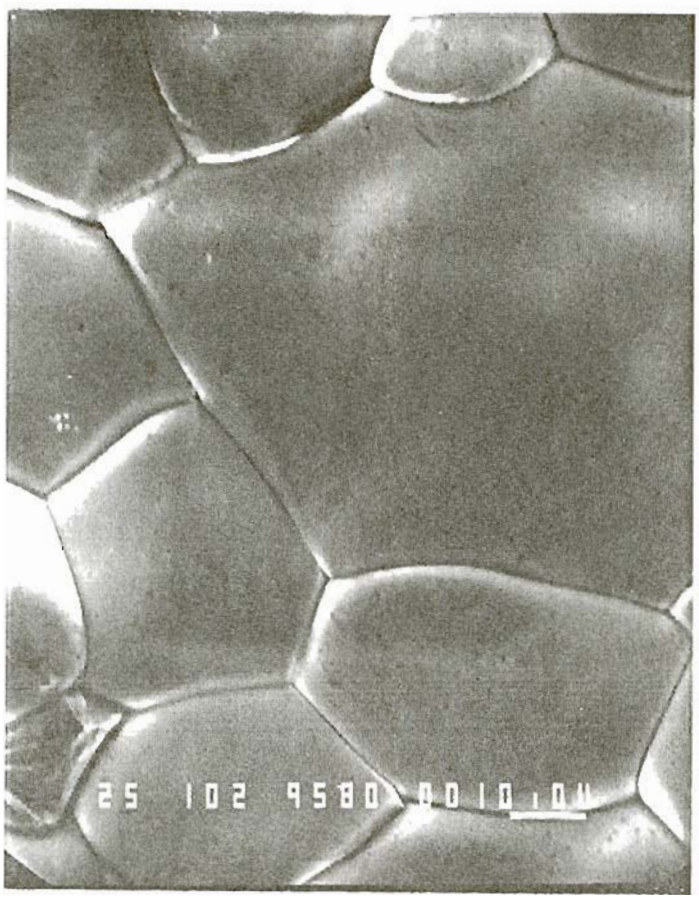

Figure 4.14. SEM micrograph of a pure commercial pellet sintered in air at 1385° C for 48 hours (1000X).

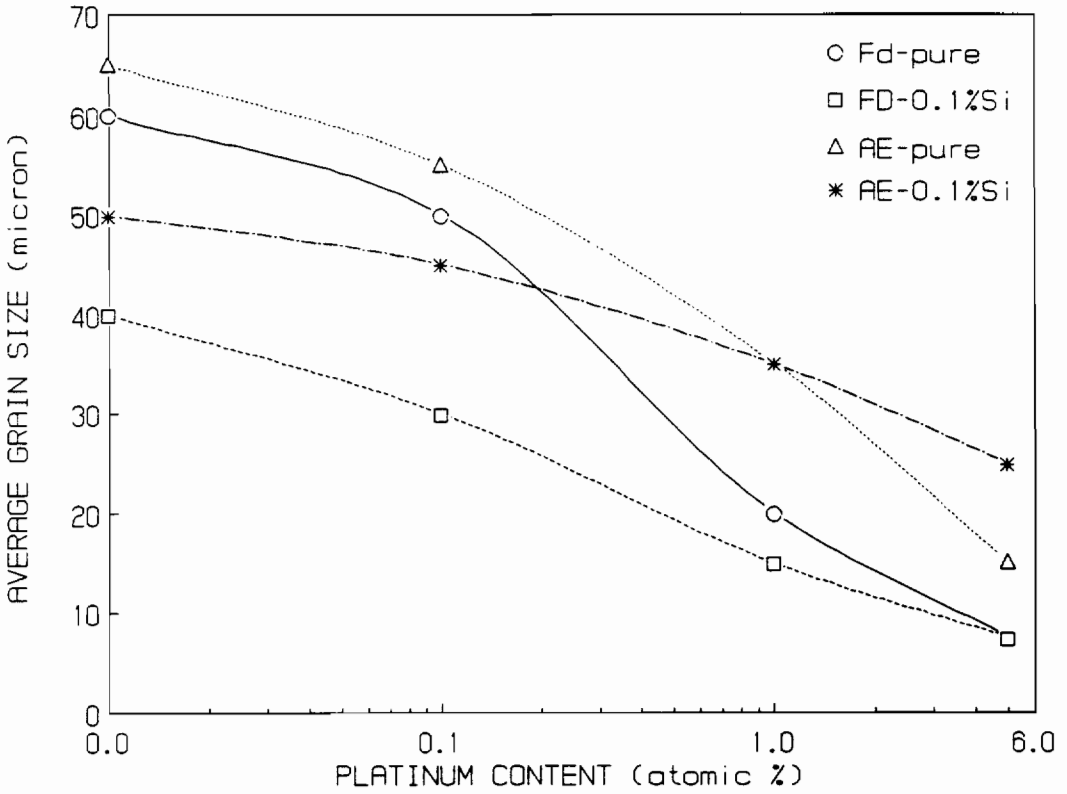

Figure 4.15. Average grain size versus platinum doping level of pure and 0.1 at. % Si doped freeze-dried (FD) and solid state mixed (AE) Fe_2O_3 samples.

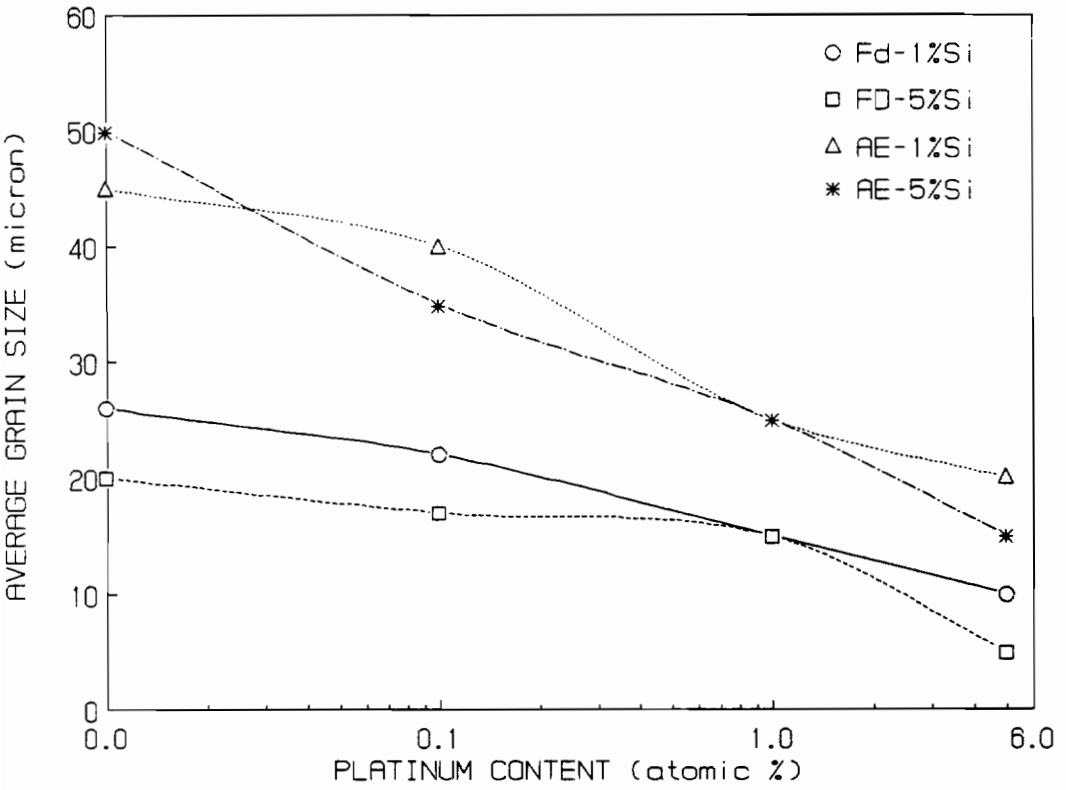

Figure 4.16. Average grain size versus platinum doping level of 1 and 5 at. % Si doped freeze-dried (FD) and solid state mixed (AE) Fe_2O_3 samples (heated to 1385° C for 48 hours).

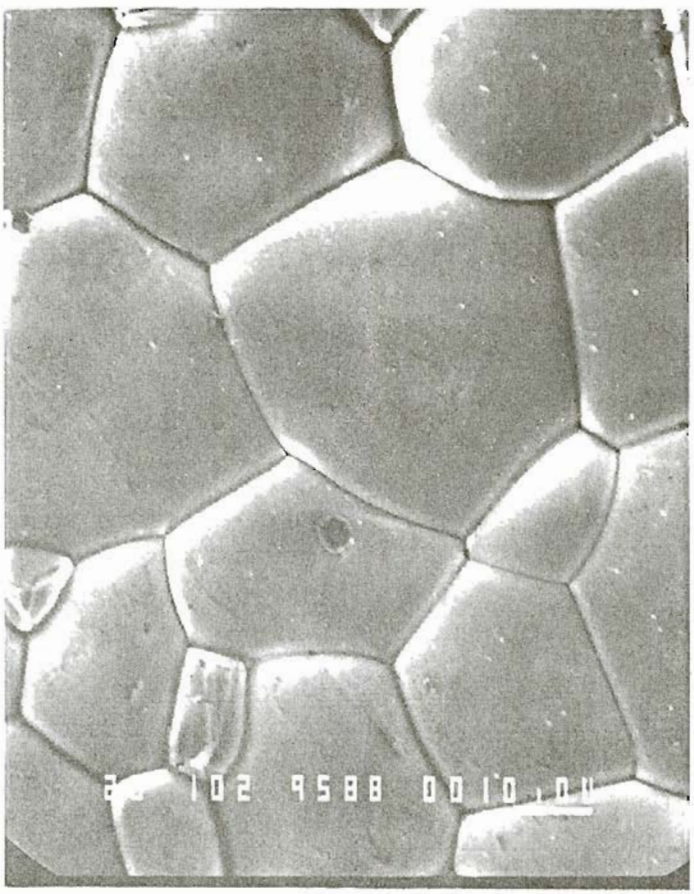

Figure 4.17. SEM micrograph of the solid state 1 at. % Pt doped Fe_2O_3 heated to 1385° C for 48 hours (1000X).

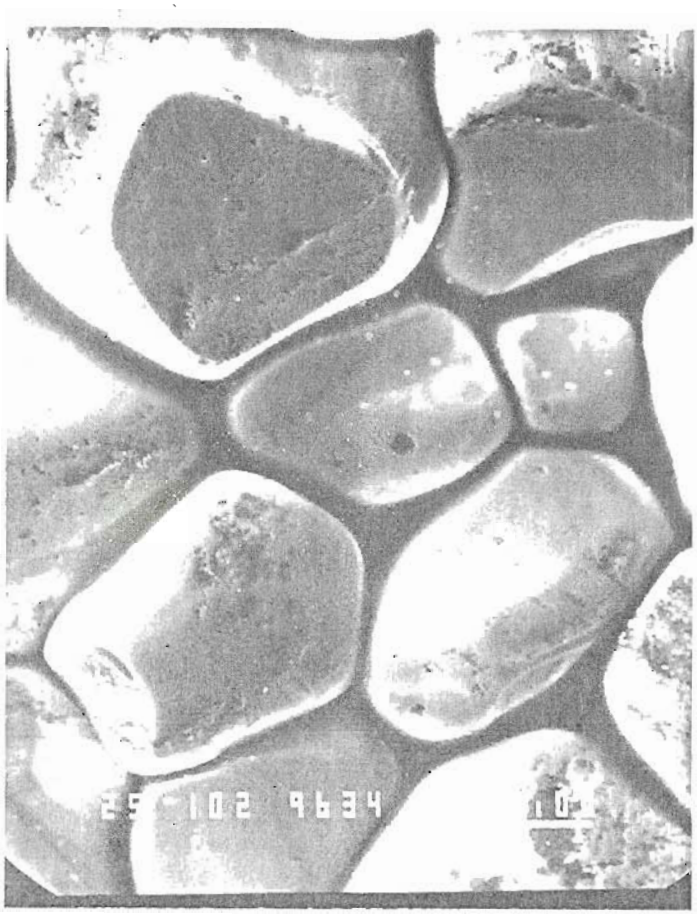

Figure 4.18. SEM micrograph of the solid state 1 at. % Si doped Fe_2O_3 heated to 1385° C for 48 hours (1000X).

by EDXS on SEM and by x-ray diffraction. The EDXS analysis revealed some Si rich regions mostly between the grains (dark regions on the SEM micrograph). This result was also expected because it is well known that the solid solubility of a divalent metals in the α-Fe_2O_3 is rather small (usually about 0.5%) [171-175]. Freeze-dried doped (>0.5 at. % Pt or Si) samples showed very homogeneous clean grains with uniform composition throughout the sample as determined by EDXS on SEM. The size of the colloidal platinum and silicon particles in the sols used for doping in the freeze-drying technique is very similar to the size of the colloidal Fe_2O_3 particles, hence the homogeneous doping and phase purity is possible. There was some phase nonuniformity observed in the 5 at. % Pt solid state doped samples.

The Mg doped Fe_2O_3 samples exhibited different behavior from the Si doped samples. Figures 4.19 and 4.20 show SEM micrographs (1000X) of 1 at. % Mg doped freeze-dried and solid state doped Fe_2O_3, respectively. The freeze-dried sample shows again uniform grain size and homogeneous dopant distribution. In the solid state doped sample we can see some phase inhomogeneity and segregation along the grain boundaries. This observation was also observed by x-ray diffraction which identified small amount of a spinel $MgFe_2O_4$ phase. At higher Mg doping levels (>1 at. % Mg) the spinel phase was pronounced in samples prepared by freeze-drying as well as solid state mixing method. Clear sign of a second phase is observed for example in the SEM picture of 5 at. % Mg freeze-dried doped Fe_2O_3 sample in Figure 4.21 (1000X). The relationship between the average grain size versus platinum content for 1 and 5 at. % Mg doped samples is presented in Figure 4.22.

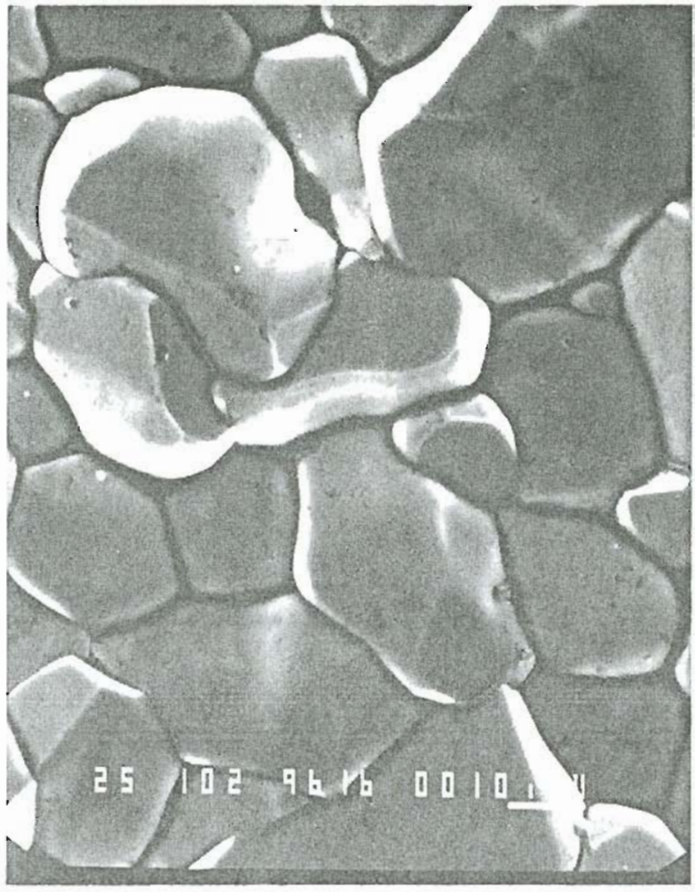

Figure 4.19. SEM micrograph of freeze-dried 1 at. % Mg doped Fe_2O_3 heated to 1385° C for 48 hrs (1000X).

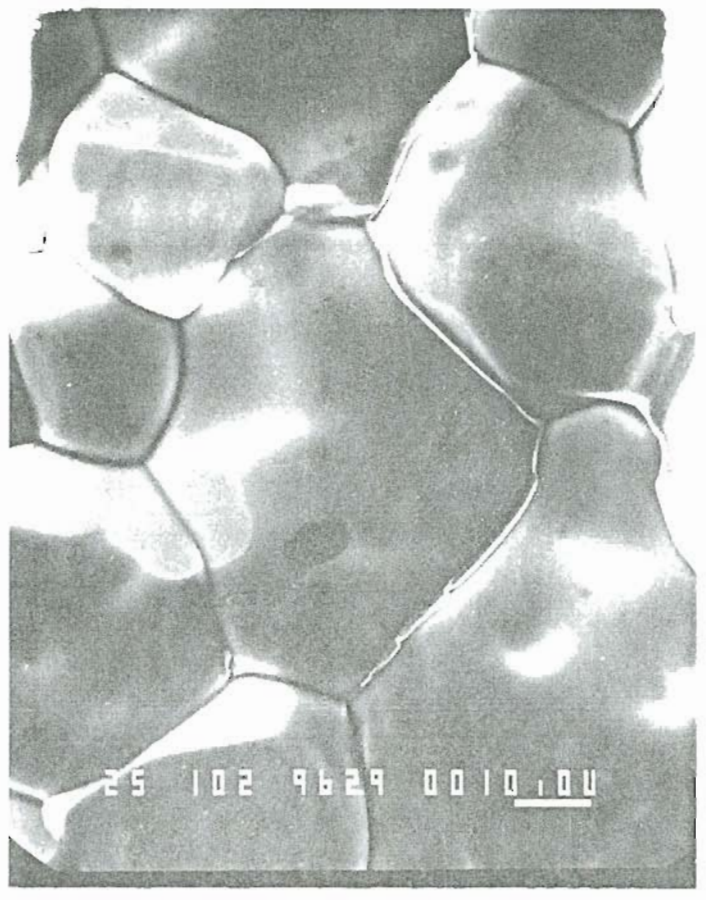

Figure 4.20. SEM micrograph of solid state 1 at. % Mg doped Fe_2O_3 heated to 1385° C for 48 hrs (1000X).

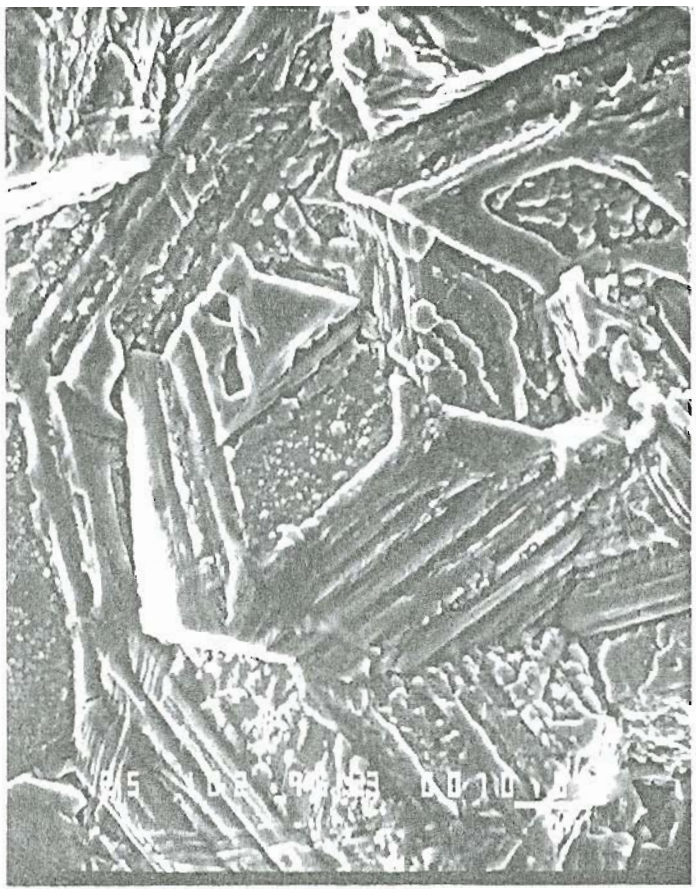

Figure 4.21. SEM micrograph of freeze-dried 5 at. % Mg doped Fe_2O_3 heated to 1385° C for 48 hrs (1000X).

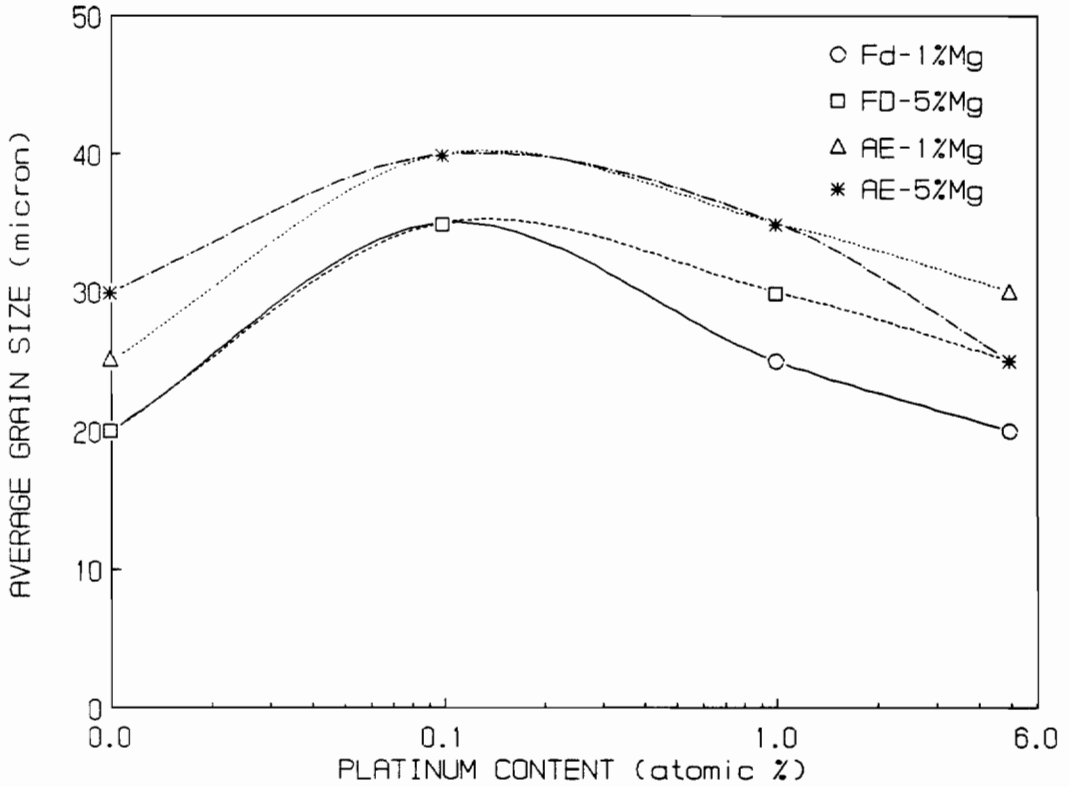

Figure 4.22. Average grain size versus platinum doping level of 1 at. % and 5 at. % Mg doped freeze-dried (FD) and solid state mixed (AE) Fe_2O_3 samples (heated to 1385° C for 48 hours).

4.2 Electrical conductivity and dielectric constant of doped Fe_2O_3

Stoichiometric α-Fe_2O_3 is an intrinsic n-type semiconductor with a band gap of 2.2 eV. The resistivity of a pure stoichiometric sample at room temperature is estimated at 10^{14} Ω-cm. The resistivity of the pure freeze-dried and commercial Fe_2O_3 sample was measured by a four probe Van der Pauw technique and with an ac impedance conductivity bridge. The measured resistivity was about 10^{11} Ω-cm. The resistivity versus platinum doping for a freeze-dried sample is presented in Figure 4.23. This resistivity is unacceptably high for use in the photo-electrochemical solar cells. It is possible to produce a less resistive Fe_2O_3 by reducing some of the Fe^{3+} to Fe^{2+} state by heating the sample in air at 1385° C or higher depending on the desired degree of reduction. This process introduces oxygen vacancies into the Fe_2O_3 and conduction may occur by the processes outlined in Equations 4.1-4.2.

$$O_O \rightarrow 1/2O_2(g) + V_O^{\cdot\cdot} + 2e' \qquad (4.1)$$

$$2Fe_{Fe} + 2e' \rightarrow 2Fe'_{Fe} \qquad (4.2)$$

This can be also achieved by adding a dopant (M) such as Si or Pt in this investigation. The mechanism for conduction in this case may occur by the process outlined in Equation 4.3 where M^{4+} ion introduces electron into the conduction band (e'_{cb}).

$$M(IV) \rightarrow M(IV)\cdot Fe + e'_{cb} \qquad (4.3)$$

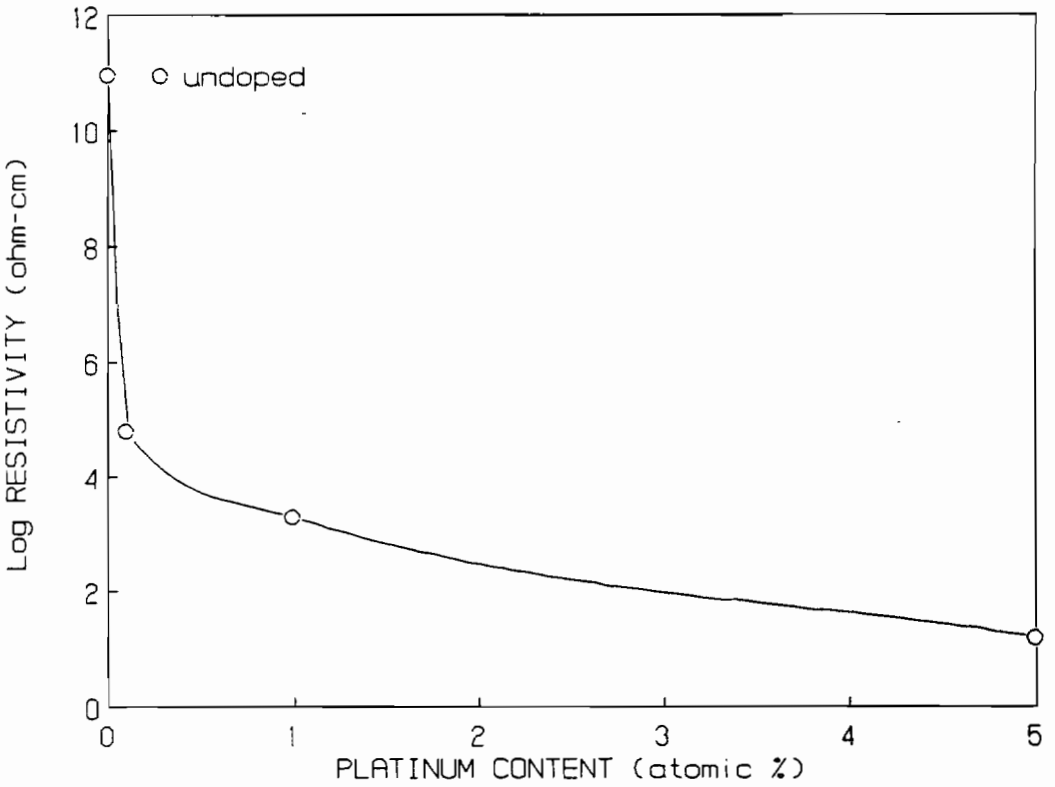

Figure 4.23. Log resistivity versus platinum doping for a pure freeze-dried Fe_2O_3 sample (sintered in air at 1385° C for 48 hours).

The Fe_2O_3 is then a mixed valence compound with enhanced conductivity at room temperature which is due to a hopping mechanism for electrons between Fe^{2+} and Fe^{3+} ions [184]. The resistivity versus platinum doping for the freeze-dried and solid state mixed Si doped samples are presented in Figures 4.24-4.25. The resistivity decreased with increasing Si or Pt doping level for all samples. The resistivities were, however, always lower for the freeze-dried samples which again demonstrates the superior dopant distribution and would support the outlined conduction mechanism.

The magnesium doped samples are p-type semiconductors since introducing Mg^{2+} into the α-Fe_2O_3 lattice to substitute for Fe^{3+} ions increases the concentration of electron vacancies. The conduction may occur by the process outlined in Equation 4.4.

$$2MgO + 1/2O_2 = 2Mg'_{Fe} + 3O_O + 2h^{\cdot} \qquad (4.4)$$

Figures 4.26 and 4.27 show the resistivity versus platinum content for Mg doped freeze-dried and solid state doped samples (heated in air to 1385° C for 48 hours), respectively. The results indicate that the resistivities of the solid state doped samples are significantly higher than the freeze-dried samples. The resistivities are also less dependent on the platinum content in the Mg doped samples. In the case of a Si doped sample, the platinum may contribute electrons into the conduction band of the semiconductor enhancing the effect of Si dopant as can be seen clearly from Figures 4.24 and 4.25 if the above proposed mechanism is correct. For the Mg doped samples, where Mg acts as an

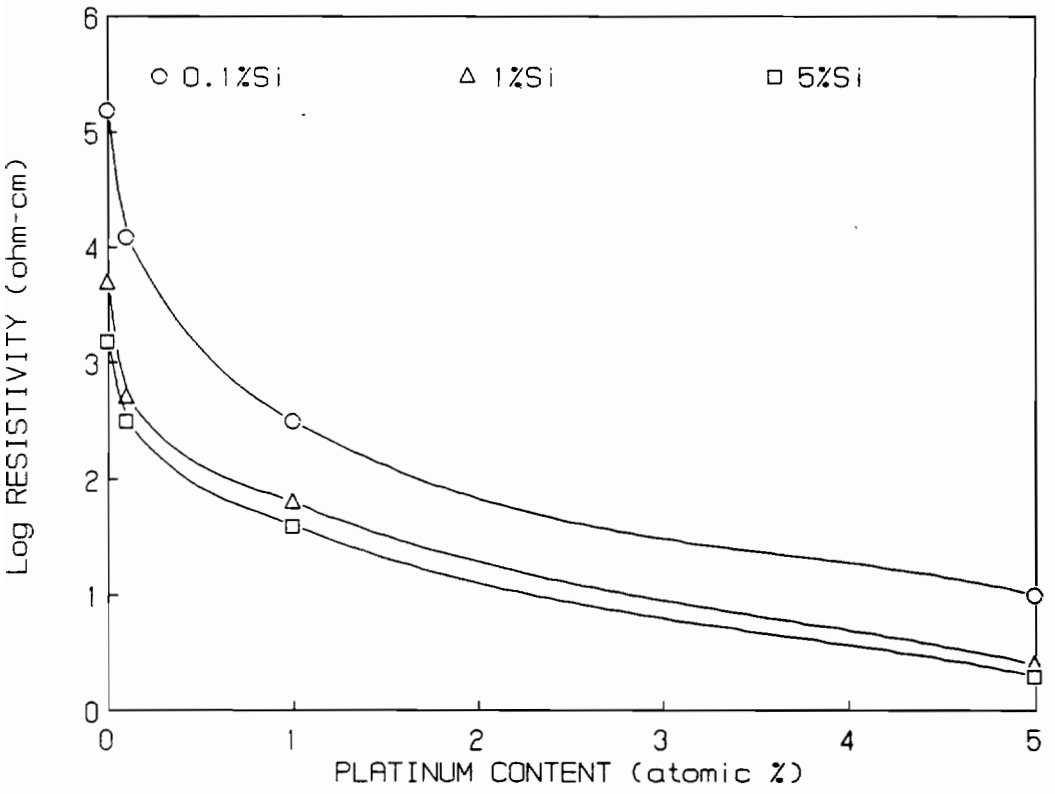

Figure 4.24. Log resistivity versus platinum doping for Si doped freeze-dried Fe_2O_3 sample (sintered in air at 1385° C for 48 hours).

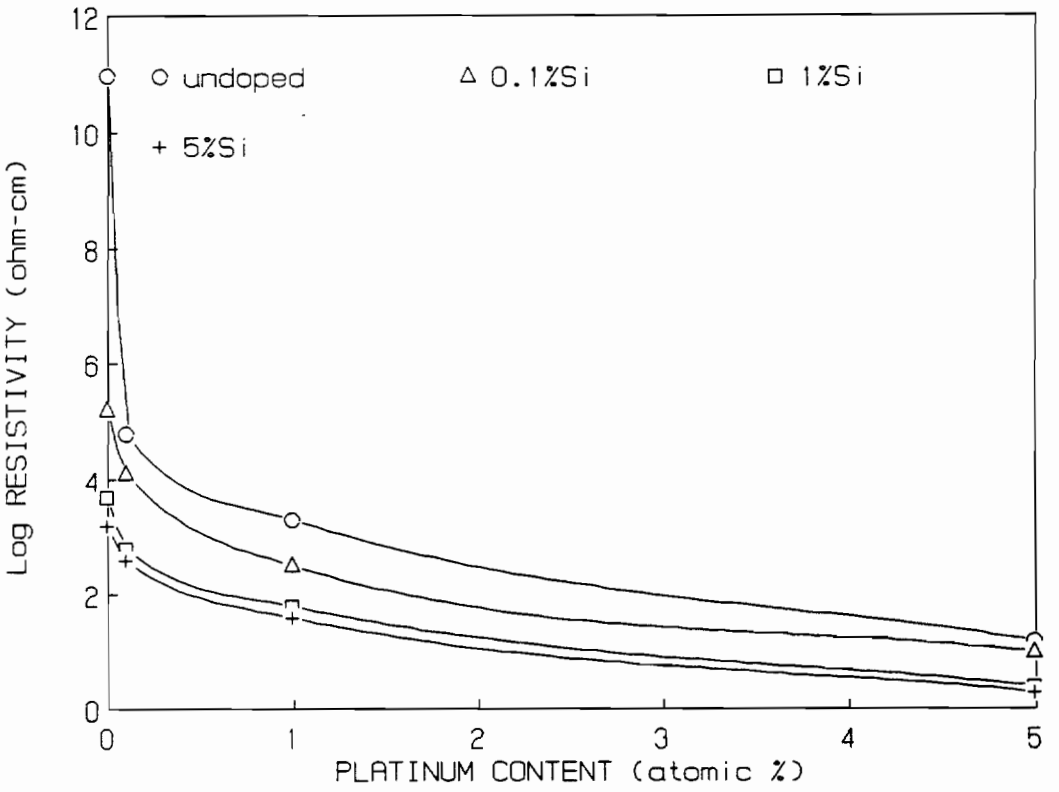

Figure 4.25. Log resistivity versus platinum doping for Si doped solid state mixed Fe_2O_3 sample (sintered in air at 1385° C for 48 hours).

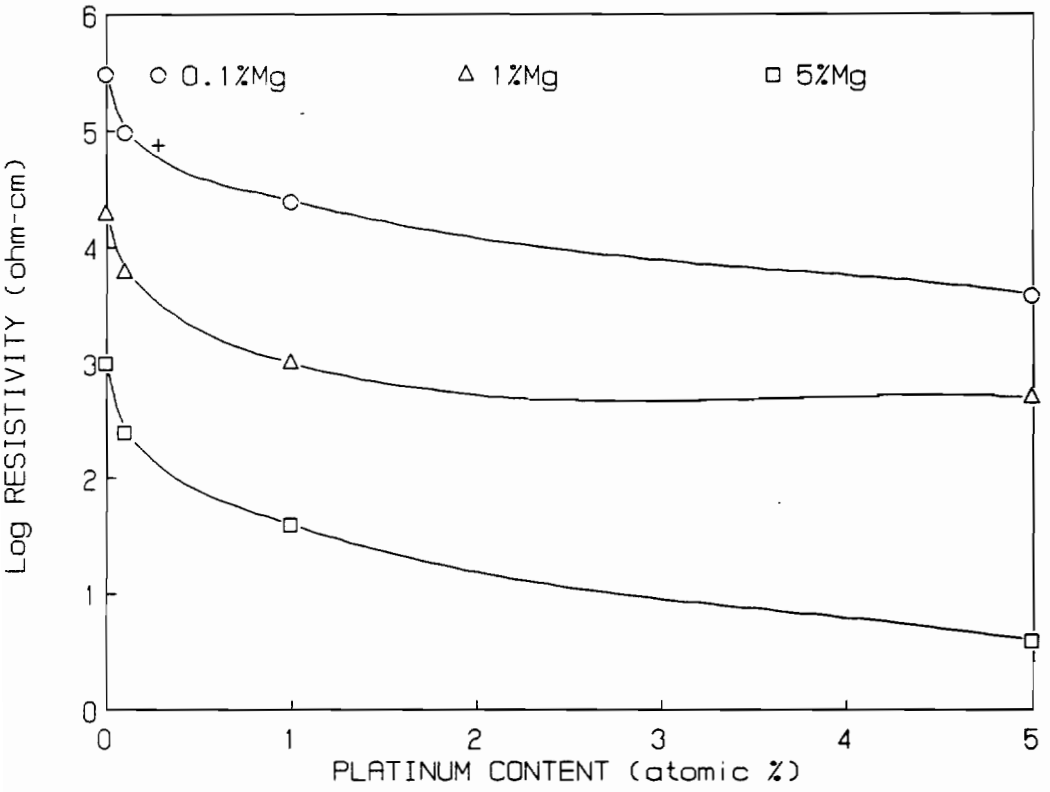

Figure 4.26. Log resistivity versus platinum doping for Mg doped freeze-dried Fe_2O_3 sample (sintered in air at 1385° C for 48 hours).

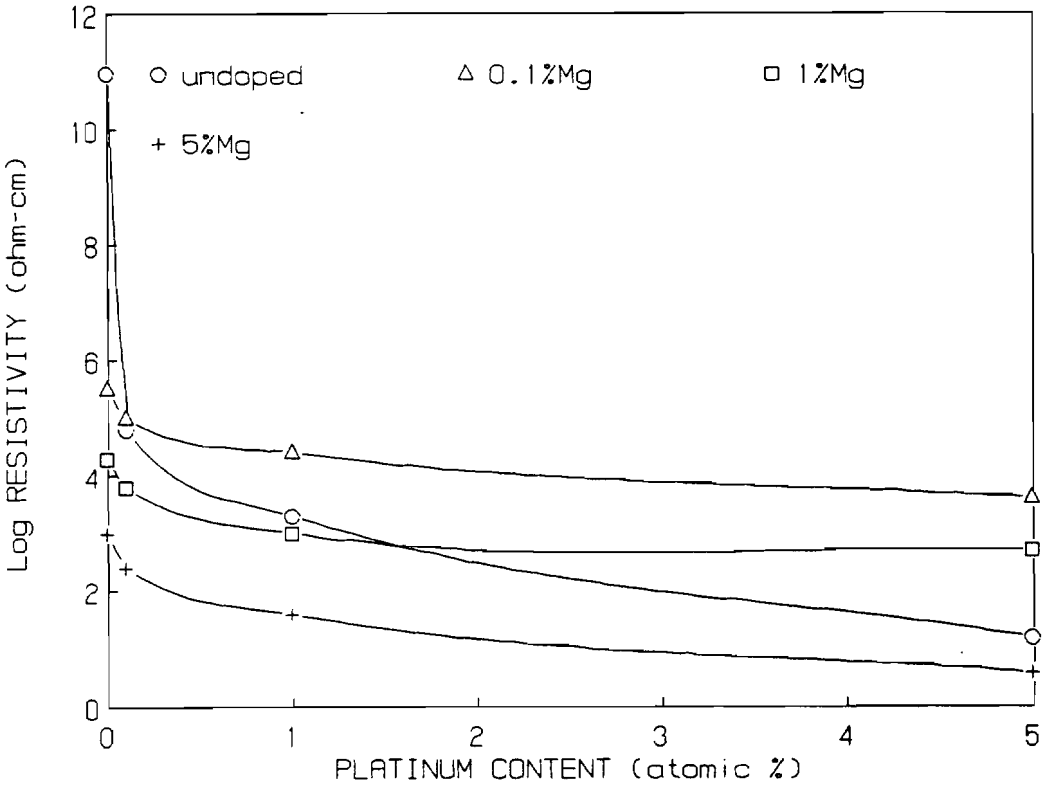

Figure 4.27. Log resistivity versus platinum doping for Mg doped solid state mixed Fe_2O_3 sample (sintered in air at 1385° C for 48 hours).

acceptor, the addition of platinum which would act as a donor might compensate the effect of Mg thus increasing the resistivity of the Fe_2O_3. That is what is observed in Figures 4.26-4.27. The bulk conductivity increases with increasing MgO content. A. H. Tinnemans et al. [316] studied the grain boundary conductivity in Mg doped Fe_2O_3. From the analysis of the small signal ac response of the symmetrical, and photoelectrochemical cells, they found that the grain boundary resistance was much larger than the bulk resistance. So the grain boundary resistance is increasing with increasing MgO content since the grain size is decreasing thus increasing number of grains. This effect is also present in our samples. The conductivity activation enthalpy is 0.52 and 0.76 eV for the 0.1 and 1 at.% Mg, respectively. From the conductivity activation enthalpy for α-Fe_2O_3 Goodenough [18] has calculated the energy required to transfer an electron from a lattice Fe^{3+} to an adjacent Fe^{3+} to amount to about 2.0 eV. This is close to the optical bandgap of α-Fe_2O_3.

The dielectric constant of the Fe_2O_3 samples was measured using a parallel plate capacitance method [179]. The capacitances obtained from a pure and doped samples ranged from 70-150. These results agree well with the literature [181].

4.3 Photoactivity of pure and platinized Si doped Fe_2O_3

The initial experiments with solid state doped Fe_2O_3 samples used in the photoelectrochemical cell (PEC) produced very inconsistent and disappointing results. The samples were sintered at 1370° C and then slowly cooled to room temperature. The samples exhibited very poor

photoactivities with very high dark currents and rather small photocurrent usually only several percent higher than the dark currents. This behavior was due to the low conductivity of the early samples. Similar effects were observed by other investigators and Goodenough et al. [18] determined that the low conductivity of these samples was caused by oxygen absorption along the grain boundaries of the samples during a cooling process after sintering. Ideally, the Fe_2O_3 should contain oxygen vacancies and some spinel phase (Fe_3O_4) homogeneously distributed throughout the sample to increase the conductivity as discussed in the previous section. If, however, the Fe_3O_4 is present mostly in the surface of the Fe_2O_3, it will help to recombine the photogenerated minority carriers with majority carriers present in the sample. The Fe_3O_4 acts as a semi-metal where it is impossible to separate the charges. The conductivity of the samples was determined at the surface and in the bulk after polishing off the top surface layer of the samples. The conductivity in the bulk was about three to four orders of magnitude smaller than the conductivity in the surface layer of the samples. This suggested that the Fe_3O_4 was present in the surface in the form of surface states where it acted, possibly, as recombination or trapping centers for the carriers. The observed photoresponses of the samples certainly supported this explanation. The photoactivities of the solid state mixed samples were improved by heating the samples at 1385° C and then quenching the samples to room temperature thus preserving a homogeneous distribution of Fe_3O_4 throughout the sample. The conductivity of the sample prepared by this process was nearly homogeneous throughout the sample.

The photocurrent density versus applied potential results for the solid state mixed Si doped photoelectrodes are shown in Figure 4.28. The samples were tested in 1M NaOH and 0.01M KNO_3 electrolyte (pH=13.5) with a platinum mesh counterelectrode and a standard calomel reference electrode. Figures 4.29-4.32 show the photocurrent density versus applied potential results for platinized and Si doped/platinized solid state mixed samples. Photovoltage of the photoelectrode was determined by connecting the working photoanode to the standard calomel reference electrode. It was generally observed that the equilibrium time to obtain stable voltage or photovoltage reading was much higher for the solid state doped electrodes than for the freeze-dried electrodes. This result was consistent with lower conductivity in the solid state samples suggesting slower charge transfer kinetics. This result will be also addressed later in the discussion. The photoactivities of the pure and Si doped samples showed very consistent results with the results reported in a literature. The photocurrent onset for a pure sample was about -0.1 V vs SCE with the photocurrent onset shifting in more cathodic direction with increasing Si doping up to about 1 at.% Si. The photocurrent was at a maximum for the 1 at.% Si doping level. The photocurrent onset for the 5 at.% Si doping level was similar to the onset for undoped sample with overall photoactivity being slightly higher than the undoped sample. This result is consistent with the effect of doping density on the width of the depletion layer in the semiconductor. As the doping density increases, the depletion layer width decreases which has a serious consequences for semiconductors with a very small absorption coefficient and small diffusion lengths of

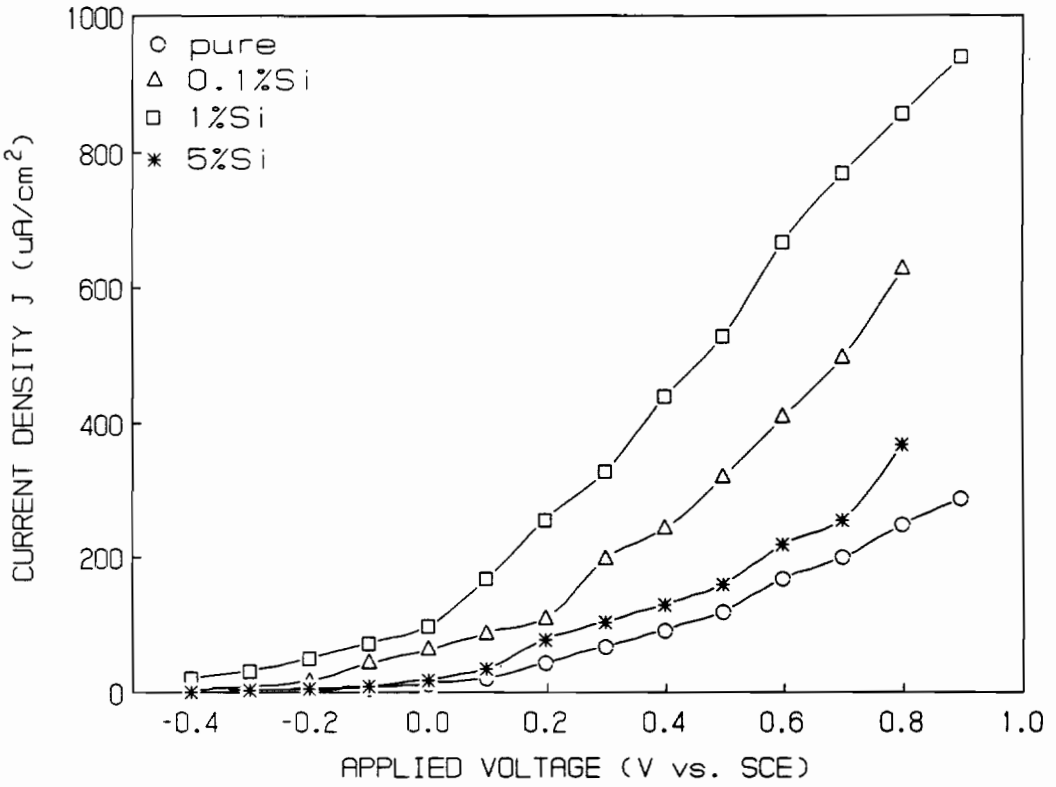

Figure 4.28. Photocurrent density versus applied potential for solid state Si doped Fe_2O_3 electrodes (1M NaOH + 0.01M KNO_3, pH=13.5).

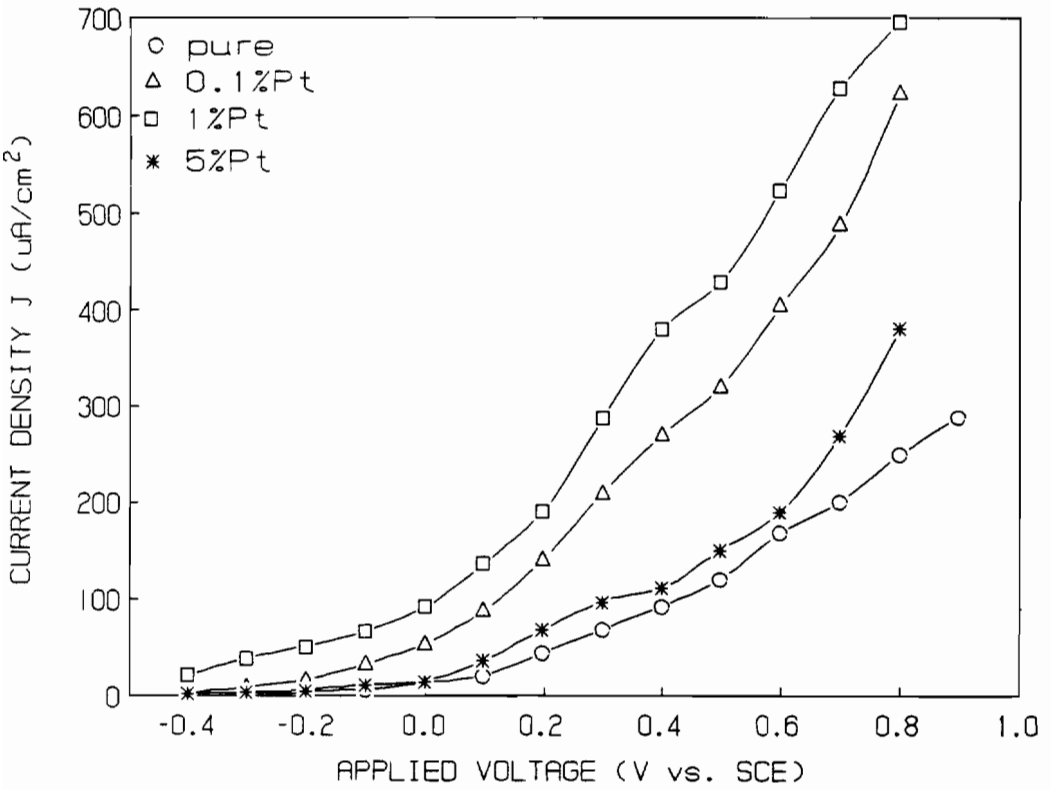

Figure 4.29. Photocurrent density versus applied potential for solid state Pt doped Fe_2O_3 electrodes (1M NaOH + 0.01M KNO_3, pH=13.5).

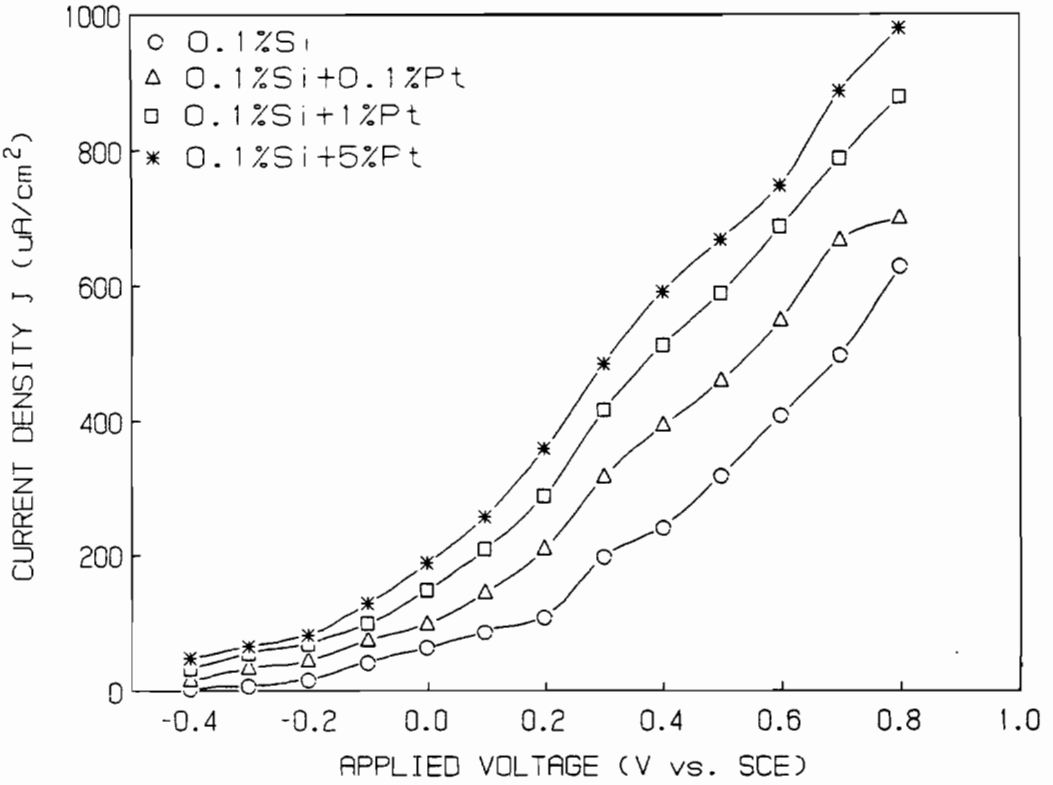

Figure 4.30. Photocurrent density versus applied potential for platinized 0.1 at.% Si solid state doped Fe_2O_3 electrodes (1M NaOH + 0.01M KNO_3, pH=13.5).

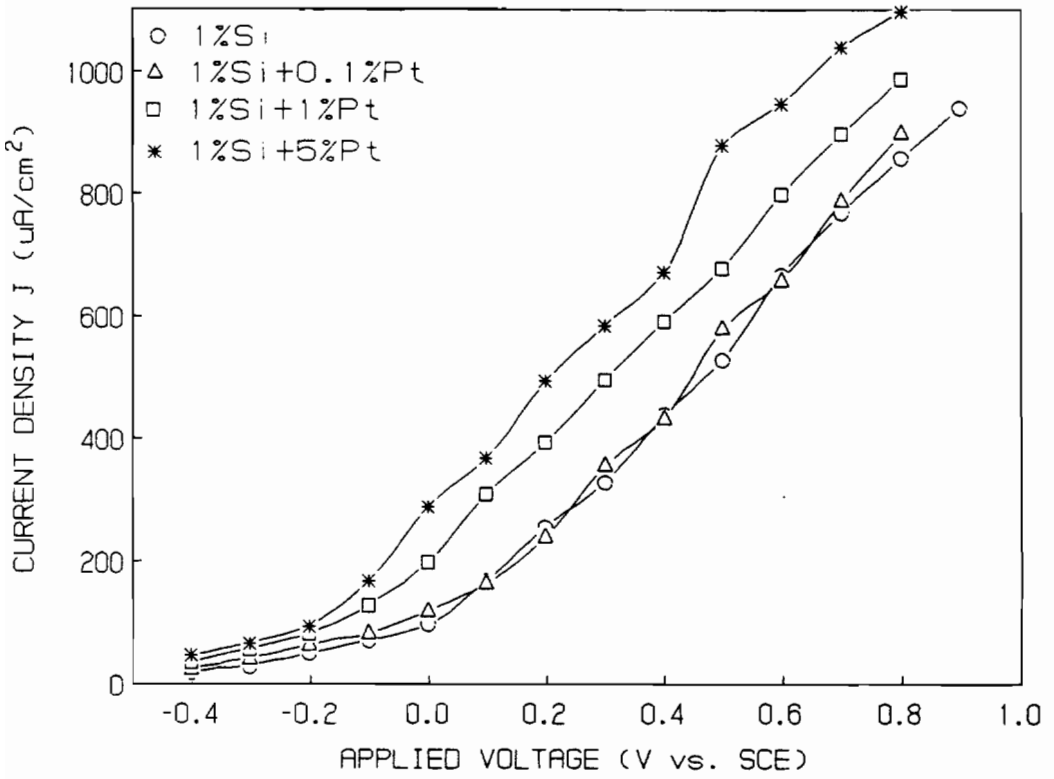

Figure 4.31. Photocurrent density versus applied potential for platinized 1 at.% Si solid state doped Fe_2O_3 electrodes (1M NaOH + 0.01M KNO_3, pH=13.5).

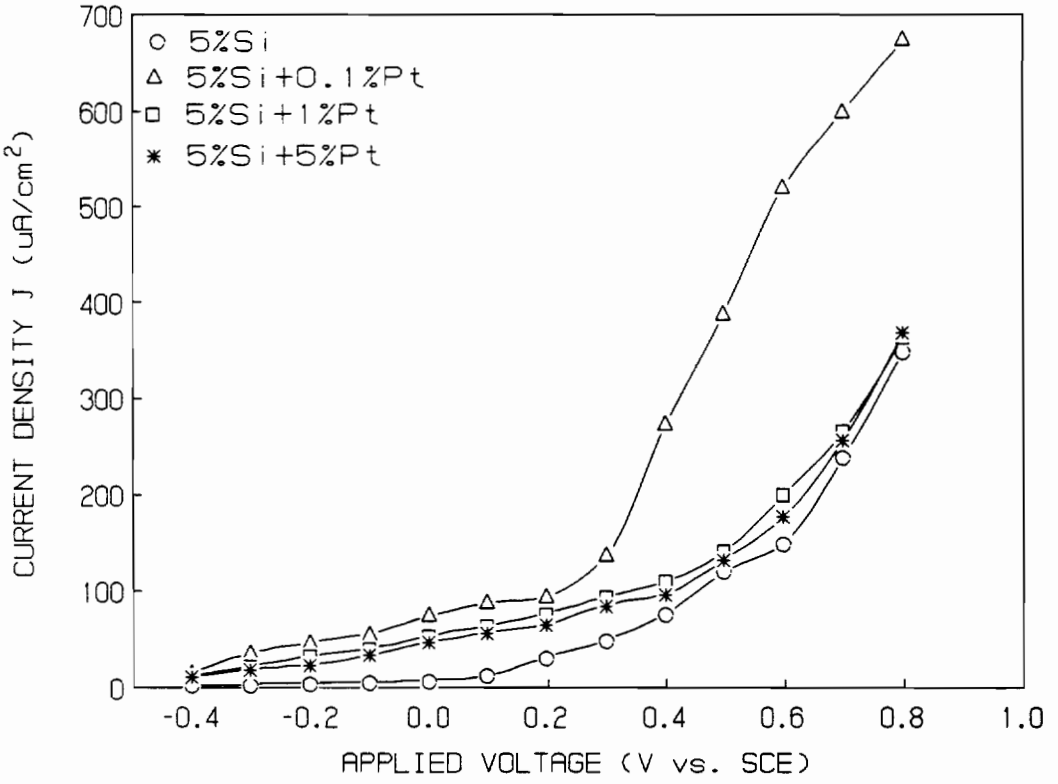

Figure 4.32. Photocurrent density versus applied potential for platinized 5 at.% Si solid state doped Fe_2O_3 electrodes (1M NaOH + 0.01M KNO_3, pH=13.5).

photogenerated carriers such as in α-Fe_2O_3. When the Fe_2O_3-electrolyte junction is illuminated with visible light, photons having energies greater than the band gap (2.2 eV) are absorbed and create electron-hole pairs in the semiconductor. Photons absorbed in the depletion layer produce electron-hole pairs that separate under the influence of the electric field present in the space charge region. Since the absorption coefficient for Fe_2O_3 is very small, most of the photons are absorbed beyond the depletion layer in the bulk of the Fe_2O_3. The photons in the bulk also generate electron-hole pairs but since there is no electric field present in the bulk and the diffusion lengths of carriers are small, the electrons recombine with the holes before they can diffuse into the depletion layer. Improved conductivity in the Fe_2O_3 samples can be achieved by increased doping which on the other hand decreases the depletion layer width and decreases overall photoactivity. This analysis explains the observed experimental results.

The anodic dark currents are not shown in the figures but they were generally higher for the solid state doped samples than for the freeze-dried samples, where in some cases the dark current was almost negligible. Dark currents for the solid state doped samples ranged from a few tens of $\mu A/cm^2$ to as high as hundreds of $\mu A/cm^2$ at higher applied voltages. Generally, n-type semiconductors exhibit little or no anodic current flow unless the minority carriers, holes, are photogenerated, but since there are a large number of electrons available dark cathodic currents might be observed. There are several possible explanation as to the origins of the anodic dark currents. Due to the disordered nature of these oxides, charge transfer at grain boundaries and

dislocations is possible. The magnitude of the dark currents should then be dependent on the amount of defects or inhomogeneity along the grain boundaries. This effect is in fact observed for the solid state mixed samples. The observed dark current is higher, which agrees well with the observed inhomogeneities in the structural and microscopic examinations. The dark currents for the freeze-dried samples are significantly lower which would be expected from the above assumptions. An increase in the dark current at an potential anodic of +0.7 V vs SCE can be explained due to direct electron tunneling across the space charge layer into the conduction band. Oxygen evolution was observed on the Fe_2O_3 electrode when the applied bias was sufficiently anodic (> +0.4 V vs SCE).

Results for the platinized samples in Figure 4.29 show a very similar trend compared to the Si doped samples. The maximum photocurrent obtained for the platinized samples was about 20-30% lower than for the Si doped samples at the same applied voltages. The incorporated platinum appears to act as a donor, although less effective than the Si species as discussed in section 4.2.

The platinized Si doped samples (Figures 4.30-4.32) showed increased photocurrent with increased platinum doping. The 1 at.% Si with 5 at.% Pt Fe_2O_3 sample showed the highest photocurrent of all ($J = 1.1$ mA/cm$_2$ at +0.8 V vs SCE). It should be noted that the dark currents in the platinized samples were slightly lower than in the unplatinized samples. The platinum role may be explained by enhancement of probabilities of electron exchange between the electrode and electrolyte species.

The exchange current densities at zero applied bias of the solid state doped samples were determined from the linear region of the Tafel plots. The exchange current densities versus platinum content for the solid state Si doped samples are presented in Figure 4.33. The charge transfer resistance (calculated from the exchange current density and from data taken from I-V curves) versus platinum content is presented in Figure 4.34.

The photocurrent density versus applied potential for the freeze-dried samples are presented in Figures 4.35-4.39. These results show the distinct advantage of the freeze-drying process for producing homogeneously doped semiconducting samples. The photocurrent densities for the freeze-dried samples are significantly higher (10x) than for the solid state doped samples. The dark currents are very small in comparison to the photocurrents or to the dark currents in the solid state mixed samples. Generally, the results follow the same pattern as in the solid state doped samples. The maximum photocurrents, however, are obtained with lower doping levels of Si or Pt than in the solid state doped samples. This observation strongly suggests better homogeneity of the dopants in the samples. The maximum photocurrent density of 10 mA/cm^2 at +0.8 V vs SCE is obtained in the 0.1 at.% Si + 5 at.% Pt sample. The oxygen evolution was also observed at more negative potentials than in the solid state doped samples. The kinetics of charge transfer were also significantly faster as was determined from the equilibration time for obtaining a stable photovoltage. The time to obtain a stable photovoltage was several orders of magnitude shorter for the freeze-dried sample than for the solid state

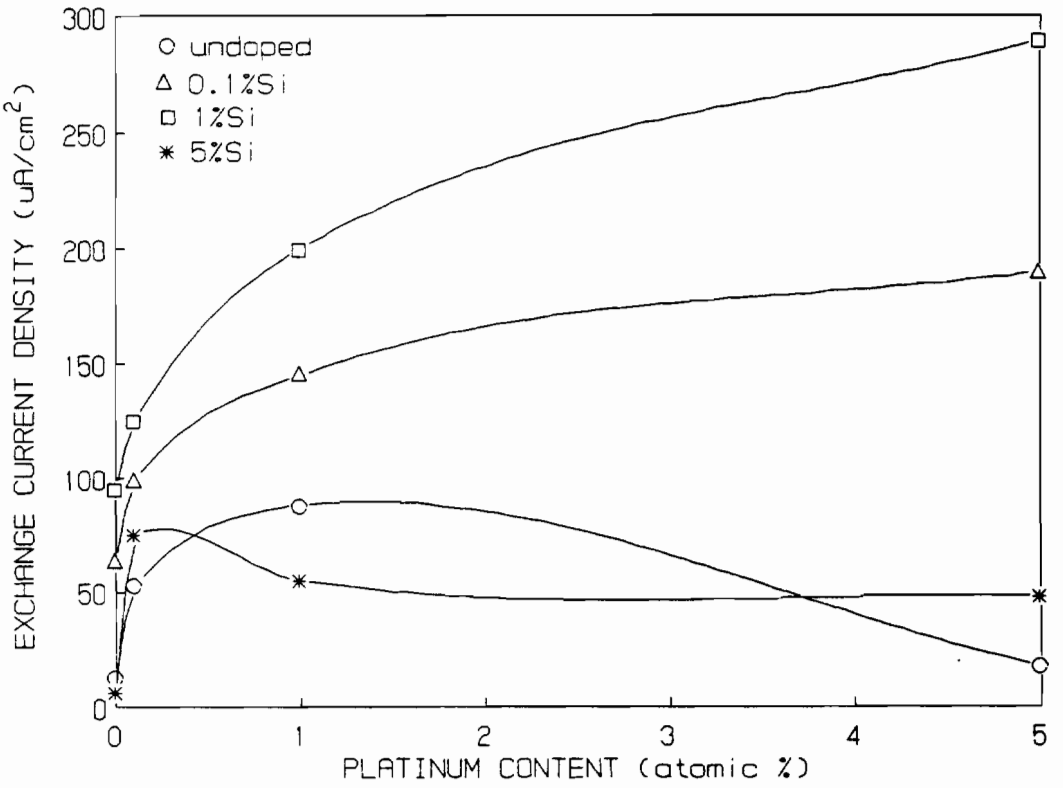

Figure 4.33. Exchange current density at 0.0 V vs SCE versus platinum content in solid state Si doped Fe_2O_3 (1M NaOH + 0.01M KNO_3, pH=13.5).

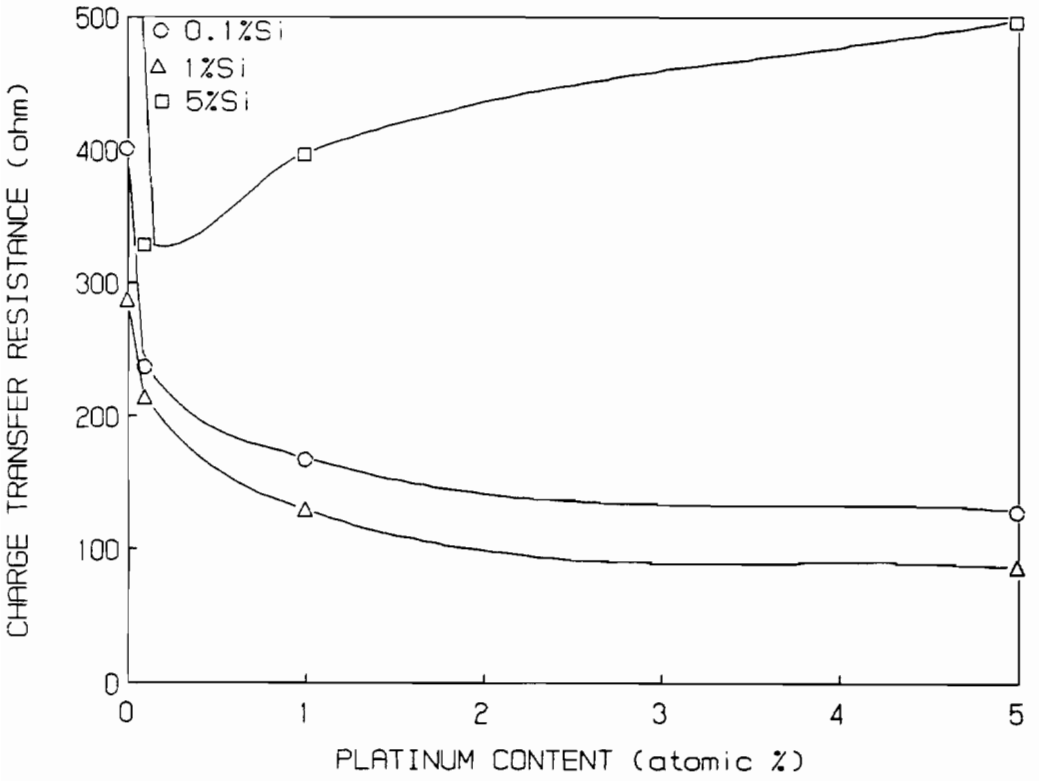

Figure 4.34. Charge transfer resistance versus platinum content in solid state Si doped Fe_2O_3 (at 0.0 V vs SCE).

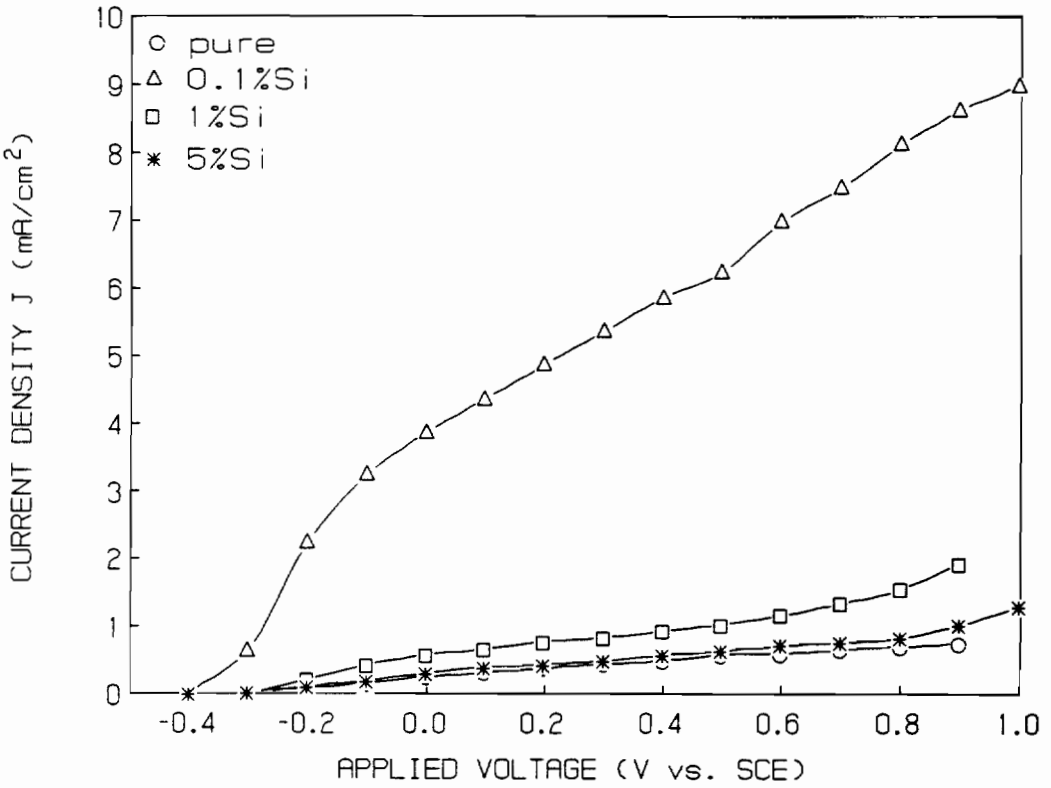

Figure 4.35. Photocurrent density versus applied potential for freeze-dried Si doped Fe_2O_3 electrodes (1M NaOH + 0.01M KNO_3, pH=13.5).

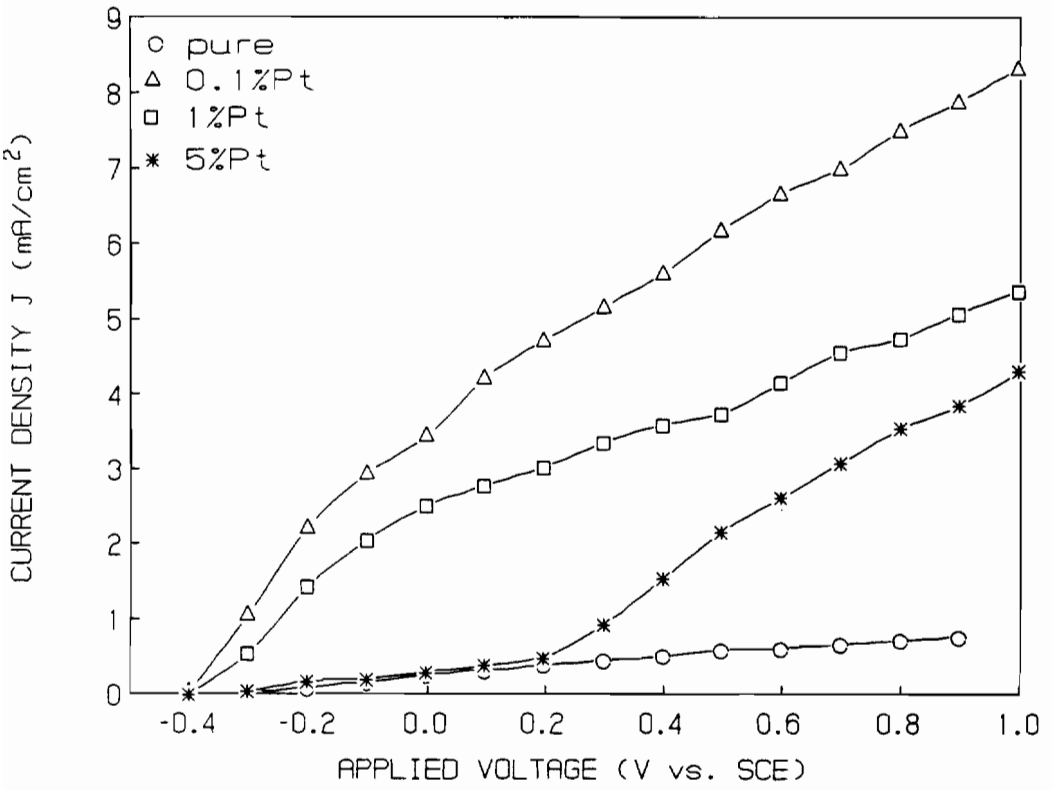

Figure 4.36. Photocurrent density versus applied potential for freeze-dried Pt doped Fe_2O_3 electrodes (1M NaOH + 0.01M KNO_3, pH=13.5).

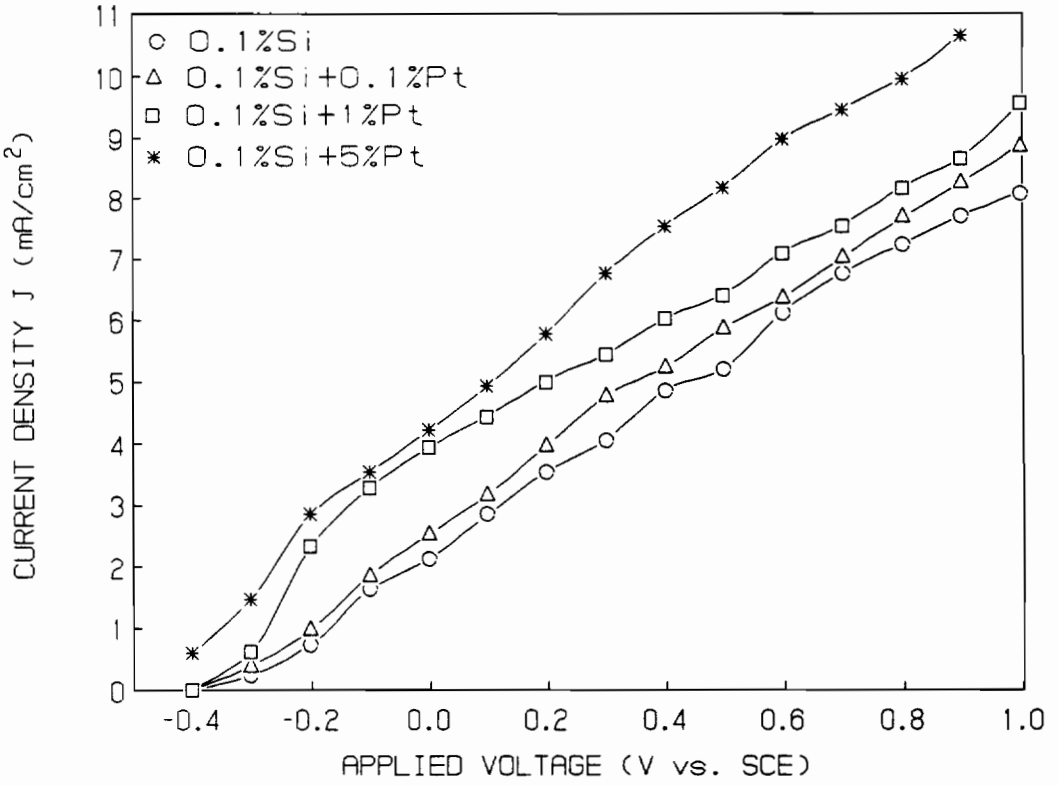

Figure 4.37. Photocurrent density versus applied potential for platinized freeze-dried 0.1 at.% Si doped Fe_2O_3 electrodes (1M NaOH + 0.01M KNO_3, pH=13.5).

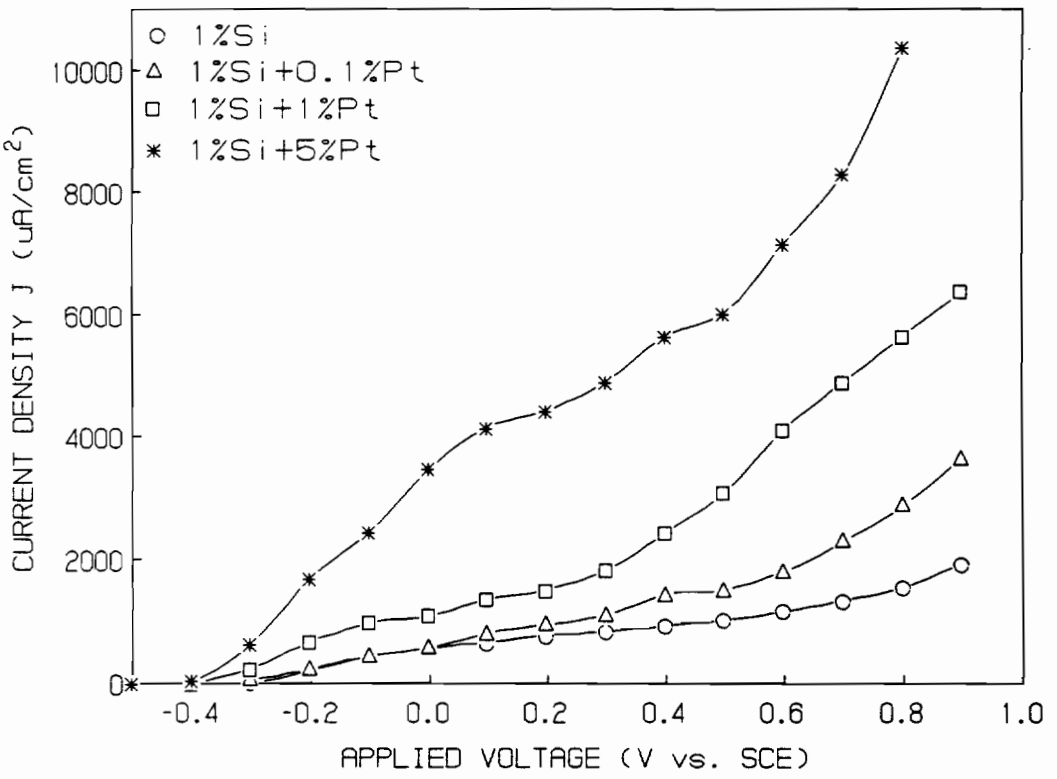

Figure 4.38. Photocurrent density versus applied potential for platinized freeze-dried 1 at.% Si doped Fe_2O_3 electrodes (1M NaOH + 0.01M KNO_3, pH=13.5).

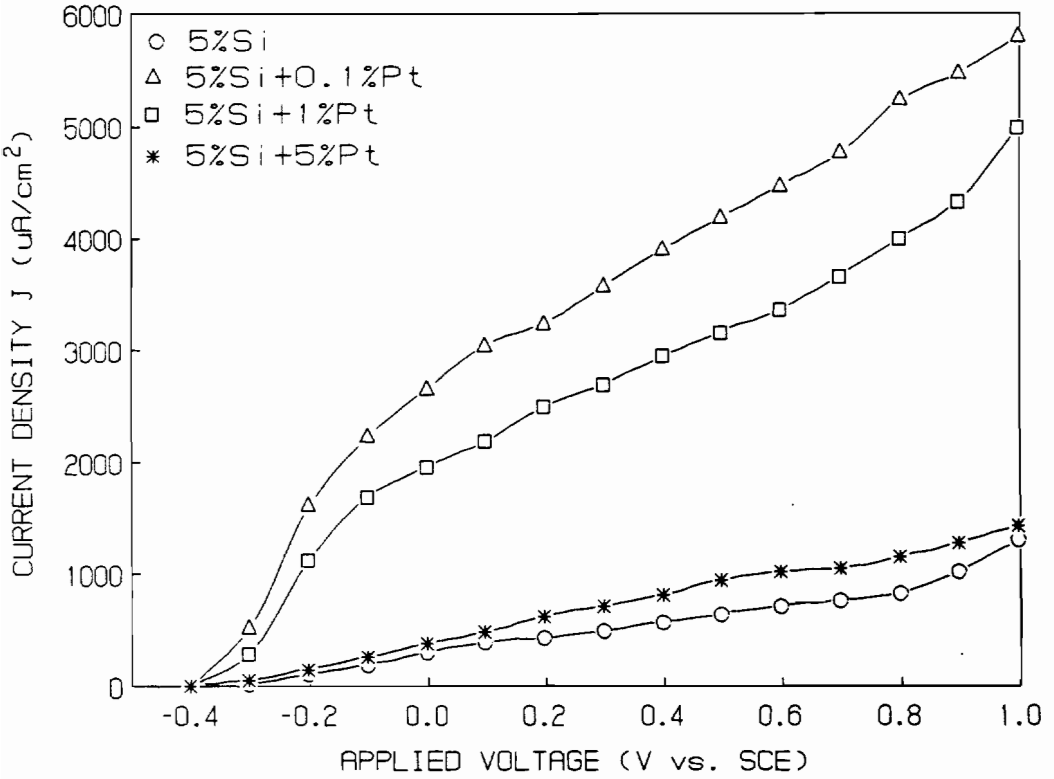

Figure 4.39. Photocurrent density versus applied potential for platinized freeze-dried 5 at.% Si doped Fe_2O_3 electrodes (1M NaOH + 0.01M KNO_3, pH=13.5).

sample. Photoactivities of the 1 at.% Pt and 1 at.% Si + 5 at.% Pt doped samples prepared by freeze-drying and by solid state doping techniques are compared in Figures 4.40 and 4.41, respectively. In each case it is shown that the freeze-dried sample produced 10 times higher photocurrent, and in turn 10 times more oxygen. Another factor in the freeze-dried samples contributes to the observed superior photocurrent. That factor is a surface area of the samples. As was discussed in section 4.1, the surface area of the sintered freeze-dried samples is two times higher than in the solid state doped samples. The current density results are corrected for geometrical area but that is different from microscopic surface area. According to this observation, the higher current density observed in the freeze-dried samples is at least partially due to higher surface area of the electrode. This conclusion is confirmed by comparing the photoactivities of the pure samples in Figure 4.42. The current density of the pure freeze-dried sample is approximately two times higher than of the commercial Fe_2O_3 sample. The higher surface area increases the possibility for increased carrier exchange with the solution thus increasing reaction rates and hence higher photocurrent.

Both freeze-dried as well as solid state Si doped samples exhibited very large transient currents that are typical of oxide semiconductors. The photocurrents were generally higher at cathodic potentials and decreased with increasing anodic potential. Figure 4.43 shows a typical relationship of the transient photocurrent versus applied potential for a pure freeze-dried sample. As can be seen the transient photocurrent is 3 orders of magnitude higher than the steady state

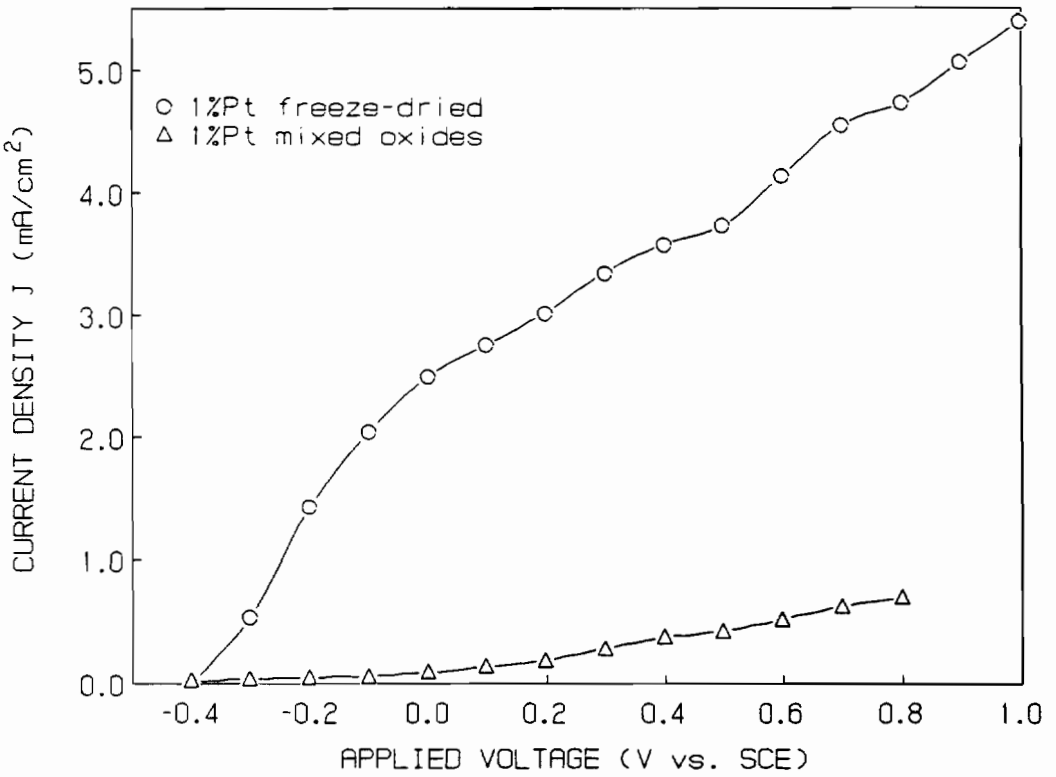

Figure 4.40. Current density versus applied voltage for 1 at.% Pt doped freeze-dried and solid state doped Fe_2O_3 (1M NaOH + 0.01M KNO_3, pH=13.5).

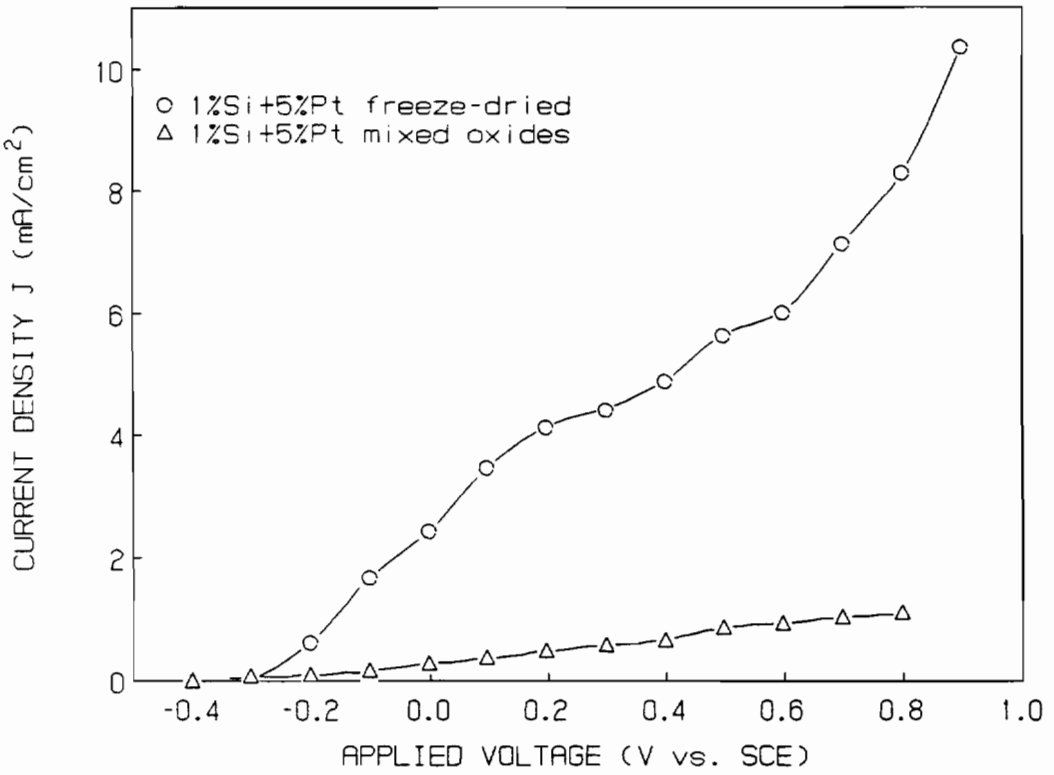

Figure 4.41. Current density versus applied voltage for 1 at.% Si + 5 at.% Pt doped freeze-dried and solid state doped Fe_2O_3 (1M NaOH + 0.01M KNO_3, pH=13.5).

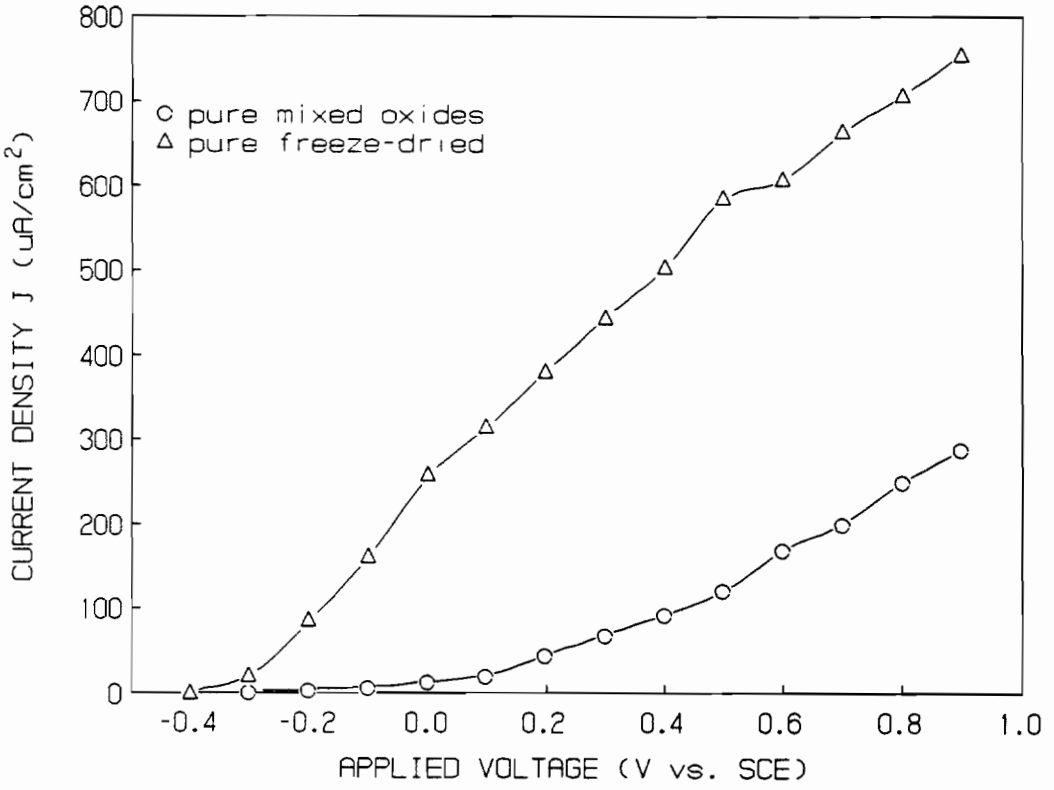

Figure 4.42. Current density versus applied voltage for pure freeze-dried and commercial Fe_2O_3 (1M NaOH + 0.01M KNO_3, pH=13.5).

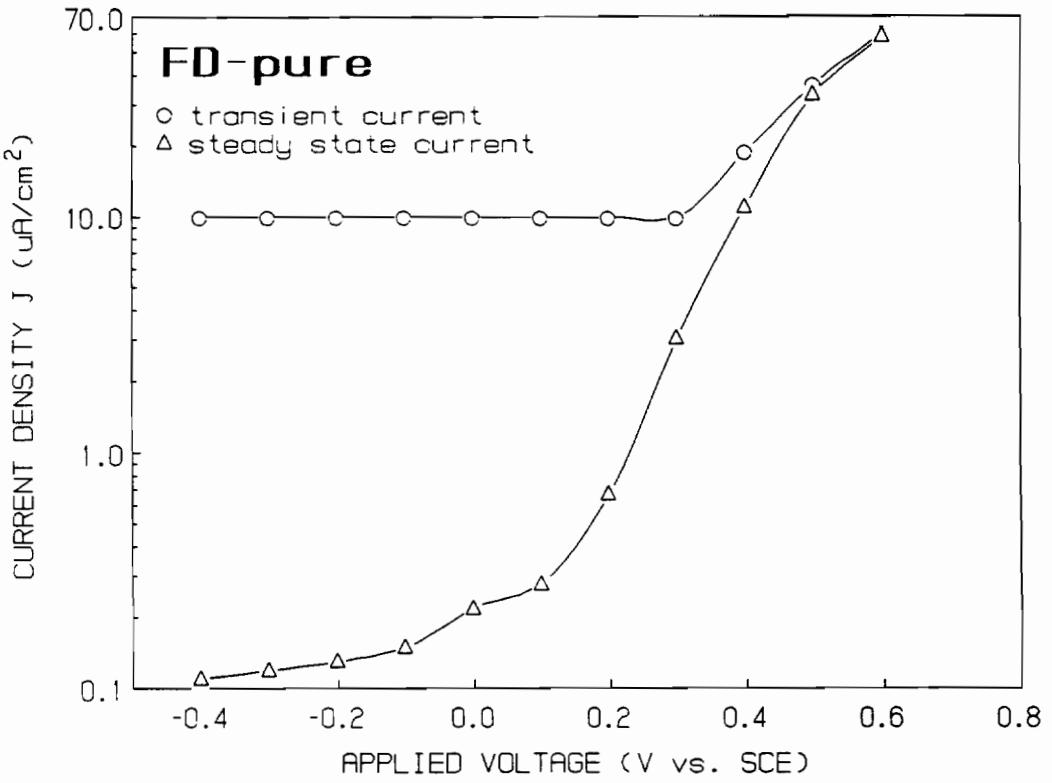

Figure 4.43. Transient photocurrent versus applied potential for freeze-dried Fe_2O_3 (1M NaOH + 0.01M KNO_3, pH=13.5).

photocurrent obtained in a fraction of a second. The kinetics of the transient current to steady state current transition for the solid state doped sample were much slower. A large anodic transient current is observed in the samples when the light is turned on and again when the light is turned off a cathodic transient current is observed. When a voltage step is applied to the interface it is expected that a transient current will be observed through the external circuit due to the charge stored in the space charge region. On returning the voltage to the original value, an equal and opposite charge is expected [264]. In practice the transient observed when turning on the anodic voltage exceeded that for when turned off. This result is considered in terms of field induced tunneling from surface levels as described previously. The falling transient can be explained in terms of surface recombination or backreaction of the photogenerated species. Thus, the oxygen or hydroxyl radical which is produced by the photogenerated holes is thermodynamically reducible at potentials on the rising portion of the I-V curve. A backreaction between these and any electrons at the surface produces a backreaction (or a surface electron-hole recombination) and a cathodic current component. Another explanation for these transient photocurrents is that the samples consist of a mixture of two oxides, Fe_2O_3 and Fe_3O_4. Fe_3O_4 is a p-type semiconductor and therefore, p-n junctions between the two oxides may be present. Photoproduced electrons in the Fe_2O_3 that are transferred to a Fe_3O_4 interface may cause an increase in the p-n potential barrier. Thus, the anodic transient currents observed may be sufficient to charge the p-n barrier before a significant photocurrent is obtained under steady

illumination. Upon removal of illumination, the cathodic transients observed may be a result of discharging the potential barrier generated under illumination. It has been previously shown that the presence of electrocatalysts of the platinum group metals can significantly improve the PEC performance of III-V photoelectrodes [297,309]. The platinum effect on the anodic transient current behavior of the Fe_2O_3 electrodes can be clearly seen in Figures 4.44-4.47. The anodic transient current in the Si doped freeze-dried sample (Figure 4.44) is an order of magnitude higher than the steady state photocurrent and at -0.2 V vs SCE the transient photocurrent is only slightly higher than the steady state photocurrent. In Figures 4.45-4.47 it is seen that the addition of even 0.1 at.% Pt into the Fe_2O_3 almost completely eliminates this anodic transient portion of the photocurrent and with increasing platinum content the transient current is absent. Figure 4.48 shows the shape of the I-V curve with and without the anodic transient current. The results of the exchange current density versus platinum content for the freeze-dried Si doped samples are shown in Figure 4.49. The charge transfer resistance versus platinum content results for the pure and Si doped freeze-dried samples are shown in Figure 4.50 and 4.51, respectively. From Figures 4.33 and 4.49 the beneficial effect of platinum on photocurrent at no applied bias for freeze-dried as well as solid state doped Fe_2O_3 electrodes can be observed. The exchange current density increases with increasing platinum content, which is also apparent from Figures 4.34 and 4.50 where the resistance of charge carrier transfer between the electrode and electrolyte decreases with increasing amount of platinum in Fe_2O_3.

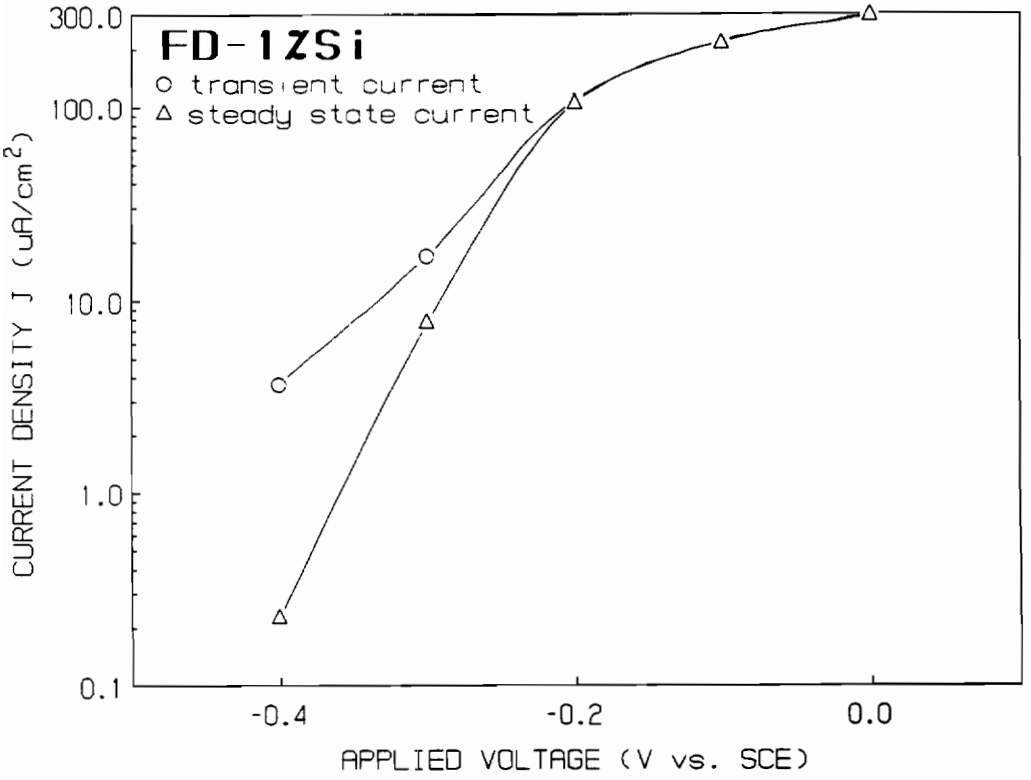

Figure 4.44. Transient photocurrent versus applied potential for freeze-dried 1 at% Si doped Fe_2O_3 (1M NaOH + 0.01M KNO_3 pH=13.5).

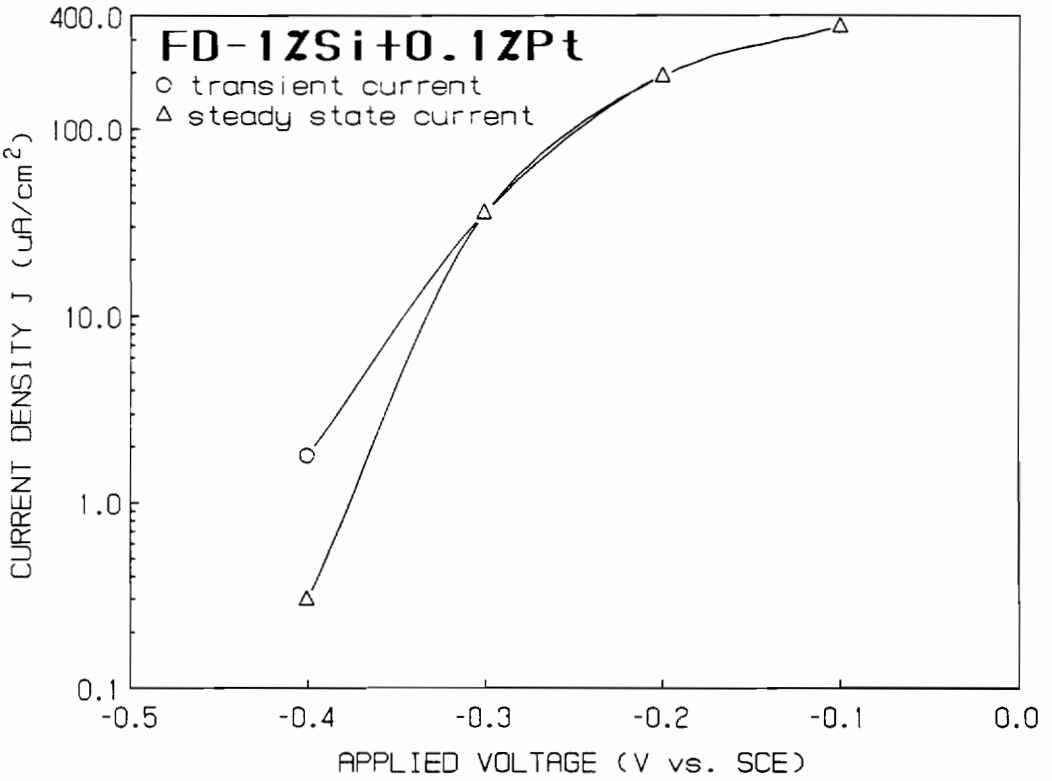

Figure 4.45. Transient photocurrent versus applied potential for freeze-dried 1 at% Si + 0.1 at.% Pt doped Fe_2O_3 (1M NaOH + 0.01M KNO_3, pH=13.5).

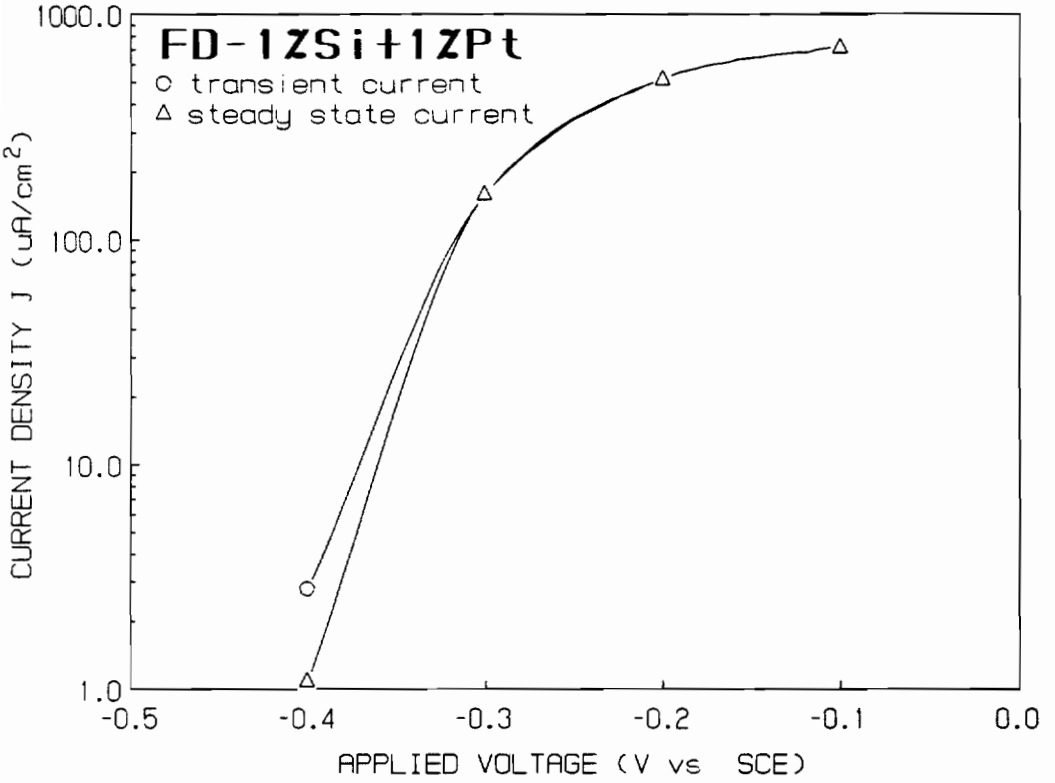

Figure 4.46. Transient photocurrent versus applied potential for freeze-dried 1 at% Si + 1 at.% Pt doped Fe_2O_3 (1M NaOH + 0.01M KNO_3, pH=13.5).

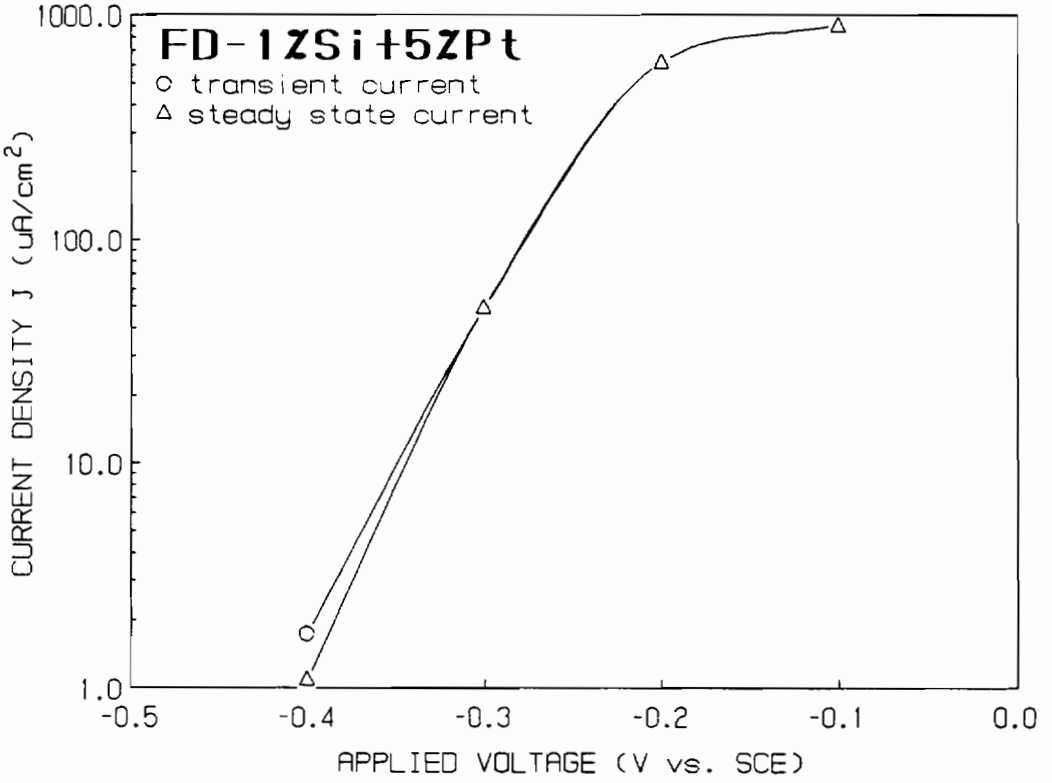

Figure 4.47. Transient photocurrent versus applied potential for freeze-dried 1 at% Si + 5 at.% Pt doped Fe_2O_3 (1M NaOH + 0.01M KNO_3, pH=13.5).

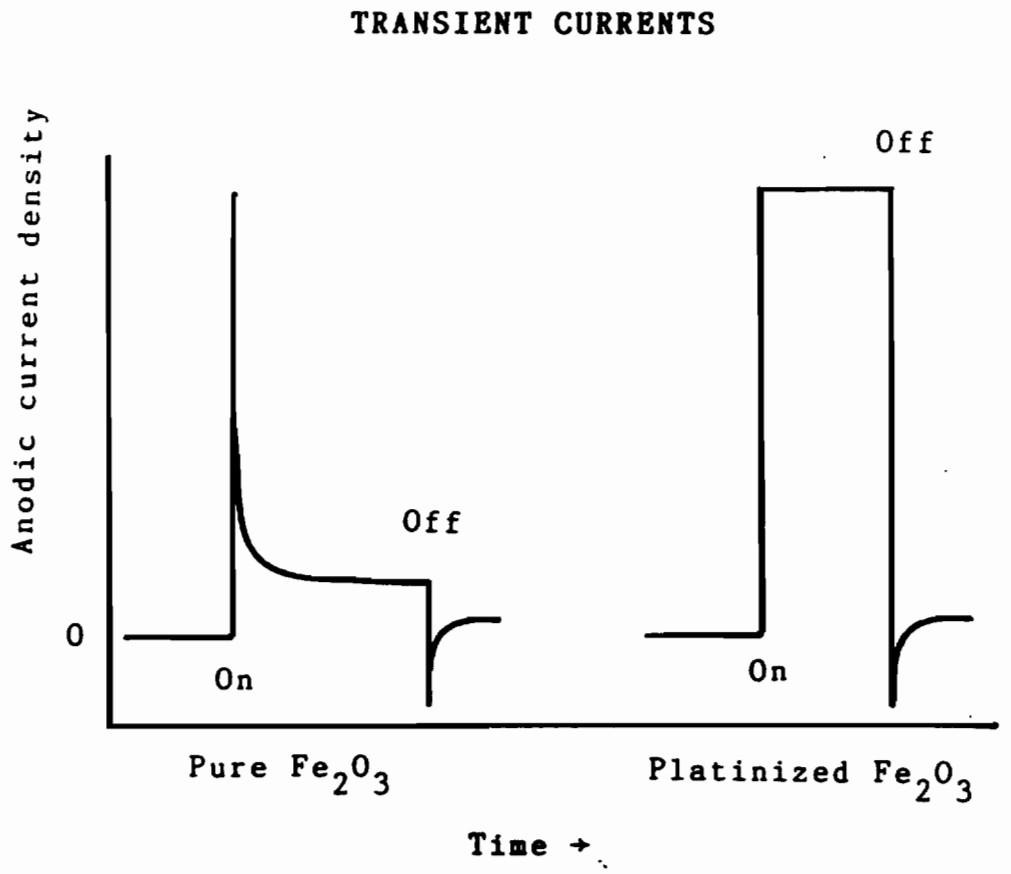

Figure 4.48. Current-potential curve with and without the anodic transient photocurrent.

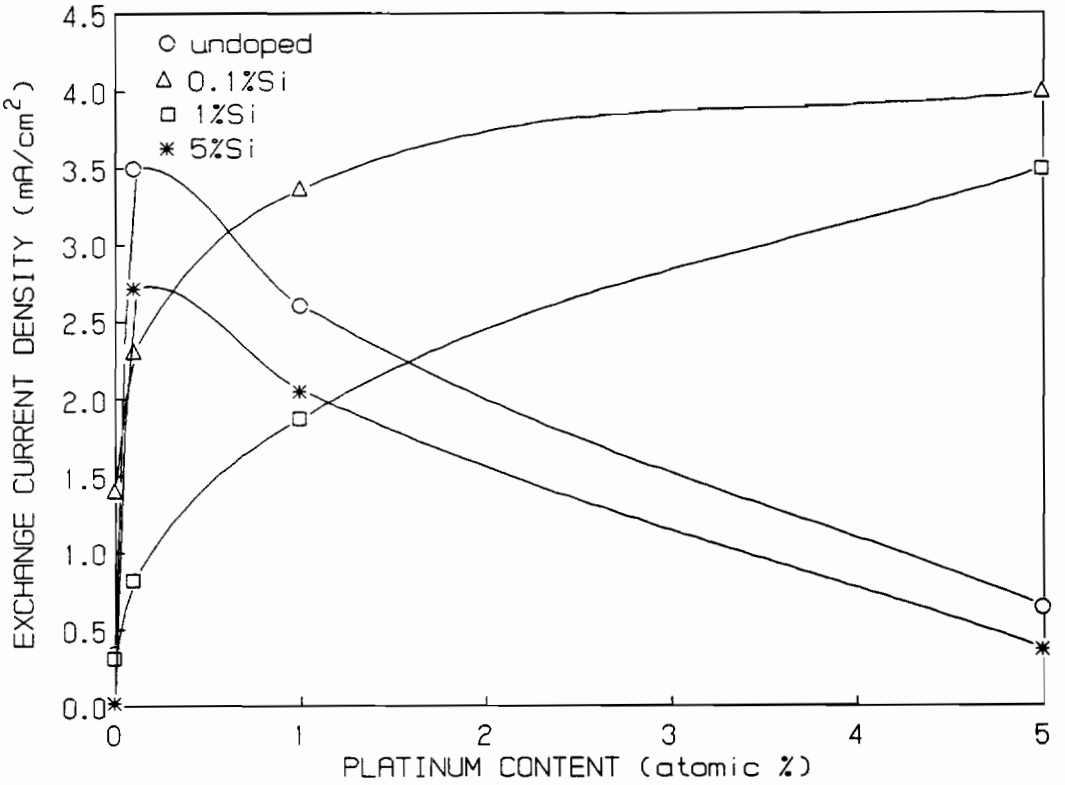

Figure 4.49. Exchange current density (at 0.0 V vs SCE) versus platinum content in Si doped freeze-dried Fe_2O_3 (1M NaOH + 0.01M KNO_3, pH=13.5).

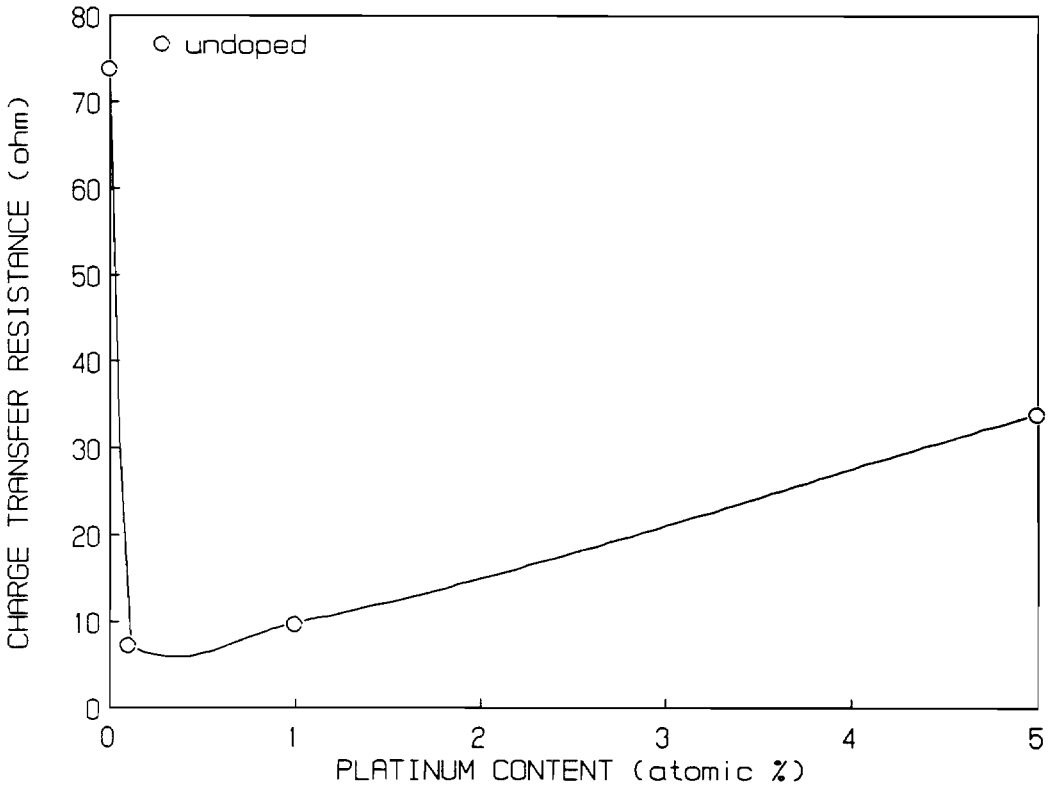

Figure 4.50. Charge transfer resistance versus platinum content in a pure freeze-dried Fe_2O_3.

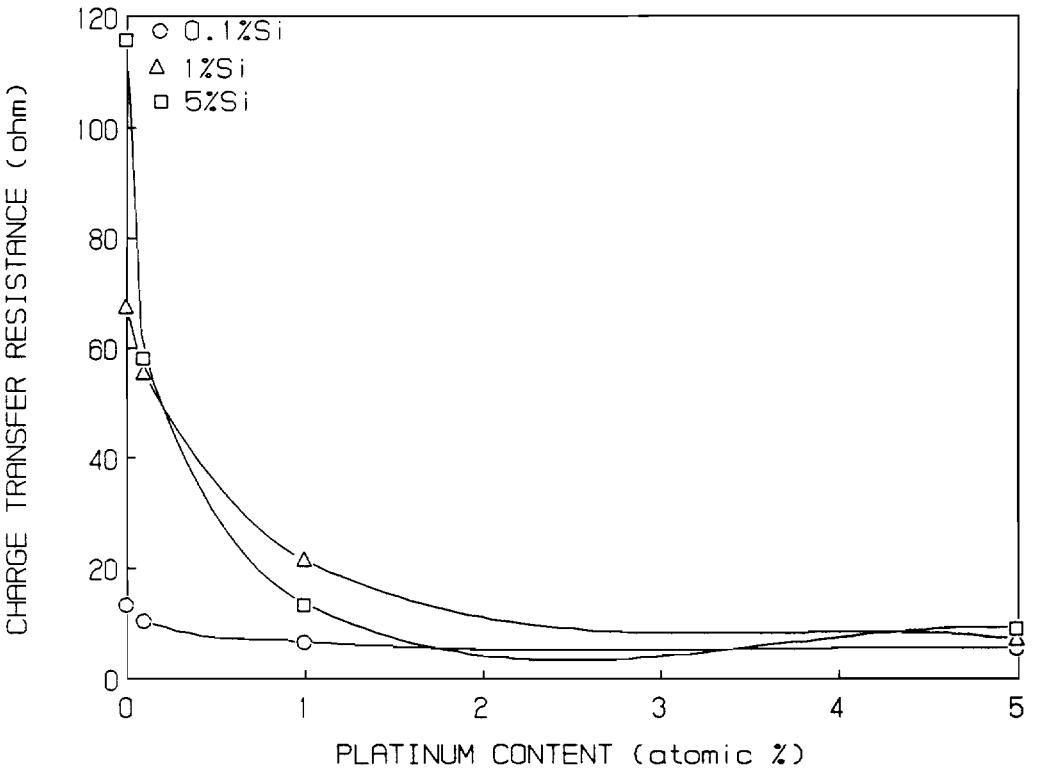

Figure 4.51. Charge transfer resistance in Si doped freeze-dried Fe_2O_3.

The platinized freeze-dried electrodes were very stable in maintaining the photocurrent in the PEC as demonstrated for example in Figure 4.52 where photocurrent (at 0.0 V vs SCE) versus time for 1 at.% Si + 1 at.% Pt doped freeze-dried Fe_2O_3 is recorded. This stability makes it possible to use these electrodes in the photoelectrochemical solar cells for producing gaseous fuels from dissociating water with visible light as will be discussed in the next section.

4.4 Photoactivity of pure and platinized Mg doped Fe_2O_3

Magnesium doped Fe_2O_3 is a p-type semiconductor [310-316] which when used in the PEC cell will act as a cathode and a cathodic current may be expected. Figures 4.53-4.58 show the photovoltage versus applied potential for pure and platinized Mg doped Fe_2O_3 prepared by freeze-drying and solid state mixing technique. From these figures we can make several observations. The photocurrent density of the freeze-dried samples was again higher than for the solid state doped samples but not as large a difference as in the Si doped samples. The photo-currents for the 0.1 and 1 at.% Mg level were rather small, most likely due to a very large resistivity of these samples as discussed in section 4.2. The cathodic photocurrent onset occurs at about 0.0 V vs SCE for the lower Mg doping level and at +0.2 V vs SCE for the 5 at.% Mg doping. Photocurrent density increases with increasing Mg levels and also with increasing platinum doping levels. The cathodic current onset is also shifted in more positive direction with increasing platinum doping. The higher photocurrents observed with increasing negative applied potential are due to hydrogen evolution from the

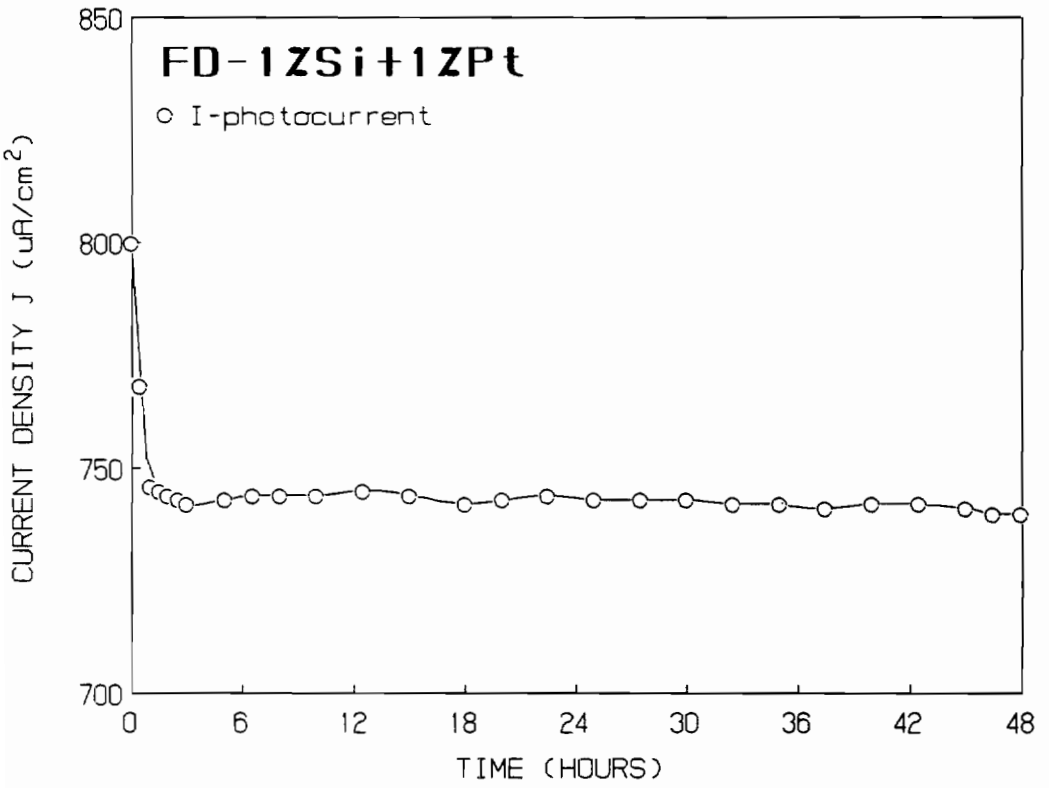

Figure 4.52. Photocurrent (at 0.0 V vs SCE) versus time for 1 at.% Si + 1 at.% Pt doped freeze-dried Fe_2O_3 (1M NaOH + 0.01M KNO_3).

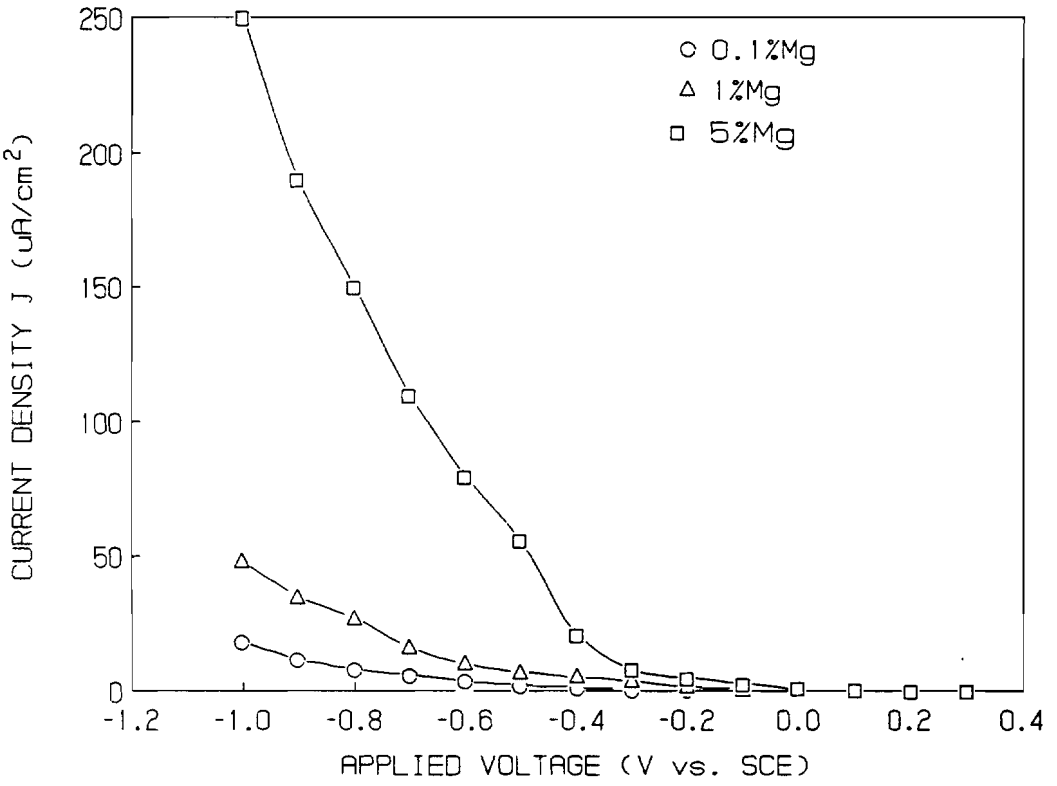

Figure 4.53. Photocurrent versus applied potential of solid state Mg doped Fe_2O_3 (1M NaOH + 0.01M KNO_3).

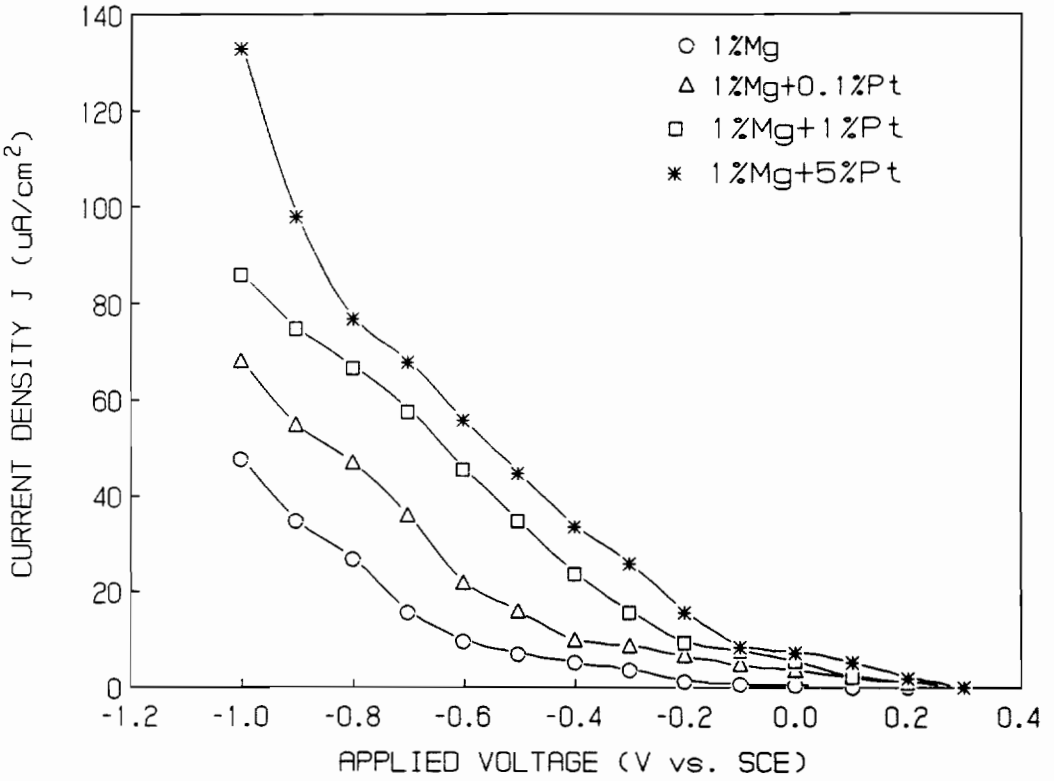

Figure 4.54. Photocurrent versus applied potential of a platinized 1 at.% Mg solid state doped Fe_2O_3 (1M NaOH + 0.01M KNO_3).

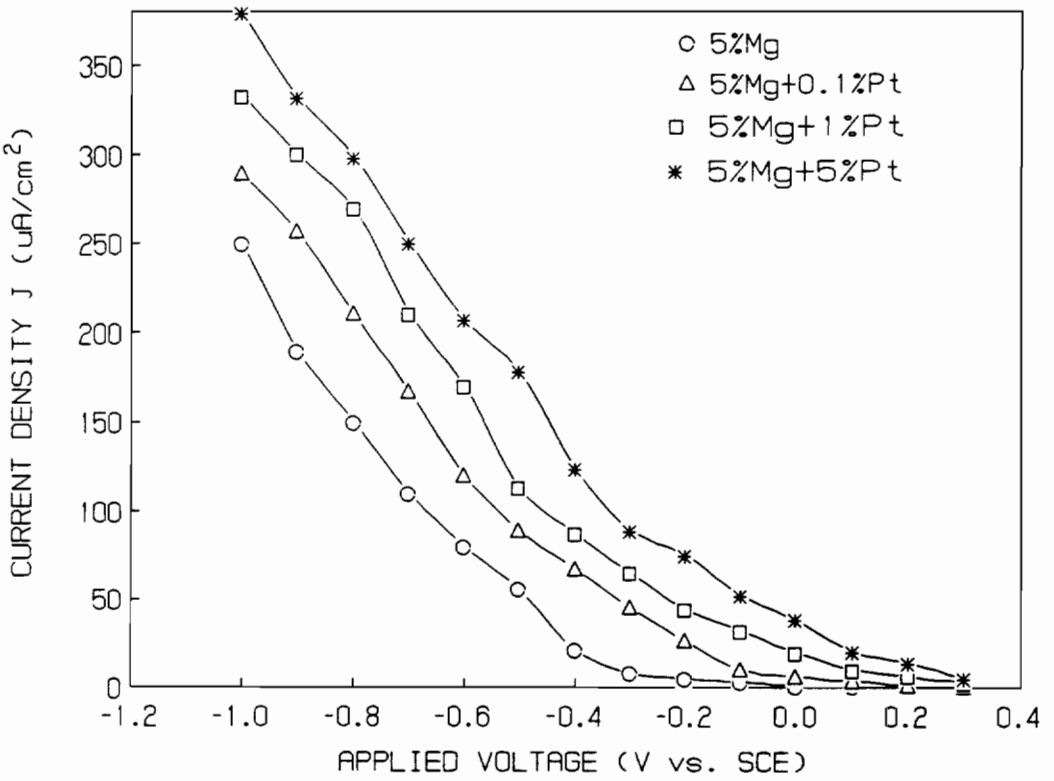

Figure 4.55. Photocurrent versus applied potential of a platinized 5 at.% Mg solid state doped Fe_2O_3 (1M NaOH + 0.01M KNO_3).

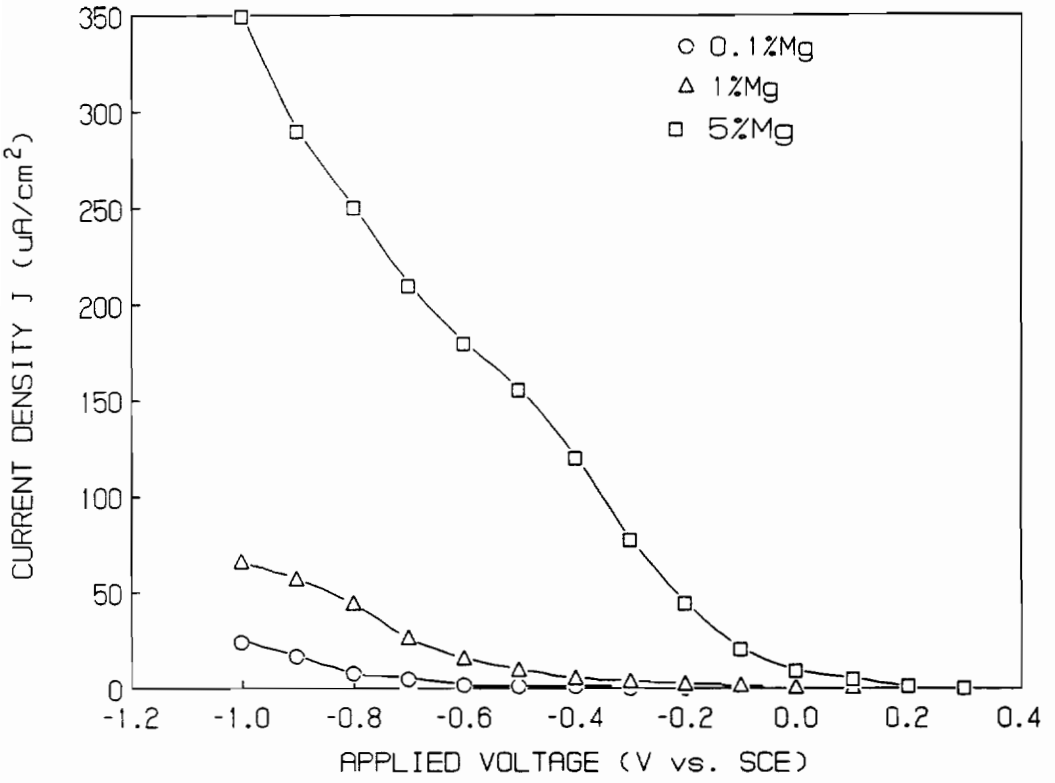

Figure 4.56. Photocurrent versus applied potential of a freeze-dried Mg doped Fe_2O_3 (1M NaOH + 0.01M KNO_3).

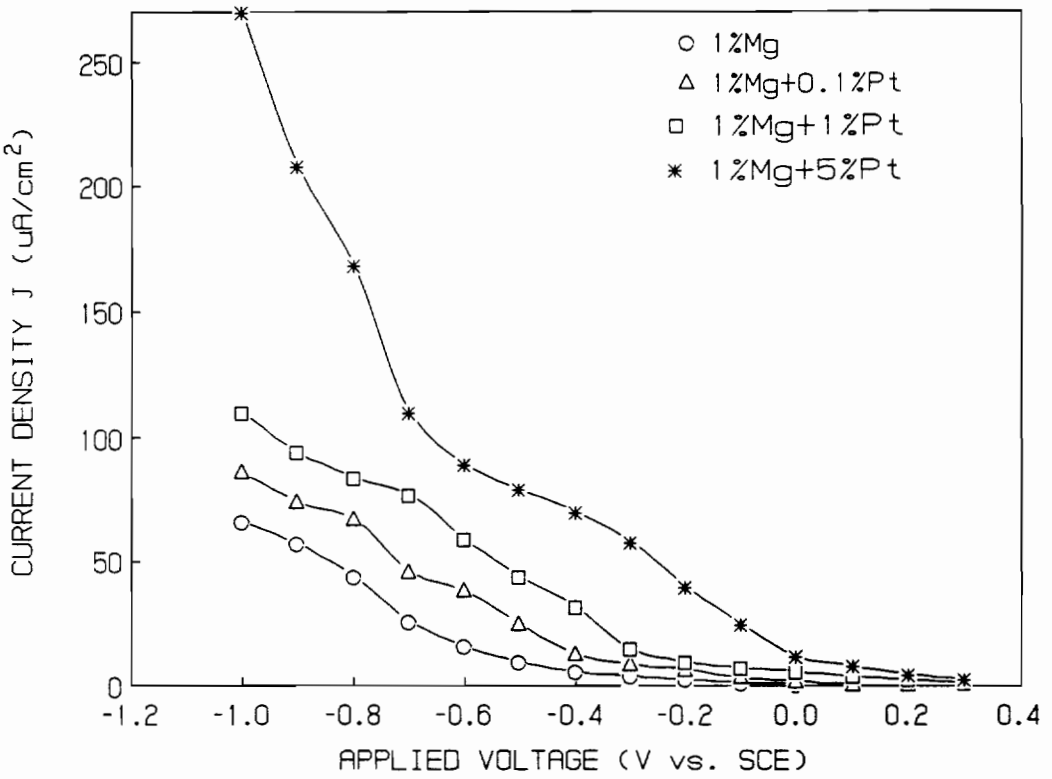

Figure 4.57. Photocurrent versus applied potential of a freeze-dried platinized 1 at.% Mg doped Fe_2O_3 (1M NaOH + 0.01M KNO_3).

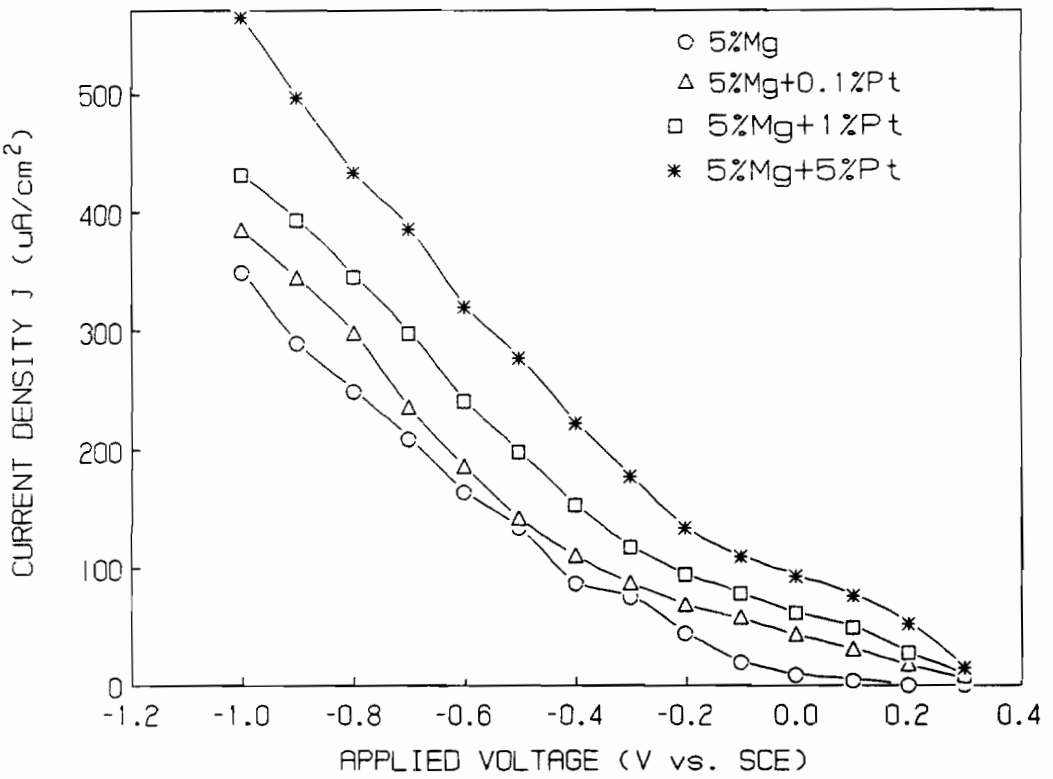

Figure 4.58. Photocurrent versus applied potential of a freeze-dried platinized 5 at.% Mg doped Fe_2O_3 (1M NaOH + 0.01M KNO_3).

Fe_2O_3 as determined by visual observation as well as with a gas chromatograph.

The ease of evolution of O_2 from the Fe_2O_3 electrode under bias when short-circuiting to platinum and the lack of evolution of gas from the oxide at open circuit suggest that the difficulty at open circuit is in the relative rate of H_2 evolution. The irradiation should raise the Fermi level in the semiconductor above the H_2/H^+ couple to allow the reduction of H_2O. But there may be only slow reduction of H_2O at the Fe_2O_3 at the potential achievable with irradiation. This slow rate of reduction may be the result of the band bending barrier, since the electrons to reduce H_2O would either have to go over the barrier or tunnel through it. There is also a substantial overvoltage for H_2 evolution from the Fe_2O_3. Both of these problems should be solved by platinizing the Fe_2O_3, since H_2 evolution from Pt occurs with only a small overvoltage and the Pt presence in the sample is almost like having the Fe_2O_3 connected to a Pt counterelectrode. Thus the platinum might play a different role in the Mg doped samples. The photocurrent increases in the cathodic direction with increasing platinum loading for all samples. The platinum is lowering the overpotential needed to reduce hydrogen on the Fe_2O_3 electrode by helping electron charge transfer across the semiconductor-electrolyte interface. This can also be seen from Figure 4.59 and 4.60. The charge transfer resistance at -0.4 V vs SCE dramatically decreases with increasing Pt content. If the platinum would be acting as a donor in these samples, the addition of platinum would actually decrease the observed cathodic photocurrent and would produce an anodic photocurrent. Due to an absence of anodic

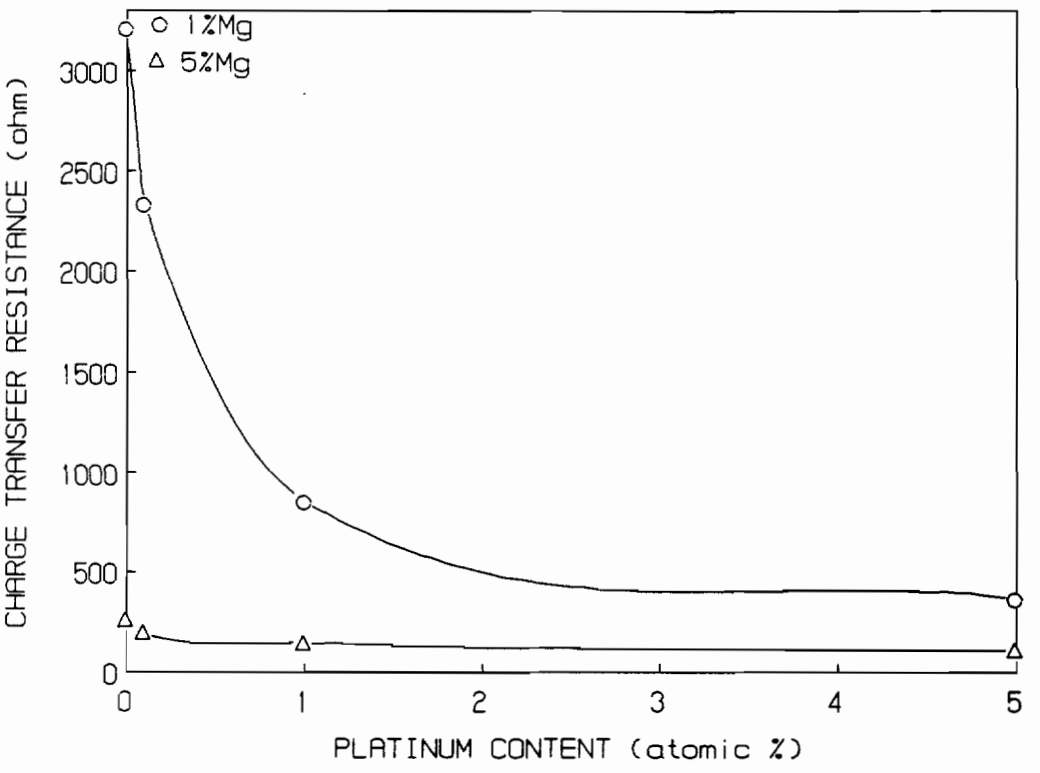

Figure 4.59. Charge transfer resistance versus platinum content for Mg doped freeze-dried Fe_2O_3 (1M NaOH + 0.01M KNO_3).

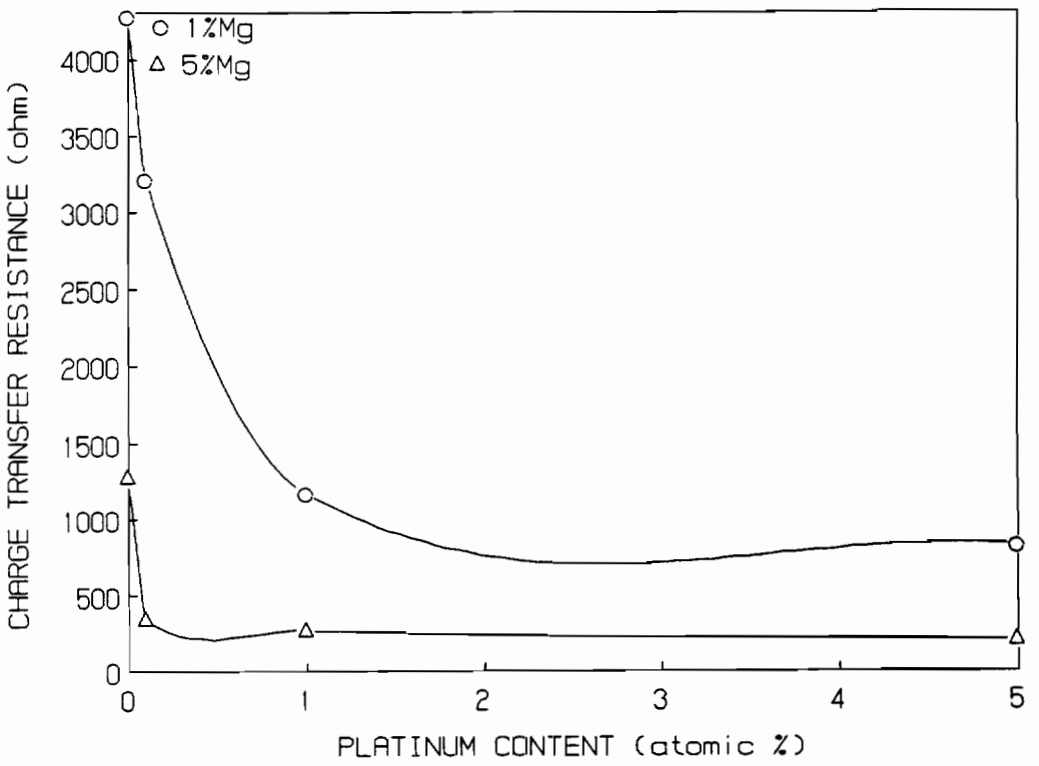

Figure 4.60. Charge transfer resistance versus platinum content for Mg doped freeze-dried Fe_2O_3 (1M NaOH + 0.01M KNO_3).

photocurrent we can assume that the platinum acts mostly as an electro-catalyst helping in the hydrogen evolution. The exchange current densities for Mg doped Fe_2O_3 versus platinum content are presented in Figures 4.61-4.62. The enhanced exchange current densities are expected for the platinized Fe_2O_3 in light of the above analysis.

The Mg-doped Fe_2O_3 photocathode was used in conjunction with the Si doped photoanode in a photoelectrochemical cell illuminated only with visible light (>420 nm) without any external bias. This p/n assembly was previously used by Somorjai et al. to dissociate water into hydrogen and oxygen without any applied voltage [273,321].

This important result was confirmed in our investigation. It was determined that the p/n assembly was capable of producing hydrogen and oxygen by illuminating only with visible light. The hydrogen was detected in small amounts in the PEC by analyzing gaseous samples from the cell by gas chromatography. The Mg-doped Fe_2O_3 sample was then substituted with the platinized Mg-doped sample in the PEC and was again irradiated with only a visible light. It was observed that the hydrogen production increased with increasing platinum doping in the Mg-doped Fe_2O_3 as was expected from the results presented in this investigation. Since our photoelectrochemical cell was not designed to be hydrogen tight these results are purely qualitative since it was difficult to determine quantitatively how much hydrogen was actually generated for each sample. This experiment was not the main objective of this investigation but was conducted to confirm the results by Somorjai et al. [273,321] and also to confirm our understanding of the role of platinum in doped Fe_2O_3 electrodes.

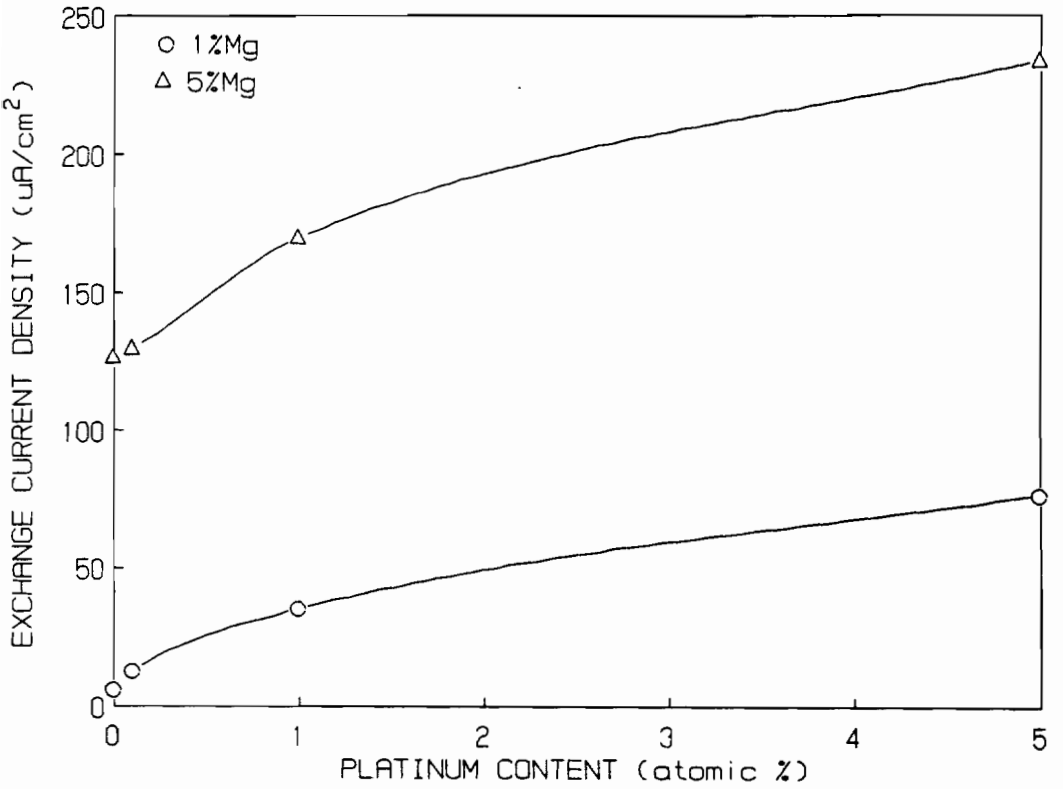

Figure 4.61. Exchange current density of Mg doped freeze-dried Fe_2O_3 (at -0.4 V vs SCE, 1M NaOH + 0.01M KNO_3, pH=13.5).

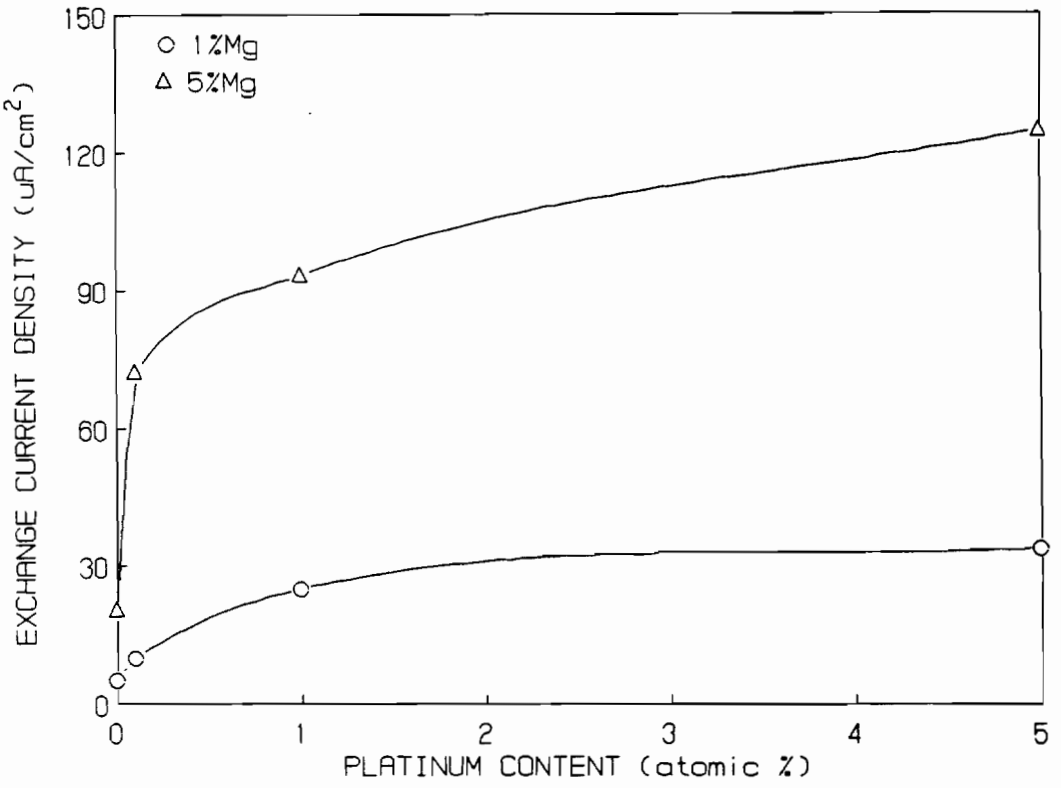

Figure 4.62. Exchange current density of solid state Mg doped Fe_2O_3 (at -0.4 V vs SCE, 1M NaOH + 0.01M KNO_3, pH=13.5).

4.5 Spectral response of doped and platinized Fe_2O_3

Figure 4.63 shows a typical spectral response of a pure freeze-dried Fe_2O_3. The quantum efficiencies are shown only on a relative scale since the results were not corrected for instrumentation optical throughput. The figure shows a photocurrent onset occurring around 575-600 nm. There is a shoulder in the photoresponse curve at 565 nm which corresponds to the band gap for the Fe_2O_3 of 2.2 eV. Overall, the curve doesn't show very much structure. For semiconductors the dependence of the absorption coefficient, α, on energy near the absorption edge usually follows the form:

$$\alpha h\nu = A(h\nu - \nu v_0)^{n/2} \qquad (4.5)$$

where A is a constant, and n depends on the nature of the optical transition, i.e. n = 1 for a direct transition, and n = 4 for an indirect transition, hv_0 corresponds to the bandgap. The photocurrent efficiency is proportional to the absorption coefficient. From the intercept of a plot of quantum response versus energy, as for example in Figure 4.64 for a pure freeze-dried sample, we can determine the energies of the direct or indirect transitions. The indirect transition for the pure Fe_2O_3 occurs at 2.18 eV requiring phonon support with a direct transition occurring at 1.78 eV. Figures 4.65-4.68 show spectral response results for pure and platinized Si doped freeze-dried Fe_2O_3. The photocurrent results are generally consistent with the results obtained in the current-voltage studies discussed in previous sections. For the platinized samples, maximum photoresponse was

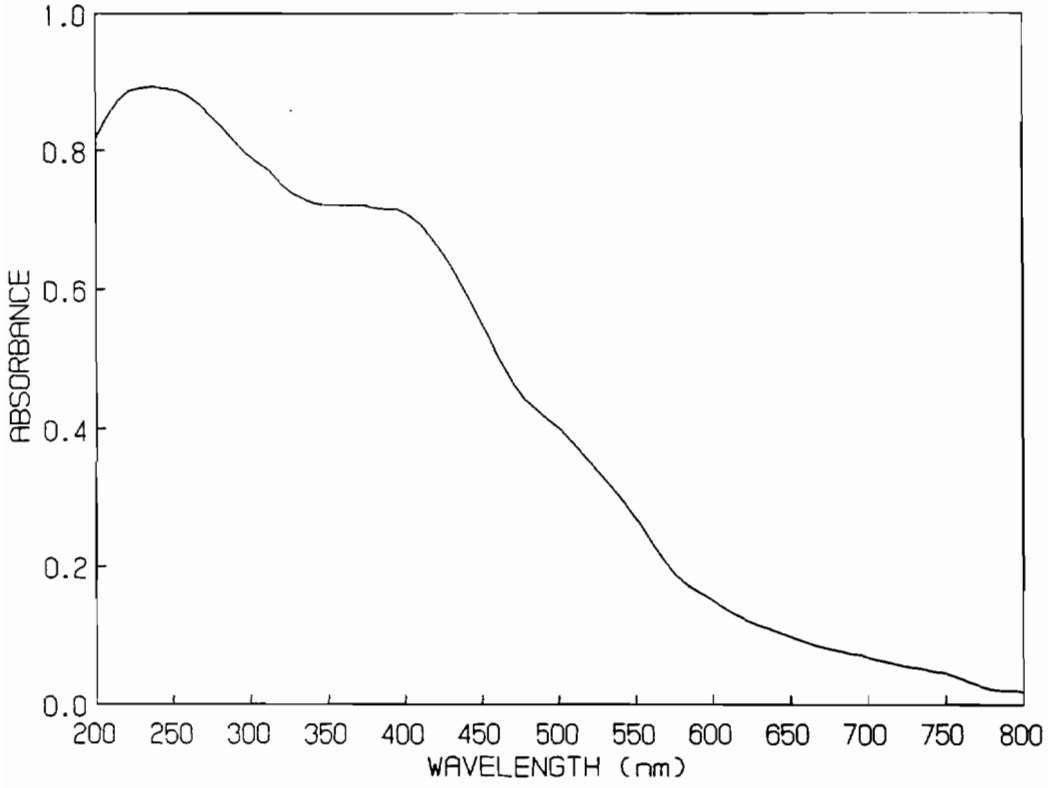

Figure 4.63. Spectral response (arbitrary units) versus wavelength of irradiated light for a pure freeze-dried Fe_2O_3 (1M NaOH + 0.01M KNO_3).

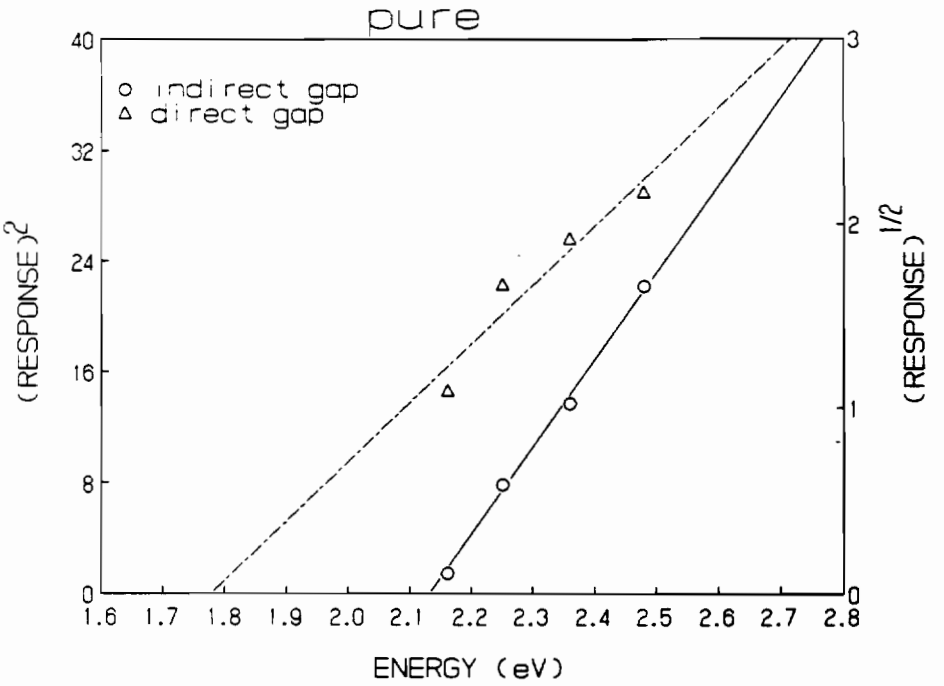

Figure 4.64. Bandgap determination from photocurrent efficiencies for a pure freeze-dried sample in 1M NaOH + 0.01M KNO_3.

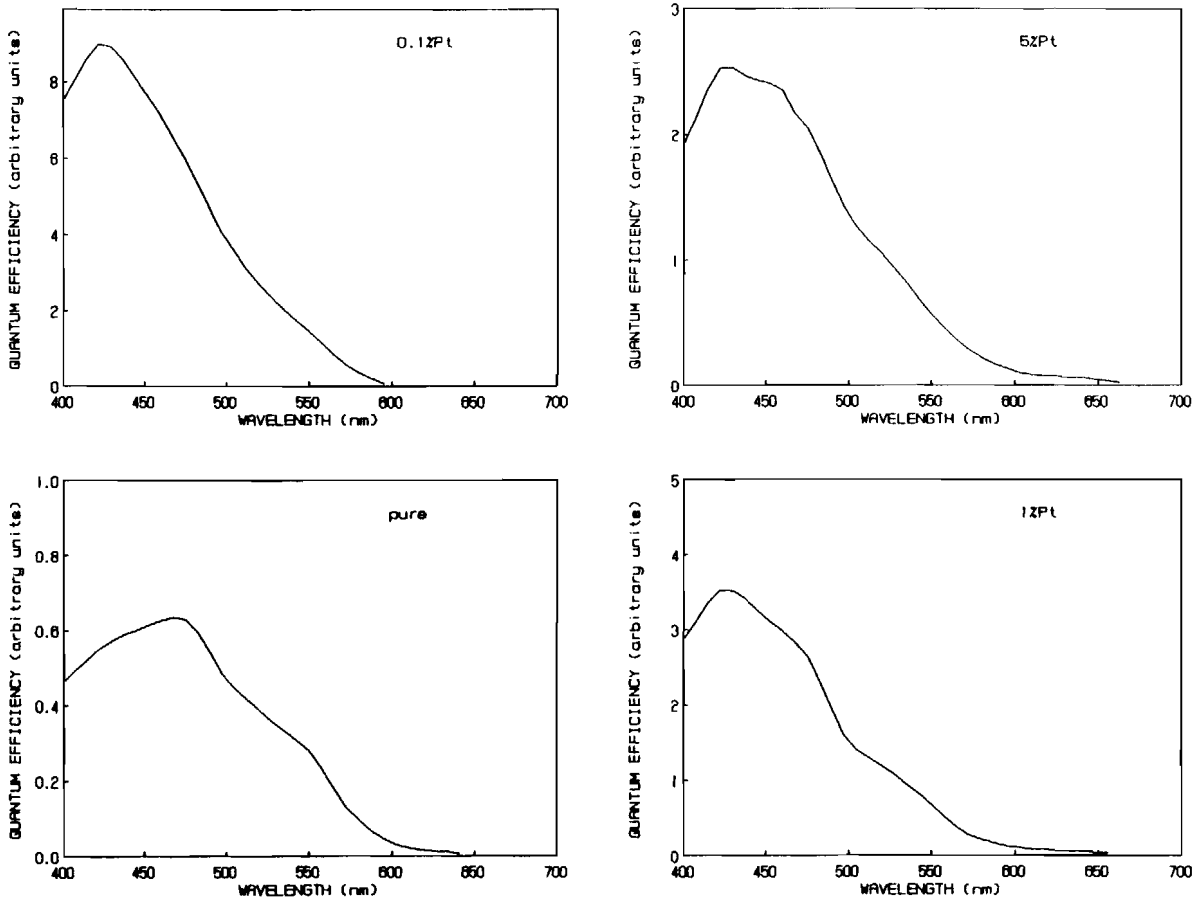

Figure 4.65. Spectral response (arbitrary units) versus wavelength of irradiated light for pure and platinized freeze-dried Fe_2O_3.

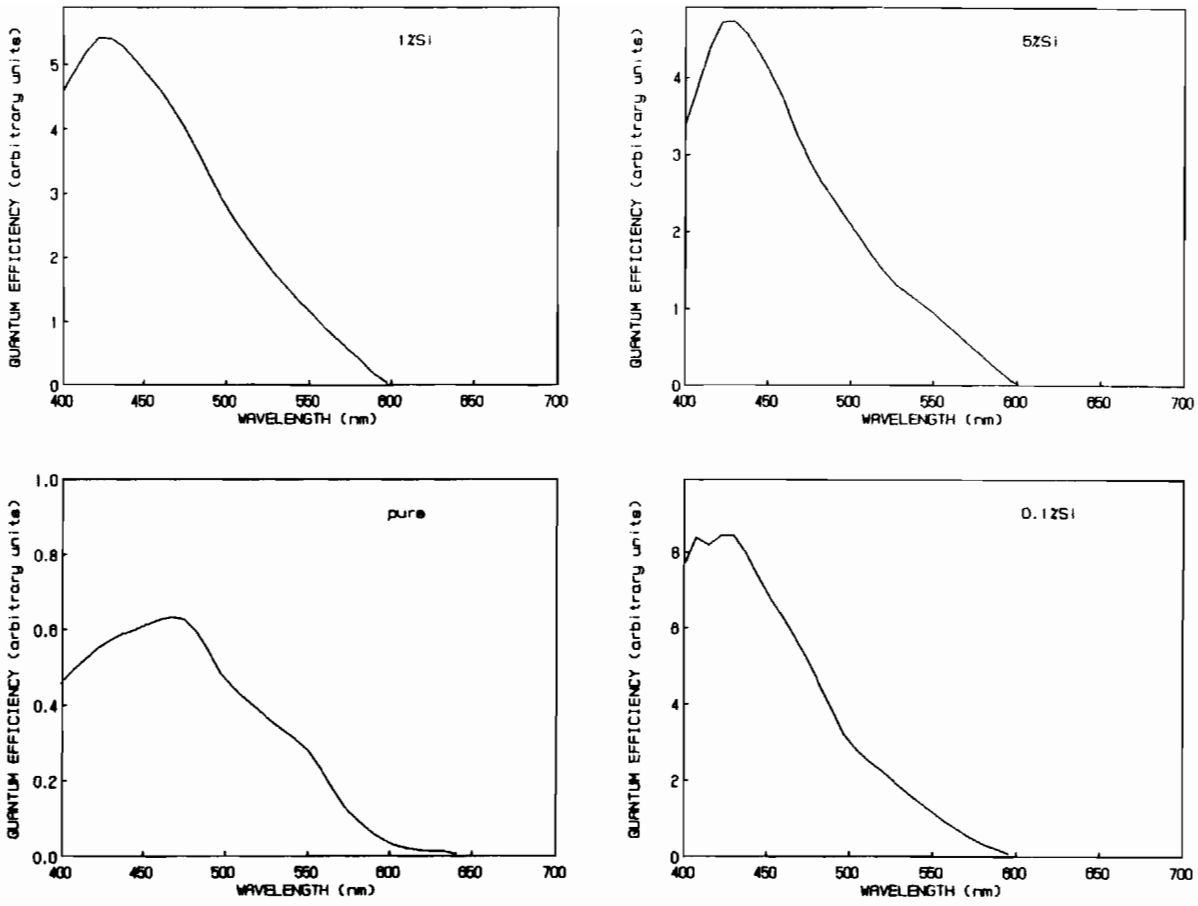

Figure 4.66. Spectral response (arbitrary units) versus wavelength of irradiated light for pure and Si-doped freeze-dried Fe_2O_3.

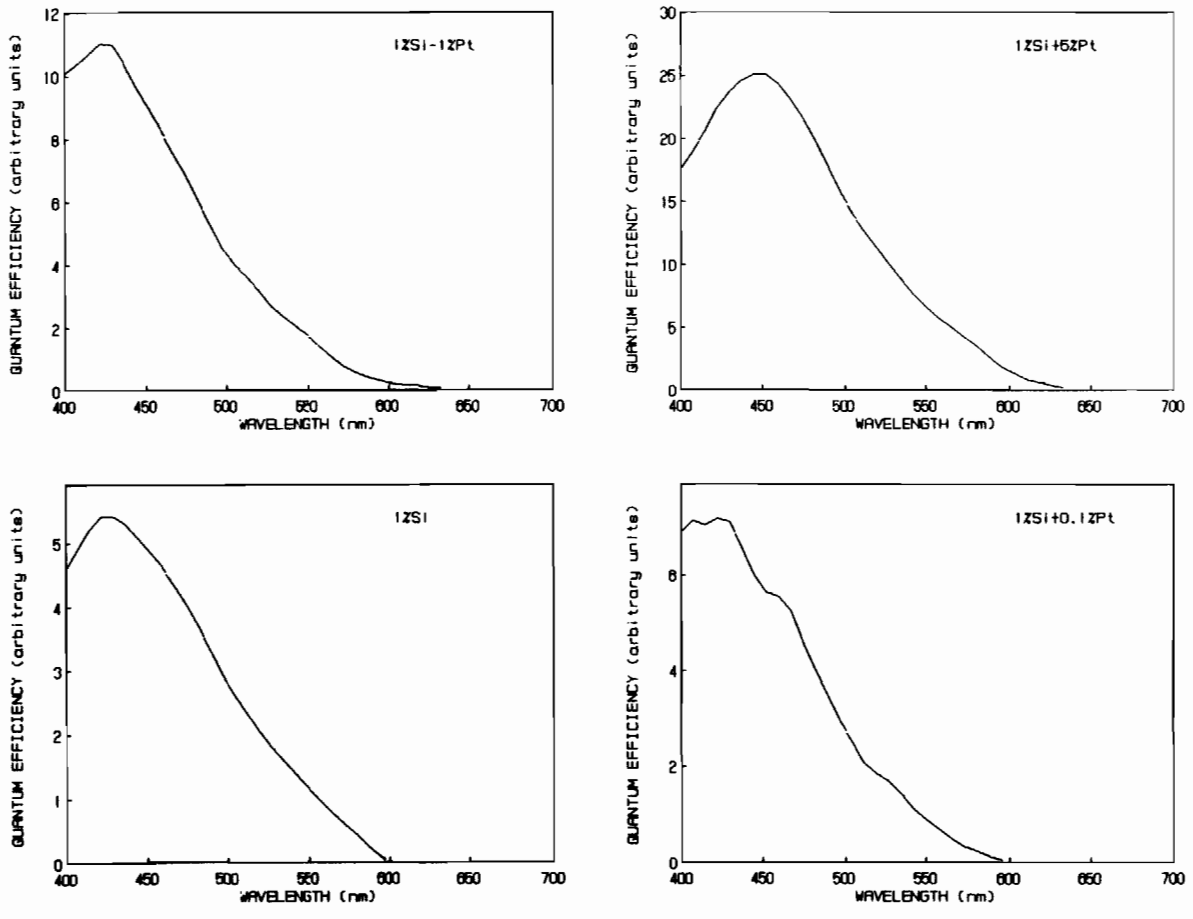

Figure 4.67. Spectral response (arbitrary units) versus wavelength of irradiated light for platinized and Si-doped freeze-dried Fe_2O_3.

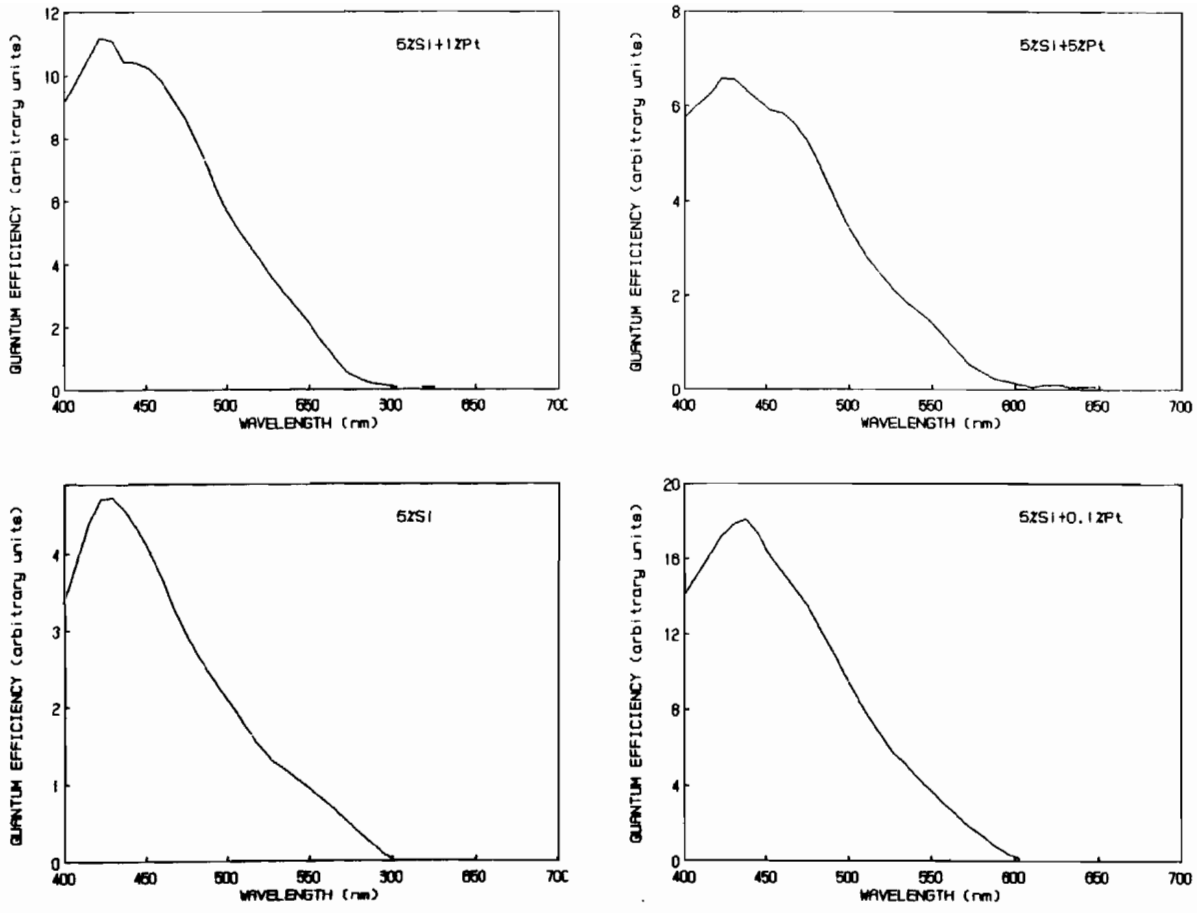

Figure 4.68. Spectral response (arbitrary units) versus wavelength of irradiated light for platinized and Si-doped freeze-dried Fe_2O_3.

observed at 0.1 at.% Pt, consistent with I-V results. With increasing Si or platinum doping level it was observed that the photoresponses were more complicated, revealing more structure. This effect is also expected due to the increased possibility of introducing deep and shallow donors into the electronic structure of these samples. This effect was seen more clearly on the photoresponse versus energy diagrams for bandgap determinations, where by plotting the response over the whole visible spectrum, different slopes were observed in samples with higher doping levels. These different slopes were attributed to different impurity levels within the bandgap of the Fe_2O_3. The same effect was also observed in capacitance studies described in the next section. The indirect and direct transitions determined from these measurements showed very little variation for the platinized and unplatinized samples. The effect of platinum on the photoactivity of the Fe_2O_3 samples was determined with the platinum deposited on the surface of the Fe_2O_3. An example of the photoresponse of 1 at.% Si doped Fe_2O_3 with about a 200Å layer of platinum on the surface is seen in Figure 4.69. The results show that the platinum on the surface decreases the spectral response of the Fe_2O_3 in visible light, thus decreasing the possible photogeneration of carriers. Consequently, a decrease in the photocurrent is observed in the current-voltage experiments. This result was expected since a continuous layer of platinum on the surface might reflect some of the incident light, thus decreasing the amount of photons available for photogeneration of carriers.

Figures 4.70-4.72 show spectral response results for the Mg-doped Fe_2O_3. Similar correlation with the photoelectrochemical experiments

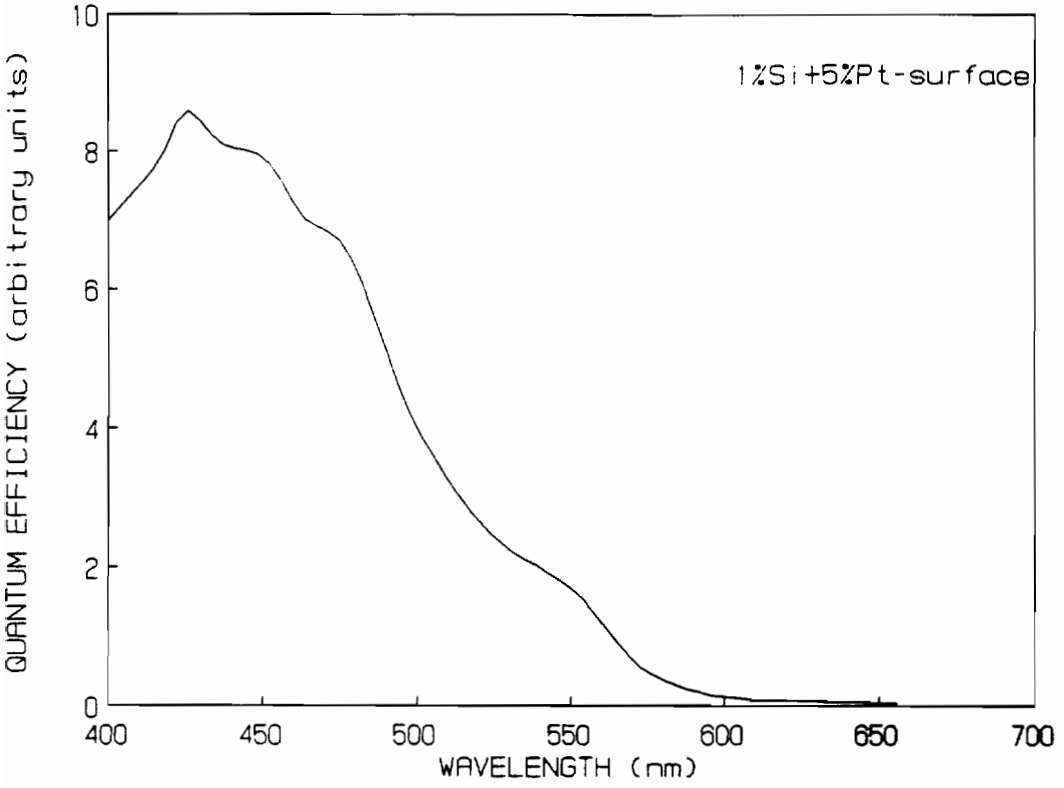

Figure 4.69. Spectral response (arbitrary units) versus wavelength of irradiated light for 1 at.% Si doped freeze-dried Fe_2O_3 with 200Å Pt layer on the surface (1M NaOH + 0.01M KNO_3).

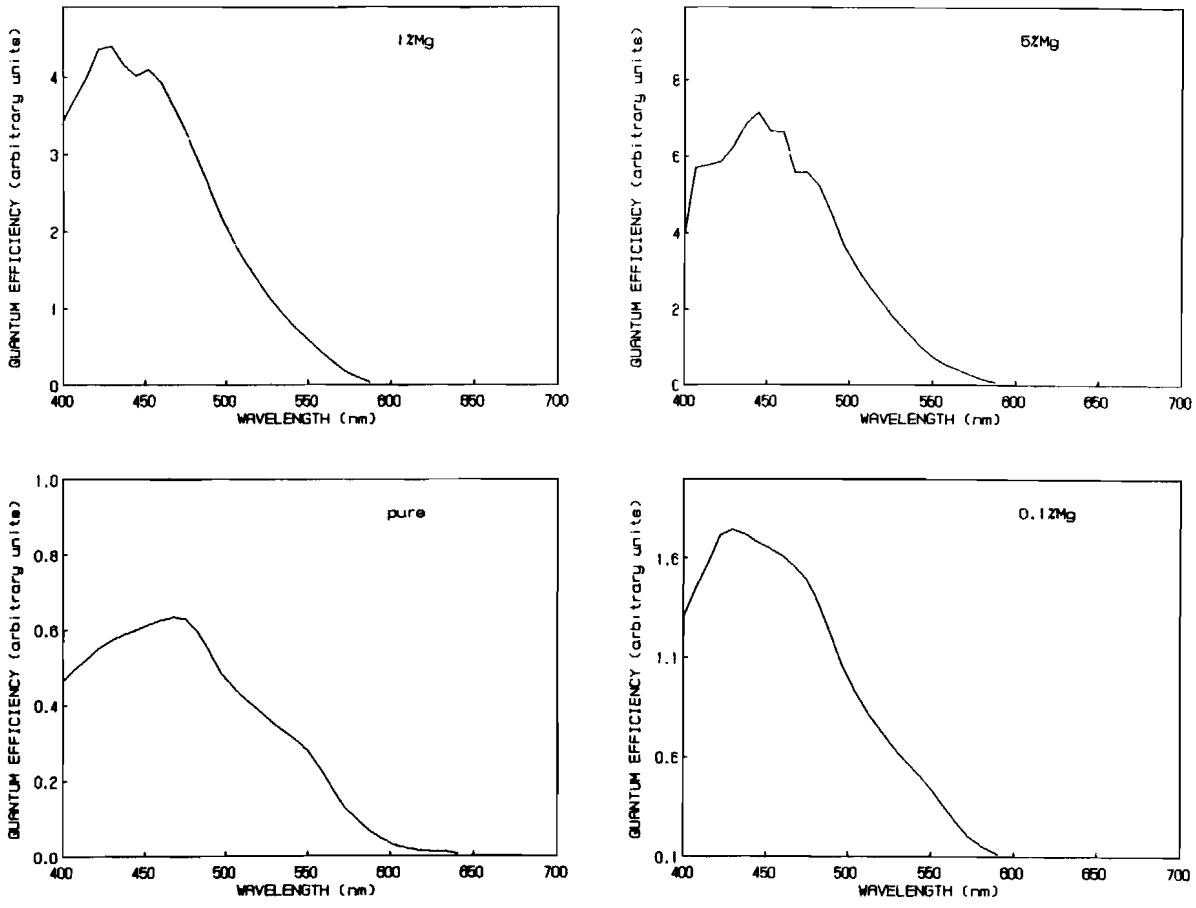

Figure 4.70. Spectral response (arbitrary units) versus wavelength of irradiated light for pure and Mg-doped freeze-dried Fe_2O_3.

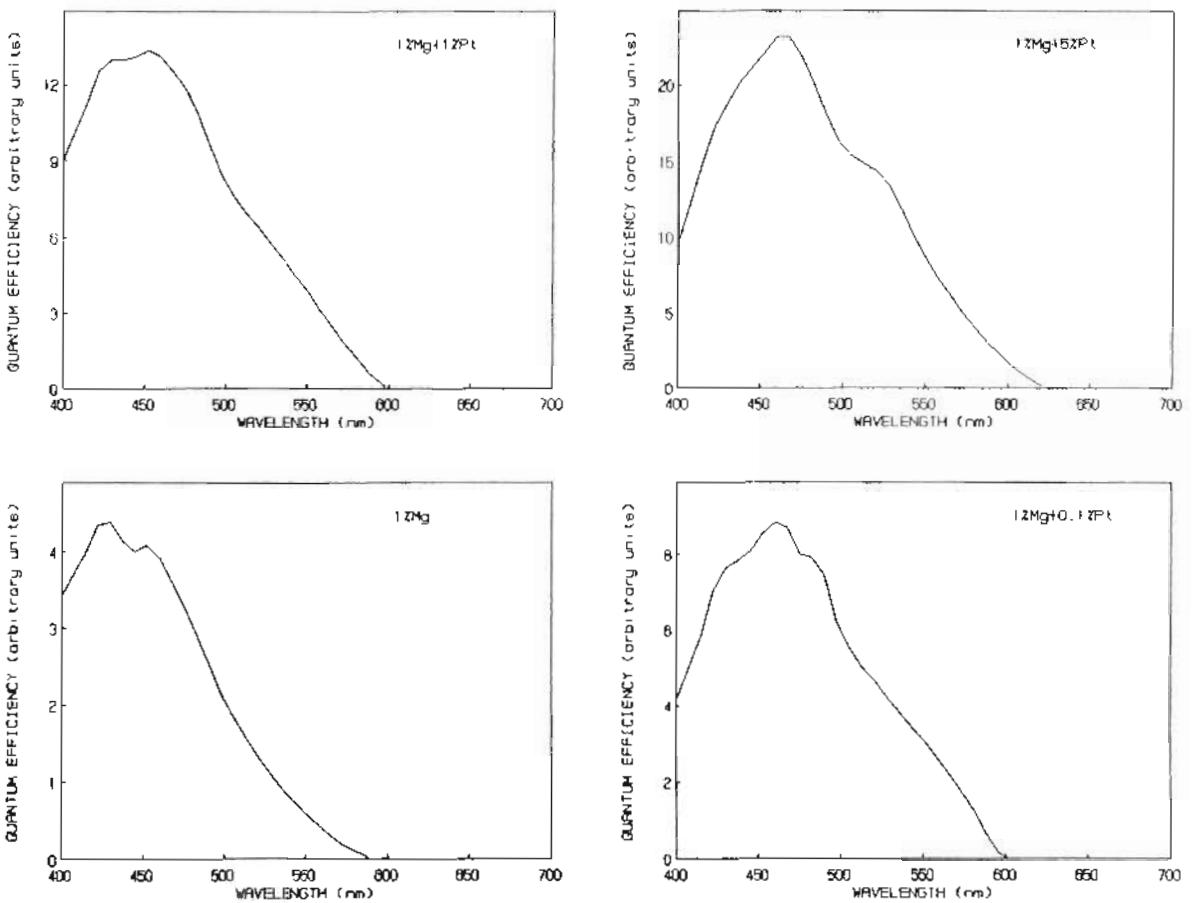

Figure 4.71. Spectral response (arbitrary units) versus wavelength of irradiated light for platinized and Mg-doped freeze-dried Fe_2O_3.

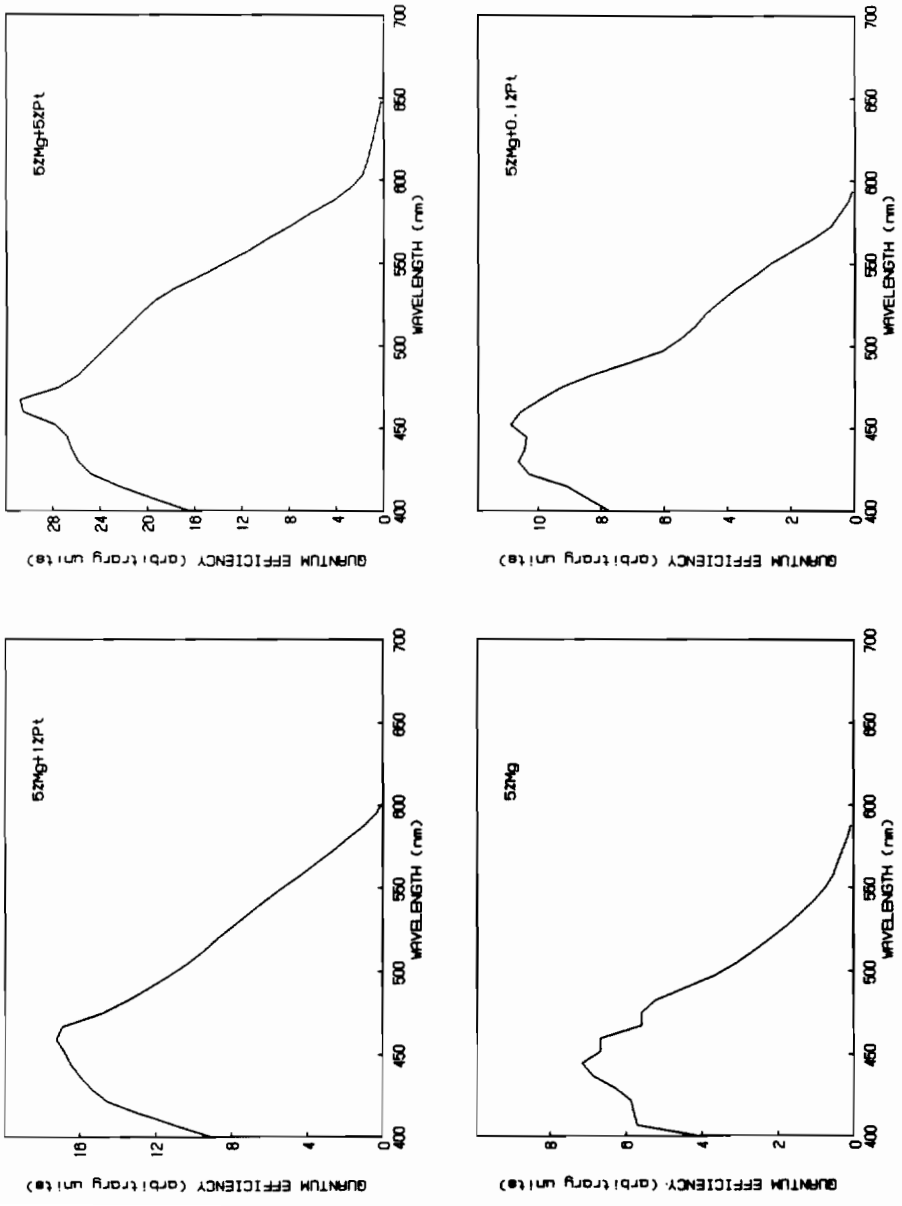

Figure 4.72. Spectral response (arbitrary units) versus wavelength of irradiated light for platinized and Mg-doped freeze-dried Fe_2O_3.

can be made, in that the photoresponse increases with increasing magnesium content. A more structured photoresponse is also observed for higher doping densities. For Fe_2O_3 a semi-empirical energy level diagram has been proposed [315]. The corresponding band structure model is characterized by a filled 2p (oxygen) band, and an empty 4s (iron) band separated by an energy gap of 5 to 6 eV in which more or less localized 3d (iron) bands are present. The optical absorption spectrum of α-Fe_2O_3 reveals an important electronic transition around 2.2 eV. It has been established that this transition represents a charge-transfer between adjacent, octahedral Fe^{3+} ions according to

$$Fe_{Fe} + Fe_{Fe} \rightarrow Fe'_{Fe} + Fe^{\cdot}_{Fe} \qquad (4.6)$$

Another charge-transfer process

$$O_O + Fe_{Fe} \rightarrow O^{\cdot}_O + Fe'_{Fe} \qquad (4.7)$$

is assumed to require an energy exceeding 3.5 eV, and may account for the photocurrent spectra in the ultraviolet region.

4.6 Capacitance studies and flat-band potentials for Fe_2O_3

The flat-band potential is the electrode potential at which the semiconductor bands are flat. This quantity is a measure of the potential which must be applied to the semiconductor, relative to a reference electrode, such that the bands remain flat as one approaches the interface. The flat-band potential also determines the relative

Fermi levels of the semiconductor and electrolyte, and amount of band bending at the interface. The flat-band potential (V_{fb}) for semiconductor photoelectrodes can be determined by several different techniques: (1) Mott-Schottky capacitance method; (2) photocurrent/potential method; and (3) onset of the photocurrent method. All of these methods were used in this investigation to determine the flat-band potentials of the Fe_2O_3 photoelectrodes. The photocurrent/potential method is based on the measurement of the photocurrent as a function of an applied potential, where the intercept of the photocurrent, I^2, versus applied voltage, V, plot yields a flat-band potential. The constraints on this method are that the optical absorption and the hole diffusion lengths be such that their product be much less than unity. This case is certainly valid for Fe_2O_3. This method relies on the assumption that the charged carriers will be distributed uniformly throughout the sample. If this assumption is not valid, then this method should not be expected to yield a linear (I^2 vs V) plot. This technique is not affected by surface states or adsorbed species and, therefore may be better than the capacitance technique for determining the flat-band potentials. The flat-band potential can also be determined from the photocurrent onset potential V_{on}. The V_{fb} and V_{on} may not be identical for the same electrode if the surface region is depleted of donors or if the recombination is occurring near the surface. In the case of near-surface recombination, V_{fb} and V_{on} determined from current-voltage plots are in agreement, but the actual onset of the photocurrent is at more positive or negative potentials for an n-type or a p-type semiconductor, respectively. Ideally, the

photocurrent onset of an n-type photoanode should occur at a potential near its flat-band potential. In practice, however, the onset and subsequent rise of photocurrents occur at potentials positive of the flat-band potential which is ascribed to surface recombination of electrons and holes. Therefore, the energetics for the hydrogen evolution at the counter electrode must be favorable and the kinetics of oxygen evolution at the photoanode should be fast as well. Figure 4.73 shows a result of the photocurrent-voltage method for the flat-band determination for a pure freeze-dried Fe_2O_3. By extrapolating the linear portion of the data, the flat-band potential of -0.15 V vs SCE was determined. The capacitance of the electrode is related to electrode potential by the Mott-Schottky relation

$$1/C_{sc}^2 = 2/q\epsilon\epsilon_o N_d(V - V_{fb} - kT/q) \qquad (4.8)$$

where C_{sc} is the capacitance per unit area of the space charge region, ϵ is the dielectric constant, ϵ_o is the permitivity in a vacuum, q is the charge of the electron, N_d is the carrier density, V is the electrode bias, and V_{fb} is the flat-band potential. The slope from a plot of $1/C_{sc}^2$ vs V is given by

$$d(1/C^2)/dV = 2/\epsilon\epsilon_o q N_d \qquad (4.9)$$

From this equation the carrier density can be determined. The flat-band potential was obtained by subtracting the quantity kT/q (=0.0259 V) from the intercept of the voltage axis by the Mott-Schottky plot.

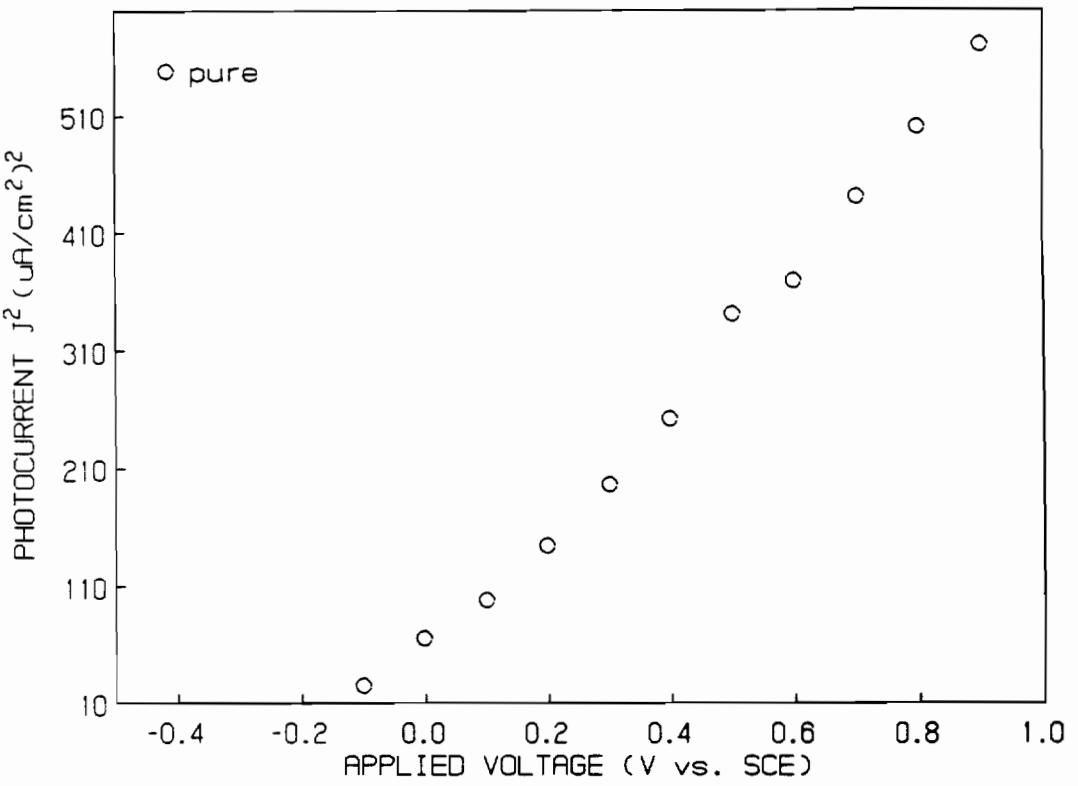

Figure 4.73. The square of the photocurrent versus applied potential for a pure freeze-dried Fe_2O_3 (1M NaOH + 0.01M KNO_3, pH = 13.5).

Figure 4.74 shows the Mott-Schottky plot for pure freeze-dried Fe_2O_3. The flat-band potential was -0.2 V vs SCE as determined from the intercept in Figure 4.74. This value agrees well with the literature. Figures 4.75-4.80 show the square of the photocurrent versus voltage relationships for the Si and Mg doped Fe_2O_3. Results for the platinized samples are also reported in these figures. Figures 4.81-4.84 show the Mott-Schottky plots for the same samples. Flat-band potentials were determined from these results. Carrier concentration of donors and acceptors were also calculated from these results as well as the position of the Fermi energy in the Fe_2O_3 samples. As can be seen from these figures the flat-band potentials determined from the two techniques were generally in agreement with the theory. The values of the flat-band potential determined from the Mott-Schottky plots were usually more negative (0.1-0.2 V vs SCE) for n-type Fe_2O_3 or more positive for the p-type Fe_2O_3 than the values determined from the photocurrent-voltage relationship. This was expected as discussed previously. The data in the Mott-Schottky plots for the doped and platinized samples show usually two distinct slopes. Such a break in the line is seen for example in Figure 4.81 for the platinum doped freeze-dried Fe_2O_3. The two slopes were attributed to two different donor levels in the energy gap. One level is a shallow donor level located just bellow the conduction band and the other is a deep donor level located deeper in the energy gap. No break in the Mott-Schottky plot is observed for the pure Fe_2O_3. The carrier concentration for the pure sample was calculated to be 1.9×10^{17} cm^{-3}. The carrier concentrations calculated for the Si doped samples were higher with increased Si

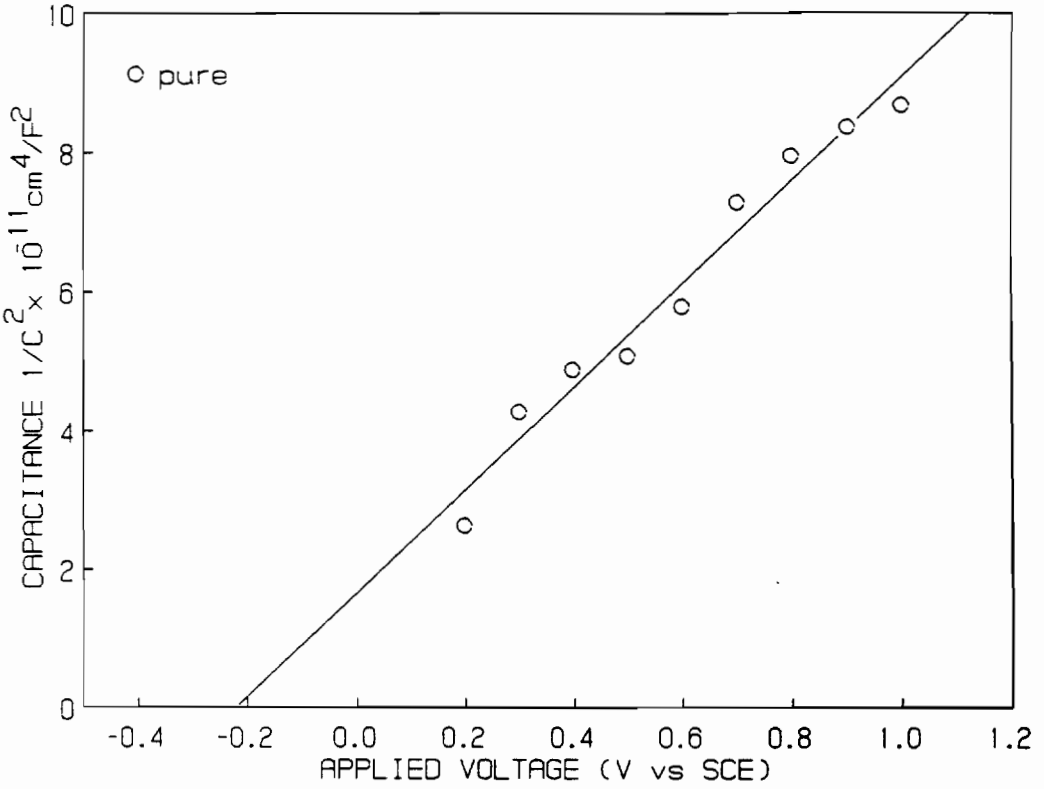

Figure 4.74. Mott-Schottky plot for a pure freeze-dried Fe_2O_3 (1M NaOH + 0.01M KNO_3, pH = 13.5).

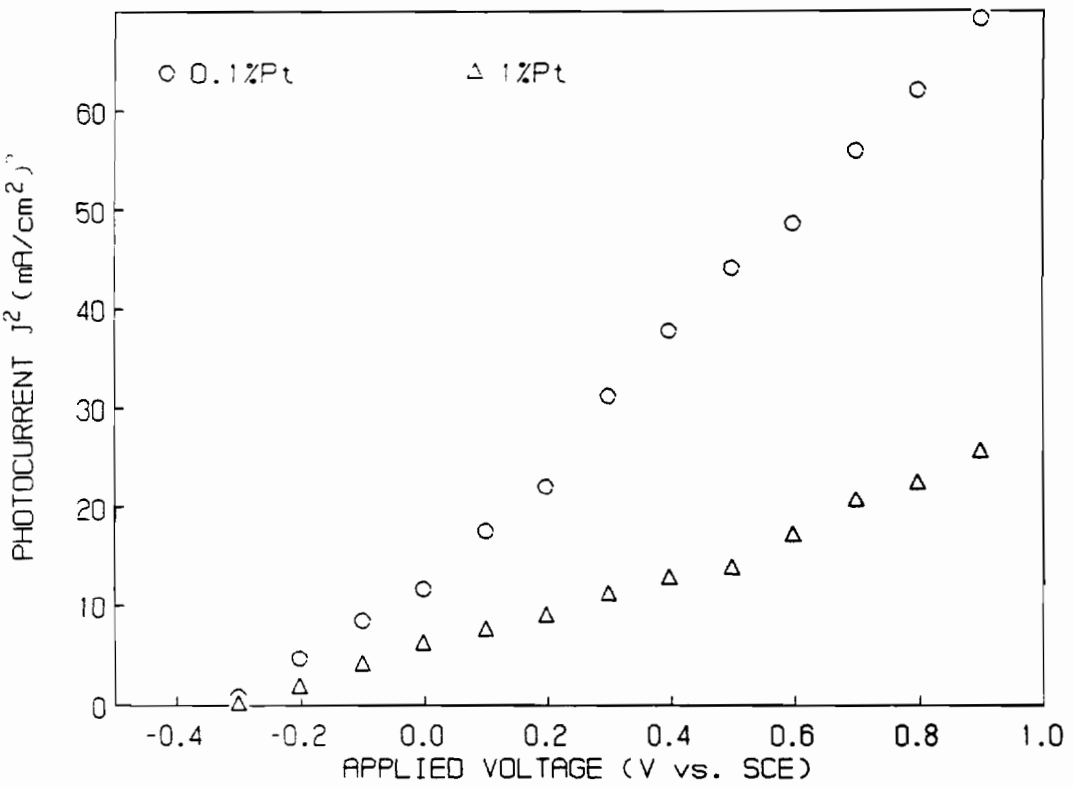

Figure 4.75. The square of the photocurrent versus applied potential for a Pt doped freeze-dried Fe_2O_3 (1M NaOH + 0.01M KNO_3, pH = 13.5).

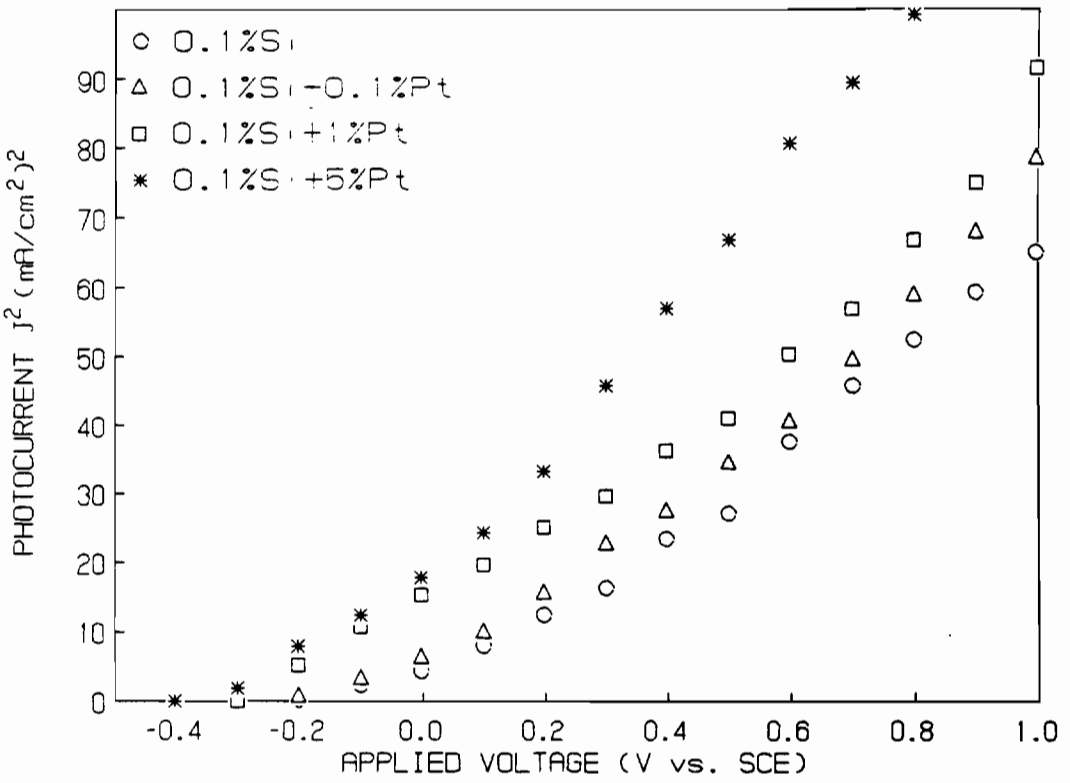

Figure 4.76. The square of the photocurrent versus applied potential for the platinized 0.1 at.% Si doped freeze-dried Fe_2O_3 (1M NaOH + 0.01M KNO_3, pH = 13.5).

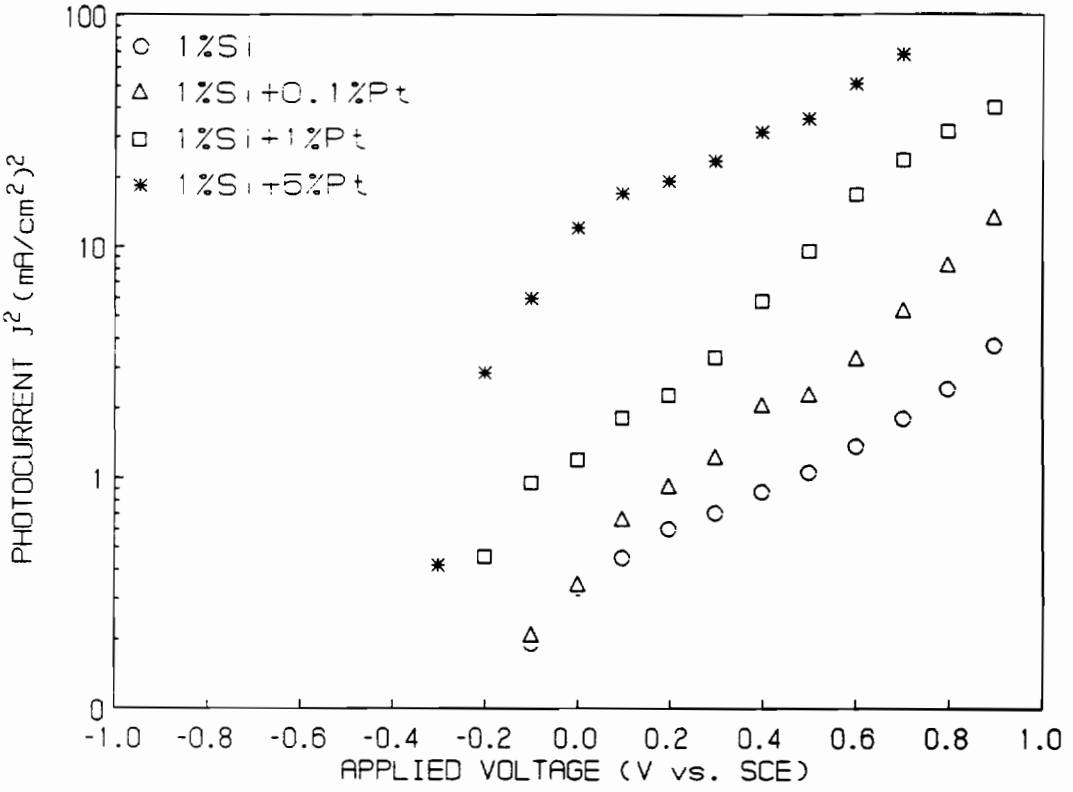

Figure 4.77. The square of the photocurrent versus applied potential for the platinized 1 at.% Si doped freeze-dried Fe_2O_3 (1M NaOH + 0.01M KNO_3, pH = 13.5).

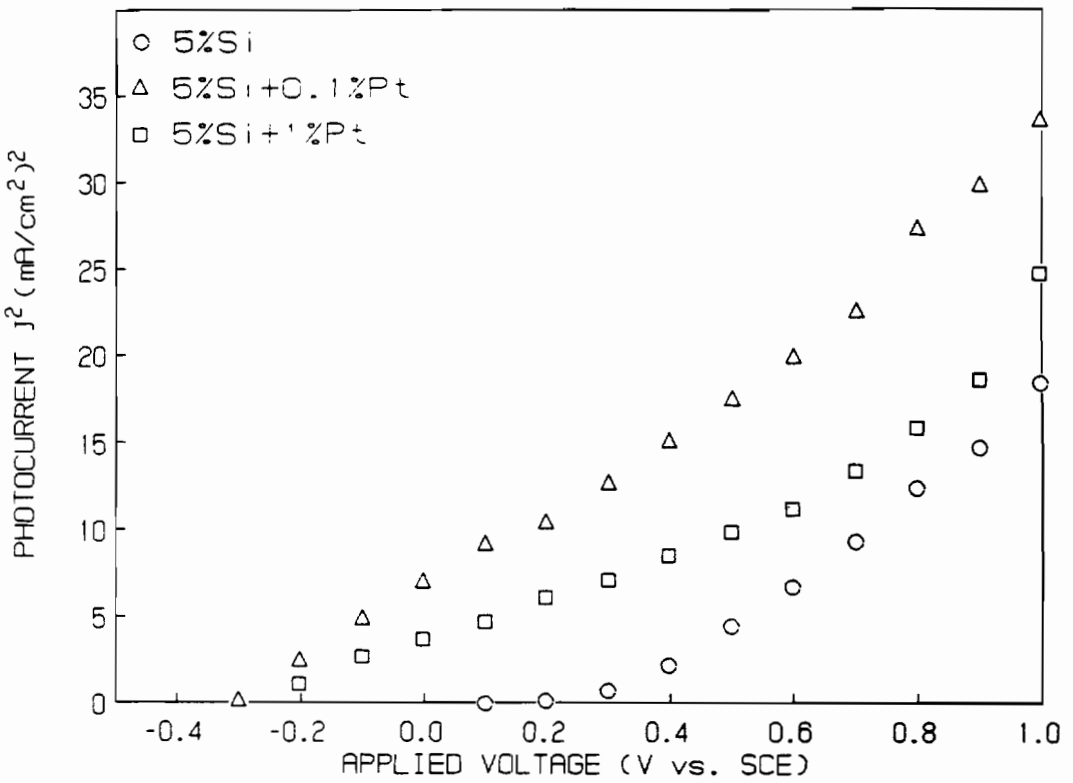

Figure 4.78. The square of the photocurrent versus applied potential for the platinized 5 at.% Si doped freeze-dried Fe_2O_3 (1M NaOH + 0.01M KNO_3, pH = 13.5).

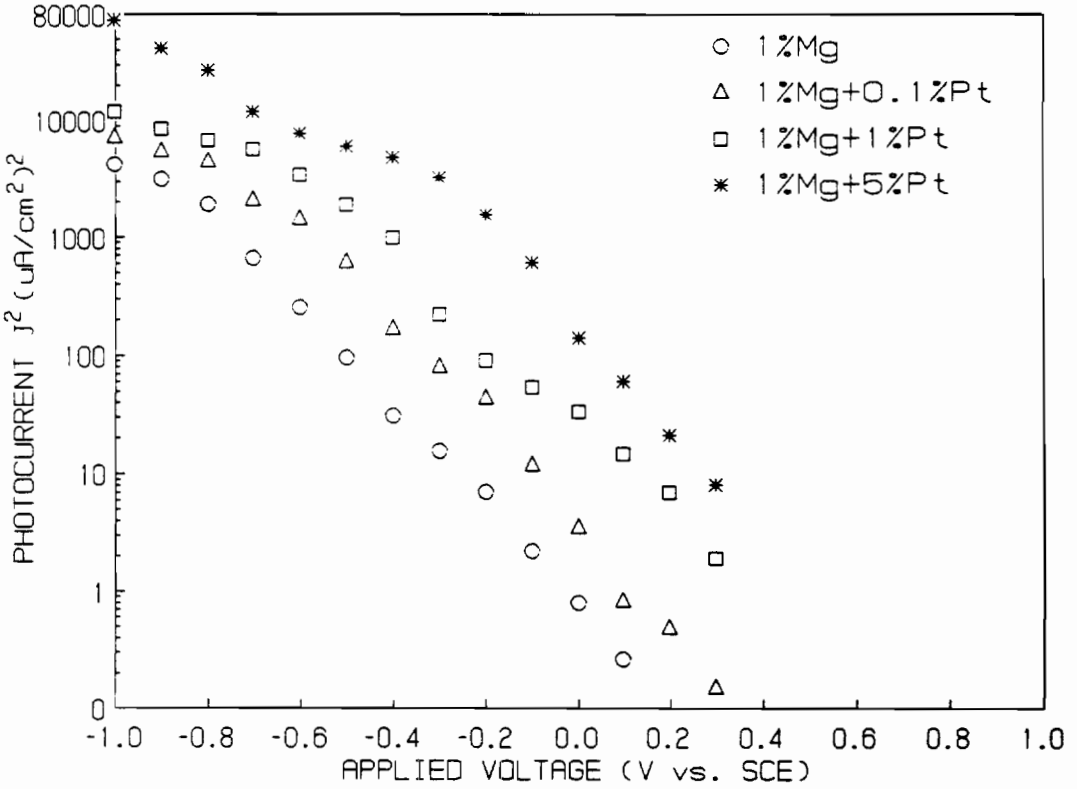

Figure 4.79. The square of the photocurrent versus applied potential for the platinized 1 at.% Mg doped freeze-dried Fe_2O_3 (1M NaOH + 0.01M KNO_3, pH = 13.5).

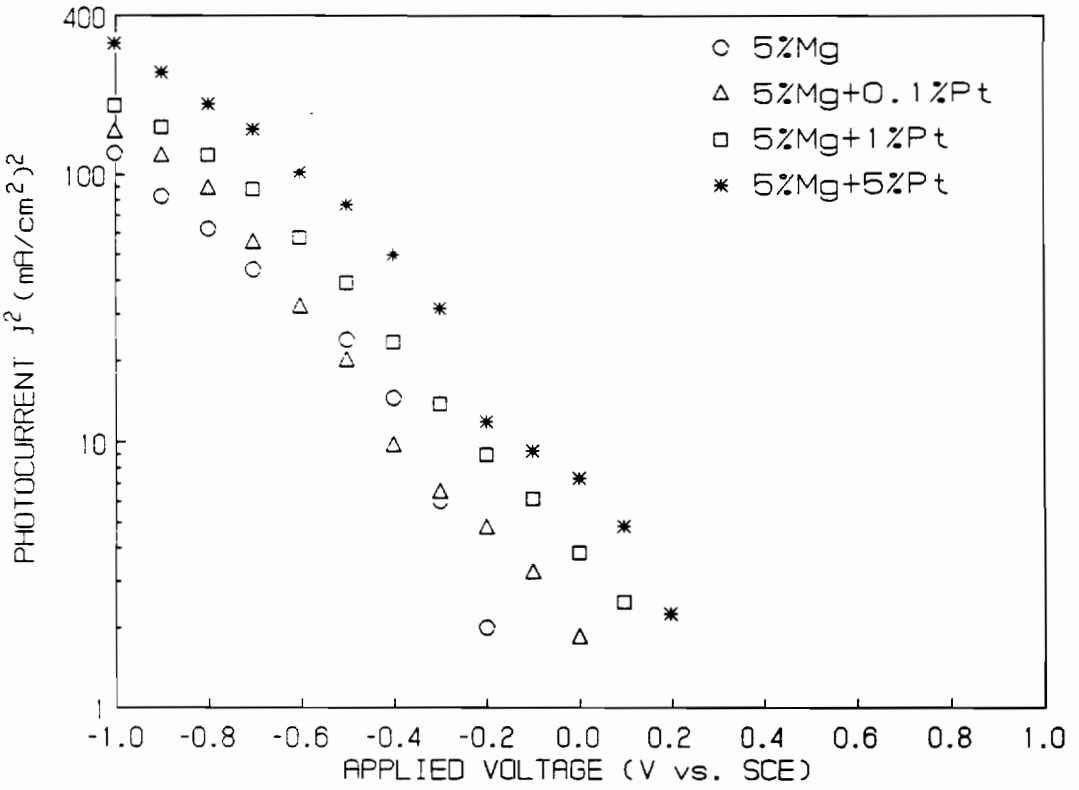

Figure 4.80. The square of the photocurrent versus applied potential for the platinized 5 at.% Mg doped freeze-dried Fe_2O_3 (1M NaOH + 0.01M KNO_3, pH = 13.5).

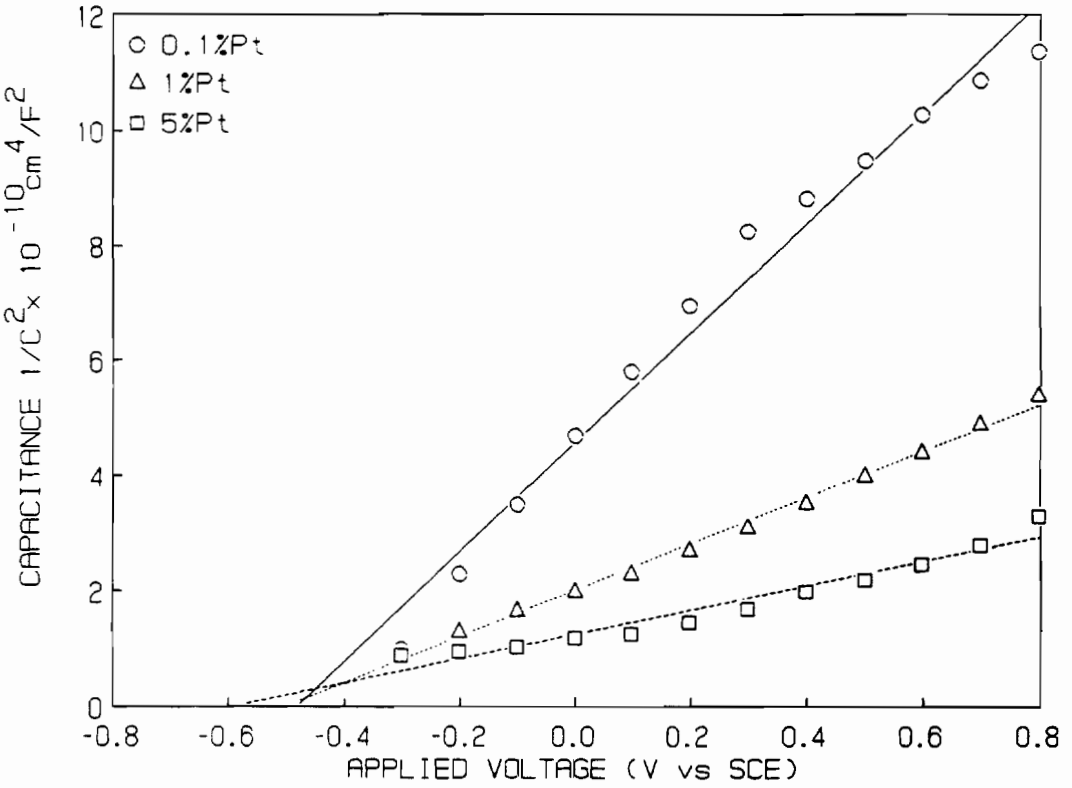

Figure 4.81. Mott-Schottky plots for platinum doped freeze-dried Fe_2O_3 (1M NaOH + 0.01M KNO_3, pH = 13.5).

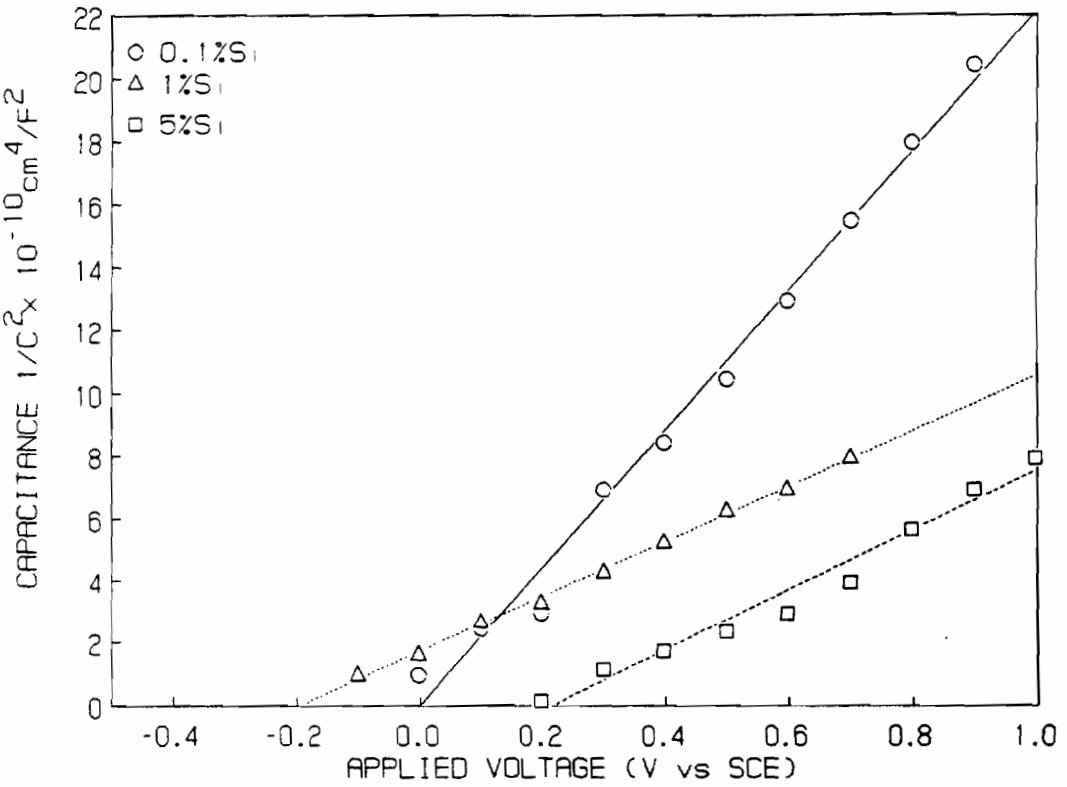

Figure 4.82. Mott-Schottky plots for silicon doped freeze-dried Fe_2O_3 (1M NaOH + 0.01M KNO_3, pH = 13.5).

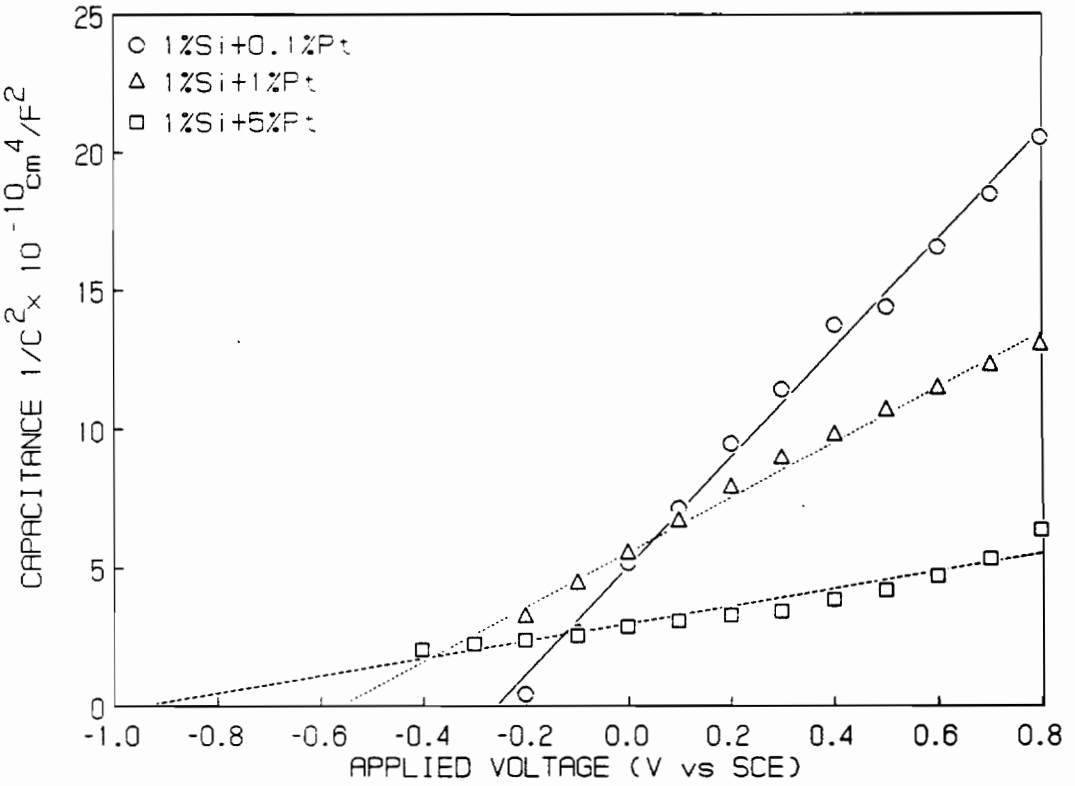

Figure 4.83. Mott-Schottky plots for platinized 1 at.% Si doped freeze-dried Fe_2O_3 (1M NaOH + 0.01M KNO_3, pH = 13.5).

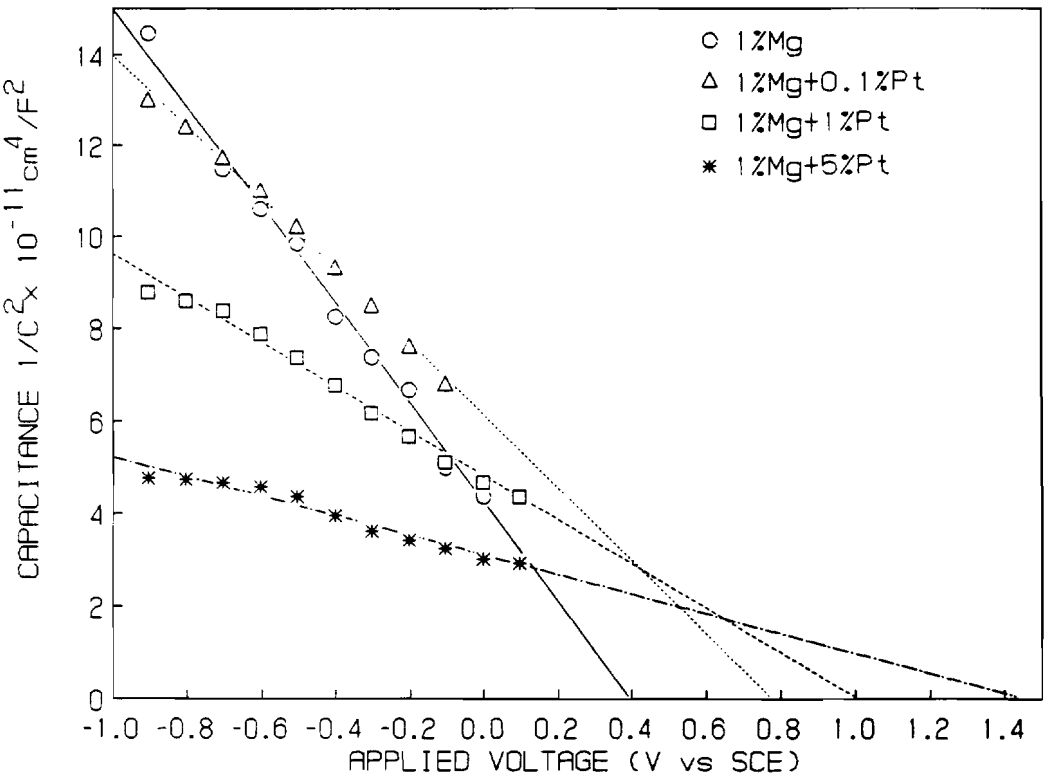

Figure 4.84. Mott-Schottky plots for platinized 1 at.% Mg doped freeze-dried Fe_2O_3 (1M NaOH + 0.01M KNO_3, pH = 13.5).

level in the sample. The donor concentration for the 1 at.% Si doped sample was calculated to be 1.66×10^{18} cm^{-3}. For heavily doped semiconductors such as these iron oxides, the flat-band is nearly coincident with the band carrying the majority carriers. Thus, for the n-type electrode, the measured flatband potential corresponds to the conduction band edge, and for the p-type electrode, the flatband corresponds to the valence band edge. Information on the flatband potentials can then be used to generate an energy level diagram as shown in Figure 4.85. The Fermi level was determined by connecting the assembly through a voltmeter to a reference electrode. The band gap determined from the photocurrent efficiency experiments was used to calculate the respective band edges. The shallow donor level for the Si doped freeze-dried sample was calculated to be about 0.29 V below the conduction band. The deep donor level for the same sample was about 0.62 V below the conduction band. These results were determined from the two slopes observed in the Mott-Schottky plots. In the Mott-Schottky figures only a single line was fitted through the points to extrapolate the flatband potential, but in reality the data actually show two slopes. It should also be noticed in these Mott-Schottky plots that the data for the two slopes deviate very slightly from the straight line as opposed to the solid state doped samples where the points were scattered extensively. This proves again the homogeneous nature of the freeze-dried samples in comparison to the solid state doped samples. The scatter of the experimental points in the capacitance measurements is a good indication of the dopant homogeneity. The non-linearity in the experimental data can be also seen in the results

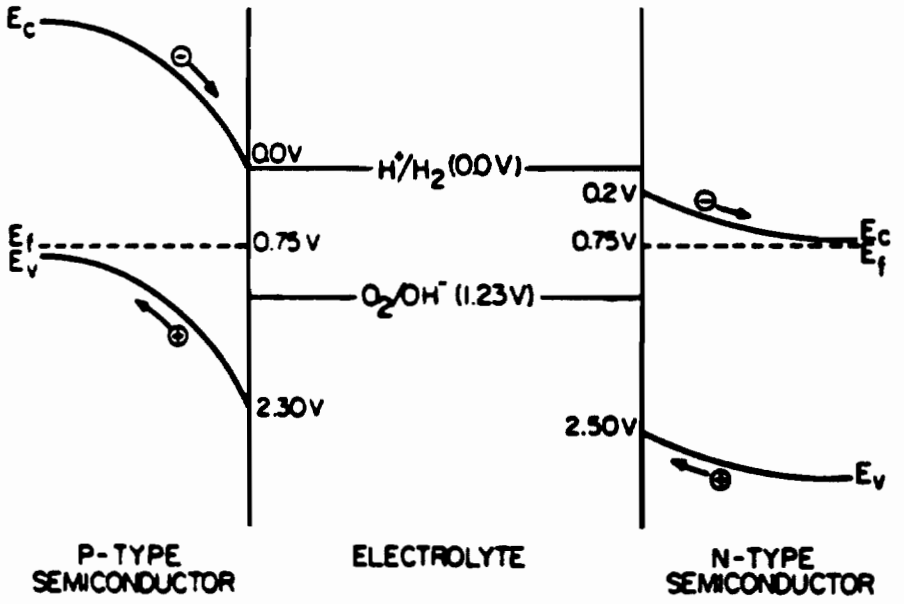

Figure 4.85. Energy level diagram showing band edge locations of doped Fe_2O_3 electrodes relative to hydrogen/oxygen redox couples (V values are normalized versus regular hydrogen electrode).

of the photocurrent-voltage relationships where the two slopes are also apparent. The Mott-Schottky plots for the platinized Fe_2O_3 reveal similar behavior to the Si doped samples except the donor levels are positioned at shallower levels than silicon. These results confirm the conclusions from the photoelectrochemical measurements that one of the roles of platinum in the Fe_2O_3 is that it acts as a donor in the Si doped Fe_2O_3. The carrier concentration in the platinized samples increased with increasing platinum content in the samples which proves this conclusion. The donor concentration increased to 9.4×10^{18} cm^{-3} for the 5 at.% of platinum. The platinum donor level is calculated to be positioned from 0.26 V (for the 0.1 at.% Pt) to 0.22 V (for the 5 at.% Pt) below the conduction band edge. The depletion layer width was also calculated from these measurements and it was on the order of 6×10^{-6} cm. The depletion layer width decreased with increased doping as expected from the theory. The flatband potential was also shifted in the negative direction for the platinized samples as can be observed from the figures which is again quite typical of the increase in the carrier concentration (donors) in the samples. Having obtained the energy band diagram for the p/n Fe_2O_3 assembly we can explain the observed hydrogen and oxygen evolution from the illuminated hetero-junction. Upon illumination in solution, electron-hole pairs are photogenerated in both the n-type and p-type Fe_2O_3. In the p-type electrode, electrons are driven through the depletion region towards the interface where they convert hydronium ions in solution to hydrogen gas. Vacancies driven to the n-type interface convert hydroxyl species to oxygen gas. In both electrodes, the majority carriers migrate away

from the surface to produce photocurrents. Doping the Fe_2O_3 electrode with Mg and Pt has shifted the p-type band edges cathodically thus making the hydrogen evolution thermodynamically feasible.

4.7 Cyclic voltammetry experiments of doped and platinized Fe_2O_3

Cyclic voltammetry experiments were performed in the PEC cell under potentiodynamic conditions to determine stability of the Fe_2O_3 electrodes in a basic environment. To approach a steady state current and minimize the charging current, slow scan rates were used, typically 5-10 mV/second. The undoped commercial Fe_2O_3 did not show any significant photoactivity in the cyclic voltammograms. It exhibited large charging currents due high sample resistance and sluggish charge transfer kinetics that are amplified in the potentiodynamic experiments. Figures 4.86 and 4.87 show a cyclic voltammogram for 0.1 at.% Pt doped freeze-dried Fe_2O_3 in the dark and under illumination with visible light, respectively. The scan in the positive direction shows a very negligible dark current. Upon revering the scan in the negative direction the large cathodic peak observed at a potential negative of -1.2 V vs SCE is due to hydrogen evolution which is thermodynamically possible at these potentials in basic solution. The Fe^{3+}/Fe^{2+} redox couple peaks are also visible in the voltammograms. When the sample was illuminated, the large anodic peak due to oxygen evolution appeared starting at +0.1 V vs SCE. The cathodic hydrogen evolution peak was also larger. These results are very consistent with the potentiostatic photoelectrochemical experiments discussed in section 4.3. The Fe^{3+}/Fe^{2+} redox couple peaks were only slightly larger suggesting small

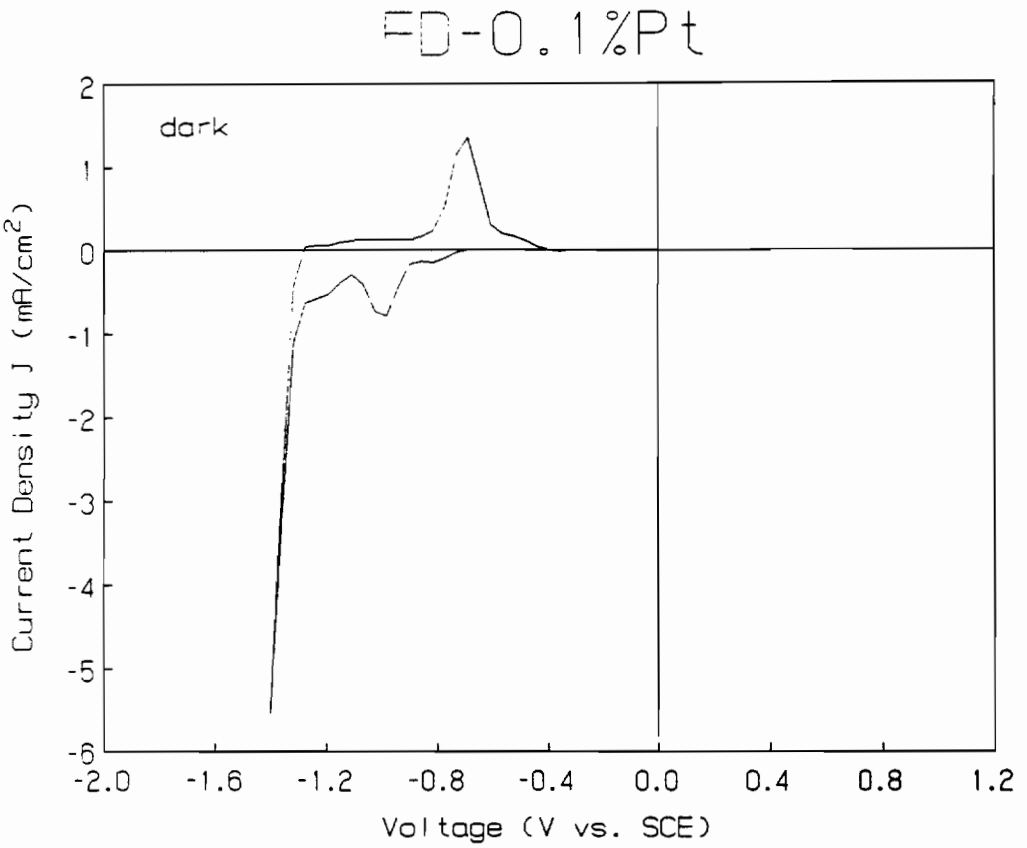

Figure 4.86. Cyclic voltammogram of the 0.1 at.% Pt doped freeze-dried Fe_2O_3 in the dark (1M NaOH + 0.01M KNO_3, pH = 13.5).

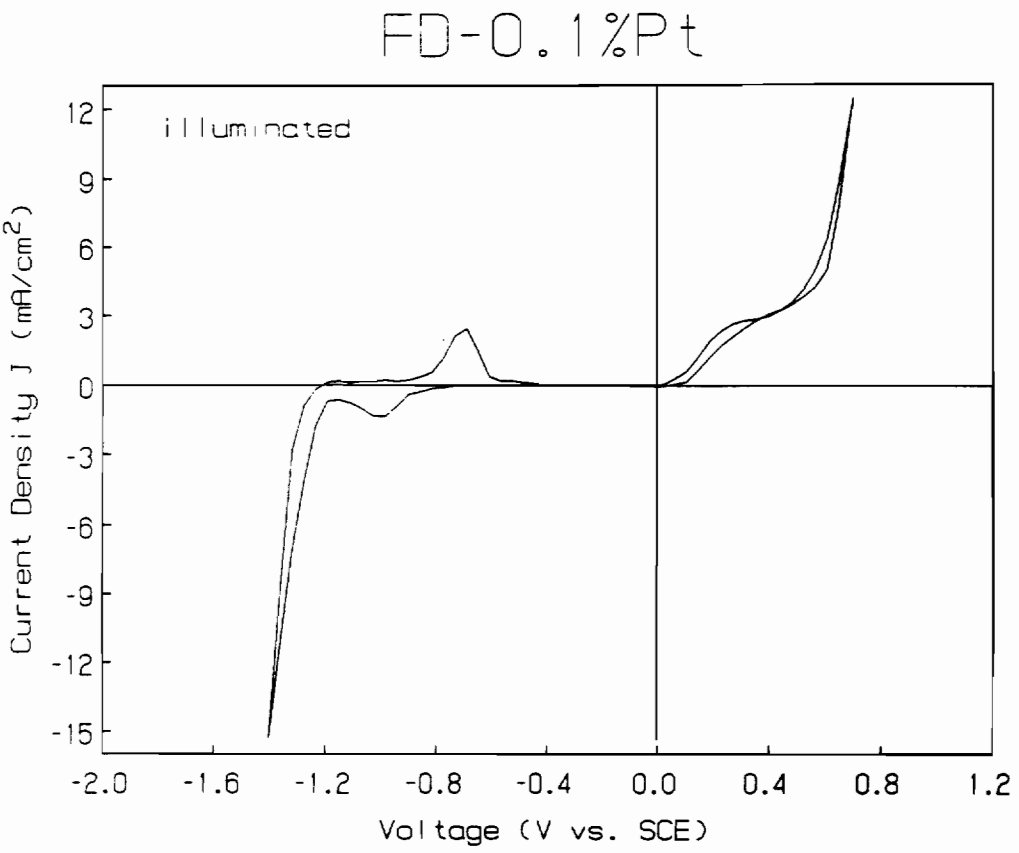

Figure 4.87. Cyclic voltammogram of the 0.1 at.% Pt doped freeze-dried Fe_2O_3 under illumination (1M NaOH + 0.01M KNO_3, pH=13.5).

photocorrosion under strong illumination. The photocorrosion in these samples was determined spectrophotometrically after the cyclic voltammetry experiments to determine the amount of dissolved iron present in the electrolyte after these experiments. It was determined that the corrosion rates were almost negligible unless the samples were held for a long time at extreme positive or negative potential under which the electrodes undergo anodic or cathodic dissolution. Figures 4.88-4.91 show cyclic voltammograms of 1 at.% Si doped freeze-dried samples with increasing amounts of platinum. We can observe the increased anodic current peak due to an increase in the oxygen evolution. The hydrogen evolution rates also increased with the increased platinum content which supports the conclusion from earlier experiments that the Pt may also act as a cathode in the n-type sample thus aiding in the hydrogen evolution. With the increased oxygen and hydrogen evolution rate, the corrosion rates increased only negligibly. Figures 4.92 and 4.93 show the results for the 5 at.% Mg doped Fe_2O_3 with 0.1 at.% Pt in the dark and under illumination, respectively. In this p-type cathode there is no anodic current observed as was also observed in the photoelectrochemical experiments. The large cathodic peak occurring at -1.0 V vs SCE is due to hydrogen evolution. The large anodic peak observed at -0.6-0.5 V vs SCE is just the reduction current from the reduction of absorbed hydrogen on the surface of the Fe_2O_3 during the cathodic scan. The hydrogen production and cathodic current increased with illumination. The cyclic voltammetry experiments complimented our earlier photoelectrochemical results. They showed that the Fe_2O_3 photoanodes and photocathodes are very stable in the basic solutions and can

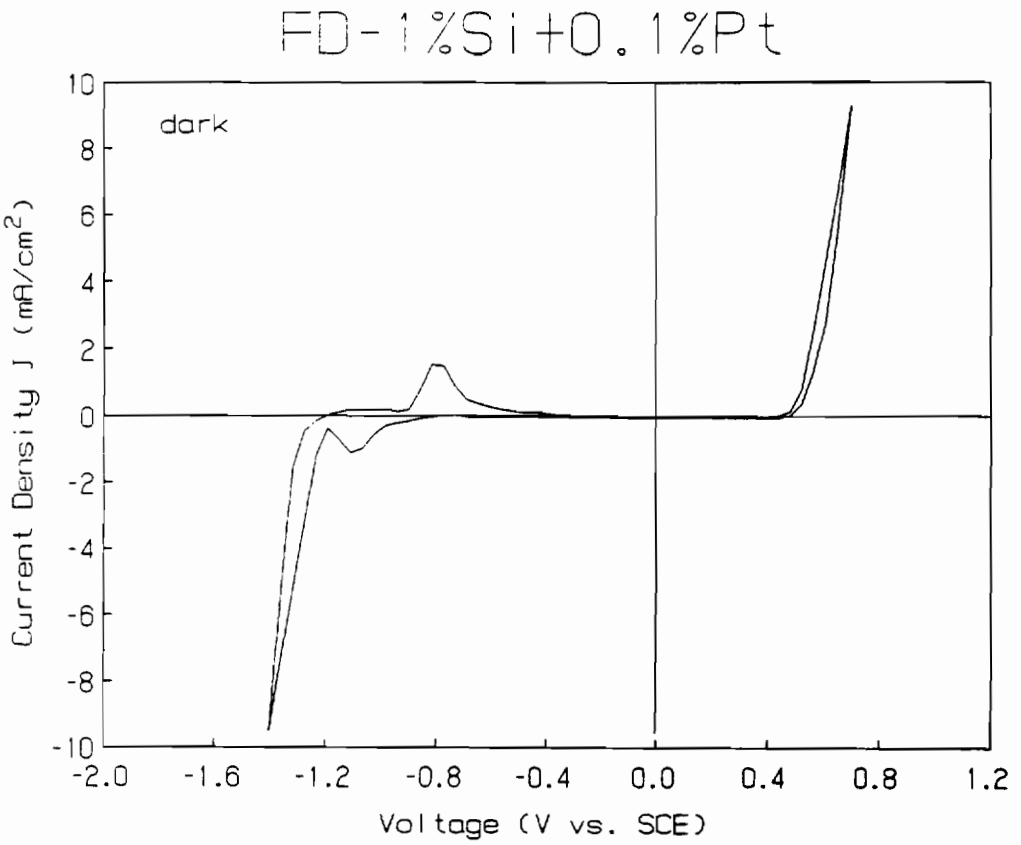

Figure 4.88. Cyclic voltammogram of the 1 at.% Si + 0.1 at.% Pt doped freeze-dried Fe_2O_3 in the dark (1M NaOH + 0.01M KNO_3, pH=13.5).

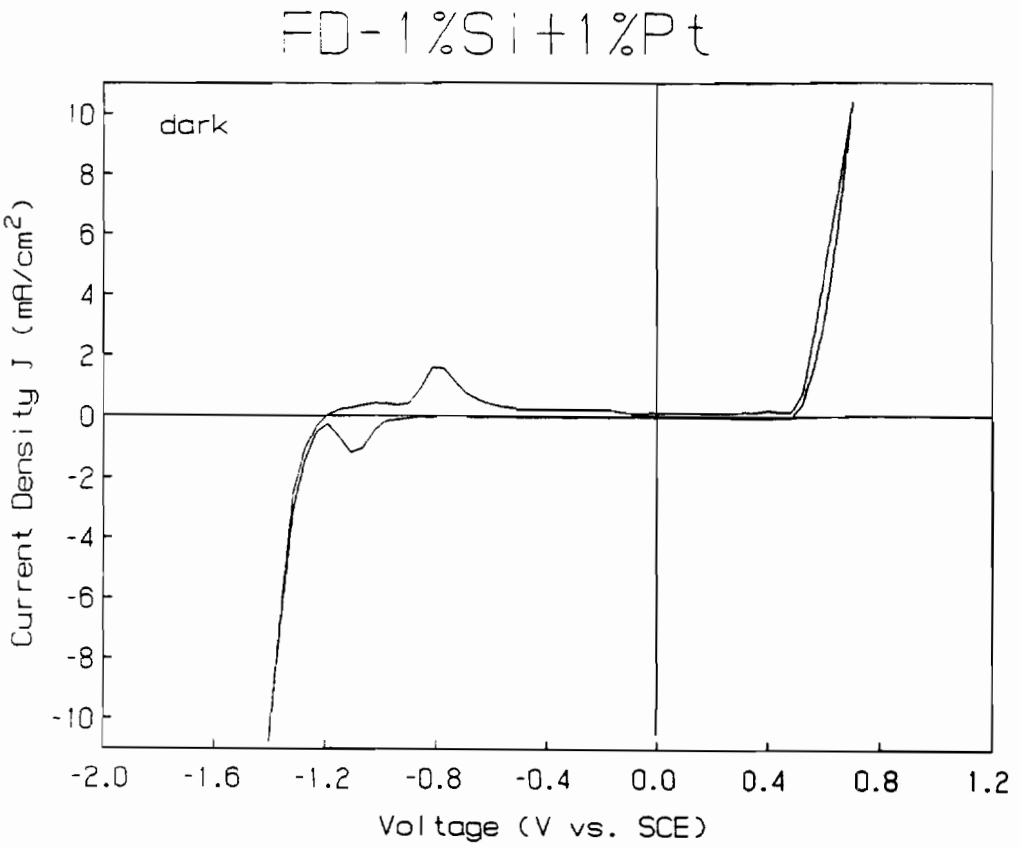

Figure 4.89. Cyclic voltammogram of the 1 at.% Si + 1 at.% Pt doped freeze-dried Fe_2O_3 in the dark (1M NaOH + 0.01M KNO_3, pH=13.5).

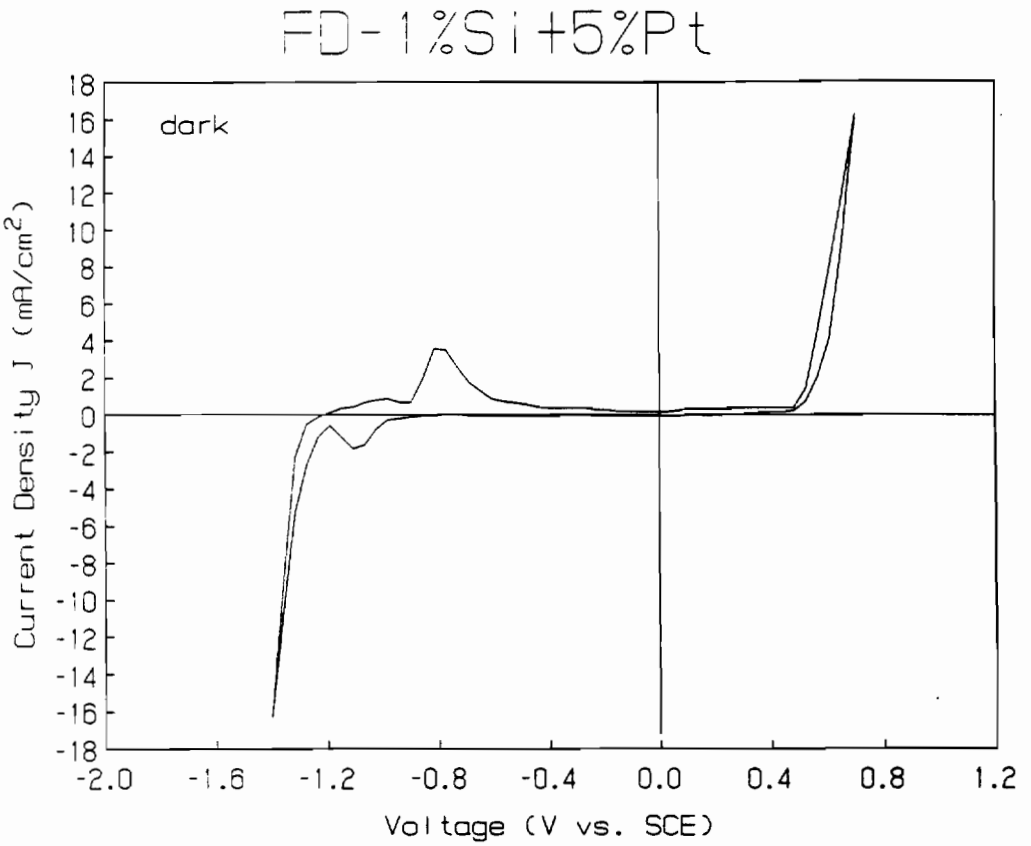

Figure 4.90. Cyclic voltammogram of the 1 at.% Si + 5 at.% Pt doped freeze-dried Fe_2O_3 in the dark (1M NaOH + 0.01M KNO_3, pH=13.5).

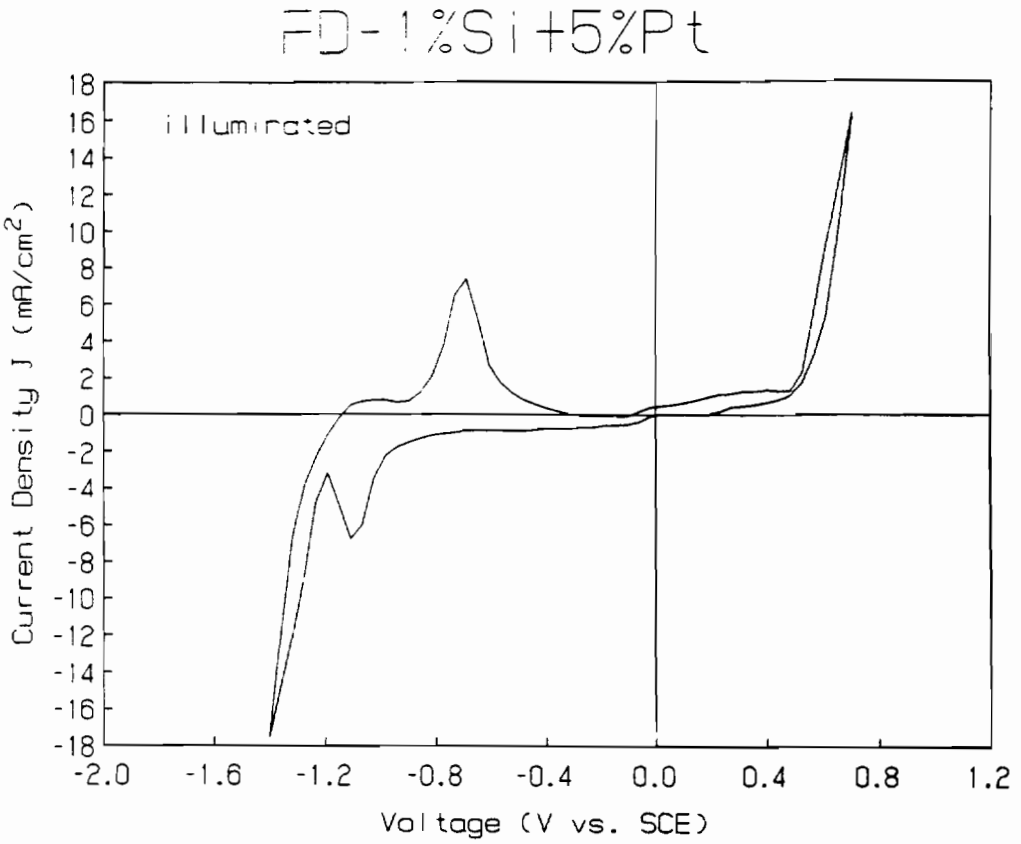

Figure 4.91. Cyclic voltammogram of the 1 at.% Si + 1 at.% Pt doped freeze-dried Fe_2O_3 under illumination (1M NaOH + 0.01M KNO_3, pH=13.5).

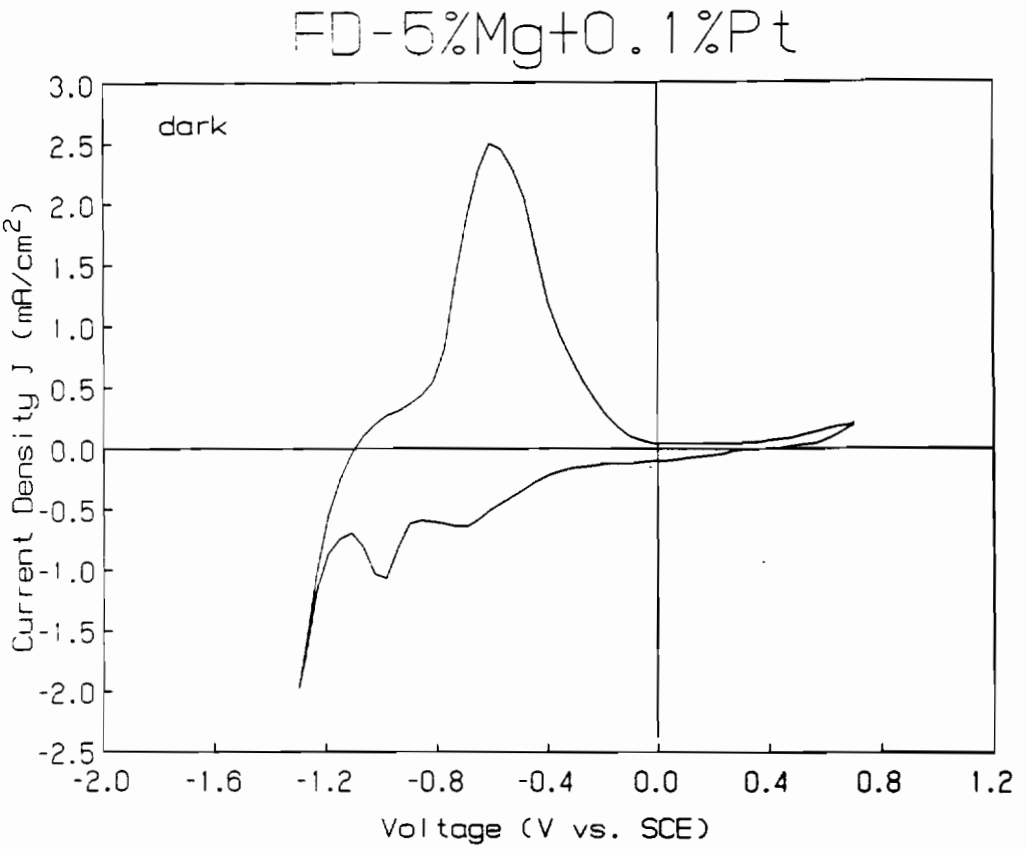

Figure 4.92. Cyclic voltammogram of the 5 at.% Mg + 0.1 at.% Pt doped freeze-dried Fe_2O_3 in the dark (1M NaOH + 0.01M KNO_3, pH=13.5).

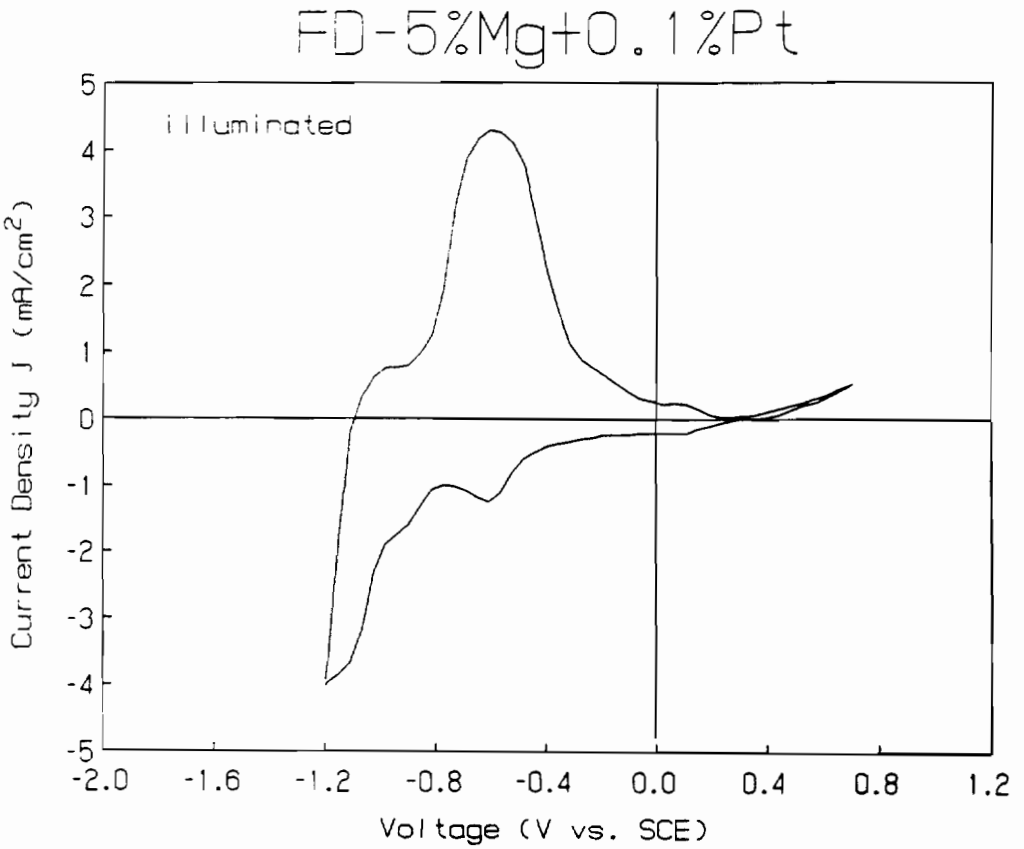

Figure 4.93. Cyclic voltammogram of the 5 at.% Mg + 0.1 at.% Pt doped freeze-dried Fe_2O_3 in the dark (1M NaOH + 0.01M KNO_3, pH=13.5).

withstand the high oxygen and hydrogen evolution rates occurring in the photoelectrochemical solar cells producing gaseous fuels.

4.8 Photocatalytic studies

Since Fe_2O_3 is an ideal material for solar energy conversion because of its convenient band gap matched to the solar spectrum, the photocatalytic studies were conducted to asses the potential use of Fe_2O_3 for the photocatalytic dissociation of water. Fe_2O_3 in the form of powder and as a colloid was used in the photocatalytic solar cell. All irradiations were done using only visible light. Figure 4.94 shows the absorption spectrum of the Fe_2O_3 sol used in these experiments. The absorption onset occurs around 575 nm corresponding to a band gap of 2.2 eV. It was discovered during photocatalytic experiments that any oxygen present in the cell would be slowly lost as determined from gas chromatography of the gaseous products above the solution in the cell. It was suspected that the Fe_2O_3 was absorbing oxygen present until some saturation point at which the oxygen was no longer consumed. Experiments were conducted with various amounts of Fe_2O_3 present in the cell where oxygen concentration was monitored versus time. The results are presented in Figure 4.95 where we can see that the oxygen consumption increased with time until a saturation point was achieved. Also the freeze-dried material showed less tendency to absorb oxygen which was ascribed to the smaller particle size of the Fe_2O_3, thus offering less chance of an oxygen being absorbed and trapped inside the Fe_2O_3 particle. A test of the oxygen content in the irradiated cell versus time was conducted using deionized water.

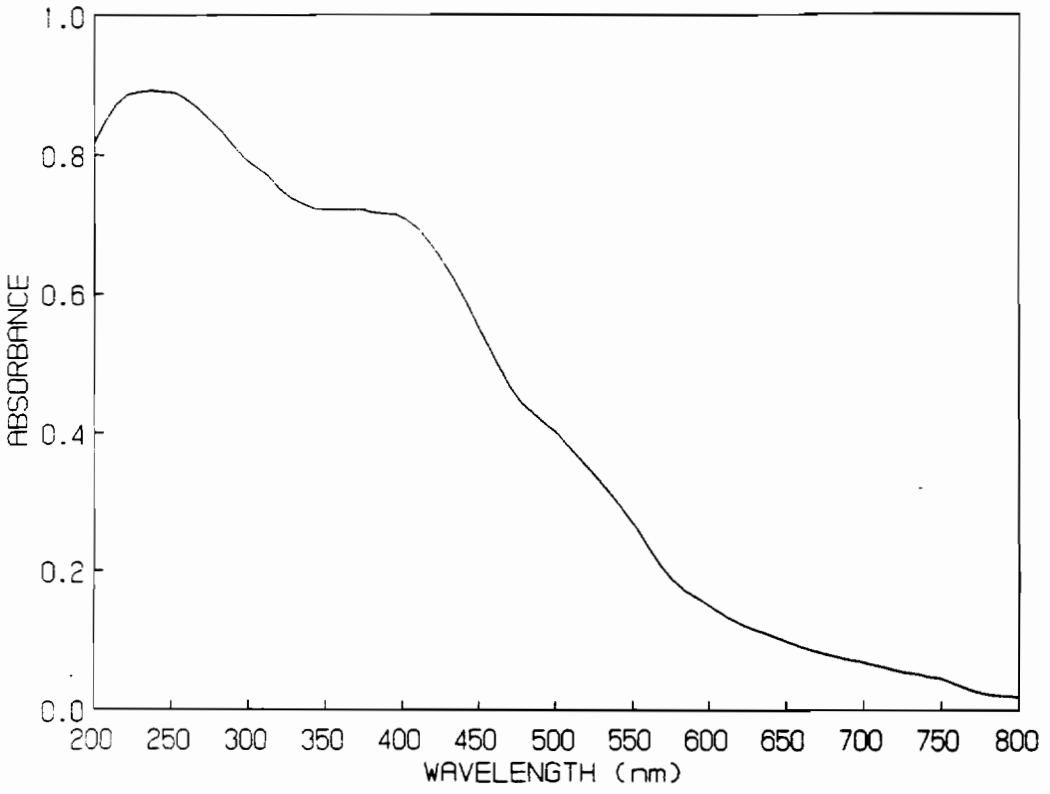

Figure 4.94. Absorption spectrum of Fe_2O_3 sol (prepared from hydrolyzed $Fe(NO_3)_3$).

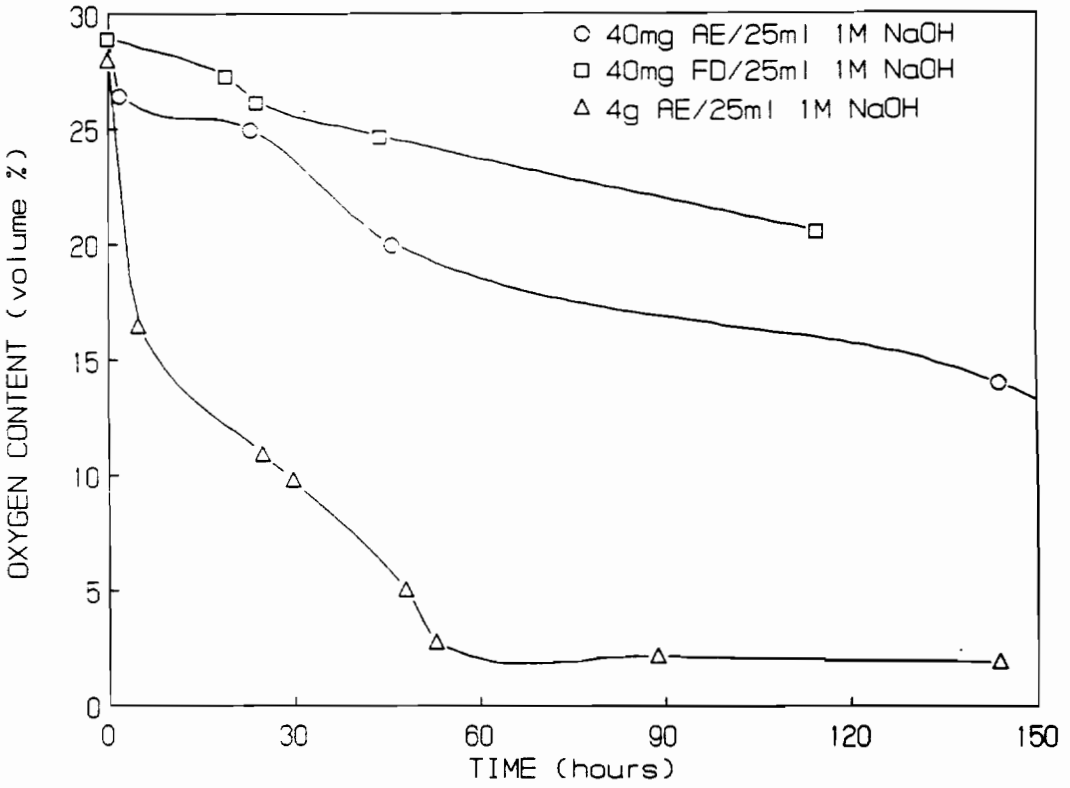

Figure 4.95. Oxygen content versus time for determination of oxygen absorption on powdered Fe_2O_3.

The results revealed no significant loss or gain of oxygen as seen in Figure 4.96. A very small oxygen absorption effect was also observed with the Fe_2O_3 sol due to a very small colloidal particle size.

Fe_2O_3 has a very small absorption coefficient as well as a very small carrier diffusion distance. These two properties limit the efficiency of Fe_2O_3 photoelectrodes. This problem may be decreased by using colloidal Fe_2O_3 of very small particle size and by using sacrificial reagents to capture either electrons or holes thus preventing fast recombination of photogenerated carriers. Oxygen evolution was observed for colloidal Fe_2O_3 with $AgNO_3$ used as an electron scavenger. Two reactions are occurring in the photocatalytic cell:

$$2H_2O + 4h^+ \rightarrow O_2 + 4H^+ \qquad (4.10)$$

$$Ag^+ + e^- \rightarrow Ag^\circ \qquad (4.11)$$

Figures 4.97-4.98 show the results of oxygen production using an electron scavenger. Oxygen production was at a maximum for 20 mg Fe_2O_3 sol/liter. The commercial Fe_2O_3 produced only negligible amounts of oxygen after very long irradiation times due to its very low surface area which decreased the efficiency of absorbing the incident light. The effect of Si or Pt doping on the photocatalytic efficiencies of the oxygen evolution is seen in Figures 4.99-4.102. It was found that the maximum oxygen was produced with 1 at.% Si + 5 at.% Pt doped freeze-dried Fe_2O_3. This result would be expected from the photoelectrochemical results. The solid state doped sample very slowly produced only a

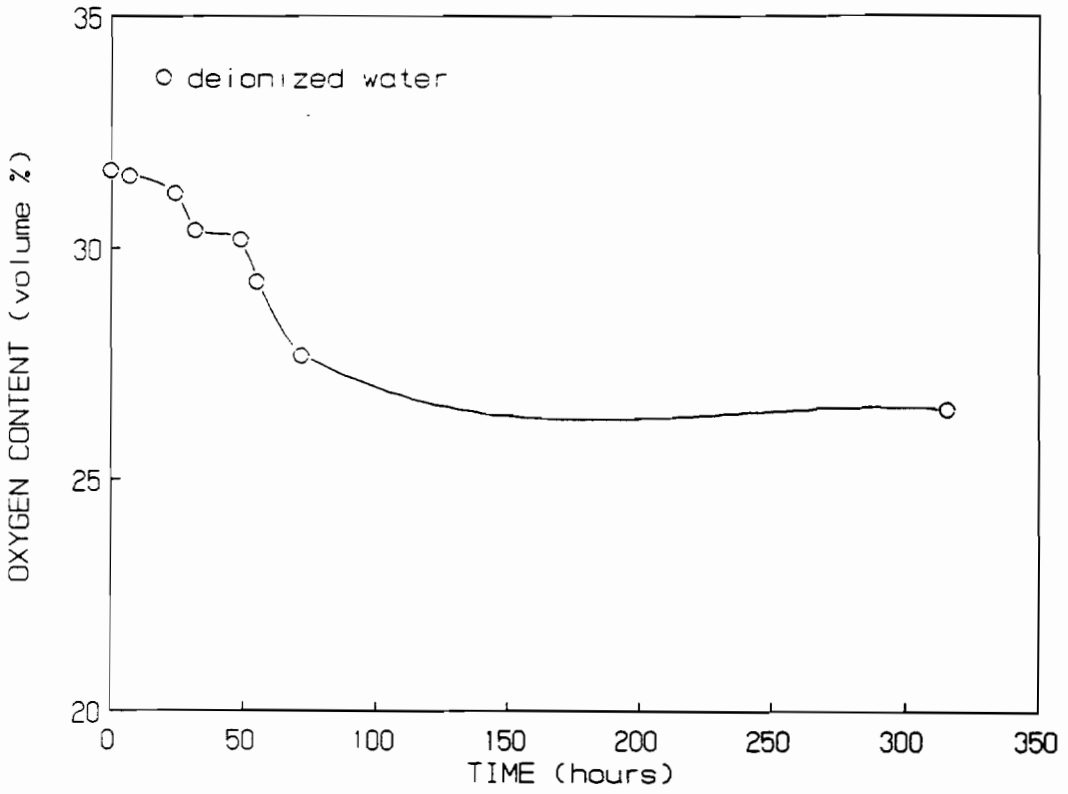

Figure 4.96. Oxygen content versus time for irradiated deionized water in the photocatalytic cell (a blank test).

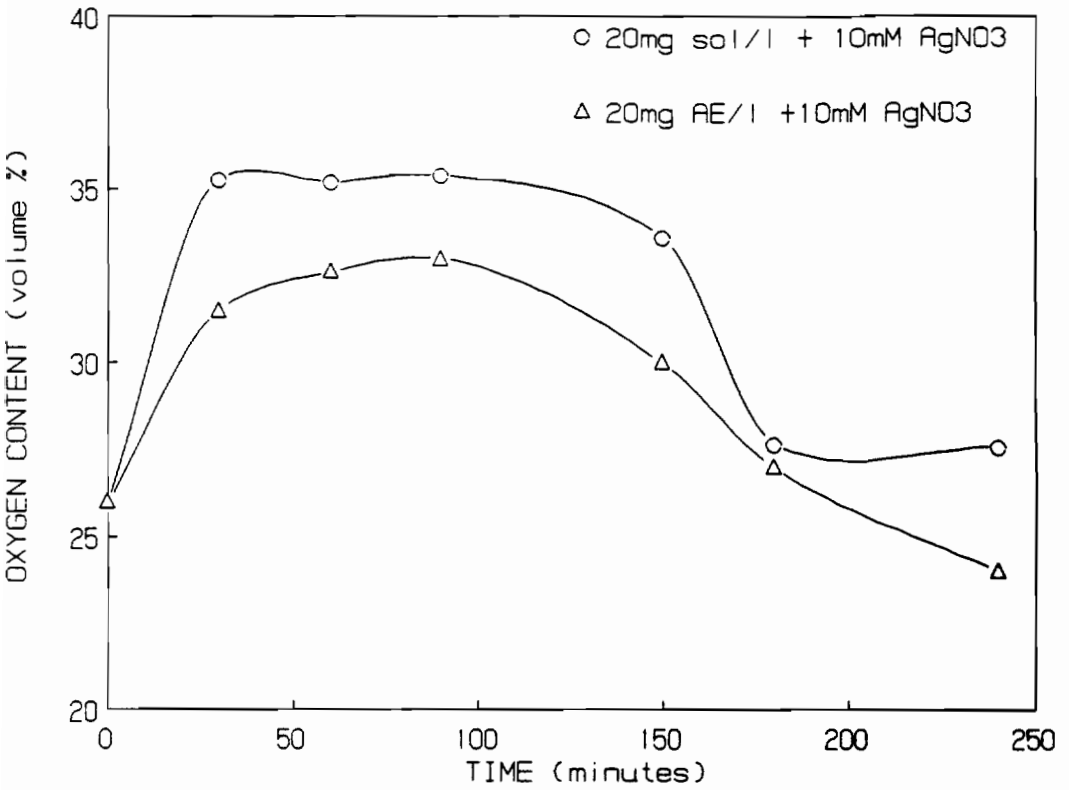

Figure 4.97. Oxygen content versus time for 20 mg Fe_2O_3/l + 10 mM $AgNO_3$ irradiated with visible light.

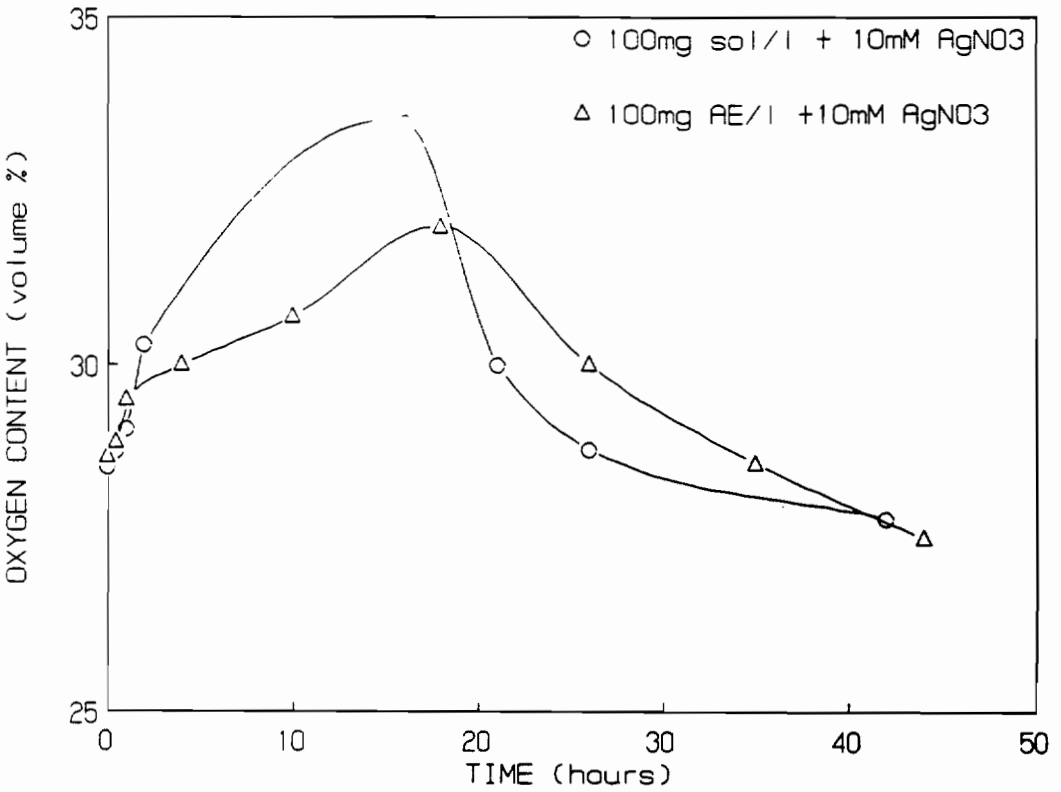

Figure 4.98. Oxygen content versus time for 100 mg Fe_2O_3/l + 10 mM $AgNO_3$ irradiated with visible light.

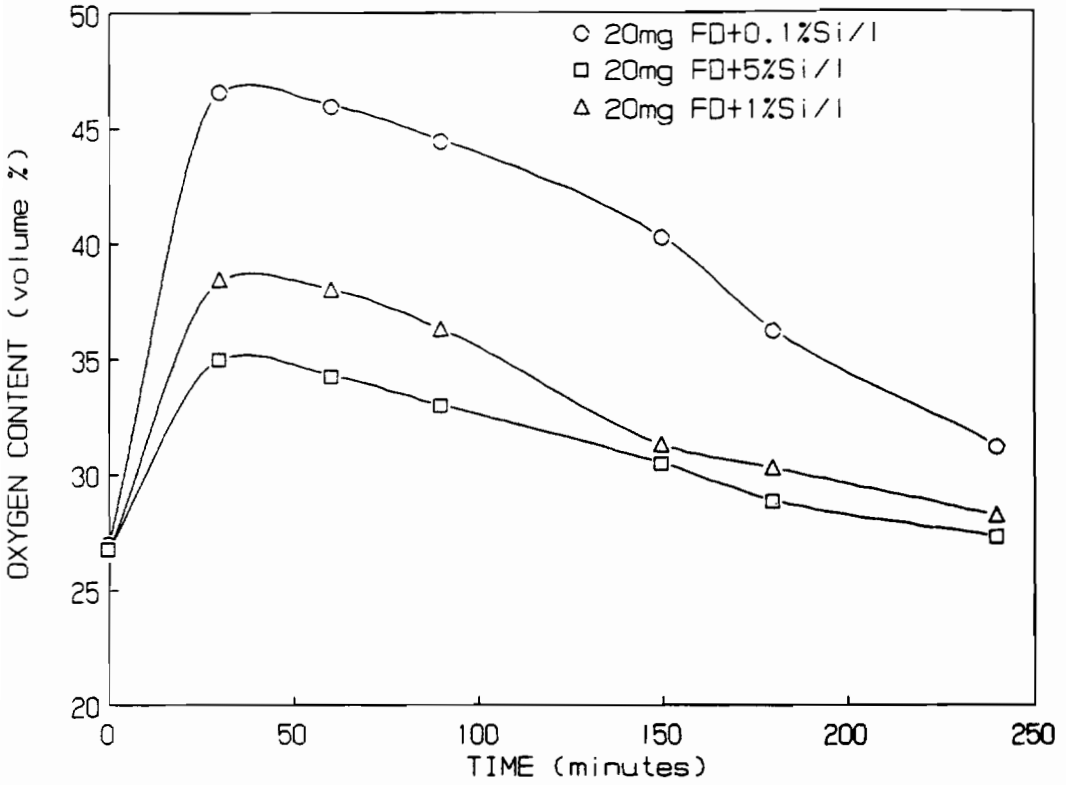

Figure 4.99. Oxygen content versus time for 20 mg Si doped freeze-dried Fe_2O_3/l + 10 mM $AgNO_3$ irradiated with visible light.

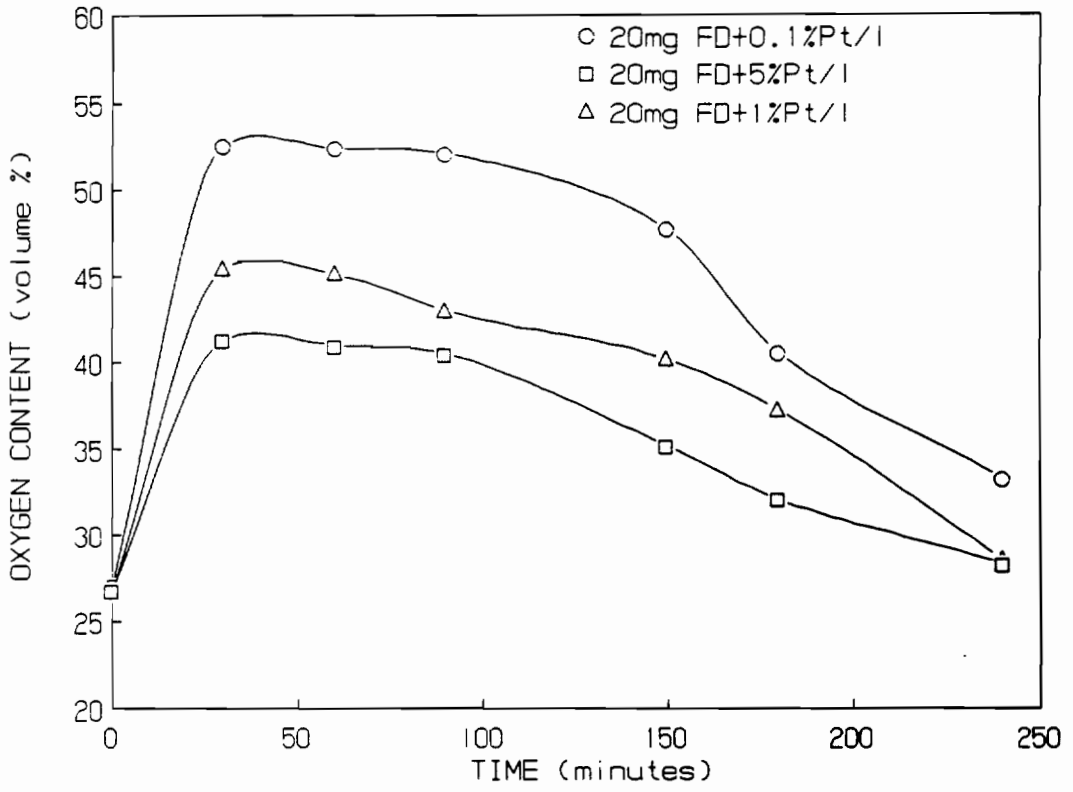

Figure 4.100. Oxygen content versus time for 20 mg Pt doped freeze-dried Fe_2O_3/1 + 10 mM $AgNO_3$ irradiated with visible light.

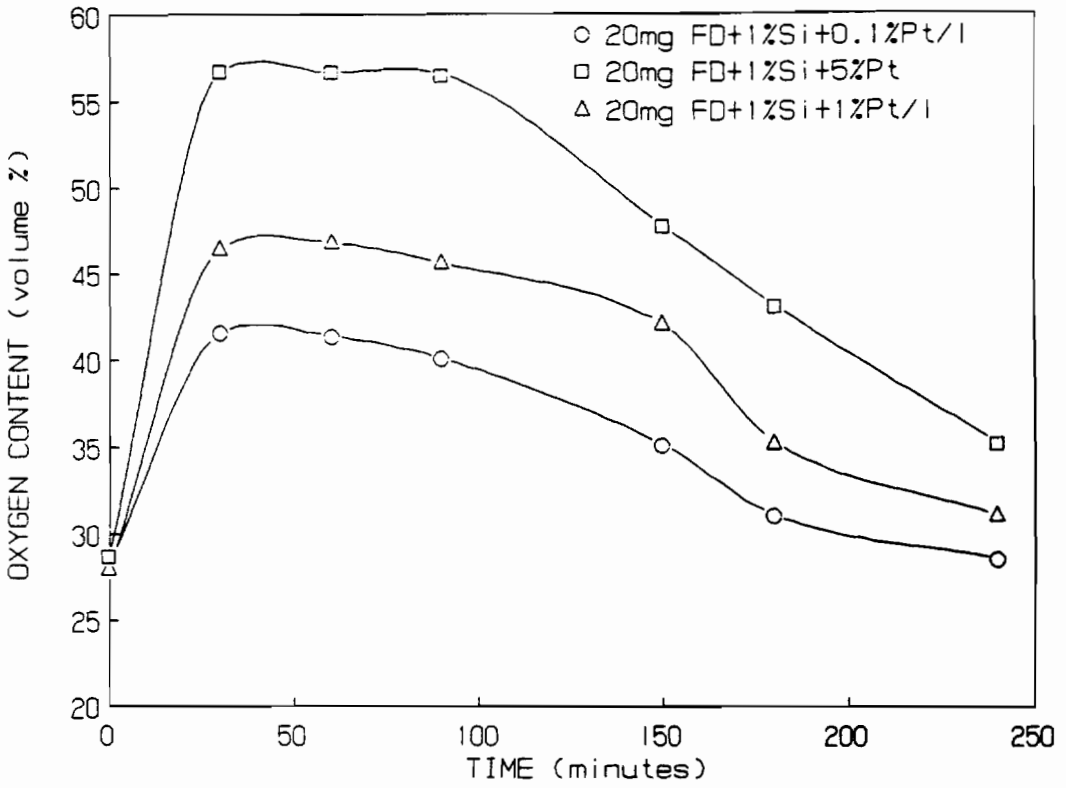

Figure 4.101. Oxygen content versus time for 20 mg Si and Pt doped freeze-dried Fe_2O_3/1 + 10 mM $AgNO_3$ irradiated with visible light.

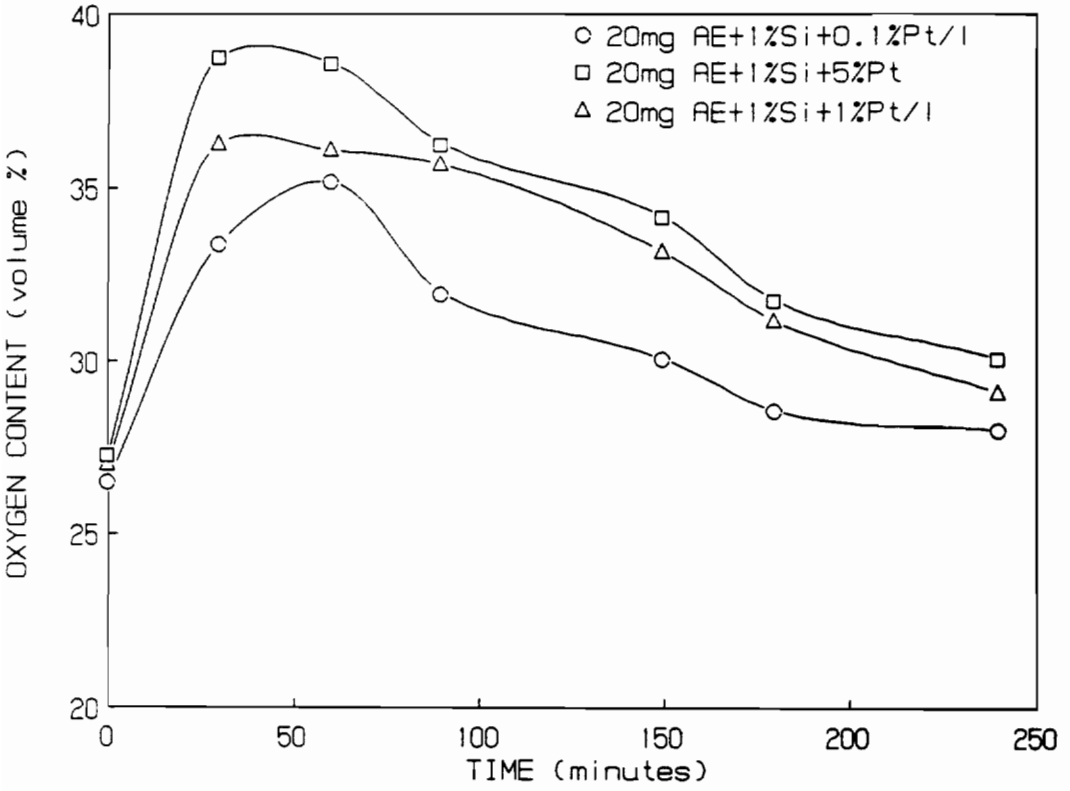

Figure 4.102. Oxygen content versus time for 20 mg Si and PT solid state doped Fe_2O_3/l + 10 mM $AgNO_3$ irradiated with visible light.

small amount of oxygen. This was also expected due to the higher resistance, poor dopant distribution, and most importantly for the photocatalysis, due to the very low surface area. The oxygen production versus platinum content is seen in Figure 4.103, where it is obvious that oxygen production increases with increasing platinum content. Quantum efficiencies (ratio of the number of electrons delivered to the number of photons absorbed by the photoelectrode) were calculated and are shown in Figures 4.104 and 4.105. Production of oxygen ceases when all the Ag^+ is reduced by collected electrons to metallic silver.

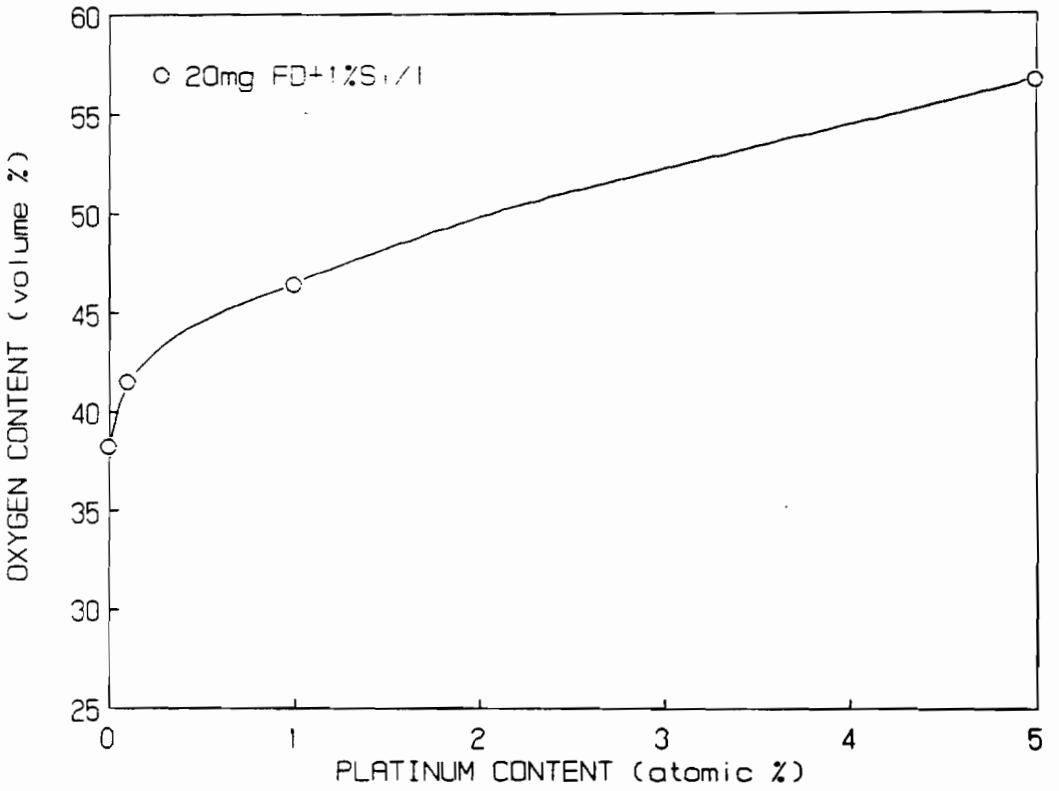

Figure 4.103. Oxygen content versus platinum content for 20 mg Si doped Fe_2O_3/l + 10 mM $AgNO_3$

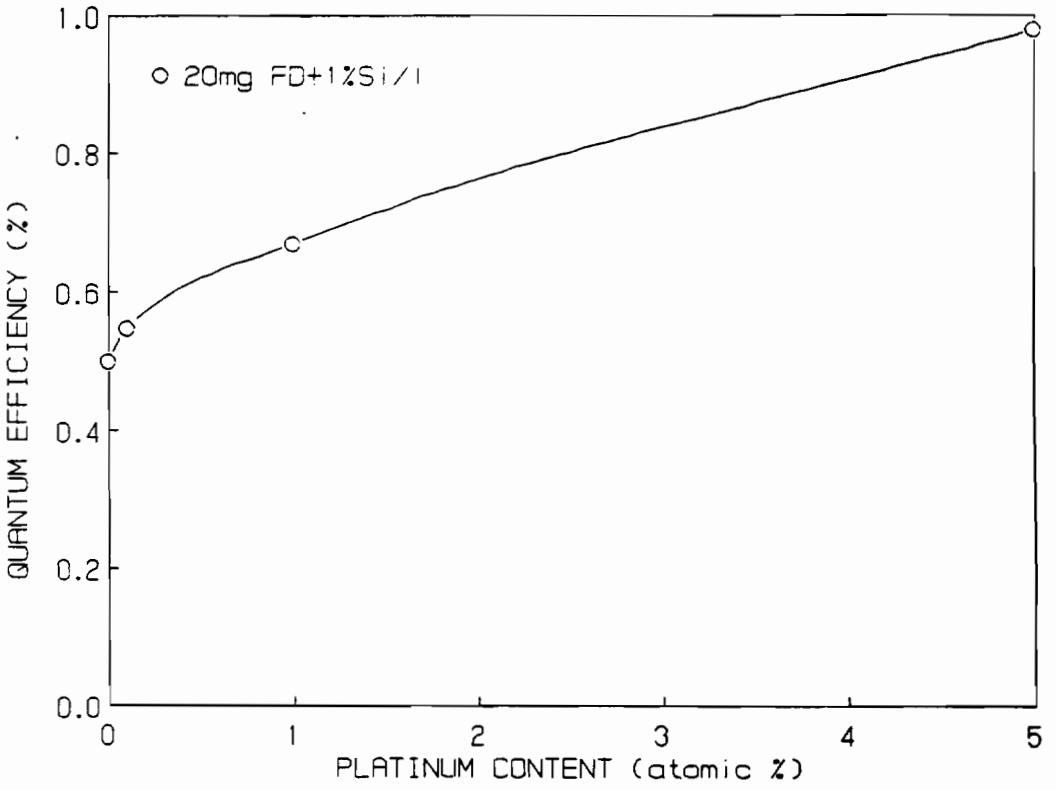

Figure 4.104. Quantum efficiencies versus platinum content for 20 mg Fe_2O_3/l + 10 mM $AgNO_3$ irradiated with visible light.

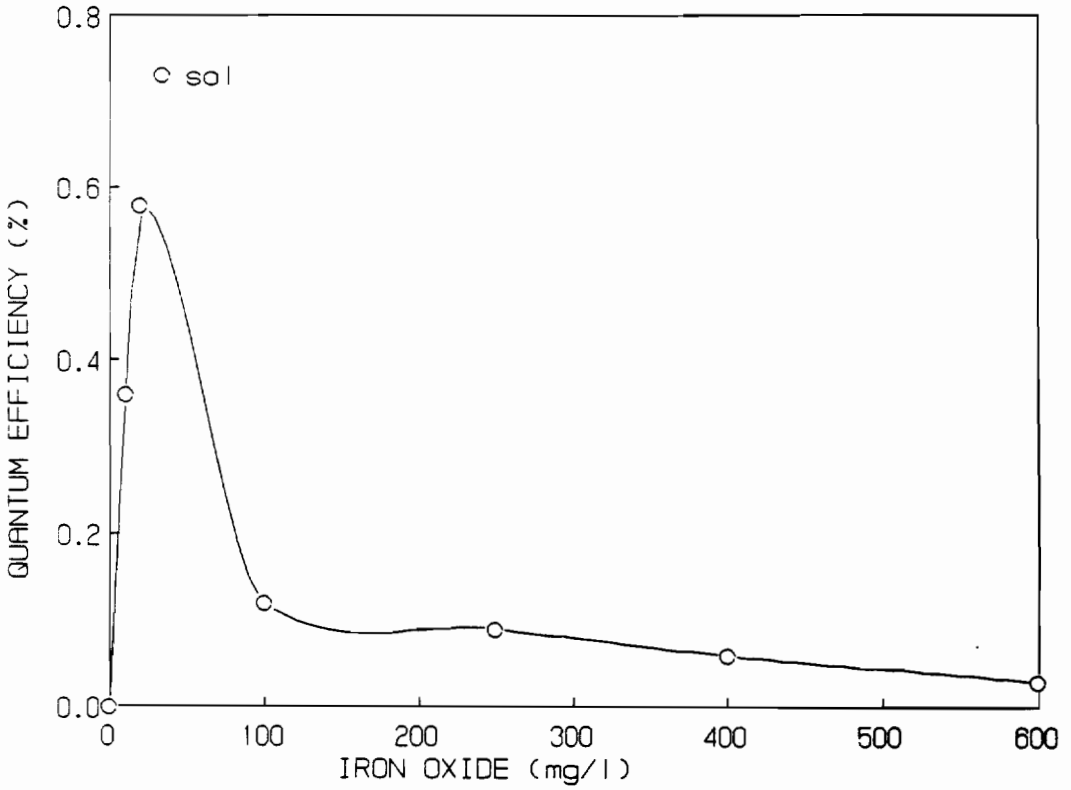

Figure 4.105. Quantum efficiencies versus Fe_2O_3 content - mg/l + 10 mM $AgNO_3$ irradiated with visible light.

CHAPTER FIVE

CONCLUSIONS

Well characterized and reproducible semiconducting Fe_2O_3 was prepared by freeze-drying. This technique produced very homogeneously doped semiconducting Fe_2O_3 that was used successfully in the photoelectrochemical and photocatalytic solar cell for the production of gaseous fuels by dissociating water. The high resistivity of the pure Fe_2O_3 was lowered by Si, Pt, or Mg doping. The Si and Pt dopants produced n-type semiconductors while the Mg dopant resulted in p-type semiconduction. In addition to doping, the optimum electrical properties were achieved by heat treating the electrodes at 1385° C in air, followed by quenching to room temperature in order to introduce some Fe_3O_4 into the structure. These semiconducting photoelectrodes were used successfully as photoanodes and photocathodes for photoproduction of oxygen and hydrogen from heterojunctions illuminated with visible light.

Photocurrents obtained with the photoelectrodes prepared from the freeze-dried Fe_2O_3 were more stable and up to ten times higher than with the samples prepared by the solid state mixing technique. The freeze-drying technique was shown to be a much superior way to produce well characterized semiconducting photoelectrodes. This observation was supported by the very consistent and reproducible results. The

surface area of the freeze-dried samples was much higher than for the corresponding solid state doped samples which resulted in an increased active area for light absorption and charge transfer between the semiconductor/electrolyte interface and hence higher efficiencies of the photoreactions were observed. The homogeneity of doping was clearly superior for the freeze-dried samples as demonstrated by SEM, TEM, and X-ray structural analysis. The superior homogeneity was also clear from the electrochemical and capacitance experiments. The Mott-Schottky plots showed a very linear relationship between capacitance and applied voltage, the flat-band potential, photocurrent onset potential, and flat-band potential determined from the capacitance measurements all agreed very well with each other which helps to support our claim that the freeze-drying technique produces superior electrodes to those from solid state mixing. The results from the solid state doped samples were very inconsistent and overall poor photoactive performance of the electrodes was mainly attributed to insufficient homogeneity of the solid state prepared samples. It is, therefore, important that the electrode preparation technique for the photoelectrochemical dissociation of water be one of the most significant factors in producing an effective and efficient solar cell for the production of gaseous fuels.

The maximum photocurrent density obtained with the freeze-dried sample was 10 mA/cm^2 at 0.8 V vs SCE for the 0.1 at.% Si + 5 at.% Pt Fe_2O_3. The photocurrent also increased with increasing amount of platinum. The added platinum was shown to have several beneficial

effects on the n-type and the p-type photoelectrodes. In the Si doped n-type semiconductor the platinum increased the carrier concentration via a shallow donor level within the bandgap. It was also shown that the platinum enhanced the probabilities of electron exchange and increased kinetics between the electrode and electrolyte species. The efficiency of the photoelectrochemical reactions was increased with added platinum by eliminating the transient currents. In the cyclic voltammetry experiments it was shown that the platinum in the n-type semiconductor at negative potentials acts as a local cathode and enhances the production of hydrogen. In the p-type Fe_2O_3, the platinum acts as an electrocatalyst and lowers the overpotential for hydrogen reduction.

The important results by Somorjai et al. [271,321] were confirmed in this investigation where a p/n Fe_2O_3 heterojunction was used in the photoelectrochemical solar cell to photodissociate water into oxygen and hydrogen with visible light. Doping the Fe_2O_3 with Mg and Pt shifted the p-type band edges cathodically and made the production of hydrogen thermodynamically feasible. This important result was further improved by using the Fe_2O_3 electrodes prepared by freeze-drying and by the addition of platinum. The photogeneration of oxygen was also achieved in the photocatalytic solar cell by irradiating doped Fe_2O_3 in the presence of an electron scavenger. The quantum efficiency of this photocatalytic reaction was increased to almost 1% by the incorporated platinum. This important result was also only possible due to the superiority of the freeze-drying technique to produce homogeneously

doped samples of very high surface area. The results for the solid state doped samples showed that this technique was unsuitable for photocatalytic oxygen production. The beneficial effect of homogeneously incorporated platinum through freeze-drying also greatly improved the efficiency of the photocatalytic reaction. The Fe_2O_3 was found to be stable against photocorrosion for extended periods of illumination and photocurrent generation in a basic electrolyte. It was shown that doped and platinized freeze-dried Fe_2O_3 can be used more efficiently than the Fe_2O_3 prepared by the solid state doped technique in the photoelectrochemical and photocatalytic cell for gaseous fuel generation using solar energy.

REFERENCES

1. S. Wagner, in "Solid State Chemistry of Energy Conversion and Storage", edited by J. B. Goodenough and M. S. Whittingham, (Advances in Chemistry Series #163), (Amer. Chem. Soc., Wash. D.C. 1977), p. 109.

2. K. Zwelbel, C&EN July 7, 1986, 34 (1986).

3. R. Memming and J. J. Kelly, in "Photoelectrochemical Conversion and Storage of Solar Energy", edited by J. S. Connoly (Academic Press Inc., New York, 1981), p. 243.

4. H. Gerischer, in "Solar Energy Conversion: Solid State Physics Aspects", edited by B. O. Seraphin (Topics in Applied Physics Series, Vol. 31), (Springer-Verlag, New York, 1979), p. 115.

5. J. B. Goodenough, A. Hamnett, M. P. Dare-Edwards, G. Campet, and R. D. Wright, Surface Sci. 101, 531 (1980).

6. S. M. Sze, in "Physics of Semiconductor Devices", (Wiley, New York, 1981), p. 245.

7. J. F. Dewald, in "Semiconductors", edited by N. B. Hannay (ACS Monograph #140), (Amer. Chem. Soc., Wash. D.C., 1959), p. 727.

8. M. A. Butler and D. S. Ginley, J. Mater. Sci. 15, 1 (1980).

9. M. S. Wrighton, C&EN, Sept. 3, 1979, 31 (1979).

10. H. Gerischer, in "Photoelectrochemistry, Photocatalysis and Photoreactors", edited by M. Schiavello, (NATO ASO Series C: #146, Mathematical and Physical Sciences, (D. Riedel Publishing Company, Netherlands 1985), p. 39.

11. A.J. Nozik, in "Annual Reviews of Physical Chemistry", Vol. 29, (Annual Reviews Inc., Palo Alto, Calif., 1978), p. 189.

12. M. S. Wrighton, Acc. Chem. Res. 12, 303 (1979).

13. J. B. Goodenough, A. Hamnett, M. P. Dare-Edwards, G. Campet, and R. D. Wright, Surface Sci. 101, 531 (1980).

14. D. S. Ginley, M. A. Butler, and C. H. Seager in "Solar Materials Science", edited by L. E. Murr, (Academic Press, New York, 1980), p. 619.

15. K. Rajeshwar, P. Singh, and J. DuBow, Electrochim. Acta 23, 1117 (1978).

16. D. E. Scaife, Solar Energy 25, 41 (1980).

17. L. A. Harris and R. H. Wilson, in "Annual Reviews of Material Science", Vol. 8, (Annual Reviews Inc., Palo Alto,Calif., 1978), p. 99.

18. J. B. Goodenough, in "Photoelectrochemistry, Photocatalysis and Photoreactors", edited by M. Schiavello (NATO ASO Series C: #146, Mathematical and Physical Sciences, Dordrecht, Netherlands, 1985), p. 155.

19. A. F. Sammells and P. G. Ang, Extended Abstracts of Electrochem. Soc. 83-1, Abstract #525, 794 (1983).

20. H. P. Maruska and A. K. Ghosh, Solar Energy 20, 441 (1978).

21. J. R. Bolton, Science 202, 705 (1978).

22. R. Memming, Electrochim. Acta 25, 77 (1980).

23. J. H. Fendler, J. Phys. Chem. 89, 2730 (1985).

24. J. O'M. Bockris, M.Szklarczyk, A. Q. Contractor, and S. U. M. Khan, Int. J. Hydrogen Energy 9, 741 (1984).

25. A. J. Nozik, Faraday Discussions of the Chemical Society 70, 7 (1980).

26. A. Heller, Acc. Chem. Res. 14, 154 (1981).

27. J. O'M. Bockris, B. Dandapani, D. Cocke, and J. Ghoroghchian, Int. J. Hydrogen Energy 10, 179 (1985).

28. J. G. Mavroides, Mat. Res. Bull. 13, 1379 (1978).

29. R. D. Rauh, J. M. Buzby, T. F. Reise, and S. A. Alkaltis, J. Phys. Chem. 83, 2221 (1979).

30. J. R. Bolton, J. Sol. St. Chem. 22, 3 (1977).

31. A. J. Bard, J. Phys. Chem. 86, 172 (1982).

32. R. C. Kainthla, S. U. M. Khan, and J. O'M. Bockris, Int. J. Hydrogen Energy 12, 381 (1987).

33. S. U. M. Khan and J. O'M. Bockris, J. Phys. Chem. 88, 2504 (1984).

34. L. Fornarini, A. J. Nozik, and B. A. Parkinson, J. Phys. Chem. 88, 3238 (1984).

35. J. A. Turner, J. Chem. Ed. 60, 327 (1983).

36. T. D. Burleigh and R. M. Latanision, Extended Abstracts of Electrochem. Soc. 85-1, Abstract #29, 41 (1985).

37. S. R. Morrison, in "Electrochemistry at Semiconductor and Oxidized Metal Electrodes", (Plenum Press, New York 1980).

38. H. Gerischer, J. Electroanal. Chem. Interfacial Electrochem. 58, 263 (1975).

39. M. A. Butler and D. S. Ginley, J. Electrochem. Soc. 125, 228 (1978).

40. M. A. Butler and D. S. Ginley, Chem. Phys. Lett. 47, 319 (1977).

41. R. De Gryse, W. P. Gomes, F. Cardon, and J. Vennik, J. Electrochem. Soc. 122, 711 (1975).

42. D. N. Bose, S. Basu, Y. Ramprakash, and K. C. Mandal, Bull. Electrochem. 1, 181 (1985).

43. V. M. Harytyunyan et. al. Extended Abstracts of Electrochem. Soc. 87-1, Abstract #467, 671 (1987).

44. S. R. Morrison, J. Vac. Sci. Technol. 15, 1417 (1978).

45. C. S. Blair and D. W. Hess, J. Electrochem. Soc. 131, 932 (1984).

46. W. P. Gomes, D. Vanmaekelbergh, and F. Cardon, Extended Abstracts of Electrochem. Soc. 86-2, Abstract #618, 920 (1986).

47. A. M. Goodman, J. Appl. Phys. 34, 329 (1963).

48. L. J. Handley and A. J. Bard, J. Electrochem. Soc. 127, 338 (1980).

49. M. A. Butler, J. Appl. Phys. 48, 1914 (1977).

50. J. F. McCann and J. Pezy, J. Electrochem. Soc. 128, 1735 (1981).

51. Ch. E. Byvik and B. Reichman, Extended Abstracts og Electrochem. Soc. 81-2, Abstract #484, 1168 (1981).

52. K. Tanaka, S. Murata, and K. Harada, Solar Energy 14, 303 (1985).

53. A. J. Nozik in "Photoelectrochemical Conversion and Storage of Solar Energy", (Academic Press, Inc., 1981), p. 271.

54. A. J. Nozik, D. S. Boudreaux, R. R. Chance, and F. Williams, in "Interfacial Photoprocesses: Energy Conversion and Synthesis", edited by M. S. Wrighton (Advances in Chemistry Series #184), (Amer. Chem. Soc., Wash. D.C., 1980), p. 155.

55. J. S. Curran and D. Lamouche, J. Phys. Chem. 87, 5405 (1983).

56. S. Fonash, M. Rose, K. Corby, and J. Jordan, Extended Abstracts of Electrochem. Soc. 81-2, Abstract #544, 1309 (1981).

57. R. Memming, in "Photoelectrochemistry, Photocatalysis and Photoreactors", edited by M. Schiavello, (NATO ASO Series C: #146, Mathematical and Physical Sciences, (D. Riedel Publishing Company, Netherlands 1985), p. 107.

58. D. B. Sepa, M. V. Vojnovic, L. M. Vracas, and A. Damjanovic, Electrochim. Acta 32, 129 (1987).

59. D. S. Ginley and M. A. Butler, in "Photoeffects at Semiconductor-Electrolyte Interfaces", edited by A. J. Nozik (ACS Symposium Series #146), (Amer. Chem. Soc., Wash. D.C., 1981), p. 79.

60. S. U. M. Khan and J. O'M. Bockris, Int. J. Hydrogen Energy 11, 373 (1986).

61. T. Pajkossy, Acta Chim. Hung. 112, 191 (1983).

62. T. Pajkossy, Hung. Acad. Sci. Cent. Res. Inst. Phys. 60, 1 (1981).

63. M. P. Dare-Edwards, J. B. Goodenough, A. Hamnett, M. H. Ramsden, A. Katty, and P. R. Trevellick, Solar Energy R & D in the European Community, Series D, p. 100 (1983).

64. H. Gerischer and W. Mindt, Electrochim. Acta 13, 1329 (1972).

65. A. Fujishima and K. Honda, Denki Kagaku 40, 33 (1972).

66. H. Gerischer, Surface Sci. 13, 265 (1969).

67. H. Gerischer, J. Electroanal. Chem. 82, 133 (1977).

68. A. J. Bard and M. S. Wrighton, J. Electrochem. Soc. 124, 1706 (1977).

69. S. L. Pohlman in "Solar Materials Science", edited by L. Murr (Academic Press, Inc., New York 1980), p. 319.

70. D. E. Scaife, from Investigation Report #137, Institute of Earth Resources, CSIRO (Australia Commonwealth Scientific and Industrial Research Organization), (1981).

71. R. M. Benito and A. J. Nozik, Extended Abstracts of Electrochem. Soc. 85-1, Abstract #555, 786 (1985).

72. K. W. Frese, Jr., M. J. Madou, and S. R. Morrison, J. Phys. Chem. 84, 3172 (1980).

73. H. Gerischer, Faraday Discussions of the Chemical Society 70, 137 (1980).

74. R. M. Benito and A. J. Nozik, J. Phys. Chem. 89, 3429 (1985).

75. H. Gerischer, J. Vac. Sci. Technol. 15, 1422 (1978).

76. M. S. Wrighton, J. M. Bolts, A. B. Bocarsly, M. C. Palazzotto, and E. G. Walton, J. Vac. Sci. Technol. 15, 1429 (1978).

77. O. J. Murphy and J. O'M. Bockris, Extended Abstracts of Electrochem. Soc. 82-2, Abstract #248, 399 (1982).

78. M. F. Weber and M. J. Dignam, Int. J. Hydrogen Energy 11, 225 (1986).

79. R. T. Ross and A. J. Nozik, J. Appl. Phys. 53, 3813 (1982).

80. P. Carlsson and B. Holmstrom, Solar Energy 36, 151 (1986).

81. B. Parkinson, Acc. Chem. Res. 17, 431 (1984).

82. S. Chandra and R. K. Pandey, Phys. Stat. Solidi (a), 72, 415 (1982).

83. G. Hodes, J. Manassen, and D. Cahen, Solar Energy Mater. 4, 373 (1981).

84. P. L.Allen and A. Hickling, Trans. Farad. Soc., 53, 1626 (1957).

85. M. S. Kazacos, J. F. McCann, and D. Haneman, Solar Energy Mater. 4, 215 (1981).

86. see for example "The Oxide Handbook" edited by G. V. Samsonov (IFI/Plenum, New York, 1982).

87. M. H. Davies, M. T. Simnad, and C. E. Birchenall, J. Metals 889 (1951).

88. T. F. W. Barth and E. Posnjack, Z. Kristallogr. 82, 325 (1932).

89. E. J. W. Verwey and J. H. de Boer, Rec. Trav. Chim. Pays-Bas 55, 531 (1936).

90. L. Pauling and S. B. Hendricks, J. Am. Chem. Soc. 47, 78 (1925).

91. L. Ben-Dor, E. Fischbein, and Z. Kalman, Acta Cryst. B32, 667 (1976).

92. S. Kachi, N. Nakanishi, K. Kosuge, H. Hiramatsu, and M. Kiyama, Ferrites. Proc. International Conf. 141 (1970).

93. G. W. Van Oosterhout, Acta Cryst. 13, 932 (1960).

94. J. D. Bernal, D. R. Dasgupta, and A. L. Mackay, Nature 180, 645 (1957).

95. D. Klissurski and V. Blaskov, J. Chem. Soc., Chem. Commun. 863 (1983).

96. Y. Nakatani, M. Sakai, S. Nakatani, and M. Matsuoka, J. Mater. Sci. Lett. 2, 129 (1983).

97. W. Weisweiler, Pakistan J. Sci. Ind. Res. 24, 160 (1981).

98. D. G. Klissurski and V. N. Bluskov, Materials Chemistry 5, 67 (1980).

99. E. Karmazsin, P. Satre, and P. Vergnon, J. Thermal Analysis 28, 279 (1983).

100. S. Hirokawa, T. Naito, and T. Yamaguchi, J. Colloid Interface Sci. 112, 268 (1986).

101. F. Watari, P. Delavignette, J. Van Landuyt, and S. Amelinckx, J. Sol. St. Chem. 48, 49 (1983).

102. J. M. Gonzalez-Calbet and M. A. Alario Franco, Thermochim. Acta 58, 45 (1982).

103. E. Mendelovici, R. Villalba, and A. Sagarzazu, Mat. Res. Bull. 17, 241 (1982).

104. E. Mendelovici, A. Sagarzazu, and R. Villalba, Mat. Res. Bull. 17, 1017 (1982).

105. D. Beruto, Mater. Chem. Phys. 8, 233 (1983).

106. O. N. Salmon, J. Phys. Chem. 65, 550 (1961).

107. A. A. El-Geassy, J. Mat. Sci. 21, 3889 (1986).

108. M. Jallouli, F. Ajersch, J. Mat. Sci. 21, 3528 (1986).

109. M. Senna, J. Appl. Phys. 49, 4580 (1978).

110. T. Leskela and M. Leskela, Thermochim. Acta 77, 177 (1984).

111. J. Subrt, A. Solcova, F. Hanousek, A. Petrina, and V. Zapletal, Coll. Czech. Chem. Commun. 49, 2478 (1984).

112. A. Solcova, J. Subrt, J. Vins, F. Hanousek, V. Zapletal, and J. Tlaskal, Coll. Czech. Chem. Comm. 46, 3049 (1981).

113. P. C. Kou, C. Y. Chang, T. S. Wu, Y. H. Chang, and T. K. Hsu, J. Mater. Sci. Lett. 1, 137 (1982).

114. J. Subrt, F. Hanousek, V. Zapletal, and H. Stepankova, J. Mat. Sci. 17, 215 (1982).

115. A. N. Christensen, P. Convert, and M. S. Lehmann, Acta Chem. Scand. A34, 771 (1980).

116. A. N. Christensen and S. Fregerslev, Acta. Chem. Scand. 22, 1043 (1968).

117. A. N. Christensen, Acta Chem. Scand. 22, 1487 (1968).

118. T. A. Kriger, O. P. Krivoruchko, and R. A. Buyanov, React. Kinet. Catal. Lett. 24, 401 (1984).

119. T. Ishikawa and K. Inouye, Bull. Chem. Soc. Jpn. 46, 2665 (1973).

120. A. Spinzi and I. V. Nicolescu, Rev. Roumaine de Chim. 20, 387 (1075).

121. P. K. Gallagher, D. W. Johnson, Jr. and F. Schrey, Cer. Bull. 55, 589 (1976).

122. P. K. Gallagher, D. W. Johnson, Jr., F. Schrey, and D. J. Nitti, Ceram. Bull. 52, 842 (1973).

123. E. Matijevic, Langmuir 2, 12 (1986).

124. E. Matijevic, Acc. Chem. Res. 14, 22 (1981).

125. E. Matijevic and P. Scheiner, J. Colloid Interface Sci. 63, 509 (1978).

126. M. Ozaki, S. Kratohvil, and E. Matijevic, J. Colloid Interface Sci. 102, 146 (1984).

127. R. S. Sapieszko and E. Matijevic, J. Colloid Interface Sci. 74, 405 (1980).

128. S. Hamada and E. Matijevic, J. Chem. Soc., Faraday Trans. I, 78, 2147 (1982).

129. W. D. Robertson, J. Phys. Chem. 56, 671 (1952).

130. S. Rajendran, V. Sitakara Rao, and H. S. Maiti, J. Mater. Sci. 17, 2709 (1982).

131. I. P. Saraswat, A. C. Vajpei, V. K. Garg, V. K. Sharma, and N. Prakash, J. Colloid Interface Sci. 73, 373 (1980).

132. K. M. Towe and W. F. Bradley, J. Colloid and Int. Sci. 24, 384 (1967).

133. S. Music, A. Vertes, G. W. Simmons, I. Czako-Nagy, and H. Leidheiser, Jr., J. Colloid Interface Sci. 85, 256 (1982).

134. A. C. C. Tseung, H. L. Bevan, J. Mater. Sci. 5, 604 (1970).

135. J. Kelly, D. B. Hibbert, A. C. C. Tseung, J. Mat. Sci. 13, 1053 (1978).

136. S. K. Sarkar, M. L. Sharma, and A. P. Jain, Indian J. Cryog. 3, 75 (1978).

137. R. J. Thibeau, C. W. Brown, and R. H. Heidersbach, Appl. Spectrosc. 32, 532 (1978).

138. T. R. Hart, S. B. Adams, and H. Temkin, Proceedings of Int. Conf. on Light Scattering in Solids, Brazil 1976, p. 259.

139. I. V. Rigina and G. S. Sakasm, Zhurnal Prikladnoi Spectroscopii 22, 554 (1975).

140. T. P. Martin, R. Merlin, D. R. Huffman, and M. Cardona, Sol. St. Comm. 22, 565 (1977).

141. F. J. Morin, Phys. Rev. 78, 819 (1950).

142. C. G. Shull, W. A. Strauser, and E. O. Wollan, Phys. Rev. 83, 333 (1951).

143. I. Dzialoshinski, J. Phys. Chem. Solids 4, 241 (1958).

144. I. R. Beattie and T. R. Gilson, J. Chem. Soc. (A), 980 (1970).

145. J. C. Hamilton, B. E. Mills, and R. E. Benner, Appl. Phys. Lett. 40, 499 (1982).

146. R. L. Farrow and A. S. Nagelberg, Appl. Phys. Lett. 36, 945 (1980).

147. C. J. Serna, J. L. Rendon, and J. E. Iglesias, Spectrochim. Acta 38A, 797 (1982).

148. G. S. Sakasm, L. S. Solnceva, and I. I. Plusnina, Zhurnal Prikladnoi Spectroscopii 16, 300 (1972).

149. S. H. Yariv and E. Mendelovici, Appl. Spectroscopy 33, 410 (1979).

150. K. Kauffman and F. Hazel, J. Inorg. Nucl. Chem. 37, 1139 (1975).

151. W. Lorenzelli and G. Busca, Materials Chem. Phys. 13, 261 (1985).

152. N. A. Hakeem, A. B. Basily, N. Sagr, and M. A. Moharram, J. Mat. Sci. Lett. 5, 4 (1986).

153. T. V. Kalinskaya, L. B. Lobanova, and I. V. Pologikh, Zhurnal Prikladnoi Khimii 55, 2226 (1983).

154. J. L. Rendon, J. E. Iglesias, and C. J. Serna, Optica Pura Y Aplicada 14, 117 (1981).

155. V. Lorenzelli, G. Busca, N. Sheppard, and F. Al-Mashta, J. Molecular Structure 80, 181 (1982).

156. G. Busca and P. F. Rossi, J. Mater. Chem. Phys. 9, 561 (1983).

157. F. Al-Mashta, N. Sheppard, V. Lorenzelli, and G. Busca, J. Chem. Soc., Faraday Trans. I, 78, 979 (1982).

158. S. Yariv, Powder Technol. 12, 131 (1975).

159. R.Feder, Phys. Stat. Solidi 58, K137 (1973).

160. H. D. Shih, F. Jona, D. W. Jepsen, and P. M. Marcus, Surf. Sci. 104, 39 (1981).

161. C. Leygraf and S. Ekelund, Surf. Sci. 40, 609 (1973).

162. G. A. Somorjai and M. Langell, J. Vac. Sci. and Tech. 21, 858 (1982).

163. C. R. Brundle, T. J. Chuang, and K. Wandelt, Surf. Sci. 68, 459 (1977).

164. G. A. Somorjai and M. Salmeron, in "Homogeneous and Heterogeneous Photocatalysis", edited by E. Pelizzetti and N. Serpone (NATO ASI Ser. C, Vol. 174, 1986), p. 445.

165. F. J. Micale, D. Kiernan, and A. C. Zettlemoyer, J. Colloid Interface Sci. 105, 570 (1985).

166. T. Morimoto, M. Nagao, and F. Tokuda, J. Phys. Chem. 73, 243 (1969).

167. D. T. Harvey and R. W. Linton, Anal. Chem. 53, 1684 (1981).

168. T. C. Huang and B. R. York, Appl. Phys. Lett. 50, 389 (1987).

169. A. M. Youssef and N. M. Amin, Surface Technology 7, 469 (1978).

170. J. H. de Wit, 2nd Eur. Conf. on Solid St. Chem., 4-6 June 1982, Veldhoven, Proceedings p. 311.

171. R. K. Coble, J. Am. Ceram. Soc. 41, 55 (1958).

172. J. H. W. De Wit and J. W. Geus, Sci. Ceramics 12, 281 (1984).

173. T. Yamaguchi and H. Kosha, Comm. Amer. Cer. Soc. 84 (1981).

174. B. R. Arora, R. K. Banerjee, N. K. Mandal, N. C. Ganguli, and S. P. Sen, Technology 8, 207 (1971).

175. S. V. Koshcheev and A. E. Cherkashin, Izvestiya Akademii Nauk SSSR, Neorganicheskie Materialy 16, 856 (1981).

176. J. A. Tossel, D. J. Vaughan, and K. H. Johnson, Nature 244, 42 (1973).

177. F. P. Koffyberg, K. Dwight, and A. Wold, Sol. St. Comm. 30, 433 (1979).

178. L. A. Marusak, R. Messier, and W. B. White, J. Phys. Chem. Solids 41, 981 (1980).

179. J. H. Kennedy and K. W. Frese, Jr., J. Electrochem. Soc. 125, 723 (1978).

180. R. K. Quinn, R. D. Nasby, and R. J. Baughman, Mat. Res. Bull. 11, 1011 (1976).

181. L. Changyi, C. Shengmin, S. M. Wilhelm, S. D. Kapusta, A. Viehbeck, and N. Hackerman, Scientia Sinica 27, 225 (1984).

182. F. J. Morin, Phys. Rev. 93, 1195 (1954).

183. F. J. Morin, Phys. Rev. 83, 1005, (1951).

184. B. M. Warnes, F. F. Aplan, and G. Simkovich, Solid St. Ionics 12, 271 (1984).

185. Y. T. Qian, R. Kershaw, S. Soled, K. Dwight, and A. Wold, J. Sol. St. Chem. 52, 211 (1984).

186. H. L. Sanchez, H. Steinfink, and H. S. White, J. Sol. St. Chem. 41, 90 (1982).

187. P. Merchant, R. Collins, R. Kershaw, K. Dwight, and A. Wold, J. Sol. St. Chem. 27, 307 (1979).

188. R. F. Menezes, V. N. Kamat Dalal, and H. V. Keer, Proc. Indian Acad. Sci. (Chem. Sci.) 89, 247 (1980).

189. K. H. Kim, S. H. Lee, and J. S. Choi, J. Phys. Chem. Solids 46, 331 (1985).

190. Y. Nakatani and M. Matsuoka, Jpn. J. Appl. Phys. 22, 233 (1983).

191. R. Dieckmann, Ber. Bunsenges. Phys. Chem. 86, 112 (1982).

192. A. Fujishima and K. Honda, Nature 238, 37 (1972).

193. A. J. Nozik, Nature 257, 383 (1975).

194. E. Pollert, J. Hejtmanek, J. P. Doumerc, J. C. Launay, and P. Hagenmuller, Z. Anorg. Allg. Chem. 528, 202 (1985).

195. H. H. Kung, H. S. Jarrett, A. W. Sleight, and A. Ferretti, J. Appl. Phys. 48, 2463 (1977).

196. C. Sanchez, M. Hendewerk, K. D. Sieber, and G. A. Somorjai, J. Sol. St. Chem. 61, 47 (1986).

197. A. M. Redon, J. Vigneron, R. Heindl, C. Sella, C. Martin, and J. P. Dalbera, Solar Cells 3, 179 (1981).

198. G. Horowitz, J. Electroanal. Chem. 159, 421 (1983).

199. M. Sharon and B. M. Prasad, Solar Energy Mater. 8, 457 (1983).

200. A. S. N. Murthy and K. S. Reddy, Mat. Res. Bull. 19, 241 (1984).

201. K. L. Hardee and A. J. Bard, J. Electrochem. Soc. 123, 1024 (1976).

202. K. L. Hardee and A. J. Bard, J. Electrochem. Soc. 124, 215 (1977).

203. R. A. Fredlein and A. J. Bard, J. Electrochem. Soc. 126, 1892 (1979).

204. G. A. Mabbott, J. Chem. Ed. 60, 697 (1983).

205. D. H. Evans, K. M. O'Connel, R. A. Petersen, and M. J. Kelly, J. Chem. Ed. 60, 290 (1983).

206. J. T. Maloy, J. Chem. Ed. 60, 285 (1983).

207. S. C. Tjong, Mater. Res. Bull. 18, 421 (1983).

208. Der-Tau Chin, J. Electrochem. Soc. 121, 527 (1974).

209. K. S. Yun, S. M. Wilhelm, S. Kapusta, and N. Hackerman, J. Electrochem. Soc. 127, 85 (1980).

210. S. M. Wilhelm, K. S. Yun, L. W. Ballenger, and N. Hackerman, J. Electrochem. Soc. 126, 419 (1979).

211. R. M. Candea, Electrochim. Acta 26, 1803 (1981).

212. S. M. Wilhelm and N. Hackerman, J. Electrochem. Soc. 128, 1668 (1981).

213. L. C. Schumacher, S. M. Afara, M. F. Weber,and M. J. Dignam, J. Electrochem. Soc. 132, 2945 (1985).

214. T. Pajkossy, J. Electrochem. Soc. 130, 632 (1983).

215. K. Itoh, M. Nakao, and K. Honda, J. Appl. Phys. 57, 5493 (1985).

216. K. Itoh and J. O'M. Bockris, J. Appl. Phys. 56, 874 (1984).

217. K. Itoh and J. O'M. Bockris, J. Electrochem. Soc. 131, 1266 (1984).

218. J. H. Kennedy, R. Shinar, and J. P. Ziegler, J. Electrochem. Soc. 127, 2307 (1980).

219. J. H. Kennedy, M. Anderman, and R. Shinar, J. Electrochem. Soc. 128, 2371 (1981).

220. R. Shinar and J. H. Kennedy, Solar Energy Mater. 6, 323 (1982).

221. N. S. McAlpine and R. A. Fredlein, Aust. J. Chem. 36, 11 (1983).

222. R. Shinar and J. H. Kennedy, J. Electrochem. Soc. 130, 392 (1983).

223. A. L. Fahrenbruch, Extended Abstracts of Electrochem. Soc. 85-2, Abstract #386, 578 (1985).

224. J. Reichman, Extended Abstracts of Electrochem. Soc. 81-2, Abstract #545, 1312 (1981).

225. A. J. Bard, F. F. Fan, A. S. Gioda, G. Nagasubramanian, and H. S. White, Faraday Discussions of the Chemical Society 70, 19 (1980).

226. K. Chandrasekaran and J. O'M. Bockris, Extended Abstracts of Electrochem. Soc.85-1, Abstract #574, 811 (1985).

227. S. R. Morrison, J. Photochem. 29, 55 (1985).

228. A. J. Bard, F. R. F. Fan, and G. Nagasubramanian, Extended Abstracts of Electrochem. Soc. 81-2, Abstract #565, 1353 (1981).

229. A. J. Bard, A. B. Bocarsly, F. F. Fan, E. G. Walton, and M. S. Wrighton, J. Amer. Chem. Soc. 102, 3671 (1980).

230. S. Sahami and J. H. Kennedy, J. Electrochem. Soc. 132, 1116 (1985).

231. R. Shinar and J. H. Kennedy, J. Electrochem. Soc. 130, 860 (1983).

232. M. Anderman and J. H. Kennedy, J. Electrochem. Soc. 131, 1565 (1984).

233. J. H. Kennedy and D. Dunwald, J. Electrochem. Soc. 130, 2013 (1983).

234. J. H. Kennedy and D. Dunnwald, Extended Abstracts of Electrochem. Soc. 83-1, Abstract #511, 775 (1983).

235. J. H. Kennedy and K. W. Frese, Jr., J. Electrochem. Soc. 125, 709 (1978).

236. M. Anderman and J. H. Kennedy, J. Electrochem. Soc. 131, 21 (1984).

237. A. J. Bard and L. R. Faulkner in "Electrochemical Methods", (John Wiley & Sons, Inc., 1980), p. 288.

238. J. H. Kennedy and M. Anderman, J. Electrochem. Soc. 130, 848 (1983).

239. M. C. H. McKubra and M. J. Madou, Extended Abstracts of Electrochem. Soc. 83-1, Abstract #53, 81 (1983).

240. Gh. Nazri and E. Yeager, Extended Abstracts of Electrochem. Soc. 83-1, Abstract #54, 83 (1983).

241. M. E. Vela, J. R. Vilche, and A. J. Arvia, Electrochim. Acta 31, 1633 (1986)/

242. H. Yoneyama and H. Tamura, Bull. Chem. Soc. Jpn. 43, 350 (1970).

243. P. Iwanski, J. S. Curran, W. Gissler, and R. Memming, J. Electrochem. Soc. 128, 2128 (1981).

244. H. Yoneyama, S. Hamamatsu, and H. Tamura, Bull. Chem. Soc. Jpn. 43, 3639 (1970).

245. K. Uosaki and H. Kita, Extended Abstracts of Electrochem. Soc. 81-2, Abstract #483, 1167 (1981).

246. A. Roy, S. S. Bhattacharyya, and S. Aditya, Int. J. Hydrogen Energy 11, 367 (1986).

247. M. Etman, Extended Abstracts of Electrochem. Soc. 86-2, Abstract #619, 921 (1986).

248. D. K. Jain and J. C. Garg, Proceedings of the Nuclear Physics and Solid State Physics Symposium 20C, 161 (1977).

249. M. Handschuh, W. Lorenz, C. Aegerter, and T. Katterle, J. Electroanal. Chem. 144, 99 (1983).

250. U. Stimming and J. W. Schultze, Ber. Bun. Gesell. Phys. Chem. 80, 1297 (1976).

251. K. I. Zamaraev, B. N. Parmon, and A. E. Cerkasmin, Sovetsko-Frantsuzskii Seminar po Katalizu 6, 1 (1983).

252. M. V. C. Sastri and G. Nagasubramanian, Int. J. Hydrogen Energy 7, 873 (1982).

253. N. Getoff, Int. J. Hydrogen Energy 9, 997 (1984).

254. V. M. Arutyunyan, A. G. Sarkisian, Z. R. Panosian, G. M. Stepanian, and G. Z. Sachnazarian, Izvestiya Akademii Nauk Armyanskoi SSR, Fizika 18, 39 (1983).

255. L. R. Yeh and N. Hackerman, Proceedings of the Electrochemical Society 77, 69 (1977).

256. V. M. Harutyunyan et. al. Extended Abstracts of Electrochem. Soc. 87-1, Abstract #514, 733 (1987).

257. M. Gori, H. R. Gruniger, and G. Calzaferri, J. Appl. Electrochem. 10, 345 (1980).

258. N. Giordano, E. Passalacqua, V. Antonucci, and J. C. J. Bart, Int. J. Hydrogen Energy 8, 763 (1983).

259. N. Giordano, V. Antonucci, J. C. J. Bart, Hydrogen Energy Progress 4, 777 (1983).

260. J. F. McCann and S. P. S. Badwal, J. Electrochem. Soc. 129, 551 (1982).

261. W. L. Ahlgren, J. Electrochem. Soc. 128, 2123 (1981).

262. B. Reichman and Ch. E. Byvik, J. Electrochem. Soc. 128, 2601 (1981).

263. Z. Lin, Y. Chen, and X. Wu, Surface Sci. 147, 377 (1984).

264. M. Faur, M. Faur, and C. Miclea, Rev. Roum. Phys. 28, 731 (1983).

265. K. G. McGregor, M. Calvin, and J. W. Otvos, J. Appl. Phys. 50, 369 (1979).

266. L. R. Yeh and N. Hackerman, J. Electrochem. Soc. 124, 833 (1977).

267. J. S. Curran and W. Gissler, J. Electrochem. Soc. 126, 56 (1979).

268. A. M. Novakovskii, N. Yu. Shibaeva, and M. P. Yashkov, Electrokhimiya 21, 473 (1985).

269. R. L. Cook, P. F. Dempsey, and A. F. Sammells, J. Electrochem. Soc. 133, 2287 (1986).

270. A. J. Nozik, B. R. Thacker, J. A. Turner, and J. M. Olson, J. Am. Chem. Soc. 107, 7805 (1985).

271. R. L. Cook, P. F. Dempsey, and A. F. Sammells, J. Electrochem. Soc. 133, 1821 (1986).

272. T. Pajkossy, I. Molnar, M. Palfy, and R. Schiller, Acta Chim. Hung. 101, 93 (1979).

273. J. E. Turner, M. Hendewerk, J. Parmeter, D. Neiman, and G. A. Somorjai, J. Electrochem. Soc. 131, 1777 (1984).

274. T. Pajkossy and L. Nyikos, Acta Chim. Hung. 117, 418 (1984).

275. M. P. Dare-Edwards, J. B. Goodenough, P. R. Trevellick, and A. Hamnett, J. Chem. Soc., Faraday Trans. I 79, 2027 (1983).

276. J. A. Tossel, D. J. Vaughan, and K. H. Johnson, Am. Mineral. 59, 319 (1974).

277. F. A. Benko, J. Longo, and F. P. Koffyberg, J. Electrochem. Soc. 132, 609 (1985).

278. R. Schiller, L. Nyikos, T. Pajkossy, and R. Mehnert, Akademie de Wissenschaftern der DDR 97, 79 (1984).

279. R. Schiller, L. Nyikos, and T. Pajkossy, Radiat. Phys. Chem. 26, 527 (1985).

280. F. A. Benko and F. P. Koffyberg, Mat. Res. Bull. 21, 1183 (1986).

281. L. G. J. de Haart and G. Blasse, J. Electrochem. Soc. 132, 2933 (1985).

282. S. Wakabayashi and T. Aoki, J. Physique Colloq. 1, 241 (1977).

283. A. Shamsi and W. E. Wallace, Mat. Res. Bull. 18, 389 (1983).

284. M. T. Mouhandess, F. Chassagneux, B. Durand, Z. Z. Sharara, and O. Vittori, J. Mat. Sci. 20, 3289 (1985).

285. Y. Matsumoto, M. Omae, I. Watanabe, and E. Sato, J. Electrochem. Soc. 133, 711 (1986).

286. F-T. Liou, C. Y. Yang, S. N. Levine, and K. Hakim, Extended Abstracts of Electrochem. Soc. 81-2, Abstract #572, 1371 (1981).

287. F. Liou, Ch. Y. Yang, and S. N. Levine, J. Electrochem. Soc. 129, 342 (1982).

288. H. Ono, H. Morisaki, and K. Yazawa, Jpn. J. Appl. Phys. 21, 1075 (1982).

289. K. Yazawa, H. Morisaki, and H. Ono, Alternative Energy Sources 4, 133 (1982).

290. T. Osaka, K. Ejiri, and N. Hirota, J. Electrochem. Soc. 131, 1571 (1984).

291. H. Tsubomura, Y. Nakato, M. Hiramoto, and H. Yano, Can. J. Chem. 63, 759 (1985).

292. H. Mettee, J. W. Otvos, and M. Calvin, Solar Energy Mater. 4, 443 (1981).

293. Ch. Leygraf, M. Hendewerk, and G. A. Somorjai, J. Phys. Chem. 86, 4484 (1982).

294. C. Leygraf, M. Hendewerk, and G. A. Somorjai, Proc. Natl. Acad. Sci. USA 79, 5739 (1982).

295. J. E. Turner, M. Hendewerk, and G. A. Somorjai, Chem. Phys. Lett. 105, 581 (1984).

296. G. A. Somorjai, and Ch. H. Leygraf, European Patent 105623, (1984).

297. M. S. Wrighton, P. T. Wolczanski, and A. B. Ellis, J. Sol. St. Chem. 22, 17 (1977).

298. R. S. Yeo, J. Orehotsky, W. Visscher, and S. Srinivasan, J. Electrochem. Soc. 128, 1900 (1981).

299. V. I. Birss, A. Damjanovic, and P. G. Hudson, J. Electrochem. Soc. 133, 1621 (1986).

300. S. Park, S. Ho, S. Aruliah, M. F. Weber, Ch. A. Ward, R. D. Venter, and S. Srinivasan, J. Electrochem. Soc. 133, 1641 (1986).

301. A. Heller, in "Energy Resources through Photochemistry and Catalysis", edited by M. Gratzel, (Academic Press, Inc., New York, 1983), p. 385.

302. M. Koudelka, A. Monnier, and J. Augustynsky, Extended Abstracts of Electrochem/ Soc. 82-1, Abstract #357, 586 (1982).

303. A. Heller, Extended Abstracts of Electrochem. Soc. 86-1, Abstract #338, 493 (1986).

304. A. Heller, D. E. Aspnes, J. D. Porter, R. G. Vadimsky, and T. T. Sheng, J. Phys. Chem. 89, 4444 (1985).

305. Y. Nakato, K. Ueda, and H. Tsubomura, J. Phys. Chem. 90, 5495 (1986).

306. T. Kobayashi, H. Yoneyama, and H. Tamura, J. Electrochem. Soc. 130, 1706 (1983).

307. A. F. Sammells and P. G. P. Ang, J. Electrochem. Soc. 126, 1831 (1979).

308. P. Richardson, P. Ang, and A. Sammells, Hydrogen Energy Progress 4, 805 (1983).

309. M. R. St. John, A. J. Tiller, R. L. Cook, and A. F. Sammells, J. Electrochem. Soc. 132, 1859 (1985).

310. K. D. Sieber, C. Sanchez, J. E. Turner, and G. A. Somorjai, Mat. Res. Bull. 20, 153 (1985).

311. C. Leygraf, M. Hendewerk, and G. A. Somorjai, J. Catal. 78, 341 (1982).

312. C. Leygraf, M. Hendewerk, and G. A. Somorjai, J. Sol. St. Chem. 48, 357 (1983).

313. J. F. Houlihan, T. Pannaparayil, H. L. Burdette, D. P. Madacsi, and R. J. Pollock, Mat. Res. Bull. 20, 163 (1985).

314. J. F. Houlihan, T. Pannaparyil, R. J. Pollock, A. Bain, and H. L. Burdette, Alternative Energy Sources 3, (Proc. Miami Int. Conf. 6th, 1983), p. 517 (1985).

315. A. H. A. Tinnemans, T. P. M. Koster, D. H. M. W. Thewissen, A. Mackor, and J. Schoonman, Ber. Bunsenges. Phys. Chem. 90, 383 (1986).

316. A. H. A. Tinnemans, T. P. M. Koster, A. Mackor, and J. Schoonman, Ber. Bunsenges. Phys. Chem. 90, 390 (1986).

317. T. Sakata and T. Kawai, in "Energy Resources through Photochemistry and Catalysis", edited by M. Gratzel, (Academic Press, Inc., New York, 1983), p. 331.

318. M. Gratzel, Acc. Chem. Res. 14, 376 (1981).

319. M. Gratzel, in "Energy Resources through Photochemistry and Catalysis", edited by M. Gratzel, (Academic Press, Inc., New York, 1983), p. 71.

320. M. Gratzel, Proc. Electrochem. Soc. 84, 441 (1984).

321. G. A. Somorjai, in "Photoelectrochemistry, Photocatalysis and Photoreactors", edited by M. Schiavello, (NATO ASO Series C: #146, Mathematical and Physical Sciences, (D. Riedel Publishing Company, Netherlands 1985), p. 389.

322. E. Borgarello, J. Kiwi, E. Pelizzetti, M. Visca, and M. Gratzel, Nature 289, 158 (1981).

323. D. S. Miller, A. J. Bard, G. McLendon, and J. Ferguson, J. Am. Chem. Soc. 103, 5336 (1981).

324. M. Gratzel, Extended Abstracts of Electrochem. Soc. 83-1, Abstract #721, 1062 (1983).

325. T. Shimidzu, T. Iyoda, and Y. Koide, J. Am. Chem. Soc. 107, 35 (1985).

326. W. Gissler and A. J. MacEyoy, Extended Abstracts of Electrochem. Soc. 83-1, Abstract #726, 1069 (1983).

327. N. N. Lichtin and K. M. Vijayakumar, Extended Abstracts of Electrochem. Soc. 83-1, Abstract #516, 782 (1983).

328. M. Fujii, T. Kawai, and S. Kawai, Chem. Phys. Lett. 106, 517 (1984).

329. K. W. Frese, Jr., and D. Canfield, Extended Abstracts of Electrochem. Soc. 83-1, Abstract #517, 784 (1983).

330. M. S. Wrighton, Extended Abstracts of Electrochem. Soc. 83-1, Abstract #720, 1061 (1983).

331. T. Yoko, K. Kamiya, A. Yuasa, and S. Sakka, J. Electroanal. Chem. 209, 399 (1986).

332. M. R. St. John, A. J. Furgala, and A. F. Sammells, Extended Abstracts of Electrochem. Soc. 81-2, Abstract #513, 1224 (1981).

333. R. D. Stramel and J. K. Thomas, J. Colloid Interface Sci. 110, 121 (1986).

334. J. K. Leland and A. J. Bard, J. Phys. Chem. 91, 5076 (1987).

335. M. Gratzel, J. Kiwi, and C. L. Morrison, J. Chem. Soc., Faraday Trans. I 81, 1883 (1985).

336. J. Moser and M. Gratzel, Helv. Chim. Acta 65, 1436 (1982).

337. N. M. Dimitrijevic, D. Savic, O. I. Micic, and A. J. Nozik, J. Phys. Chem. 88, 4278 (1984).

338. J. Haupt, J. Peretti, and R. Van Steenwinkel, Nouv. J. Chim. 8, 633 (1984).

339. H. Nakanishi, C. Sanchez, M. Hendewerk, and G. A. Somorjai, Mat. Res. Bull. 21, 137 (1986).

340. M. M. Khader, N. N. Lichtin, G. H. Vurens, M. Salmeron, and G. A. Somorjai, Langmuir 3, 303 (1987).

341. R. K. Iller, U.S. Patent 3969266, July 13, 1976.

342. J. F. Kovarik, U.S. Patent 3864142, February 4, 1975.

343. M. Maestri and D. Sandrini, Nouv. J. Chim. 5, 637 (1981).

BIBLIOGRAPHICAL NOTE

The author was born May 25, 1960 in Prague, Czechoslovakia where he lived until 1979. He attended Chemical Technical Institute in Prague where he majored in Chemical Engineering. In 1979 he came to Portland, Oregon, wherehe worked first at Tektronix Inc. as an electrocatalytic deposition operator. In September, 1980, he began study at the Portland State University where he graduated with B.S. in Chemistry in June, 1983. In September, 1983, he began study at the Oregon Graduate Center where he completed the requirements for the degree Doctor of Philosophy in Materials Science and Engineering in 1988. He is leaving the Graduate Center to accept a Research Analyst position at Boeing Aerospace Company in Seattle, Washington, where he will be working in Sesearch and Development on high transitiontemperature ceramic superconductors.